Modeling Leigh syndrome using patient-specific induced pluripotent stem cells

Inaugural-Dissertation

to obtain the academic degree

Doctor rerum naturalium (Dr. rer. nat.)

Submitted to the Department of Biology, Chemistry and Pharmacy

of Freie Universität Berlin

by

GIZEM INAK-GIRRBACH

From Istanbul

July 2019

The work was conducted from April 2015 until May 2019 under
supervision of M.D. Dr. Alessandro Prigione
at the Max Delbrück Center for Molecular Medicine
in the Helmholtz-Association.

I hereby confirm that I have written the thesis independently using solely
the aids mentioned and without illicit assistance from third parties.

1. Reviewer: Prof. Dr. Erich Wanker
2. Reviewer: Prof. Dr. Helge Ewers

Date of defense: 06.12.2019

Acknowledgment

First of all, I would like to thank Prof. Dr. Erich E. Wanker for allowing me to conduct this Doctoral Thesis at the Max-Delbrück-Center Berlin-Buch and also for his valuable feedbacks during the lab meetings as well as for reviewing this work. Furthermore, I would like to express my gratitude to Prof. Dr. Helge Ewers from Freie Universität Berlin, who took an interest in my project and kindly agreed to review this doctoral thesis.

Special thanks are owed to my supervisor Dr. Alessandro Prigione, for giving me the opportunity to work on this interesting project and guiding me with excellent and patient care. He has always been available and given me valuable advice. His honest feedback certainly helped me to become an independent scientist. I greatly enjoyed our regular scientific discussions, which motivated me to stay focused on the project. I shall not be forgetting to thank Prof. Dr. Markus Schülke-Gerstenfeld for providing patient skin fibroblasts for the project, valuable advice throughout the project, as well as providing his lab space and equipment for the complementation of some critical experiments.

Furthermore, I am deeply grateful to our collaboration partners within this project. In particular, I would like to thank Dr. Agnieszka Rybak-Wolf for generating the 3D cerebral organoid models. Special thanks to Peter Glazar for his valuable contribution in analyzing the transcriptomics data and to Dr. Chris Secker for providing the lentivirus encoding SURF1.

Moreover, I would like to thank all my colleagues and lab mates in the Prigione Group, who made it possible to work in a supportive and harmonic environment. I would like to thank Dr. Barbara Mlody for her constant availability for answering all kind of questions and for making the lab days more entertaining with her humorous nature. Thanks to Annika Zink for her presence and support. Her constant motivation to keep an eye on the stocks of small molecules needed for differentiation protocols and giving me advice on critical time points was very helpful. Also, I would like to thank Carmen Lorenz, who walked me through cell culture and other important techniques when I started working in the lab. Special thanks to Dr. Pawel Lisowski; without his knowledge and help, generating an isogenic line would not have been possible in such a short time. Thank you to Celina Kassner for her technical assistant. There were several bachelor and master students who worked in our lab. In particular, I would like to thank Tobias Hahn for finding the right corrected clone after months of screening. I want to express special gratitude to Ummi Ciptasari who was a motivated, and dedicated student who helped me get through the last phase of my Ph.D. period. Also would like to thank Group Wanker members for their cooperation and for providing a pleasant working atmosphere.

I express my deepest appreciation to my husband Kai for his constant support and confidence at all times and walking me through the hard and good times hand in hand. In addition, I would like to thank my close circle of friends who were great listeners. Especially, I would like to thank Basak Arslan for her unlimited support. Lastly, I cannot thank my lovely family enough. They were there whenever I needed them, supporting me regardless of distance.

Summary

Leigh syndrome (LS) is a severe early-onset neurodegenerative childhood disorder characterized by bilaterally symmetrical necrotic lesions in the basal ganglia region of the brain. It is a rare disease affecting 1/36,000 newborns, and affected ones display psychomotor regression and also lactic acidosis with peak mortality mostly before the age of three. It is a genetically and biochemically heterogeneous disorder caused by mutations of nuclear DNA (nDNA) or mitochondrial DNA (mtDNA) in more than 75 genes leading to disturbances in the mitochondrial respiratory chain. Mutations in the mitochondrial complex IV assembly factor, Surfeit locus protein 1 (SURF1), represent the most common cause and a severe form of LS. So far, *SURF1*-deficient animals have failed to recapitulate the neuronal pathology of human LS, hindering the understanding of the disease mechanisms. Thus, there is no effective therapy available.

To investigate the molecular mechanisms underlying the disease-specific neuronal cell death, I generated the first mechanistic human induced pluripotent stem cell (iPSC)-derived neuronal model of LS harboring *SURF1* mutations. *SURF1* iPSC-derived cultures showed aberrant bioenergetics already at the level of neural progenitors, disrupting their neurogenic potency. A biallelic correction of *SURF1* via CRISPR/Cas9 restored the bioenergetics and enhanced neuronal sprouting as well as synaptogenesis in *SURF1* iPSC-derived cultures. To study the manifestation of the spatial defects, cerebral organoids were generated. In contrast to corrected iPSC-derived organoids, *SURF1* iPSC-derived organoids appeared smaller in size and displayed neurodevelopmental defects. Ultimately, analyzing the transcriptomics data of iPSC-derived 2D and 3D cultures, some novel hints for possible therapeutic strategies were revealed. Different treatment strategies were tested on iPSC-derived neural progenitor cells (NPCs) function to find a potential strategy and two candidates were shown to have beneficial effects on the phenotypes: Coactivator of PGC1-α receptor, Bezafibrate, was shown to rescue bioenergetic defects via PPAR signaling pathway and inhibition of TGF-β1 receptor via SB-431542 was shown to rescue neurite outgrowth defects in *SURF1* iPSC-derived NPC cultures.

Altogether, this study is the first human iPSC-neuronal model for LS and gives insight into the role of *SURF1* mutations in neuronal cells in the context of LS pathogenesis. *SURF1* mutation caused aberrant energy metabolism and prevented neuronal maturation. With this study, NPCs were shown to be the first affected cell type in the neurodevelopmental cascade. Moreover, two candidate therapeutic targets have been suggested to improve the bioenergetics, and neuronal differentiation defects seen in patients derived neuronal cell model, which could be helpful for clinical disease research.

Zusammenfassung

Leigh-Syndrom (LS) ist eine schwere neurodegenerative Erkrankung bei Kindern, die sich durch bilateral symmetrische nekrotische Läsionen in der Basalganglienregion des Gehirns auszeichnet. Es ist eine seltene Krankheit, die 1 von 36.000 Neugeborenen betrifft. Betroffene Personen zeigen eine psychomotorische Regression und auch eine Laktatazidose und haben die höchsten Sterblichkeitsrate meist vor dem dritten Lebensjahr. Es handelt sich um eine genetisch und biochemisch heterogene Störung, die durch Mutationen von Zellkern-DNA (nDNA) oder Mitochondrien-DNA (mtDNA) in mehr als 75 Genen verursacht wird und zu Defekten der Atmungskette in den Mitochondrien führt. Mutationen im mitochondrialen Komplex IV Assemblierungsfaktor *SURF1* stellen die häufigste Ursache und eine schwere Form von LS dar. Bisher ist es nicht gelungen die neuronale Pathologie des menschlichen LS in *SURF1*-defizienten Tieren zu rekapitulieren, was das Verständnis der Krankheitsmechanismen erschwert. Daher ist bisher keine wirksame Therapie verfügbar.

Um die molekularen Mechanismen zu untersuchen, die dem krankheitsspezifischen neuronalen Zelltod und (auch der Gliazellenfunktionsstörung) zugrunde liegen, erstellte ich mittels humaner induzierter pluripotenter Stammzellen (iPSCs), das erste mechanistische Modell von LS welches *SURF1*-Mutationen enthält. Von *SURF1*-iPSCs abgeleitete Kulturen zeigten bereits auf der Ebene der neuronalen Vorläufer eine abweichende Bioenergetik, die ihre neurogene Potenz störte. Eine biallelische Korrektur von *SURF1* über CRISPR / Cas9 stellte die Bioenergetik und das verstärkte Sprießen von Neuronen sowie die Synaptogenese in von *SURF1*-iPSCs abgeleiteten Kulturen wieder her. Um die Manifestation der räumlichen Defekte zu untersuchen, wurden zerebrale Organoide erzeugt. Im Gegensatz zu den von iPSC-abgeleiteten Organoiden der korrigierten Linie, schienen die von *SURF1*-iPSC abgeleiteten Organoide kleiner zu sein und zeigten neurologische Entwicklungsstörungen. Letztendlich wurden bei der Analyse der Omics-Daten von iPSC-abgeleiteten neuronalen Kulturen einige neuartige Hinweise für mögliche Therapiestrategien aufgedeckt. An iPSC-abgeleiteten neuronalen Vorläuferzellen (NPCs) wurden verschiedene Behandlungsstrategien getestet und es wurde gezeigt, dass zwei Kandidaten vorteilhafte Auswirkungen auf die Phänotypen haben: Mit dem Coactivator von PGC1-α-Rezeptor Bezafibrate konnten bioenergetische Defekte durch Modifikation des PPAR Signalweg behoben werden. Es wurde gezeigt, dass die Hemmung des TGF-β1-Rezeptors durch SB-431542, Neuritenwachstumsdefekte in *SURF1*-iPSC-abgeleiteten NPC-Kulturen retten.

Zusammengenommen ist diese Studie das erste humane iPSC-neuronale Modell für LS und gibt einen Einblick in die Rolle von *SURF1*-Mutationen in neuronalen Zellen im Kontext der LS-Pathogenese. Die *SURF1*-Mutation verursachte einen abnormen Energiestoffwechsel und

verhinderte die neuronale Reifung. In dieser Studie wurde gezeigt, dass NPCs der erste betroffene Zelltyp in der neurologischen Entwicklungskaskade sind. Darüber hinaus wurden zwei mögliche therapeutische Ziele vorgeschlagen, um die Bioenergetik und neuronale Differenzierungsdefekte zu verbessern, die in einem vom Patienten abgeleiteten neuronalen Zellmodell auftreten und für die klinische Krankheitsforschung hilfreich sein könnten.

Table of contents

1. Introduction

More than a billion years ago, anaerobic bacteria were captured by primordial eukaryotic cells lacking the ability to use oxygen metabolically (Vafai et al., 2011). As this endosymbiotic relationship developed, the bacteria evolved into mitochondria and equipped host cells with aerobic metabolism, which is a much more efficient way of producing energy compared to anaerobic glycolysis. Although mitochondria are referred to as semi-autonomous organelles since they possess DNA, after years of evolution, they have become hard-wired with the host eukaryotic cell, and they are now under the dual control of nDNA and mtDNA (McFarland et al., 2010).

Mitochondrial diseases are described as a group of multisystem disorders caused by defects in components of the mitochondrial respiratory chain (RC), leading to the disruption of cellular energy processes. One of the significant challenges in mitochondrial diseases is their extreme clinical variability. Similar mitochondrial mutations associated with various distinct disorders and the same clinical condition may arise from several RC defects. For instance, *ATPase6* mitochondrial mutation can lead to diseases such as Neuropathy, ataxia, and retinitis pigmentosa (NARP), maternally inherited Leigh syndrome (MILS), and familial bilateral striatal necrosis (FBSN), while the nuclear mutations *SURF1, NDUSF4, and BCS1L* can all lead to Leigh syndrome (DiMauro et al., 2003). Additionally, they exhibit phenotypic heterogeneity affecting various organs in the body, whereas they mostly manifest themselves in cell types with high energy demands, such as muscle cells and neurons (Wallace et al., 2005). Brain energy metabolism is complex and highly relies on oxidative phosphorylation (OXPHOS), which is the ATP synthesis by the oxygen-consuming RC. Thus, the role of mitochondrial respiratory chain deficiencies in the pathogenesis of a wide range of neurological disorders has been the focus of the scientific community recently and more intensively. There are also common neurodegenerative diseases that are secondary mitochondrial dysfunctional such as Alzheimer´s, Spinal muscular atrophy (SMA), or Friedrich Ataxia which are not caused by mitochondrial mutations but involve mitochondrial dysfunction in their disease pathology (Inak et al., 2017).

Currently, there is no effective therapy for primary mitochondrial disease Leigh Syndrome. Investigating the underlying pathological mechanism is essential to identify molecular targets for specific and compelling therapeutic intervention, which then also could be useful for other common neurological diseases with a dysfunctional mitochondria component.

1.1 Leigh syndrome

1.1.1. Prevalence and clinical manifestations

LS (OMIM #256000), or subacute necrotizing encephalomyopathy, is a hereditary early-onset progressive neurodegenerative disorder. Neuropathologist Denis Leigh first described Leigh syndrome in 1951 (Leigh, 1951). It is considered a rare disorder, whereas it is relatively common as the incidence of 1 in 36,000 newborns (Darin et al., 2001). Higher incidences have also been reported in specific populations such as in the Faroe Islands (1:1700) and Saguenay Lac-Saint-Jean region of Quebec, Canada (1:2000) (Ostergaard et al., 2007; Morin et al., 1993). The clinical presentation of LS can be highly variable as the disease onset range starts from the neonatal period through adulthood. Mostly, the symptoms typically manifest during the first year of life, with congenital onset occurring in one-fourth of the cases. The disease is mostly leading to early death with a course that is variable but usually severe and has a peak of mortality before the age of three. Later onset and slower progression have also been reported (Rahman et al., 1996; Sofou et al., 2014; Rahman et al., 2017).

The first signs of LS seen in infancy are usually recurrent episodes of vomiting, difficulty in swallowing, which also leads to failure to thrive. Later on, during late infancy or early childhood, they exhibit severe muscle and movement problems as they may develop weak muscle tone (hypotonia), involuntary muscle contractions (dystonia), and problems with movement and balance (ataxia). These symptoms are mostly combined with the loss of sensation and weakness in the limbs (peripheral neuropathy). Additionally, incoordination of ocular movements is present in different forms. Individuals may develop weakness of the muscles moving the eyes (ophthalmoparesis) as well as rapid, involuntary eye movements (nystagmus), or degeneration of optic nerves (Lake et al., 2015; Lake et al., 2016). During the childhood period, they exhibit mental regression along with epileptic seizures. In most of the cases, patients undergo acute respiratory failure, and they may develop hypertrophic cardiomyopathy. Microcephaly cases have also been reported (Rahman et al., 2017).

1.1.2. Neuropathology and diagnostic methods

The pathology of the disease has relied on postmortem studies in the past, by the advent of computed tomography and magnetic resonance images (MRI), detection of the lesions have aided the diagnosis of the disease and the understating of its progression. The progressive encephalopathy is characterized pathologically by symmetric and focal necrotic lesions mainly in the basal ganglia which control movement. Its connected regions the cerebellum, which controls the ability to balance and coordinates movement; and the brainstem, which connects the brain to the spinal cord and controls functions as swallowing and breathing; also optic

nerves, which conveys visual information (Tiranti et al., 1998; Pecina et al., 2003; Rossi et al., 2003) (Figure 1.1.2.). Lesions were characterized histologically, and they showed necrotic lesions with vacuoles accompanied by demyelination. Demyelination is associated with a loss of oligodendrocytes directing the myelination of axons, which suggests an impairment in the electric transmission between the cells. There was relative preservation of neurons, whereas the presence of degenerated neurons was also high, and they showed the swelling or shrinking of neuronal cell bodies. The glial cells looked swollen as an indication for gliosis, a hypertrophic state of astrocytes, probably as a response to damage or insult in the central nervous system (CNS). Additionally, capillary proliferation has also been observed in some of the cases (Lake et al., 2015).

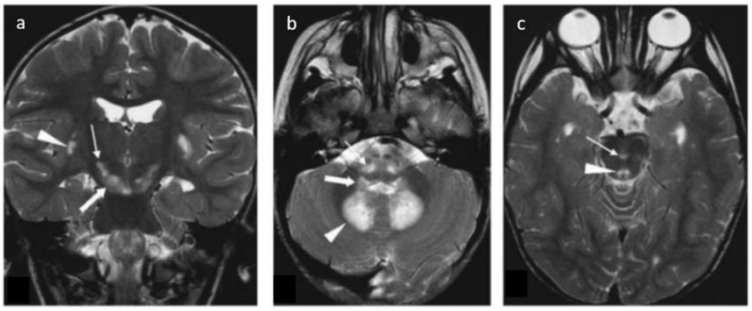

Figure 1.1.2: Magnetic resonance imaging of a LS patient
a, *Coronal T2-weighted image shows symmetric T2 prolongation involving the subthalamic nuclei (**thin arrow**). The substantia nigra (**thick arrow**), the posteroinferior portion of the putamina (**arrowhead**).* ***b,*** *T2 prolongation involves the medulla (**thin arrow**), inferior cerebellar peduncles (**thick arrow**), and dentate nuclei (**arrowhead**).* ***c,*** *Involvement of the interpeduncular nucleus (**thin arrow**) and central tegmental tract (**arrowhead**) (Image was adapted from Rossi et al., 2003).*

The other hallmark of LS is high lactate levels in the blood, urine, and cerebrospinal fluid. These measurements are used for the diagnosis of LS in addition to MRI imaging. Recently, tests for mitochondrial dysfunction, more specifically defects in oxidative OXPHOS, were suggested to be included for the diagnostic criteria for LS (Pecina et al., 2003; Baertling et al., 2014). Detailed family pedigree and the molecular genetic testing analysis should be conducted to understand if the cause is due to mitochondrial or nuclear mutations.

1.1.3. Disease genetics

The genetic cause of LS is exceptionally heterogeneous and can be inherited in different patterns. The genetic cause of the mitochondrial disease can reside in either mtDNA or nDNA and also can be X-linked (Gerards et al., 2016); NMIH). All of the affected genes are

directly or indirectly involved in the maintenance of mitochondrial OXPHOS, making LS one of the most prevalent mitochondrial disorders. Newly identified nuclear genetic causes are increasing, thanks to the use of next-generation and whole-exome sequencing and also attention to rare disease like LS has also been growing.

The inheritance pattern of mtDNA mutations is different from nDNA mutations since the traits do not segregate by Mendel´s law. It has a maternal inheritance pattern that mutations pass from an affected mother to the progeny. There are multiple mtDNA per mitochondrion and a few dozen mitochondria per cell, which leads to normal and abnormal mtDNA to be present in the same cell (Ruhoy et al., 2014). When mtDNA mutations can occur in a homoplasmic state, where all mtDNA molecules carry the same mutation, or in a heteroplasmic state, where only a proportion of mtDNA molecules carries the mutation (Darin et al., 2007; Inak et al., 2017). Both situations can give rise to LS. Also, cellular dysfunctions and clinical manifestations are believed to occur only after a certain threshold of mutation load has been exceeded. However, the mitochondrial threshold concept has been recently challenged as the same level of *MT-ATP6* mutations have been shown to cause both mild and severe neurological syndromes (Childs et al., 2006). The mtDNA mutation load cannot entirely explain the phenotypic variability since the patient-specific nuclear background attributes to the phenotype as well (Bénit et al., 2010; Inak et al., 2017). The single match between nDNA and mtDNA should, therefore, play an essential role in the disease pathogenesis of the mitochondrial disease.

nDNA mutations are, on the one hand, inherited in a Mendelian fashion, with autosomal recessive and X-linked inheritance as the etiology of LS. An autosomal recessive pattern of inheritance, where the cell has the two copies of the mutated allele, applies to most of Leigh syndrome-associated genes. For instance, recessive mutations in *SURF1* occur in about one-third of all LS cases and represent the single most common cause of LS (Darin et al., 2001; Ruhoy et al., 2014; Gerards et al., 2016). On the other hand, a small number of affected individuals display X-linked recessive inheritance when the mutated gene is on the X-chromosome, and one altered copy of the gene is sufficient to cause the disease. Thus males are affected by X-linked recessive disorders more frequently than females (NMIH). The most common form has been reported to be the X-linked pyruvate dehydrogenase (E1) alpha subunit gene (PDHA1) (Matthews et al., 1993).

Overall, whether of mtDNA or nDNA mutations, eventually all of these mutations exhibit their pathogenic effects on the mitochondrial respiratory chain where the primary source of energy production occurs. OXPHOS supplies the cell with energy in the form of ATP.

1.2. Cellular respiration in mitochondria

Mitochondria are about 0.5-1 µm in diameter and up to 7 µm long, whereas their shape and number per cell can vary on the particular tissue and their energy requirements (Krauss et al., 2001). They may appear in different shapes, but the general architecture is the same. They structurally have four compartments: the outer membrane, the inner membrane, the intermembrane space, and the matrix. They are all involved in various tasks that are pivotal for the cells. Cristae structures are formed by the enclosure of the inner membrane where they labyrinth into the mitochondrial matrix aiming to increase the surface of the inner membrane where OXPHOS takes place (Cogliati et al., 2016). Cristae are dynamic and undergo continuous remodeling according to mitochondria dynamics, which are biogenesis, fission, fusion, mitophagy, and motility. These mitochondrial dynamics also differ in different types of cells corresponding to changes in the energetic state requirements.

Mitochondria play a crucial role in cellular metabolism by producing the majority of cellular ATP via participating in several vital anabolic and catabolic pathways. Glucose, lipid fuels, and amino acids are the primary respiratory fuels, and mitochondria´ tasks can range from pyruvate oxidation to metabolism of fatty acids or amino acids to the generation of energy (DiMauro et al., 2003). Competition for respiration between substrates has always been indicated, whereas each organ has a unique metabolic profile, and they favor different use of fuels to meet their energy needs. For instance, under normal physiological conditions, glucose is considered as the sole fuel of the brain, while fatty acids are the heart´s primary source of fuel (Panov et al., 2014). The classical widely known cellular respiration via glucose could be divided into four main steps: glycolysis (where glucose is converted to pyruvate), pyruvate oxidation (where pyruvate enters mitochondrial matrix and produces Acetyl-CoA), citric acid cycle (Acetly-CoA goes through a series of reaction and produces NADH, $FADH_2$, and CO_2) and OXPHOS (where ETC and ATP synthesis take place) (Fernie, et al., 2004). The significant pathways take place in the mitochondrial matrix, and only glycolysis takes place in the cytosol.

In the context of mitochondrial disorders, peculiarly LS, the main focus is narrowed down to the disorders caused by disturbances in the OXPHOS system where the final biochemical reaction produces the fuel of the cell as adenosine triphosphate (ATP).

1.2.1. OXPHOS

OXPHOS is embedded in the lipid bilayer of the inner mitochondrial membrane and composed of five multimeric protein complexes (I, II, III, IV, and V) where many sequential biochemical reactions are coordinated. First, the energy released by the oxidation conserved in

the reduced forms of electron carriers NADH and $FADH_2$ is transported along with the complexes to molecular oxygen (with the aid of two electron carriers, ubiquinone (Q) and cytochrome c (cyt c) thereby reducing oxygen to water. Simultaneously, protons are pumped across the mitochondrial inner membrane from the matrix to the intermembrane space by complexes I, III, and IV. Lastly, ATP is generated by the influx of these protons back into the mitochondrial matrix through complex V. Cristae are also essential part of OXPHOS as 94% of complex III, and ATP synthase and approximately 85% of total cytochrome c are stored in this compartment (Scorrano, et al., 2002; Cogliati et al., 2016). It was reported that the number and density of cristae might reflect a cell´s demand for ATP.

This complex OXPHOS mechanism seems to be all handled in the inner membrane of mitochondria from a structural standpoint of view, whereas from a genetic point of view, OXPHOS is the teamwork of mtDNA and nDNA as it was mentioned before (Signes et al., 2018). Each of the complexes is assembled from multiple subunits, and these subunits could be encoded by both nDNA and mtDNA. Overall, 13 mtDNA-encoded structural proteins and approximately 77 structural nuclear-encoded proteins are present (Smeitink et al., 2006) (Figure 1.2.1.).

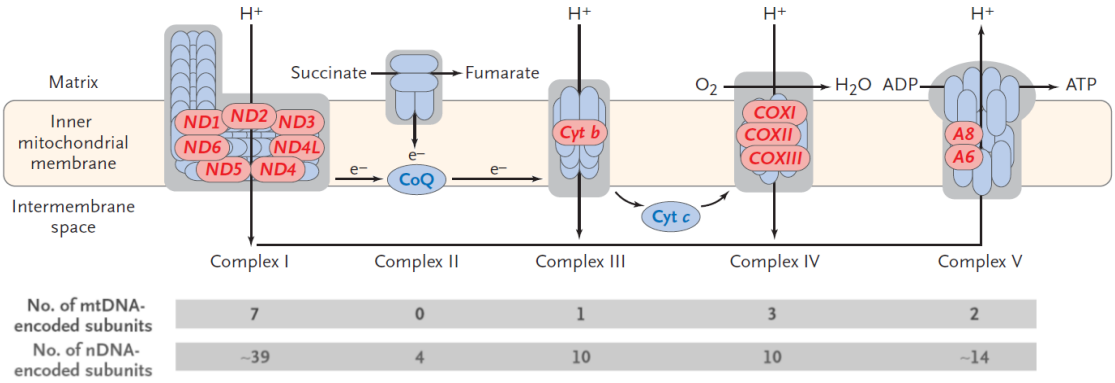

Figure 1.2.1.: The mitochondrial respiratory chain complexes

Multimeric five complexes are located in the inner mitochondrial membrane: reduced nicotinamide adenine dinucleotide (NADH) dehydrogenase–ubiquinone oxidoreductase (complex I, approximately 46 subunits), succinate dehydrogenase–ubiquinone oxidoreductase (complex II, 4 subunits), ubiquinone–cytochrome c oxidoreductase (complex III, 11 subunits), cytochrome c oxidase (complex IV, 13 subunits), and ATP synthase (complex V, approximately 16 subunits). The respiratory chain also requires two small electron carriers, ubiquinone (coenzyme Q10) and cytochrome c. The subunits encoded by mtDNA are highlighted in red, and the rest of the subunits are encoded by nDNA. Some encoded subunits by mtDNA or nDNA are indicated (Image was adapted from DiMauro et al., 2003).

Peculiarly, LS can be caused by mutations in more than 35 different genes of both nuclear and mitochondria origin and defects of the complexes impair OXPHOS, which leads to a

critically low level of cellular energy (Ruhoy et al., 2014). Every complex has a different composition, and the frequency of each mutation, causing a defect on a specific complex is different. Complex II, for instance, is the smallest complex of the respiratory chain, and all four subunits are nuclear-encoded. Mutations in complex II are relatively rare. While complex I is the first and largest enzyme of the respiratory chain with an abnormal respiratory chain enzyme activity under physiological conditions. Complex I mutations are also a common cause of LS (DiMauro et al., 2003; NMIH) and mutations in the NADH Dehydrogenase (Ubiquinone) Fe-Sulfur protein 4 (NDUFS4) subunit are reported to be the most frequent ones (Lake et al., 2016).

On the other hand, the mutations in the *MT-ATP6* gene result in the most common form MILS by changing the function of the proton channel of complex V which results in a loss of ATP activity (Santorelli et al., 1996). Additionally, loss of ATP synthase dimers is reported to disrupt crista architecture in LS mitochondria (Siegmund et al., 2018). Defects in respiratory subunits can display themselves in different ways such as increased reactive oxygen species (ROS), decreased mitochondrial membrane potential, increased mitochondrial and cytoplasmic NADH, and increased cytoplasmic calcium addition to low levels of ATP (Herst et al., 2017). The most common cause of nuclear-encoded mutation in LS is defects of complex IV.

1.2.2. COX enzyme

Cytochrome C oxidase (COX, Complex IV, EC 1.9.3.1) is the terminal enzyme of the ETC catalyzing the oxidation of cytochrome c and the reduction of oxygen to water. The redox centers, two copper centers (CuA and CuB) and two heme A moieties (a and a3), are involved in transferring the electrons from cytochrome c to molecular oxygen. It assists proton translocation, setting up the electrochemical proton gradient that drives the synthesis of ATP from ADP and phosphate by ATP synthase (complex V). Since COX is the terminal enzyme, without is function, OXPHOS cannot be carried to completion, and no ATP can be generated from mitochondria.

Mammalian COX from the bovine heart was crystallized and shown to consist of thirteen subunits, ten of which (COX4, COX5a, COX5b, COX6a, COX6b, COX6c, COX7a, COX7b, COX7c, COX8) are encoded by nDNA. Very recently a fourteenth subunit candidate, NDUFA4, which was initially thought to be part of complex I and also encoded by nDNA, was proposed to be part of COX (Balsa et al., 2012). Out of fourteen subunits, three of which (COX1, COX2, and COX3) are encoded by the mitochondrial DNA (mtDNA) and very similar to those from bacterial COX (Figure 1.2.1.). These three mtDNA encoded subunits constitute the hydrophobic catalytic core that is assembled first during the formation of the complex. The three core subunits alone

are sufficient to produce a fully functional COX enzyme complex in bacteria (Kadenbach et al., 2015). However, in mammalian COX, the catalytic core is surrounded by eleven nuclear-encoded structural subunits. COX biogenesis process is not fully known, but it first involves the maturation of the catalytic subunits COX1 and COX2, then the rest of the subunits are thought to be necessary for the stabilization of the catalytic core and its activity. Recently, it was shown that COX3 does not play a direct role in the catalytic core (Wirkström et al., 2018). Although the exact functions of these nuclear-coded subunits are not fully understood, they have been suggested to be a requirement for the stabilization and dimerization of the active holoenzyme complex. High catalytic capacity is highly dependent on the correct assembly of COX subunits, and it was shown to be the central rate-limiting control of mitochondrial respiration, and also mitochondrial membrane potential (Villani et al., 1998; Dalmonte et al., 2009).

There are also more than 30 known assembly factors involved in the integration of all the COX subunits and the maturation of the catalytic core, therefore the functionality of the enzyme. Most of the current knowledge of COX assembly is based on studies of mutant yeast strains with defective assembly (Barrientos et al., 2009) or human cell-line derived from patients with mutations in the structural subunits or assembly is assembly factors of COX (Williams et al., 2004). The assembly process is well conserved between yeast and human, and many of the assembly factors identified in yeast have known homologs in mammals. Improper assembly of COX due to assembly factors leads to malfunction of this enzyme, and defects give fatal damage, especially to the cells with high energy demands.

1.2.3. COX defects

COX defects are mainly categorized as assembly defects, either due to mutations in the mtDNA genes encoding structural components of the COX or in nDNA genes encoding assembly factors (Leary et al., 2013). They also show heterogeneity in the clinical phenotype, whereas the most common form of the disease is LS. The pathogenic mutations causing LS identified so far originate from nDNA encoded genes and are summarized in Table 1.2.3. Subunits are thought to be necessary for the stabilization of the catalytic core and its activity. COX3 was shown recently that not be playing a direct role in the catalytic core (Wirkström et al., 2018). High catalytic capacity is highly dependent on the correct assembly of COX subunits, and it was shown to be the central rate-limiting control of mitochondrial respiration, and also mitochondrial membrane potential (Villani et al., 1998; Dalmonte et al., 2009; Kadenbach et al., 2015).

Gene	Defect	Location	Reference
COX10	Complex IV	Nuclear	Antonicka *et al., 2003*
COX11	Complex IV	Nuclear	Böhm *et al*
COX15	Complex IV	Nuclear	Bugiani *et al., 2005*
LRPPRC	Complex IV	Nuclear	Debray *et al., 2011*
NDUAF4	Complex IV	Nuclear	Pitceacthly *et al., 2013*
PET100	Complex IV	Nuclear	Lim *et al.,2014*
SCO2	Complex IV	Nuclear	Joost *et al., 2010*
SURF1	Complex IV	Nuclear	Rossi *et al., 2003*
TACO1	Complex IV	Nuclear	Weraarpachai *et al., 2009*

Table 1.2.3.: Complex IV genes are known to be associated with LS

The regulation of COX activity is quite exceptional as it is the only OXPHOS complex containing tissue-specific, and it has developmentally regulated isoforms (Kadenbach et al., 2015; Kovářová et al., 2016). Therefore there are tissue-specific isoforms of COX that underlie the tissue-specific expression and the different degrees of severity seen in patients due to enzyme deficiency. For instance, mutations in the *SURF1* primarily affect the brain, whereas the mutations in *SCO2* or *COX15* affect the heart and the brain primarily while the mutations in *COX10* affect kidney and *SCO1* liver tissues (Böhm et al., 2006). One explanation proposed for the requirement of a fine-tuned regulation stems from the fact that COX and cytochrome-c to be the rate limiting step of ETC in cells and tissues under physiological conditions (Sinkler et al., 2017). Additionally, the free energy released in this reaction is much higher compared to the energy released from complexes I and III, which could make the target of regulation more important (Kennaway et al., 1990). Therefore the function of COX is tightly regulated and probably optimized according to the varying metabolic demands of the tissues.

Up to now, several pathogenic mutations causing LS in several assembly factors have been described, and the most common ones are shown to be in the *SURF1* gene (Ruhoy et al., 2011). The first identified and the most common form of the disease is due to defects of COX assembly factor SURF1 (Tiranti et al., 1998; Zhu et al., 1998; Péquignot et al., 2001; Pecina et al., 2003).

1.2.4. *SURF1* gene mutations

SURF1 gene of 4.7 kb is located on chromosome 9q34, the long arm of chromosome 9 at position 34.1, encodes a highly-conserved protein SURF1. It contains 9 exons and codes for 30 kDa protein of 300 amino acids. The domain structure of SURF1 protein is well conserved among eukaryotes and prokaryotes, which emphasizes its functional importance. It is located in the inner mitochondrial membrane and has been identified as a critical player in the early

assembly of COX (Hannappel et al., 2011), whereas its precise function remains unknown. However, the first results suggested that SURF1 may act in the formation of heme a3-CuB center (Yao et al., 1999) and later on, SURF1 has also been suggested to facilitate the insertion of heme a3 into the active site of COX (Khalimonchuk et al., 2010; Smith et al., 2005). The maturation and stability of the binuclear heme a3-CuB center limit the association of COX2 with COX1 and thus could lead to defects in the assembly of COX.

Recessive mutations in *SURF1* occur in about one-third of all LS cases and represent the single most common cause of LS (Zhu et al., 1998; Ruhoy et al., 2014). There have been approximately 80 mutations reported in the *SURF1* so far, and almost 40 of them were shown to be pathogenic. The truncating mutations are a result of nonsense mutations, aberrant splicing, or frameshift deletions (Wedatilake et al., 2013; Ruhoy et al., 2014). They cause translation of incomplete forms of SURF1 protein that are rapidly degraded or instability of SURF1 mRNA. In both cases, it prevents the synthesis of the protein and leads to loss of function of SURF1 protein. Without SURF1 assembly factor, COX does not correctly assemble, which impairs the mitochondrial energy production. It has been shown that the absence of SURF1 or its yeast homolog Shy1 causes a severe deficiency of COX (Tiranti et al., 1998; Péquignot et al., 2001) and the experiments that done in cultures of LS^{SURF1} fibroblasts or muscle fibers displayed decreased COX activity, low oxygen affinity and impaired maintenance of mitochondrial membrane potential (Pecina et al., 2004).

The molecular mechanisms underlying the neurological impairment caused by *SURF1* defects in still needs to be elucidated, but the significant obstacle in our understanding of the disease pathogenesis has been the scarcity of adequate model systems.

1.3. *In vivo* models of *SURF1* gene mutations

SURF1 is a highly conserved protein, and the studies conducted on its yeast homolog SHY1 suggest a role for SURF1 in the formation of catalytic centers. Both *SURF1* null-mutant human samples, as well as in yeast strains lacking Shy1, lead to functional alterations of the COX activity. However, SURF1 and Shy1 do not complement each other's defects, indicating functional divergence during evolution (Mashkevich et al., 1997; Nijtmans et al., 1998). There have been various *SURF1*-deficient *in vivo* models generated so far, ranging from invertebrates to mammals. In most cases, they have not mimicked the neuropathological symptoms seen in patients.

First *in vivo* models to study *SURF1* defects came from Zeviani group. They have generated two KO mice in which they have targeted different parts of the exons of *Surf1*. In the

first model, they disrupted the gene by targeted insertion of a neomycin cassette and replacement of exons five to seven. This has led to embryonic lethality in the majority of the KO mice (Agostino et al., 2003). The surviving ones showed different severity of COX deficiency among the tissues, mostly in muscle and liver, whereas not in the heart and brain. Defects in muscle tissues led to deficits in motor skills. However, *Surf1* null mice did not display any apparent neuropathological abnormalities. In the second model, the exon seven in *Surf1* was targeted. They again showed similar levels of COX defects like in the first mouse model, whereas the second model mice showed a prolonged lifespan. Once more, the new model also failed to show any neurodegenerative pathology (Dell'agnello et al., 2008). A prolonged lifespan phenotype was also observed in CNS specific *Surf1* knock-down Drosophila model (Zordan et al., 2006) and biochemical, and assembly COX defects were present. However, they also failed to show neuropathological symptoms and displayed a prolonged lifespan. This time, they tried to mimic the neurological phenotype by treating primary neurons of *Surf1* KO mice with kainic acid (glutamate agonists that induce Ca^{2+} excitotoxicity) which is known to lead to massive Ca^{2+} influx through NMDA receptors and consequently induces neuronal death (Dell'agnello et al., 2007). Primary neurons taken from these mice showed significantly reduced the rise of cytosolic and mitochondrial Ca^{2+}, and reduced mortality compared to controls.

Moreover, calcium-induced apoptosis was absent in KO mice, whereas it was prominent in control mice. This complete protection from Ca^{2+} dependent neurotoxicity induced might explain longevity phenotype seen in *Surf1* KO mice. A *surf1* knock-down zebrafish model, where they knocked down the gene expression with morpholine oligonucleotides, displayed reduced COX activity and developmental defects in endodermal tissue were observed (Baden et al., 2007). Interestingly, the development of secondary motor neurons was severely impaired (Baden et al., 2007). In the ubiquitous knock-down of Surf1 in Drosophila impaired larval development and lethality whereas the neuron-specific KD flies bypassed this lethality. They had abnormal photo behavior responses, whereas they did not show any sign of neurodegeneration (Zordan et al., 2006). Recently, there is another Drosophila model of LS based on the post-transcriptional silencing of CG9943, the Drosophila homolog of *SURF1*. Silencing of *Surf1* expression in Drosophila S2R cells led to selective loss of COX activity associated with decreased oxygen consumption and respiratory reserve (Da-Re et al., 2014), which strongly suggest SURF1 is essential for COX assembly and activity, hence mitochondrial function. After the sequential failure of small animal models, particularly in rodents; *SURF1* knock-out in piglets was generated very recently (Quadalti et al., 2018). *SURF1*−/− pig, the first swine model of mitochondrial disease, resulted in a severe lethal phenotype but the neurological defects were mild as there

was no overt neurodegeneration was detected in sections of entire CNS. However, they displayed a delay of CNS development with a significant reduction in the cortical thickness of the cerebrum along with cortical layering differences. Strikingly, a higher cellular density and a disorganized cortical structure with several immature neurons. There was no lactic acidosis and apparent COX deficiency. Moreover, *SURF1*−/− piglet revealed a different glial cell distribution pattern and microgliosis, whereas no demyelinating process.

Overall, *in vivo* models due to *SURF1* mutations have not necessarily recapitulated the human neuropathological condition. Specifically, *Surf1*-knock-out rodents show extended lifespan and no neurological defects. The failure of *Surf1* models probably arises from the fact that COX activity in humans is more dependent on SURF1 than other species (Kovarova et al., 2016). Moreover, the fundamental interspecies differences make it challenging to model the disease precisely in general, and also it is difficult to test the efficacy and the toxicity of potential drugs from rodents to the human. Interspecies differences have led to the failures of many clinical trials of potential drugs for many neurological and mitochondrial diseases in recent years (Inak et al., 2017). In order to develop treatments, the mechanisms underlying human disease pathologies have to be clarified. Thus human iPSCs have emerged as an attractive platform for overcoming these current limitations of animal models for disease modeling and drug discovery (Takahashi & Yamanaka, 2006; Shi et al., 2016; Sayed et al., 2016)

1.4. iPSCs for disease modeling [1]

iPSC technology, the groundbreaking discovery by Shinya Yamanaka and Kazutoshi Takahashi in 2006, enables the reprogramming of somatic cells into embryonic stem cells (ESCs)-like cells by the ectopic expression of four exogenous factors: *OCT3/4*, *SOX2*, *KLF4*, and *c-MYC* (collectively called OSKM factors) (Takahashi & Yamanaka, 2006). iPSCs are very similar to ESCs in their morphology, proliferative capacity, and developmental potential despite their background, which makes them a perfect model for disease modeling. Recent work has shed new light on the gene expression profiles confirming that human iPSCs share a typical signature with human ESCs, and they exhibit highly comparable global gene expression and epigenetic profiles (Guenther et al., 2010; Zhao et al., 2017). However, the gene-delivery methods of reprogramming can affect the quality of resulting iPSCs, and non-integrating methods have been suggested to generate iPSCs closer to ESCs in their transcriptional profiles (Kang et al., 2015).

[1] *The text and figures in section 1.4 partially have been reused with modifications from the published version:* ***Inak, G.****,. et al. Concise Review: Induced-pluripotent stem cell-based drug discovery for mitochondrial disease. Stem Cells. https://doi.org/10.1002/stem.2637 (2017).*

iPSCs have the capacity for self-renewal and differentiation, and can also be generated from the patients' skin fibroblasts or other somatic cell sources like blood cells. Following the generation of iPSCs, they can be differentiated into several cell types that are known to be affected by the individual patient. There has been an enormous advancement *in vitro* differentiation protocols, which increases the robust generation of the affected cell types and decreases the cell-to-cell variability. In our review, it is also explained why patient iPSC-derived neurons appear as an ideal cell type for dissecting the pathogenetic mechanisms of mitochondrial neurological diseases. Since they represent the disease-affected cell type with the correct OXPHOS-dependent metabolism and carry the patient-specific nDNA and mtDNA match (Inak et al., 2017). On the other hand, iPSC-derived neural progenitor cells (NPCs) have also been suggested as a useful cellular model system for drug discovery of the mitochondrial disease previously and also in our lab. Mitochondria within NPCs derived from mouse iPSCs (Choi et al., 2015) or human iPSCs (Beckervordersandforth et al., 2017; Lorenz et al., 2017) acquire an elongated morphology with defined cristae and dense matrices. This morphological change is accompanied by a metabolic shift toward OXPHOS metabolism that resembles that of differentiated iPSC-derived neurons.

Despite the advantages stated above, a significant challenge in the field of disease modeling using iPSCs is to discriminate the *in vitro* phenotype from the specific causative mutations and the individual´s genetic background. The field of precision medicine has become very important to overcome the heterogeneity of disease manifestations among patients. These days, gene editing of nuclear mutations in patient iPSCs has almost become a standard protocol. The most commonly used ones are TAL effector nucleases (TALENs) or the clustered regularly interspaced short palindromic repeats (CRISPR/ Cas9) system (Shi et al., 2017; Liu et al., 2018). These precise isogenic controls differ only at the genome-edited loci from the parental lines, which helps researchers to correlate the genetic mutations with the disease phenotypes without any other confounding influences from the genetic background.

The advantage of iPSC technology that iPSCs allow the development of innovative and effective cellular model systems in a personalized approach. Their use may significantly benefit the search for treatments against debilitating diseases. In the past, phenotype-based assays were limited by the lack of high throughput techniques, the weakness of disease-associated read-outs, and the limited access to biological material. This has now radically changed following the discovery of iPSCs. Patient-derived iPSCs can be differentiated into disease-relevant cell types, including those that are commonly not available, such as neurons and glia. Screenings conducted on such differentiated cells could be based on highly significant cellular phenotypes

that become apparent within patient-specific disease-relevant cellular contexts (Khurana et al., 2015; Liu et al., 2018). Once the correct iPSC-derived neural cell model has been selected, several technological platforms may be applied for compound screenings. One of the most commonly used techniques is the cellular image-based high-content screening (HCS) analysis (Xia et al., 2012). Also, target-centered screenings can be performed in iPSC derivatives, where the effects of the target modulation can already be monitored within the correct cellular environment. All these approaches might enable the identification of drug candidates that have a higher chance of success rate and the potential to be applied in a personalized manner. Additional challenges of iPSC-based drug discovery are inherent to all *in vitro* cellular models, which may be dependent on the culture conditions and may not fully recapitulate the complex response of a whole organism. Cellular systems, e.g., neurons, cardiomyocytes, hepatocytes that are differentiated from the same iPSC lines can be tested for particular compounds. This "patient-in-a-dish" approach has the potential to predict the effect of a drug within different disease-relevant biological environments (Figure 1.4.).

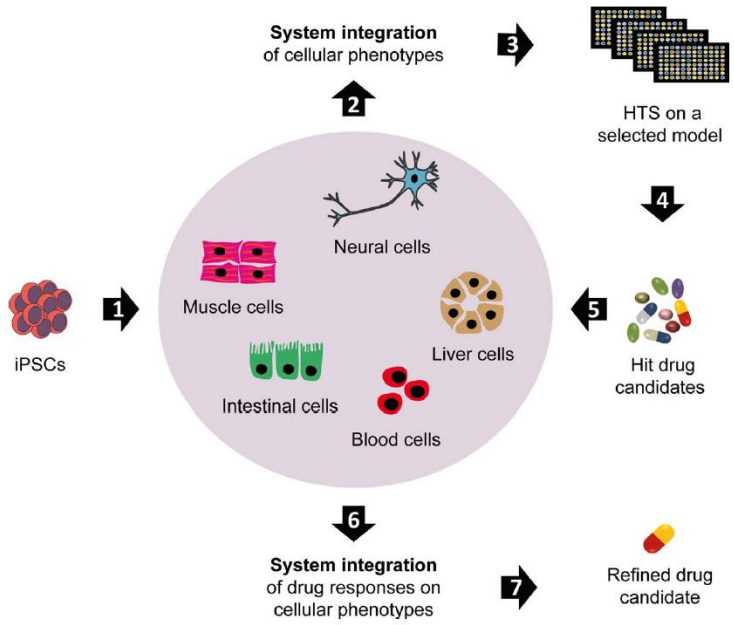

Figure 1.4.: iPSC disease modeling and drug discovery
iPSCs can be differentiated into several cell types that are known to be affected by the individual patient. Using these cell types, it may be possible to identify disease phenotypes that are patient-specific and/or cellular-specific. One of the analyzed cell types can then be used as a model for carrying out HTS (high-throughout screening). The obtained hit drug candidates can be applied on all the iPSC-derived cell types to analyze the efficacy and toxicity of the compounds within different patient-specific cellular systems. The integration of these responses may allow identifying with increased predictive power those drugs that have a higher chance to succeed once administered to the individual patient (Image from Inak et al., 2017).

A more physiological approach would involve the use of three-dimensional (3D) organoids, which are complex brain region-specific structures containing both neuronal and glial cells (Keleva et al., 2016). Cerebral organoids can be derived from human PSCs through spontaneous differentiation and allow modeling of whole brain development. Also, it is possible to use patterning factors to derive brain region-specific organoids. These structures enable the investigation of individual brain regions and have been used to demonstrate a direct connection between the Zika virus and human microcephaly (Lancaster et al., 2013; Qian et al., 2017). Human PSC-derived cerebral organoids still do not show the signs of functional maturation of the post-natal and adult human brain. However, the use of miniaturized spinning bioreactors may significantly improve the future applications of cerebral organoids for HT screenings (Qian et al., 2017). Finally, the reproducibility should be critically improved to reach a state in which the derived 3D structures consistently exhibit similar traits—shape, size, and cellular composition- under the same experimental conditions (McCauley et al., 2017).

Overall, the combination of iPSC, gene editing, and genome-wide technologies along with fast-growing knowledge of efficient differentiation protocols allow us to systematically and faithfully model human disease in relevant human cell types. This also appears as a robust model system which may allow conducting personalized drug discovery of disorders which may ultimately enable the identification of curative treatments against these debilitating conditions. Recent advancements in the development of human iPSC-derived three-dimensional (3D) models allowing mimicking *in vivo* tissues and organs eventually could aid to explore complex disease etiologies in a meaningful way to create precise therapeutic strategies in the upcoming era.

2. Aim of the study

The main aim of this study was to develop a novel human iPSC-based model of Leigh syndrome carrying homozygous *SURF1* mutations (LS^{SURF1}) to investigate the molecular mechanisms underlying the neuronal pathology of predominantly basal ganglia region. Ultimately, this model may enable the development of novel treatment strategies against a debilitating and, so far, untreatable condition.

The objectives planned to fulfill the aim were:

a) Generating isogenic iPSC pairs via using genome editing technologies

b) Differentiating generated iPSCs into neuronal/astrocyte composite cultures

c) Investigating the genotype and phenotype interplay in the obtained iPSC-derived composite cultures

d) Screening for potential therapeutic strategies on the identified disease-associated phenotypes

3. Results

3.1. LS patient donors (LS^{SURF1})

The skin fibroblasts were obtained from three LS^{SURF1} patients from two distinct consanguineous families: SURF1 A (S1A) line carries the homozygous mutation c.530T>G (p.V177G), and SURF1 B (S1B) and SURF1 C (S1C) lines which were taken from siblings carry the same homozygous mutation c.769>A (p.G257R). All of the mutations are missense mutations which lead to a change from one amino acid to a different amino acid in a protein. The healthy control fibroblasts BJ and CON1 were previously characterized in our lab and used in our study (Lorenz et al., 2017). All of the fibroblast cell lines used in this study are summarized in Table 6.1.1.A. with the background information.

3.1.1. Case reports

Prof. Schülke reported that the boy S1A (A.II.1) was the only child of healthy parents, who are first-degree cousins from Turkey (Figure 3.1.2. a). His disease manifested with a pronounced action tremor and prolonged episodes of hyperventilation at the age of 2 years. Due to progressive ataxia, he was only able to walk independently between 1-3 years of age. Severe dystonic episodes responded well to L-DOPA/Carbidopa (1.5 mg/kg BW) initially, but the effect wore off despite dosage increase to 12 mg/kg BW. From the age of 6 months, his growth fell below the third percentile. At 18 years of age, his height was 45 cm below and his head circumference 8 cm below the third percentile. Seizures were treated successfully with Levetiracetam. From the age of 15 years, frequent metabolic crises with respiratory insufficiency required intermittent mechanical ventilation at home through a tracheostoma. His clinical situation improved under therapy with the PPAR-agonist bezafibrate (8 mg/kg BW). In his later years, the patient was unable to speak, but he was very aware of things happening around him and able to understand spoken language. Due to his swallowing difficulties, he was fed through a percutaneous gastrostoma from the age of 15 years. The patient died at the age of 25 years from a bacterial infection and sepsis.

Another family´s both affected children, a girl S1B (**B.II.1**) and a boy S1C (**B.II.2**) were born to healthy consanguineous parents from Turkey (Figure 3.1.2. b). In the girl, parents observed psychomotor regression and ataxia from the age of 3 years with problems swallowing liquids, repeated cyanotic attacks, and ptosis. Seizures started at 4 years of age, and she died at the age of 8 years in a catabolic crisis with global respiratory failure. The boy was born with hypospadias grade II and was very hirsute from birth. By the age of 3.5 years, he lost muscle force and the ability to walk, sit, and speak. Triggered by a febrile *Mycoplasma pneumoniae*

infection, he developed choreiform movements of arms and legs with hyperventilation. The boy died from global respiratory and cardiac failure at the age of 5 years.

3.1.2. Molecular and functional characterization

Sequencing of *SURF1* in S1A fibroblast line showed a homozygous variant (c.530T>G, NM_003172) in exon six that was heterozygous in both parents. Segregation of the mutation was verified by primer induced restriction analysis (PIRA). The PCR primer sequences and are listed in supplementary data. The PCR product of 141 bp was cut by *Sma* I into 23+118 bp in the presence of the mutation (Figure 3.1.2. a). The mutation causes the exchange of an evolutionary highly conserved valine for a glycine (p.V177G). The variant was absent in the ExAC database. On the other hand, the sequence analysis of *SURF1* in S1B and S1C fibroblasts showed a homozygous c.769G>A variant in exon 8 causing the exchange of a highly conserved glycine for an arginine (p.G180R). The PCR product of 437 bp was cut by *Ava* II into 292 + 145 bp fragments only in the of the mutation (Figure 3.1.2. b). The PCR primer sequences are listed in Section 6.2.4. To understand if the protein SURF1 was expressed in the patient fibroblasts, Western blot analysis was conducted, and SURF1 protein was absent in all of the patient fibroblast lines (S1A, S1B, and S1C) (Figure 3.1.2. c).

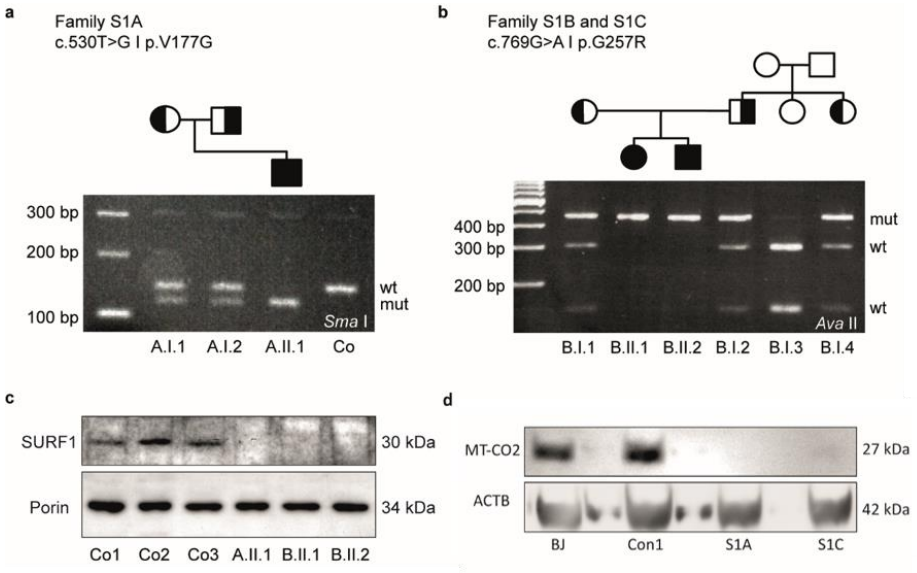

Figure 3.1.2.: Molecular and functional characterization of LS^{SURF1} fibroblast lines

a-b, *Pedigrees of both families; segregation between the LS phenotype with homozygosity for the c.530T>G mutation in the families of S1A patient* ***(A.II.1)*** *and for the c.769G>A mutation in the family of S1B* ***(B.II.1)*** *and S1C patients* ***(B.II.2****). The mutations were assessed via PIRA using SmaI and AvaII, respectively.* ***c-d,*** *Immunoblot analysis showed that cultured skin fibroblasts from patient lines do not express SURF1 or MT-CO2, probably due to the instability of the mutant protein. The mitochondrial protein*

Porin (VDAC1) and ACTB were used a loading control, respectively. (Contributions are indicated in section 8.3).

In the second Western blot analysis, an antibody against mitochondrial subunit MT-CO2 (COX2) was used. Patient fibroblast lines S1A and S1C did not express MT-CO2 protein while healthy control fibroblasts expressed both SURF1 and MT-CO2 protein (Figure 3.1.2. d). (*The role of COX2 in the assembly and functionality of COX enzyme was previously discussed in the section 1.2.1.*).

3.1.3. Clinical and neuropathological features

Cranial MRI uncovered bilateral basal ganglia necroses and T_2-signal intensities in the brainstem in the *Area postrema* for patient S1A (Figure 3.1.3. a-c) and the characteristic basal ganglia necroses of Leigh syndrome for patient S1C (Figure 3.1.3. d-f).

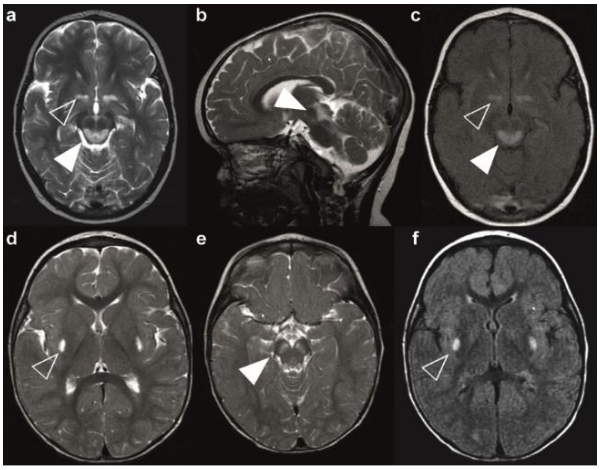

Figure 3.1.3.: MRI images of LS^{SURF1} patients
a-c, *Cranial MRI images of S1A patient at 2.3 years and* ***d-f,*** *of S1C patient at 1.7 years of age. Open arrowheads depict T2-signal intense lesions in the basal ganglia as the pathological hallmark of LS. The closed arrowheads point at brainstem lesions compromising the formatio reticularis (**a, b**) and the substantia nigra (**e**) likely being associated with hyperventilation and dystonia.* ***c*** *and* ***f****, The lesions are accentuated further in the FLAIR sequences. (Contributions are indicated in section 8.3).*

The other vital signatures of the disease are high lactate levels in the blood, urine or CSF samples, and the defects of COX activity in muscle biopsies. It was reported that CSF lactate was elevated to 4.3 mmol/l (N: <2) in patient S1A. Muscle biopsy at two years revealed a pronounced reduction of COX staining and an increase of neutral lipids. Low cytochrome C oxidase activity in the muscle (15 mU/mg NCP, N: 90-281) and the mitochondria-enriched fraction of cultured skin fibroblasts (130 mU/U CS, N: 680-1190) confirmed COX deficiency. Enzyme activities of the other respiratory chain complexes were normal. S1C patient had lactate levels at 4.5 mmol/l (N: <2). The biochemical investigation confirmed the COX deficiency in the

muscle (158 mU/U CS, N: 520-2080) and in cultured fibroblasts (100 mU/U CS, N: 342-627). The mitochondrial morphology appeared normal in the muscles of LS^{SURF1} patients in the EM images even though they had COX deficiency (Suppl. Figure 3.1.3.). Muscle biopsy of patient S1B also revealed a negative COX-staining. Other OXPHOS complex activities were average.

3.1.4. The bioenergetic profile

SURF1 mutations impair the oxidative phosphorylation system of the mitochondria the first aim was to understand if *SURF1* mutations have an exclusive effect on the bioenergetic profile of the skin fibroblasts. In order to dissect the functional consequences of *SURF1* mutations on cellular bioenergetics, the Seahorse XF Cell Mito Stress assay was conducted. The assay gives multiple parameters which give an insight into the mechanism of mitochondrial dysfunction in living cells. *(Detailed explanation of this assay is provided in section 7.1.8.).*

Therefore fibroblasts of LS^{SURF1} patients (S1A and S1C) and healthy controls (BJ and CON1) were used. The mitochondrial respiration was assessed by measuring the oxygen consumption rate (OCR), ATP production-coupled respiration, and maximal respiration. All of the measurements were conducted under basal condition followed by sequential addition of oligomycin (1 μM), FCCP (1 μM), rotenone and antimycin (1 μM) as indicated in (Figure 3.1.4. a). There were no differences in mitochondrial between healthy controls and LS^{SURF1} patients at the level of skin fibroblasts (Figure 3.1.4. b).

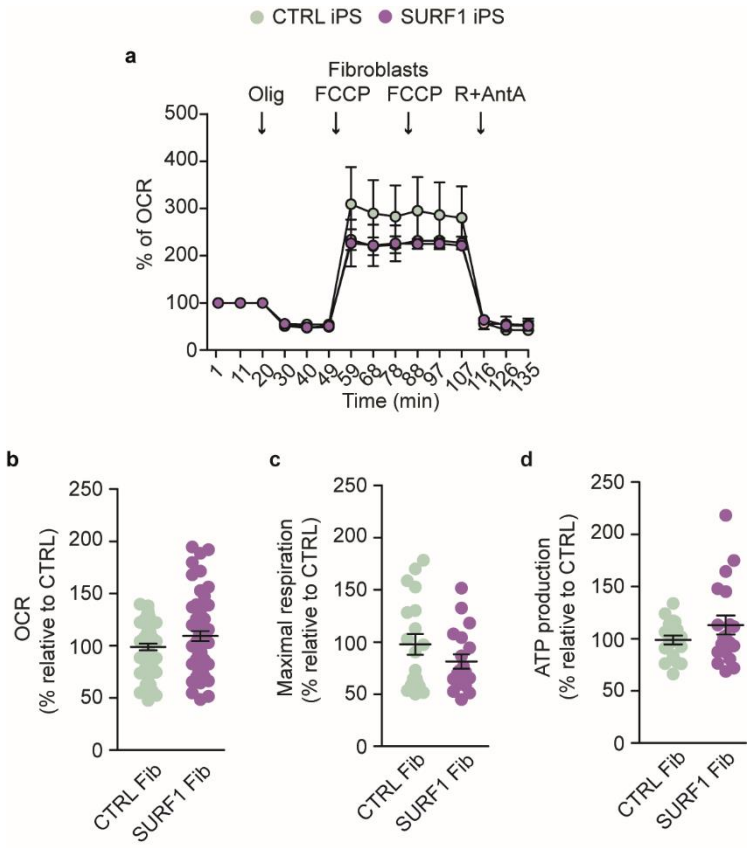

Figure 3.1.4.: Bioenergetic profiling of fibroblast cultures of healthy controls and LS ^{SURF1}
***a**, Oxygen consumption rate (OCR) profile in SURF1 fibroblasts (S1A and S1C) and healthy controls (BJ and CON1) (mean +/- s.e.m.; n=2 independent experiments).* ***b-e**, OCR, maximal respiration, and ATP production in fibroblasts cultures (mean +/- s.e.m.; n=2 independent experiments; Mann-Whitney U test; not significant).*

3.2. Generation of LS^{SURF1} iPSCs

3.2.1. Non-integrative reprogramming method

The four ``Yamanaka factors´´ were delivered into skin fibroblasts S1A, S1B, and S1C using CytoTune-iPS 2.0 Sendai reprogramming kit which has been an efficient integration-free method of iPSC production available (Ban et al., 2011; Fusaki et al., 2009; Seki et al., 2010; Tokusumi et al., 2002). After delivering Sendai virus to patient skin fibroblasts; elongated cell morphology has been slowly changed, and round shape morphologies began to form after 14 days of post-transduction (Figure 3.2.1.). As the PSC-like colonies got more prominent, they were picked and used for pluripotency characterization (Figure 3.2.1. b). There were no colony formations observed in S1B fibroblast culture. Only two patient fibroblasts were reprogrammed into iPSCs in this study, and I labeled them as SVS1A and SVS1C (Figure 3.2.1. b). The pluripotent stem cell lines used in this study were summarized in Table 6.1.1.B. with the background information.

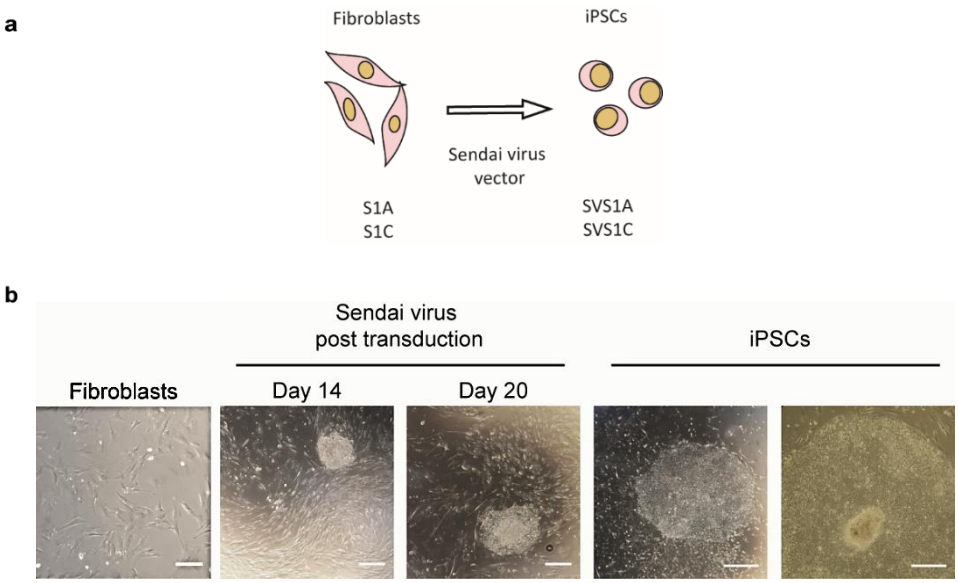

Figure 3.2.1.: Generation of LS^{SURF1} iPSCs from skin fibroblasts

a, *A diagram representing the reprogramming of fibroblasts using Sendai virus (SeV). Skin fibroblasts from SURF1 (S1A and S1C) were transduced with the CytoTune-iPS 2.0 Reprogramming kit forming SURF1 iPSCs SVS1A and SVS1C.* ***b,*** *Bright field images of fibroblasts show the morphological changes of the cells (from elongated shape towards round shape) around day 14. Bright field image showing mature iPSC colony morphologies after 20 days of transduction. Scale bars: 50 µm.*

3.2.2. Molecular and functional characterization

The cultured iPSC colonies can be detected under the microscope by their morphology, whereas detailed characterization of iPSCs is required for the registration of stem cell lines.

3.2.2.1. Mutation analysis

Next aim was to confirm the genetic identity of generated iPSC lines, genomic DNA from the respected lines was isolated, and it was used as a template for PCR amplification of the *SURF1* sequence after checking the purity on Nanodrop. The primers for each patient lines were designed separately and are listed in section 6.2.4. Amplification of a nuclear DNA region containing the c.530T>G for SVS1A line and c.769>A for SVS1C line was carried out along with a control line. The PCR protocol is listed in section 7.2.5. PCR products of the expected size were identified by agarose gel electrophoresis (Suppl. Figure 3.2.2.1.). Next, the PCR products were sent for Sanger sequencing after the gel-extraction procedure, and the sequencing results conducted by forward and reverse primers confirmed the mutations on the specific locations retain (Figure 3.2.2.1.). This confirms that Sendai virus reprogramming did not cause any alterations on the mutation site for both lines SVS1A and SVS1C.

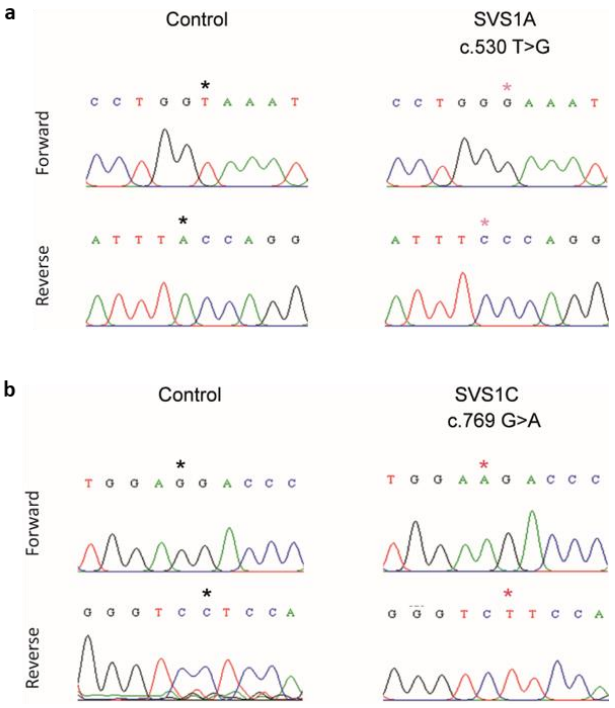

Figure 3.2.2.1.: Molecular characterization of iPSCs of LS^{SURF1}

***a-b**, Electropherograms showing both forward and reverse wild-type sequences of SURF1 labeled as control and the nucleotide changes in patient iPSCs SVS1A (left), and in SVS1C (right). Stars in pink represent the nucleotide substitutions, c.530 T>G (SVS1A) and c.769 G>A (SVS1C). Stars in black represent the wild-type condition of the mutation site.*

3.2.2.2. Pluripotent identity analysis

In order to show the pluripotent identity of the generated iPSCs, first immunohistochemistry analysis was conducted. Both lines expressed endogenous protein markers associated with pluripotency, including NANOG, TRA-1-60, and LIN28 (Figure 3.2.2.2. a). Next, the pluripotency-associated transcription factors were evaluated by quantitative real-time polymerase chain reaction (qPCR), and human embryonic stem cell (hESC) line H1 was used as a positive control. SVS1A and SVS1C expressed pluripotency-associated genes, including *OCT4, NANOG, SOX2*, *GDF3, DPPA4, and DNMT3B* in a similar fashion as the hESC line H1 (Figure 3.2.2.2. b). Only SVS1A showed fewer expression levels for *NANOG and SOX2* compared to the control line. Lastly, to check the *in vitro* differentiation potential of reprogrammed cell lines was checked. iPSCs were kept in suspension culture, they formed embryoid bodies and differentiated into different germ layers expressing markers of ectoderm (PAX6), mesoderm (SMA), and endoderm (SOX17) (Figure 3.2.2.2. c).

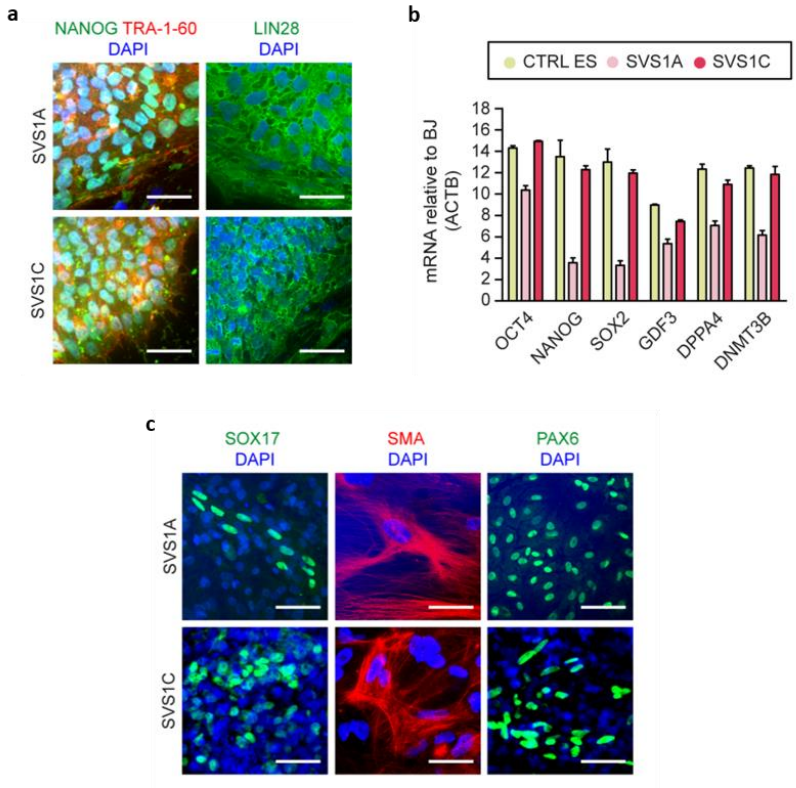

Figure 3.2.2.2.: Functional characterization of iPSCs of LS ^{SURF1}

a, *Representative images of immunofluorescence analysis showing pluripotency-associated marker proteins such as NANOG, TRA-1-60, and LIN28 in SVS1A and SVS1C. Scale bar: 50 µm.* ***b****, Quantitative real-time RT-PCR of pluripotency-associated markers in CTRL ES (H1) and SURF1 iPSC (SVS1A and SVS1C). Data were normalized to ACTB (mean +/- s.d.; n=2 independent experiments).* ***c****, Embryoid body based in vitro differentiation analyses of SVS1A and SVS1C showing their ability to differentiate into three germ layers and demonstrated here by positive markers for endoderm (SOX17), mesoderm (SMA), and ectoderm (PAX6). Nuclei were counterstained with Hoechst. Scale bar: 50 µm.*

3.2.2.3. Characterization of genome rearrangements

Reprogramming of fibroblasts to iPSCs, routine *in vitro* maintenance of iPSCs, and genetic manipulation of iPSCs could cause genomic instability. Therefore, frequent evaluation of the genomic integrity of stem cells is required. There are different methods to detect genomic aberrations or mutations on a genome-wide scale. In order to reach a higher resolution, the method of choice in this study is array-based technology, which allows us to investigate copy number variations (CNVs) across the whole genome at kb resolution (Le Scouarnec et al., 2011). A single nucleotide polymorphism (SNP) array method, shows a variation at a single site in DNA. The virtual karyotyping analysis showed no abnormalities, which means there is no gain or loss of variations in a deleterious way. The genomic integrity between fibroblasts and iPSCs was maintained (Figure 3.2.2.3.).

In order to have a complete profile of chromosomal DNA sequence as well as the information of the mitochondrial DNA of the generated lines, we have provided DNA samples for whole genome sequencing (WGS). The analysis is ongoing.

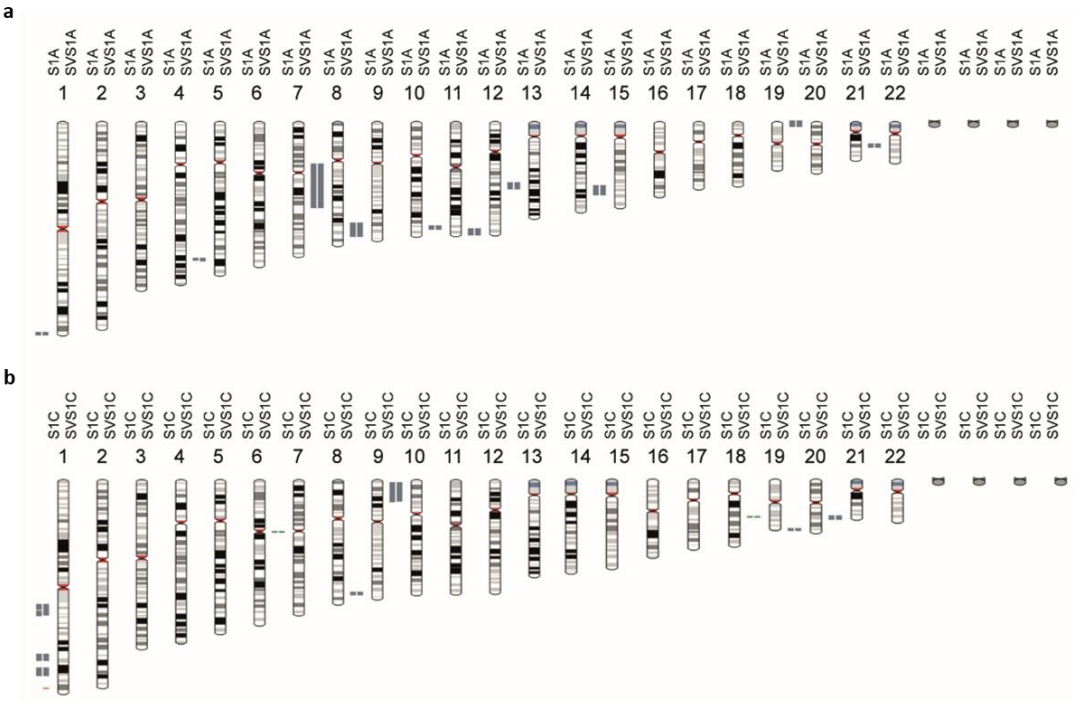

Figure 3.2.2.3.: Virtual karyotyping analysis to evaluate the genomic integrity of LS^{SURF1} iPSCs
a-b, *SNP array analysis confirmed that SVS1A and SVS1C carried a normal karyotype and were derived from the original fibroblast cells S1A* ***(top)*** *and S1C* ***(bottom)****, respectively. Virtual karyotyping is digital information reflecting a karyotype to evaluate genomic integrity, and it can detect genomic copy number variations at a higher resolution level. (Contributions are indicated in section 8.3).*

3.3. Generation of isogenic pairs via genome editing technology

The next step was to employ gene editing techniques on generated lines to create isogenic pairs which can provide the best experimental design for accurate disease modeling. The strategy was to have isogenic pairs for patient iPSC lines SVS1A and SVS1C by correcting the mutations on the *SURF1* gene. The isogenic line pairs would come from the same origin; match in genetic background, epigenetics, differentiation capacity, derivation, and adaptation to culture.

3.3.1. TALEN-based isogenic pair for SVS1A line

After generating clinically feasible SVS1A iPSCs, the aim was to employ TALENs system for precise correction of 530T>A on *SURF1* gene in SVS1A iPSCs and to introduce the mutation 530T>A on both alleles in *SURF1* gene in control TFBJ iPSC line. The strategy of generating TALEN-based

isogenic pair for SVS1A is schematized in Figure 3.3.1. There are different kits provided for TALEN technology, and the method of choice was Musunuru/Cowan Lab TALEN kit. Instructions were provided on the Addgene website for engineering transcription activator-like effectors (TALs) to bind to the desired DNA sequence. Each codon has a specific position on the well plate provided by the kit, and the designed sequences are listed in section 6.2.4.

After the target sequence was identified, string pairs (TALE 1 & 2) were designed to correct the mutation 530T>A on *SURF1* gene in SVS1A iPSC line. Also, another pair of strings (TALE 1 & 3) was designed to introduce the same mutation 530T>A on *SURF1* gene on both alleles in control iPSC in parallel line (Figure 3.3.1. b-c). The strings with specific restriction sites from Geneart and HR vector MV-PGK-Puro-TK were ordered (Figure 7.2.1.).

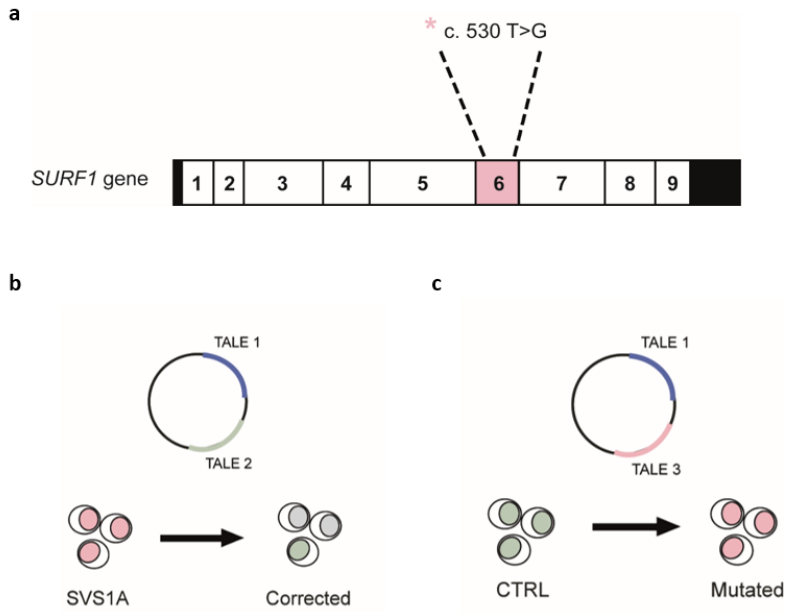

Figure 3.3.1.: The strategy of generating TALEN-based isogenic iPSC pair for SVS1A
***a**, Scheme of the SURF1 gene and where the mutation c. 530 T>G resides. **b,** To correct the mutation on SVS1A iPSCs, TALE 1 and TALE2 strings will be used. **c,** To introduce the mutation on the control iPSC TFBJ line, TALE1 and TALE3 strings will be used. Both strings will be integrated into the HR vector by the designed restrictions sites, respectively.*

3.3.1.1. Screening for the corrected clones in SVS1A iPSC culture

Once the TALEN constructs were assembled (section 7.2.1.), the focus was given to correct the mutation first. The target cells were transfected with the plasmids, followed by puromycin selection, and the clones were picked. Once the clones grew (assuming derived from single cells), PIRA PCR was done to screen for the corrected clones in SVS1A culture. The BsaJI enzyme cuts the

WT and SVS1A sequences at different sites. WT band would give two bands (15 + 56 bp) while SVS1A band would give three bands (92+23+56 bp) (Figure 3.3.1.1.). In PCR gel, it is recognizable from upper bands if the patient line is corrected or not. This is only the case for clone 2, whereas it is probably heterozygous or mixed (Figure 3.3.1.1.). On the other hand, clone 1 is not corrected as there is only a lower band. However, attempts have failed to find the pure and corrected clone, and TALENs experiments were not pursued any further.

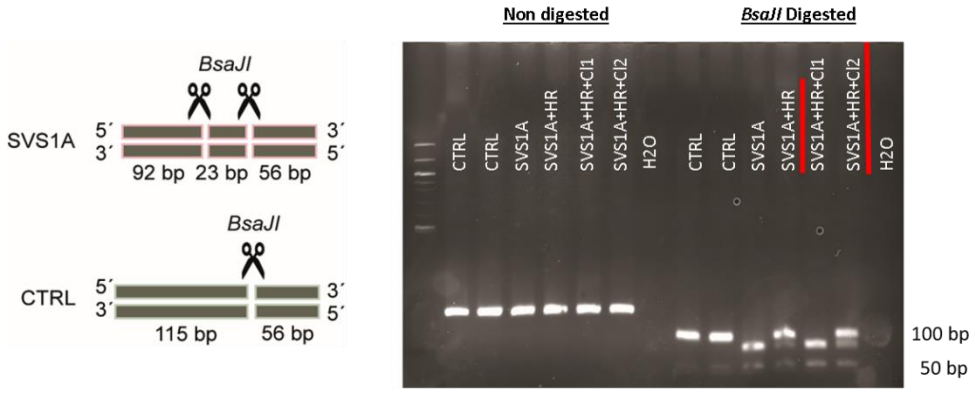

Figure 3.3.1.1.: PIRA PCR to screen for the right clones including HR + TALE1 + TALE 2
To confirm the presence of the mutation, we used primer induced restriction analysis (PIRA). BsaJ cut the PCR product of 550 bp into 92 + 23 + 56 bp fragments only in the presence of the mutation c.530 T>G or was cut into 115 + 56 bp in the presence of correct base pair. SVS1A+ HR and Clone 12 (red underlined) seem to have both upper bands 115 and 92 bp, which indicates the heterozygous situation.

3.3.2. CRISPR/Cas9-based isogenic pair for SVS1C line

After generating clinically feasible SVS1C iPSCs, the aim was to employ the clustered regularly interspaced short palindromic repeats (CRISPR/Cas9) system for precise correction of 769G>A on *SURF1* gene in SVS1C iPSCs.

3.3.2.1. CRISPR/Cas9 vector construction and design

In order to correct the mutation c.769G>A on both alleles in SVS1C iPSCs, the cells were transfected with a pU6 vector coding for a specially designed gRNA and the endonuclease high fidelity eCas9. A specific pU6 vector, including a specially designed gRNA, is prepared and amplified in MACH1 bacteria cells. iPSCs harboring the 769G>A mutation (SVS1C) were transfected by Lipofectamine 3000 and with the vector. An ss HDR repair template carrying the knock-in sequence was also delivered at the same time. Two silent mutations were introduced to help to trace the SVS1C.C clones and confirm the accurate correction of the mutation in the HDR template. The sequence of the template is listed in section 6.2.4. In order to increase the success rate of targeted

correction, plasmids expressing RAD52 and dominant-negative p53-binding protein 1 (dn53BP1) were delivered to promote homologous direct repair (HDR) and inhibit non-homologous end joining (NHEJ) (Paulsen et al., 2017) (Figure 3.3.2.1.). (The vector construction was explained in detail in section 7.2.2.)

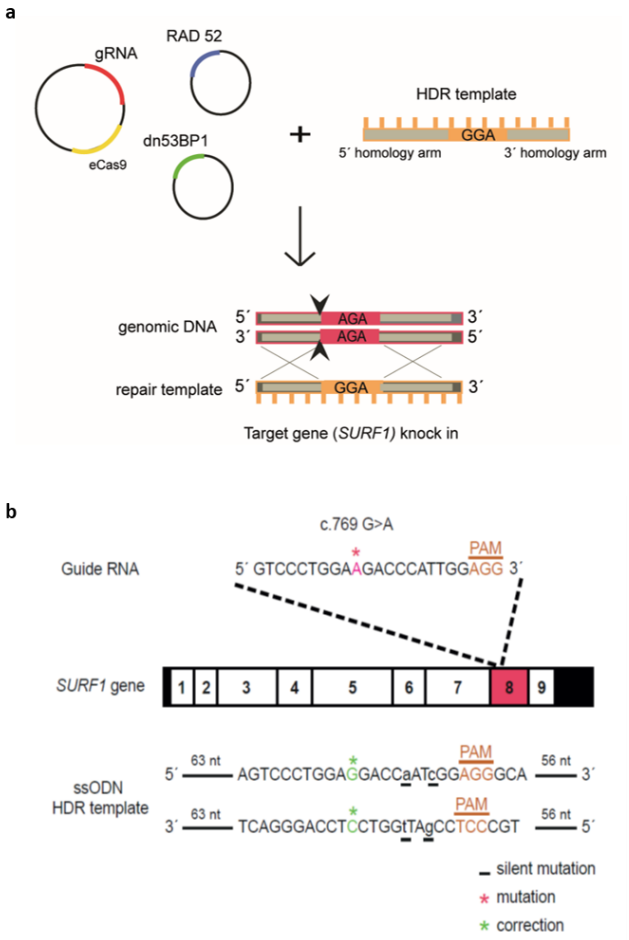

Figure 3.3.2.1.: The strategy of generating CRISPR/Cas9-based isogenic line pair for SVS1C
a*, Schematics of the CRISPR/Cas9 knock-in strategy showing the plasmids and (HDR) template. Plasmid #1 is a pU6(BbsI)-CAG-eCas9-venus-bpA(#1) 10,146bp vector (coding for a specific designed gRNA and for the endonuclease Cas9).Plasmid #2 is a 614.pCAG-hRad52-EF1BFP 8,207 bp coding for RAD 52. Plasmid #3 is a 602.pCAG-i53-EF1BFP 7,175bp vector coding for dn53BP1.* ***b****, Detailed schematics of the gRNA and the HDR template carrying the knock-in sequence for repairing the mutation c.769G>A on both alleles in SVS1C. Underline represents Silent mutations; pink stars and black stars represent the mutations and the corrections, respectively. (Contributions are indicated in section 8.3.).*

3.3.2.2. Screening for the corrected clones

Plasmid RAD52 has a Venus reporter (positive-green), and plasmid including dn53BP1, has a BFP reporter (positive-blue). As the vector codes a Venus reporter, three days after transfection, the cells were sorted by FACS (Suppl. Figure 3.3.2.2.). The confluence of the cells was low; therefore, only 8.76 % of double positive cells were sorted. They were plated on MEFs plates to support single

cells growing. Following the transfection and fluorescent sorting, the picked and grown clones were screened using restriction PIRA PCR. The PCR product of 550 bp was cut by BbSI into 221+324 bp fragments only in the presence of the mutation c.769G>A (Figure 3.3.2.2.). Since clones 3p, 3bb, and 3c show one band visible indicates the corrected clones, whereas the PCR product of 3k after digestion shows two bands which indicates the non-corrected clone.

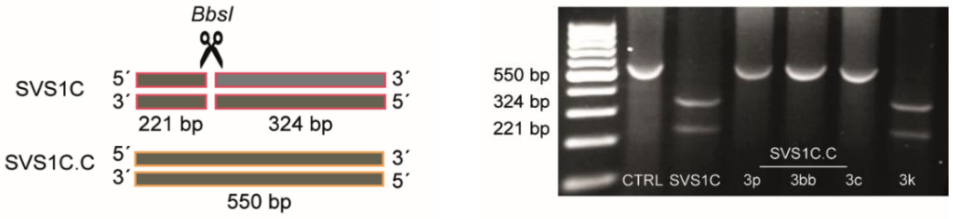

Figure 3.3.2.2.: A primer-introduced restriction (PIRA) PCR analysis to screen for corrected clones
The PCR product of 550 bp was cut by BbsI into 221 + 324 bp fragments only in the presence of the mutation c.769 G>A. Clones 3p, 3b, and 3c have the same band sizes as the CTRL, indicating a successful homozygous correction. (Contributions are indicated in section 8.3.).

3.3.2.3. Molecular and functional characterization

3.3.2.3.1. Mutation Analysis

PIRA PCR gave the first evidence that three clones (3p, 3bb, and 3c) were corrected (Figure 3.3.2.2.). To confirm the genetic identity of corrected mutation c.769G>A in iPSC clones, desired fragments of intact DNA of the clones were extracted from an agarose gel and sent for Sanger sequencing which confirmed the homozygous correction of the mutation (Figure 3.3.2.3.1.). Additionally, two silent mutations in the HDR template were also visible in the sequence of newly formed clones which confirms the successful correction of the mutation. The background information of the corrected SVS1C.C clones is summarized in Table 6.1.1.C.

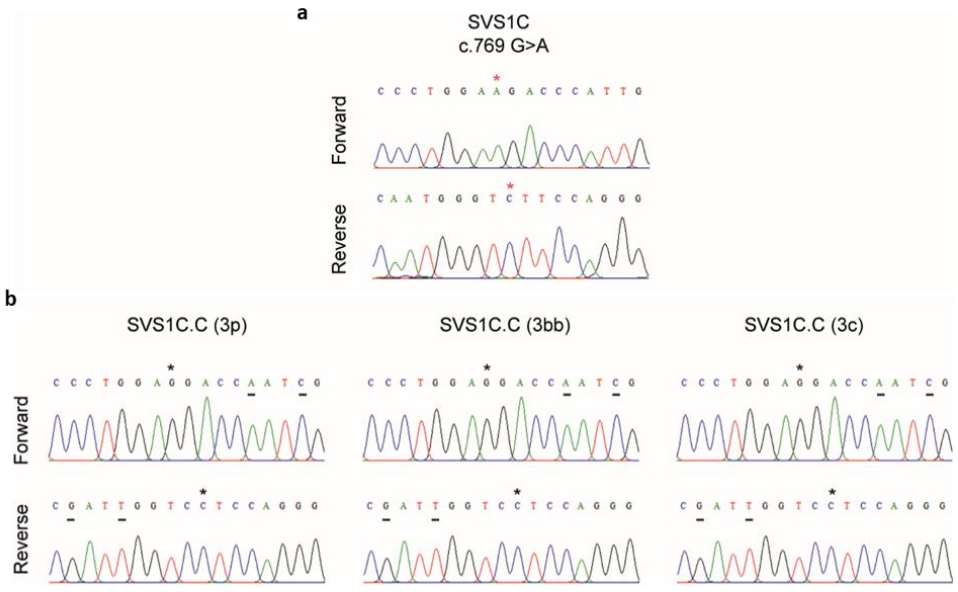

Figure 3.3.2.3.1.: Molecular characterization of CRISPR-Cas9-based corrected iPSCs (SVS1C.C)
a-b*, Electropherograms showing both forward and reverse sequences of patient line SVS1C and genetically corrected clones of SVS1C.C line (clones 3p, 3bb, 3c). Stars in black represent the corrected base pair of the mutation c.769 G>A. The corrected clones have the same sequence as the repair template; underlines indicate two silent mutations.*

3.3.2.3.2. Pluripotent identity analysis

Characterization of the generated iPSCs was done to prove their pluripotent identity. Immunohistochemistry analysis was conducted. All lines expressed endogenous markers associated with pluripotency, including OCT3, SOX2, NANOG, and TRA-1-60. The corrected lines retain features of pluripotency (Figure 3.3.2.3.2.).

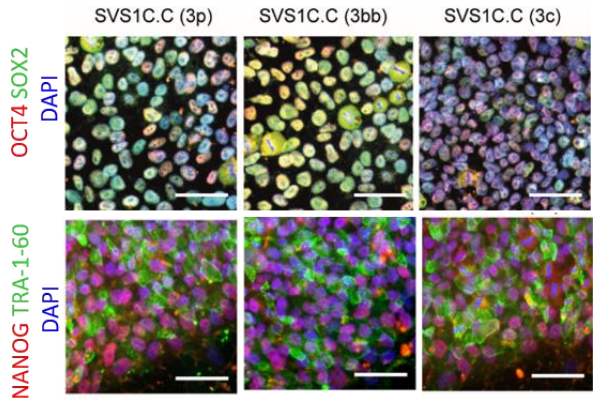

Figure 3.3.2.3.2.: Functional characterization of CRISPR-Cas9-based corrected iPSCs (SVS1C.C)
Corrected iPSC lines (3p, 3bb, 3c) retained pluripotent identity. Representative images of immunofluorescence analysis showing pluripotency-associated marker proteins such as OCT4, SOX2, NANOG, and TRA-1-60. Nuclei were counterstained with Hoechst. Scale bar: 50 µm.

3.3.2.3.3. Characterization of genome rearrangements

SNP array was done at the Berlin Institute of Health (BIH) Stem Cell Core facility to look at the genomic integrity. The virtual karyotyping analysis showed no abnormalities, which means there is no gain or loss of variations in a deleterious way. The corrected clones of SVS1C.C iPSCs had normal karyotypes (Figure 3.3.3.3.2.).

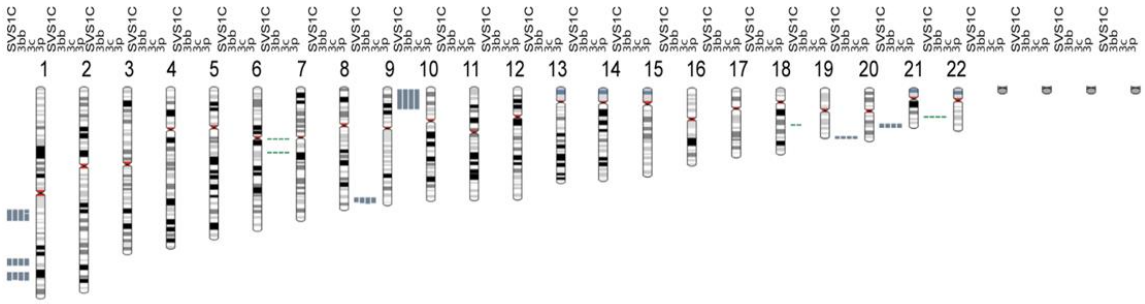

Figure 3.3.3.3.2.: Molecular characterization of CRISPR-Cas9-based corrected iPSCs (SVS1C.C)
Karyotype analysis confirmed that SVS1C.C clones (3p, 3bb, 3c) carried a normal karyotype and were derived from the original iPSC line SVS1C. (Contributions are indicated in section 8.3.).

3.3.2.4. The bioenergetic profile

The second aim was to understand if *SURF1* mutations have an exclusive effect on the bioenergetic profile of the iPSCs *(Detailed explanation of this assay is provided in section 7.1.8.).* Skin fibroblasts, which were reprogrammed to iPSCs, should have become more glycolytic. Thus they would not be necessarily affected by the disturbances of OXPHOS due to *SURF1* mutations. In fact, there were no differences in the oxygen consumption rate or in any other other mitochondrial respiration parameters between SVS1C and SVS1C.C iPSC lines (Figure 3.3.2.4.). However, unexpectedly, the corrected line showed higher glycolytic capacity compared to patient lines.

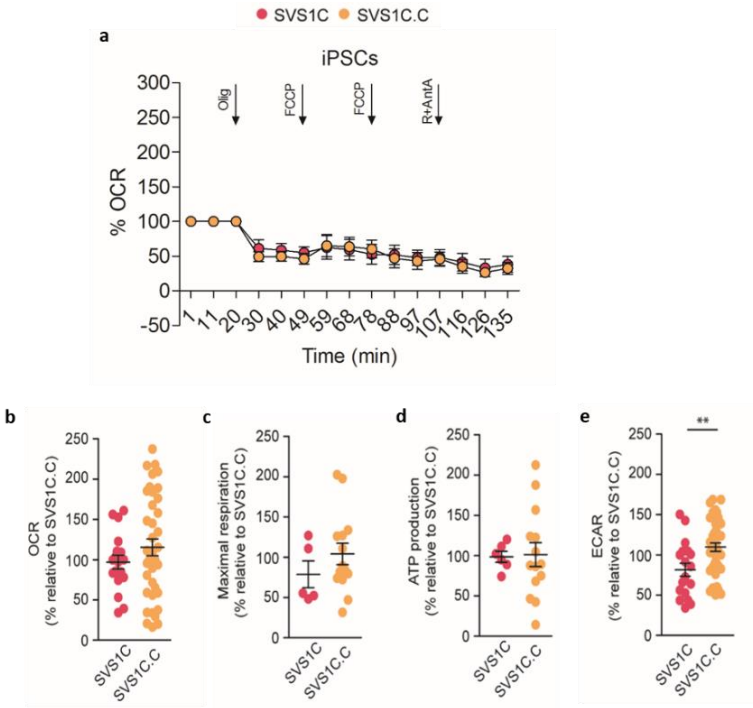

Figure 3.3.2.4.: Bioenergetic profiling in iPSC cultures of SVS1C isogenic line pair

***a**, Oxygen consumption rate (OCR) profile in iPSCs derived from SVS1C and SVS1C.C (mean +/- s.e.m.; n=2 independent experiments). **b-e**, OCR, maximal respiration, ATP production, and extracellular acidification rate (ECAR) in iPSC cultures (mean +/- s.e.m.; n=2 independent experiments).*

3.4. Differentiation of iPSCs into dopaminergic neuron enriched composite cultures

Degeneration of dopaminergic (DA) neurons is the predominant basal ganglia pathology seen in LS patients. Thus next step was to differentiate healthy control, patient and genetically corrected iPSCs into functional dopaminergic neurons through the first generation of neural progenitor cells using small molecules (smNPCs). I adopted a small molecule-based protocol was to generate NPCs and DA-enriched composite cultures from iPSCs (Reinhardt et al., 2013; Choi et al., 2015). It takes around ten days to get NPCs from iPSCs and 4 or 8 weeks to retrieve dopaminergic neurons at different maturation stages. During the first stage of retrieving NPCs from iPSCS, the cells go through different states and form different cell types such as neurospheres and neural epithelial cell cells (Figure 3.4. b). Once they grow as a uniform monolayer on Matrigel-coated plates, they are directed towards DA neuronal identity by neuronal maturation media. The phase contrast images of the cell types display the morphological changes of the cells undergoing as they acquire a neuronal identity. For instance,

while there are more round spheres in neurosphere cultures, and there are more elongated axonal structures in mature neuronal cultures.

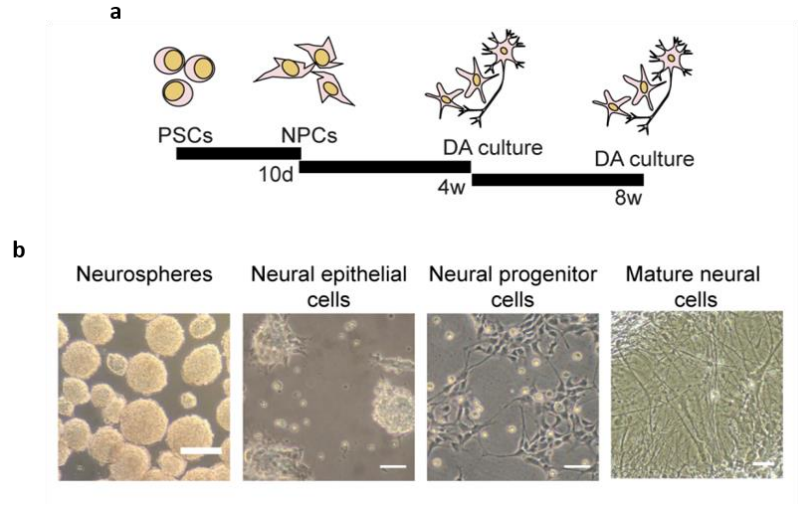

Figure 3.4.: Derivation of neural progenitor cells (NPCs) and dopaminergic (DA)-enriched composite cultures

a, *Summary graph of the progression of PSCs to fully differentiated NPC-derived neurons.* ***b,*** *PSCs were differentiated to NPCs via the first generation of embryoid bodies (EBs). EBs were plated on Matrigel-coated plates and induced to differentiate to neural epithelial cells. The microscopic images of the transformation of the cells from EBs to DAs. Scale bar: 20 µm, 50 µm, 50 µm, 50 µm.*

3.4.1. Characterization of iPSC-derived NPCs

3.4.1.1. NPC identity analysis

Characterization of iPSC-derived NPCs was done to prove they are neural progenitor cells via immunohistochemistry analysis. All lines expressed endogenous protein markers associated with neural progenitor cells such as NESTIN, PAX6, SOX2, and HES5, as well as neuronal cells such as TUJ1 and MAP2 (Figure 3.4.1.1.).

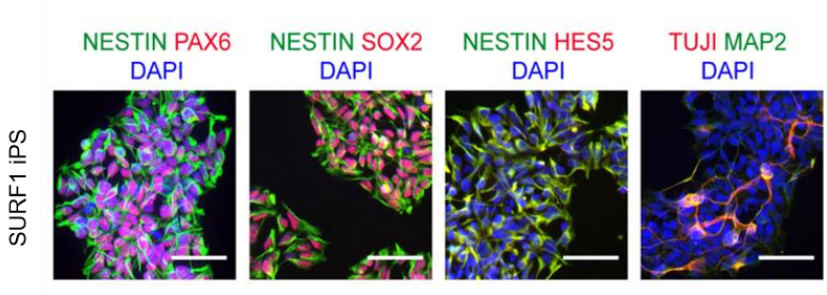

Figure 3.4.1.1.: Characterization of NPCs cultures of LS^{SURF1} *Differentiated neural epithelial cells were stained for neuronal progenitor markers NESTIN, PAX6, and HES5. TUJ1 and MAP2 mature neural markers were also present to indicate they have a premature neuronal character. Nuclei were counterstained with Hoechst. Scale bar: 50 µm.*

3.4.1.2. The functional characterization of COX

SURF1 protein is a key assemble factor of COX and helps the core subunits (COX1, COX2, and COX3) to assemble in the right way so the enzyme can function adequately (*The role of COX2 in the assembly and functionality of COX enzyme was previously discussed in the section 1.2.1.*). Here the aim was to understand if there is any detectable MT-CO2 protein in NPC cultures of LS^{SURF1}. Western blot analysis showed that MT-CO2 protein was almost undetectable in NPCs derived from patient lines (SVS1A and SVS1C) while NPCs from healthy controls and corrected lines all expressed MT-CO2 (Figure 3.4.1.2. a). SURF1 is most likely involved in an early assembly of COX through MT-CO2.

The transmission electron microscopy (TEM) images of the mitochondria in patient-NPCs were taken to understand if the mitochondria have any structural abnormalities due to *SURF1* defects. Mitochondria in NPCs from all lines displayed healthy mitochondrial structure (Figure 3.4.1.2. b). They also showed a fused ultrastructural morphology with well-developed cristae, which was an indication of OXPHOS dependence of NPCs. Then the functional analysis of complex II and IV activity were done; NPCs derived from healthy controls and corrected lines gave a brown indamine polymer product upon providing 3,3'-diaminobenzidine (DAB) substrate. In contrast, there was no brown color seen in NPCs derived from patient lines since DAB product was not saturated due to dysfunction of COX (Figure 3.4.1.2. c). The activity of complex II succinate dehydrogenase (SDH) remained similar in all NPCs, which was confirmed by a blue formazan end product upon reduction of nitroblue tetrazolium (NBT).

These confirmed that the defects in *SURF1*-mutant cells were specific for complex IV and that they have a functional defect rather than structural. Overall, the findings demonstrated that the mutation repair in SVS1C.C had led to functional recovery of *SURF1*-mediated COX assembly.

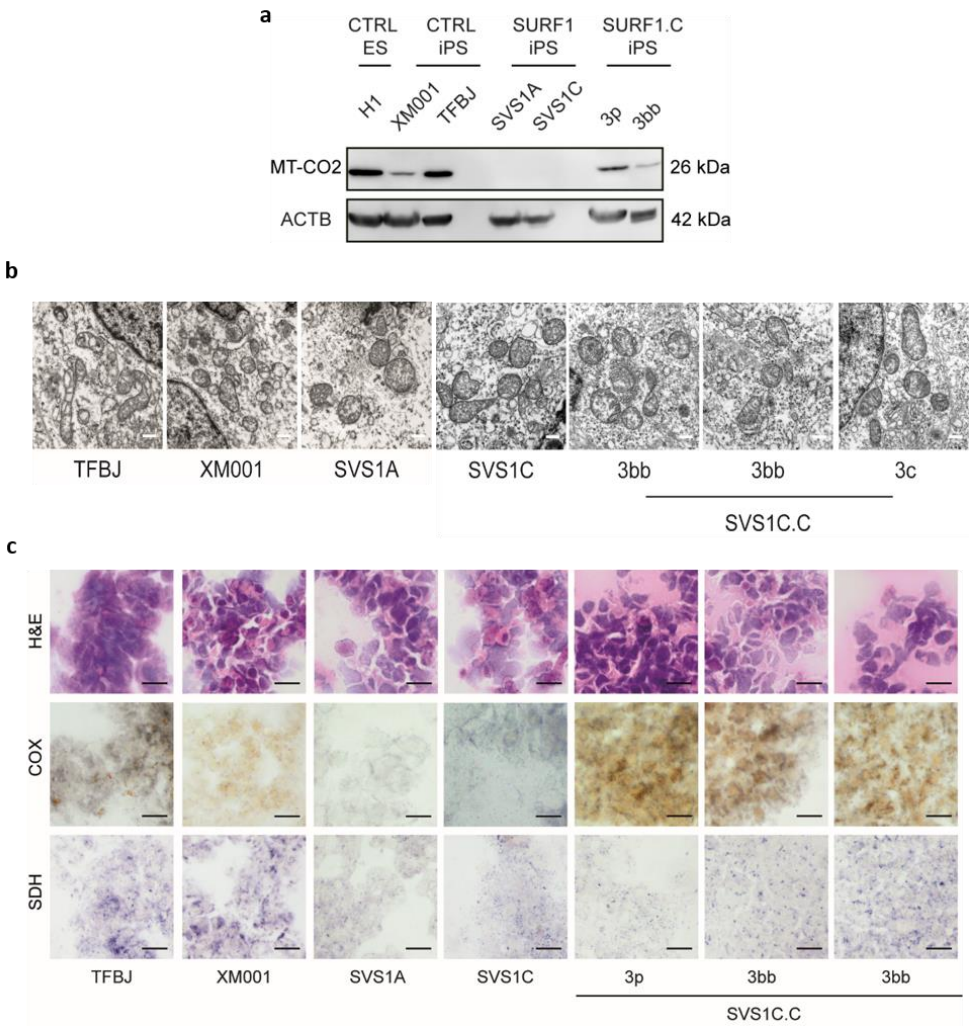

Figure 3.4.1.2.: The functional defects of COX in NPC culture of LS^{SURF1}

a, *Representative immunoblot analysis of MT-CO2 in iPSC-derived NPCs from CTRL ES (H1), CTRL iPSC (XM001 and TFBJ), SURF1 iPSC (SVS1A and SVS1C), and genetically corrected SVS1C.C (clones 3p and 3bb). Protein levels were normalized to ACTB. MT-CO2 protein was absent in patient lines. Similar results were obtained in n=2 independent experiments.* ***b****. Transmission electron microscopy (TEM) of mitochondria showing normal structure in all NPC lines. Scale bar: 500 nm.* ***c.*** *Mitochondrial enzyme activity in NPCs derived from all lines is presented. The activity of complex IV cytochrome c oxidase (COX) was not detectable in patient lines (SVS1A and SVS1C), while the activity of complex II succinate dehydrogenase (SDH) was present in all cell lines. Similar results were obtained in n=2 independent experiments. Scale bar: 500 nm. (Contributions are indicated in section 8.3.).*

3.4.1.3. The bioenergetic profile

Patient-derived NPC cultures displayed defects in COX activity (Figure 3.4.1.2.). Thus in order to dissect the bioenergetics consequences of the NPC cultures of LS^{SURF1}, the Seahorse XF Cell Mito Stress assay was conducted. The mitochondrial respiration analysis was done by measuring the OCR, ATP production-coupled respiration, and maximal respiration. Additionally, glycolytic

capacity analysis was done by measuring ECAR (Figure 3.4.1.3.A. a). NPCs derived from patient lines exhibited significantly reduced mitochondrial respiration parameters (Figure 3.4.1.3.A. b-d), and the mitochondrial bioenergetics was restored upon mutation correction in SVS1C.C-derived NPCs (Figure 3.4.1.3.B b-d). NPCs should have become a bit more OXPHOS dependent as they are differentiated from iPSCs. This is the first evidence that *SURF1* mutations lead to bioenergetic defects. On the contrary, NPCs derived from patient lines displayed high ECAR levels compared to NPCs derived from healthy controls and corrected lines (Figure 3.4.1.3.A e, Figure 3.4.1.3.B e). *(Detailed explanation of the seahorse assay is provided in section 7.1.8.).*

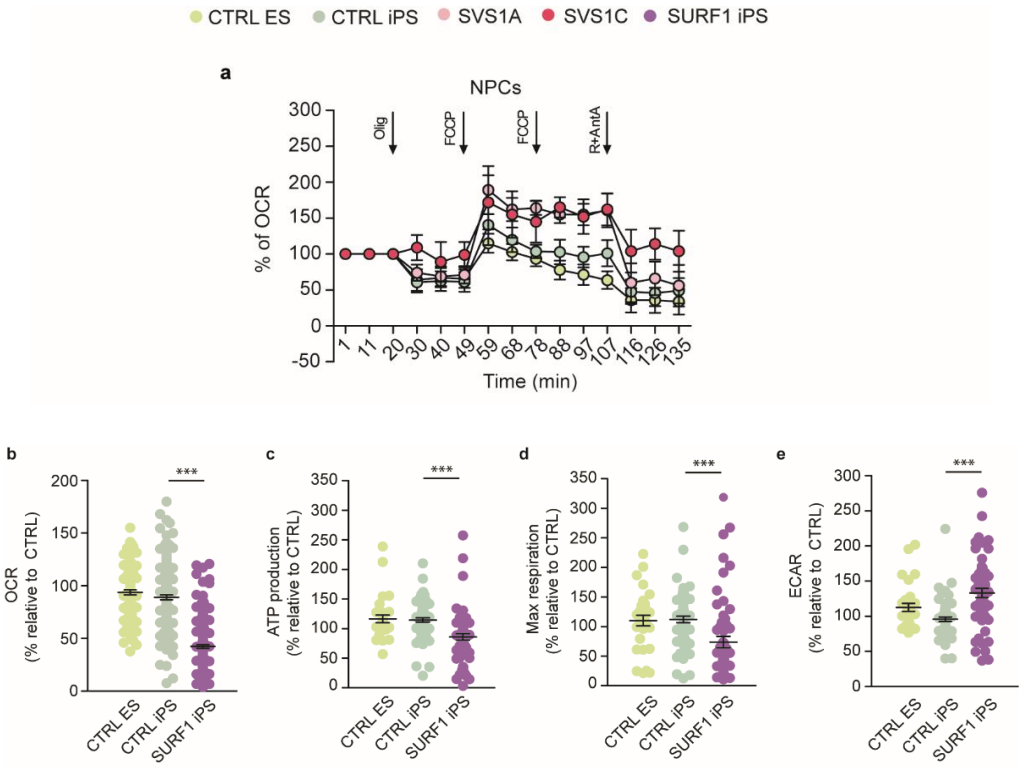

Figure 3.4.1.3.A.: Impaired bioenergetics in NPC cultures of LS^{SURF1}

a, *Oxygen consumption rate (OCR) profile in iPSC-derived NPCs from CTRL ES (H1) from CTRL iPSC (TFBJ and XM001) and SURF1 patients (SVS1A and SVS1C).* ***b-e,*** *OCR, maximal respiration, ATP production and extracellular acidification rate (ECAR) in NPC cultures (mean +/- s.e.m.; n=5 independent experiments; *** p<0.001; Mann-Whitney U test; one-way ANOVA followed by Bonferroni multiple comparison test, *** p<0,001).*

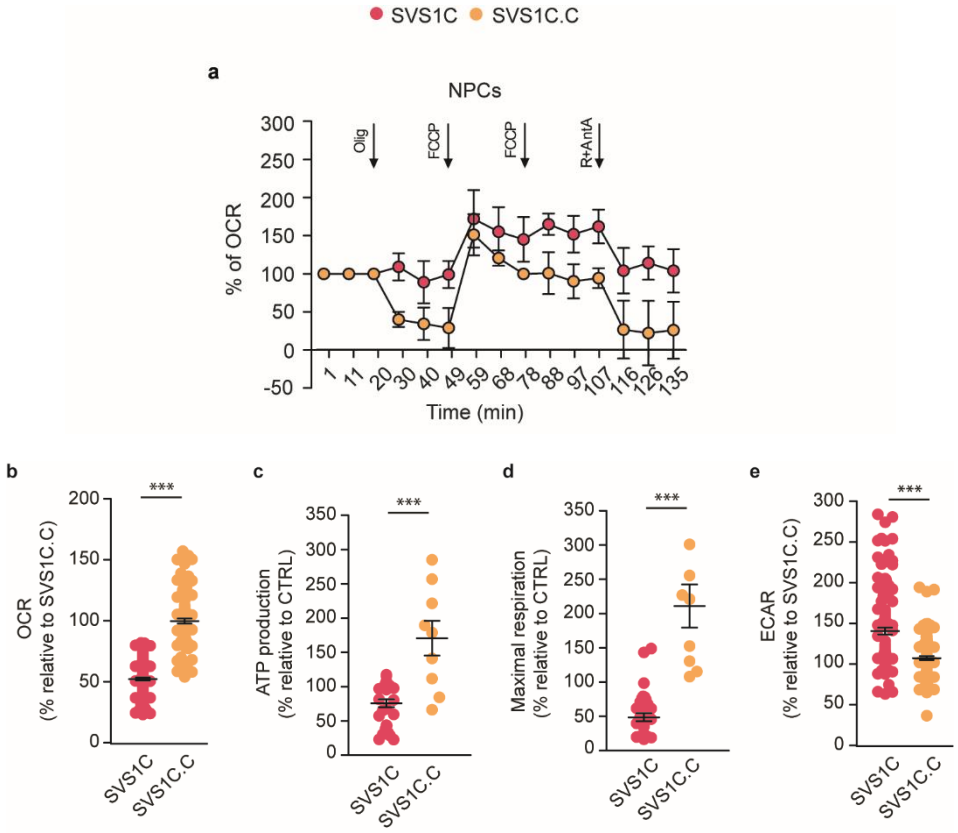

Figure 3.4.1.3.B : Restored bioenergetics upon mutation correction in NPC cultures of SVS1C.C

***a**, Oxygen consumption rate (OCR) profile in iPSC-derived NPCs from SVS1C and SVS1C.C (mean +/- s.e.m.; n=5 independent experiments).* ***b-e**, OCR, maximal respiration, ATP production and extracellular acidification rate (ECAR) in NPC cultures (mean +/- s.e.m.; n=5 independent experiments; *** p<0.001; Mann-Whitney U test).*

3.4.1.4. Enzymatic assessment of lactate production

NPCs derived from patient lines exhibited lower levels of OCR and high levels of ECAR. Through glycolysis, glucose is converted into pyruvate and transported into the mitochondria for aerobic respiration, or converted into lactate for anaerobic respiration.

The supernatants collected from the NPC cultures were used for enzymatic lactate assay. NPCs derived from patient lines tend to have higher lactate levels compared to NPCs from healthy controls (Figure 3.4.1.4. a), which were also detected in the liquor and serum of most LS patients. High lactate levels were reduced upon mutation correction (Figure 3.4.1.4. b). An increase in lactate production over time might suggest increased glycolysis to generate ATP as a compensation mechanism to OXPHOS defects. Additionally, NPCs from patient lines might have more progenitor cell character than neuronal character. Neural stem cells/progenitor cells usually rely on more glycolytic activity, and as they differentiate to neuronal cells, metabolic switch from glycolysis towards OXPHOS occur. If they are more neuronal progenitor cells, it

suggests them to be more proliferative and cellular proliferation assay done in NPC cultures of isogenic line pair showed that patient NPCs proliferate more compared to the corrected line (Suppl. Figure 3.4.1.4.) (Candelario et al., 2013; Mlody et al., 2016). Less proliferative capacity of NPCs from healthy controls and corrected lines might be because they might have more neuronal character.

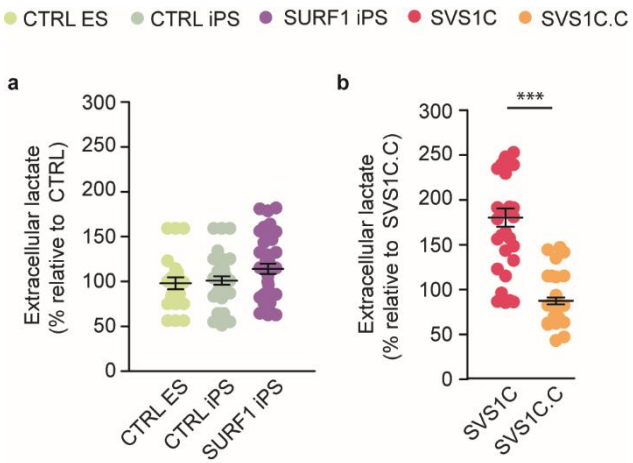

Figure 3.4.1.4.: Quantification of extracellular lactate in NPC cultures of all lines
a, *Quantification of extracellular lactate in the supernatant of iPSC-derived NPCs from CTRL ES (H1), CTRL iPS (TFBJ and XM001) and SURF1 iPS (SVS1A and SVS1C) (mean +/- s.e.m.; n=4 independent experiments; one-way ANOVA followed by Bonferroni multiple comparison tests, not significant).* ***b,*** *Quantification of extracellular lactate in the supernatant of NPC cultures from isogenic lines SVS1C and SVS1C.C (mean +/- s.e.m.; n=4 independent experiments; *** p<0.001; Mann-Whitney U test).*

3.4.1.5. Neuronal profiling

NPC identity and bioenergetic characterization of NPCs showed that within the NPC cultures, there are already immature neuronal cells that express neuronal protein markers such as TUJ1 and MAP2 addition to NPC markers (Figure 3.4.1.1.). Accordingly, mitochondria in NPCs already exhibit cristae structures similar to those of mature neurons (Figure 3.4.1.2 b) (Lorenz et al., 2017).

Patient-derived NPC cultures showed higher glycolytic activity and were more proliferative. The next aim was to quantify the number of cells expressing TUJ1 protein marker, neurite outgrowth capacity, and branching capacity in NPC cultures. High-content (HCA)-based automated fluorescent imaging-based analysis of neuronal morphology was done in NPC cultures of isogenic iPSC lines in multi-well format (Figure 3.4.1.5. a). There was no difference in the number of NPCs expressing TUJ1 protein markers between the isogenic lines, whereas the

neurite length per neuron and branch points per neuron were significantly lower in NPC cultures derived from patient line SVS1C (Figure 3.4.1.5. b).

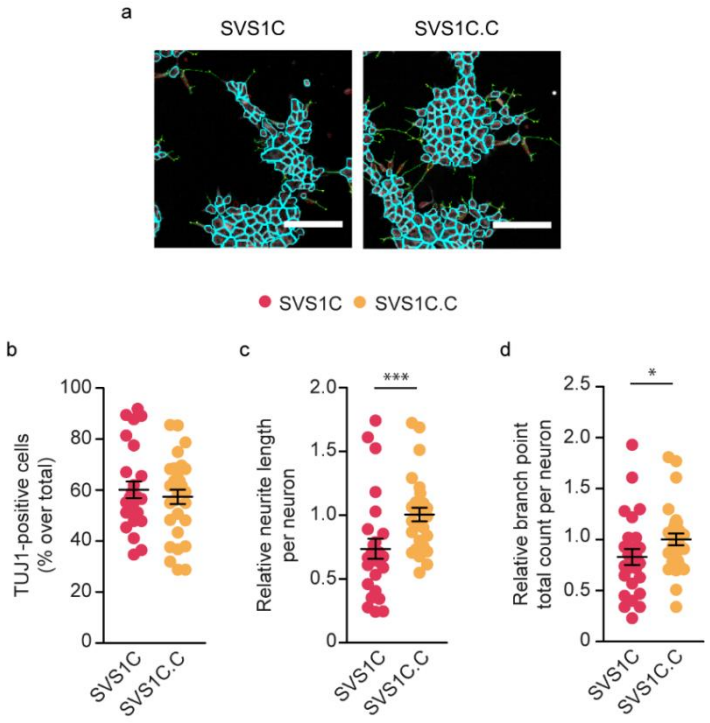

Figure 3.4.1.5.: Restored neuronal branching upon mutation correction in NPC cultures of SVS1C.C ***a,*** *Representative images of the high content analysis (HCA) mask for neuronal profiling showing shorter neurites (in green and red), fewer branch points (in pink) in iPSC-derived NPCs from SVS1C. Scale bar: 25 µm.* ***b,*** *HCA-based quantification of neuronal profiling based on TUJ1-expressing neurons in NPC cultures of SVS1C and SVS1C.C (mean +/- s.e.m.; n=5 independent experiments; *** p<0.001; Mann-Whitney U test).*

Neuronal profiling analysis of iPSC-derived NPCs showed that *SURF1* defects disrupt neuronal branching capacity already at the level of NPC state. The mutation repair in SVS1C.C restored the neurite outgrowth capacity and branching capacity of the NPCs. It would be a necessity to confirm this phenotype in DA enriched composite cultures to understand if this phenotype is real.

3.4.2. Characterization of iPSC-derived DA-enriched composite cultures

3.4.2.1. Dopaminergic neuron identity analysis

After the initial generation of NPCs, patient lines were differentiated further into DA enriched cultures and were let in cultures for 4, 6, and 8 weeks for different stages of maturity. In order to characterize the DA cultures in more detail, there were several experiments conducted:

First, extensive immunohistochemical analysis was performed, and large populations of TUJ1 and MAP2 expressing neuronal cells were found. They also expressed the synaptic markers SYP and VAMP2, the DA markers NURR1, FOXA2, and TH at 8 weeks (Figure 3.4.2.1.A. a, 3.4.2.2.B. a). After they were proven to express neuronal and DA-related markers, HCA-based quantification of TUJ1 analysis was conducted to compare the number of neurons expressing TUJ1 markers between the lines. DA cultures derived from patient lines at 4w and 8w showed significantly fewer cells expressing TUJ1 protein markers compared to DA cultures derived from healthy controls (Figure 3.4.2.1.A b). Mutation correction increased the neuronal percentage in DA cultures of SVS1C.C at 8w, suggesting a restored neurogenic potential of the patient-derived DA cells (Figure 3.4.2.1.B b). There was no significant difference observed at 4w DA cultures between the isogenic lines.

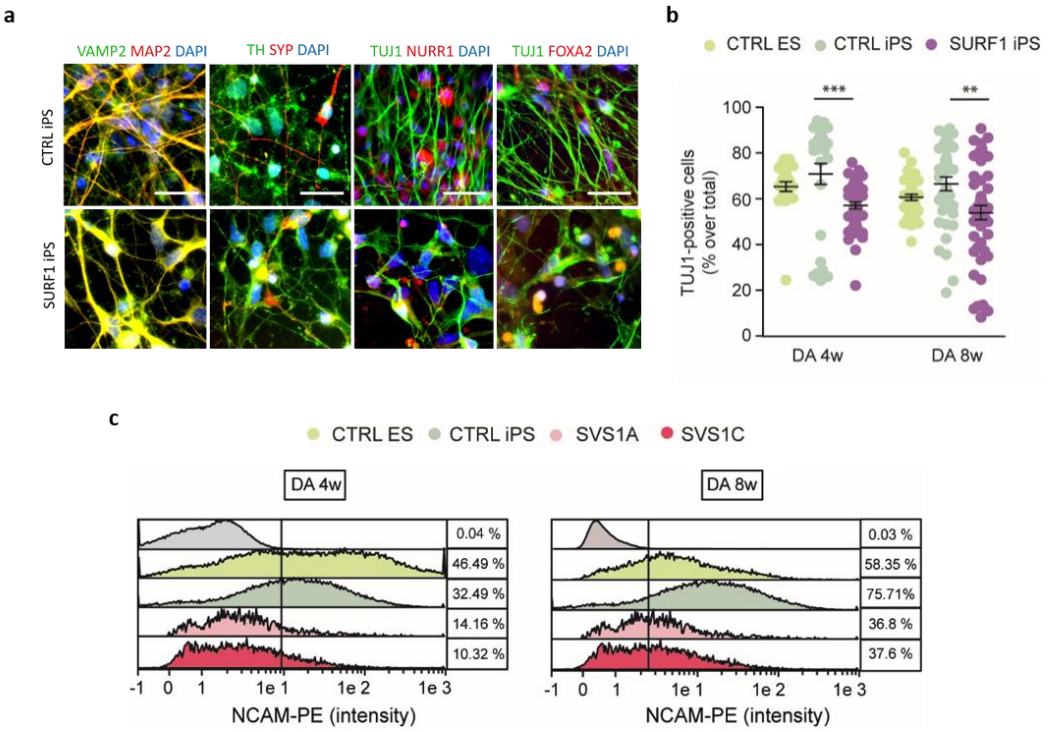

Figure 3.4.2.1.A.: Impaired neuronal generation in DA-enriched composite cultures of LS^{SURF1}

a, *iPSC-derived Dopaminergic (DA)-enriched composite cultures from CTRL ES (H1), CTRL iPSC (TFBJ and XM001), SURF1 iPSC (SVS1A and SVS1C) expressed the neuronal markers TUJ1 and MAP2, the synaptic markers SYP and VAMP2, the DA markers NURR1, FOXA2, and TH. (Scale bar: 50 µm).* ***b,*** *High content analysis (HCA)-based quantification of TUJ1-expressing neurons in iPSC-derived 4w and 8w dopaminergic (DA)-enriched neuronal cultures from CTRL ES (H1), CTRL iPSC (TFBJ and XM001), SURF1 iPSC (SVS1A and SVS1C) ((mean +/- s.e.m.; n=3 independent experiments; ** p<0.01; *** p<0.001; Mann-Whitney U test; one-way ANOVA followed by Bonferroni multiple comparison test, *** p<0,001).* ***c,*** *Representative Magnetic-Activated Cell sorting (MACS)-based histogram plots of NCAM-positive cell population in 4w DA and 8w DA cultures in comparison to negative sorted cells (in grey). Fluorescence intensity (x-axis) was plotted against the relative*

cell number (y-axis). Percentage values refer to the number of positive cells over the total number of cells (n=3 independent experiments).

Additionally, magnetic-activated cell sorting (MACS) analysis was conducted to quantify the cells with the cell surface marker of neural cell adhesion molecule (PSA-NCAM), which is a distinctive marker of immature neuronal-restricted progenitors. They play a role during neurogenesis, which entails the migration, survival, and process of outgrowth of newly generated neurons. DA cultures from patient lines (SVS1A and SVS1C) showed a reduced amount of NCAM-positive neuron-restricted progenitors compared to cultures from healthy controls, which suggests impaired neurogenesis (Figure 3.4.2.1.A c). Altogether, the mutation correction restored the neuronal generation (Figure 3.4.2.1.B.).

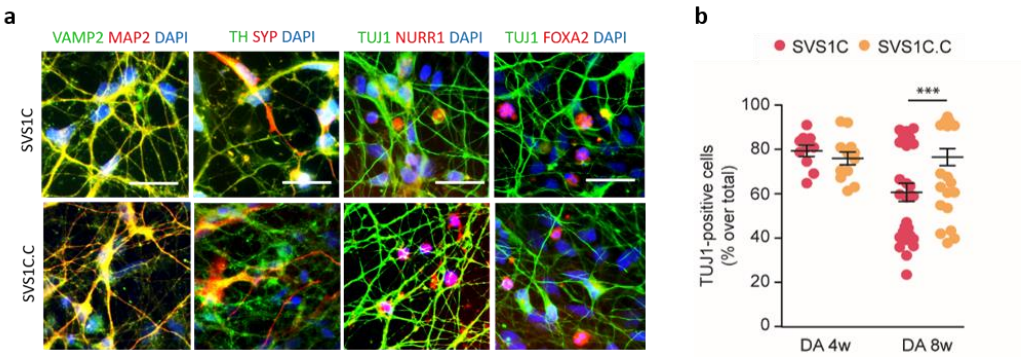

Figure 3.4.2.1.B.: Restored neuronal generation upon mutation correction in DA-enriched composite cultures of SVS1C.C

a, *iPSC-derived DA-enriched composite cultures from SVS1C and SVS1C.C at 8 weeks expressed the neuronal markers TUJ1 and MAP2, the synaptic markers SYP and VAMP2, the DA markers NURR1, FOXA2, and TH. (Scale bar: 50 µm).* ***b,*** *High content analysis (HCA)-based quantification of TUJ1-expressing neurons in iPSC-derived 4w and 8w dopaminergic (DA)-enriched neuronal cultures from CTRL ES (H1), CTRL iPSC (TFBJ and XM001), SURF1 iPSC (SVS1A and SVS1C) ((mean +/- s.e.m.; n=2 independent experiments; *** p<0.001; Mann-Whitney U test).*

3.4.2.1.1.Transcriptomic profile of DA neuronal identity

In order to understand the disease-associated disrupted neuronal profile better and characterize DA-enriched composite cultures in a more obvious way, RNA sequencing was performed on 4w and 8w cultures from CTRL ES (H1), CTRL iPSC (XM001), and *SURF1* iPSC (SVS1A and SVS1C). Principle component analysis (PCA) showed a clear separation between the transcriptomic profile of the patient and control lines (Figure 3.4.2.1.1.A a). Transcriptome analysis was also performed on 4w and 8w DA cultures from isogenic lines (SVS1C and SVS1C.C)

using ribo-zero total RNA-seq to analyze the potential differences in a more precise way. PCA analysis also showed a clear separation between the transcriptomic profiles of DA cultures of isogenic lines for both weeks (Figure 3.4.2.1.1.A. b).

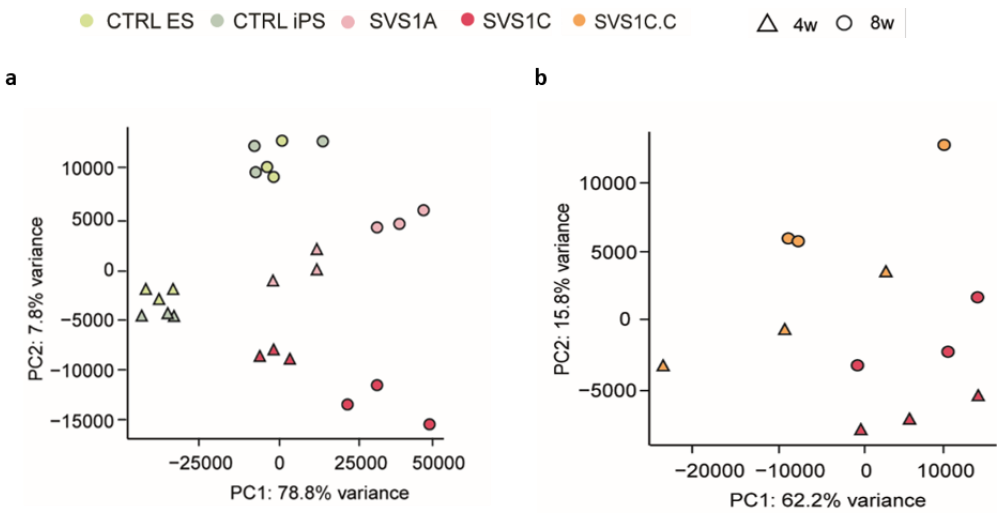

Figure 3.4.2.1.1.A.: PCA plot of DA-enriched composite cultures of all lines
a, *Principal component analysis (PCA) of the mRNA-based transcriptome (polyA) of 4w and 8w DA cultures derived from SURF1 iPSC (SVS1A and SVS1C) vs. CTRLS (H1 and XM001) (n=3 independent experiments). x and y-axis represent the principal component 1 and 2 explaining 78.8% and 7.8% of the variance, respectively (n=3 independent experiments).* ***b,*** *PCA of ribo-zero total RNA-seq based transcriptome of 4w and 8w DA cultures derived from isogenic lines. x and y-axis represent the principal component 1 and 2 explaining 62.2% and 15.8% of the variance, respectively (n=3 independent experiments). (Contributions are indicated in section 8.3.).*

After the first characterization of DA-enriched composite cultures and finding defects in the neuronal generation, the transcriptomic data was used to give more depth to the findings. Interestingly, patient-derived cultures at 4w and 8w exhibited upregulation of genes associated with embryonic development and pluripotency such as *LIN28A, POU5F1, USP44, DPPA3*, and *DPPA4* (Figure 3.4.2.1.1.B. a). Moreover, *SURF1*-mutant cultures displayed downregulation of genes involved in neuronal differentiation such as *NCAM1, PHOX2B, FOXA2*, or interneurons like *REEL*, which is also known to control neuronal migration. This downregulation was even more evident in the cultures of 8w. Additionally, there was a downregulation in *FOXA1* and *FOXA2* genes, which are known to regulate DA neurogenesis (Figure 3.4.2.1.1.B. c). Moreover, a set of DA genes were also analyzed, and patient-derived DA cultures exhibited different gene expression profile at both weeks. Overall, data suggest that *SURF1* mutations caused a transcriptional reconfiguration suggestive of suppression of neuronal differentiation and fate

specification, which was accompanied by a failure to repress the pluripotent and precursor fate identities.

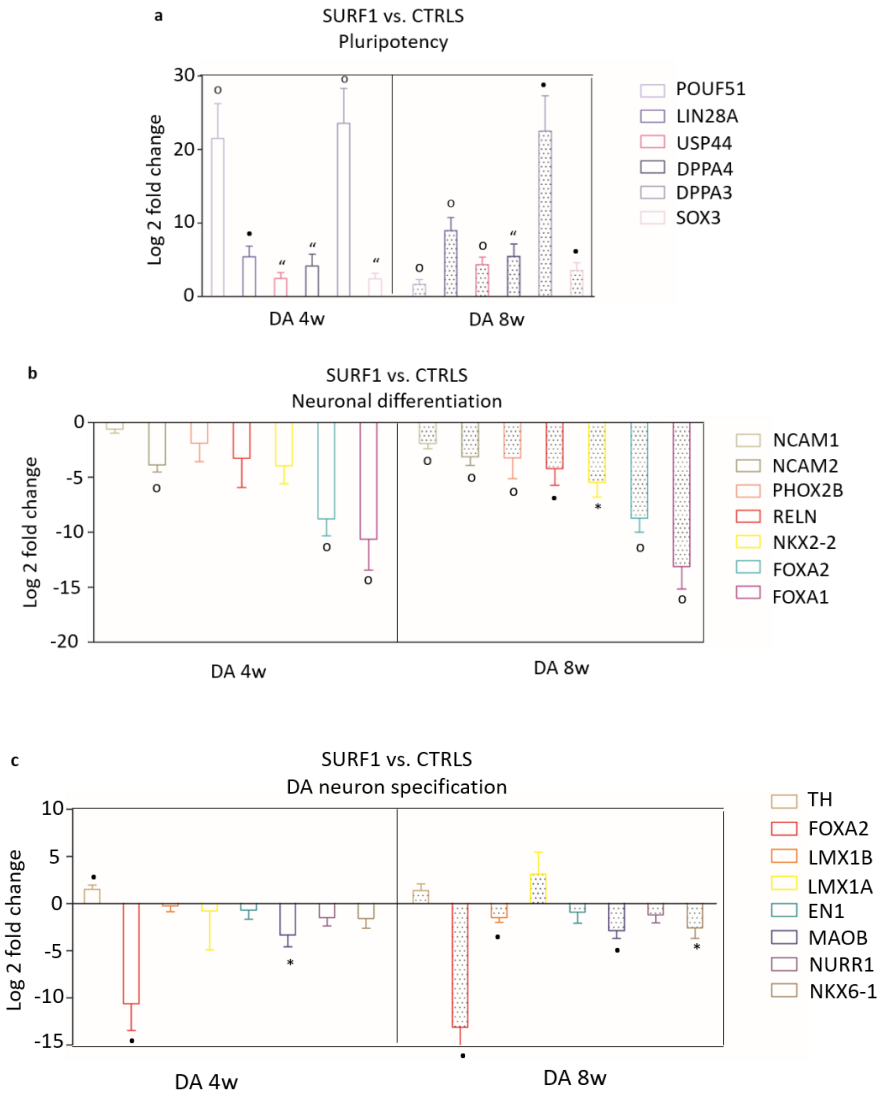

Figure 3.4.2.1.1.B.: Differentially regulated neuron-specific genes in composite cultures of LS^{SURF1}
a-b, *Log fold changes (LFC) of genes regulating pluripotency, neuronal differentiation, and DA specification in iPSC-derived 4w (empty bars) and 8w (dotted bars) DA cultures from SURF1 iPSC (SVS1A and SVS1C) vs. CTRL (H1 and XM001) (* p<0.05, ´´ p<0.01, o p<0.001, • p<0.0001).*

Transcriptome dataset of isogenic line pair highlighted the defects in neuronal differentiation and DA neuronal fate specification more distinctively as SVS1C was compared to genetically corrected SVS1C.C line. Usually, each cell has the same developmental potential at the beginning, whereas as they mature, they choose different paths due to their fate specification. In *SURF1* patient-derived DA neuronal cultures, the data suggest cell culture to

entail more premature neuronal cells, or more progenitor cell types as all of the pluripotent genes were significantly upregulated (Figure 3.4.1.1.1.C. a), neuronal differentiation (Figure 3.4.1.1.1.C. b) and DA specific genes very significantly downregulated (Figure 3.4.1.1.1.C. c). For instance, *LMX1B* is known to be involved in the differentiation of mDA progenitors and maturation of post-mitotic DA neurons along with *NURR1*. There was also a significant downregulation of *MAOB* at both weeks, which suggests a defective metabolism of dopamine (Figure 3.4.1.1.1.C. c).

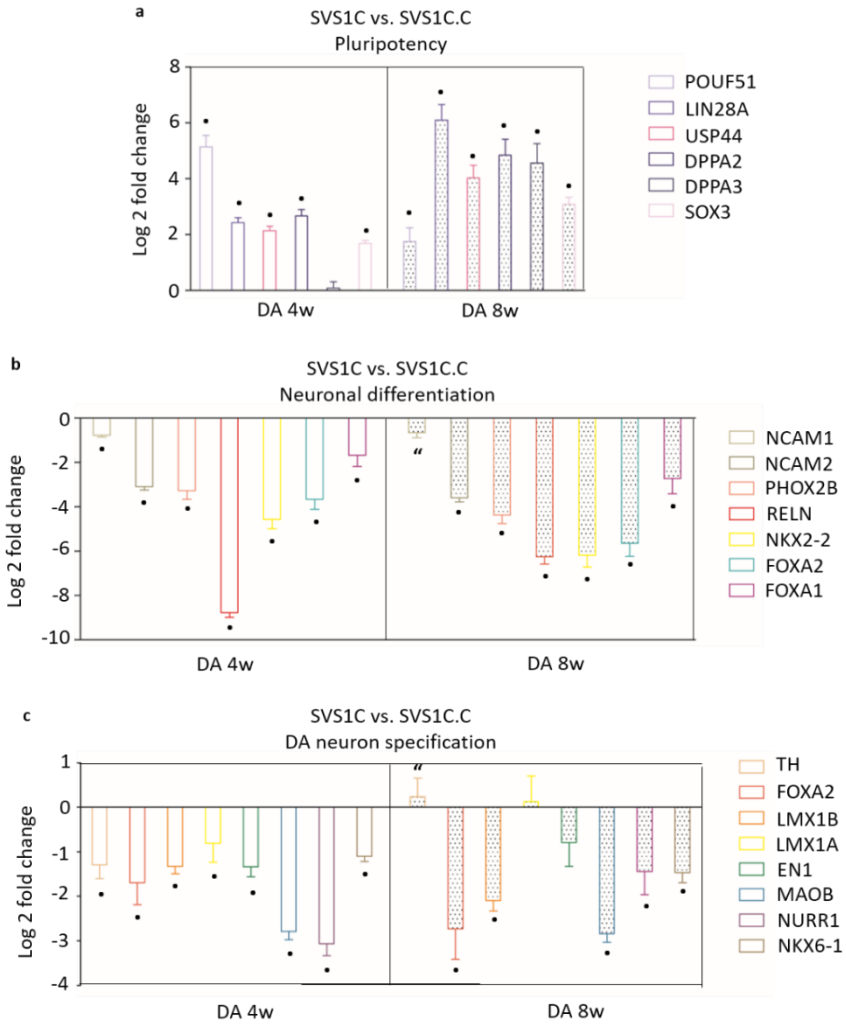

Figure 3.4.2.1.1.C.: Differentially regulated neuron-specific genes in composite cultures of SVS1C isogenic line pair

a-c, *Log fold changes (LFC) of genes regulating pluripotency, neuronal differentiation, and mDA neuron specification in iPSC-derived and 4w (empty bars) and 8w (dotted bars) DA cultures from SVS1C and SVS1C.C (* p<0.05, ´´ p<0.01, o p<0.001, • p<0.0001).*

3.4.2.2. Glial cell identity analysis

After doing neuronal characterization in NPC-derived DA-enriched composite cultures, the focus was then given to understand if there were any glial cell types in the culture. First, immunohistochemical analysis was performed on 4w and 8w DA cultures from CTRL ES (H1), CTRL iPSC (XM001), and *SURF1* iPSC (SVS1A and SVS1C), and isogenic lines (SVS1C and SVS1C.C). All cell lines expressed mature glial cell marker S100ß and the astrocyte marker GFAP (Figure 3.4.2.2. a). Each line showed variability in GFAP and S100ß expression and, in some cases, there was no co-localization of the markers. The morphologies of the glial cells also varied from each other in each experiment. In order to quantify the glial cells and to understand if they exhibit any differences in number, magnetic-activated cell sorting (MACS) analysis was performed with the glial progenitor marker (A2B5) and mature astrocyte marker (GLAST). The number of A2B5-positive glial-restricted progenitors and the number of GLAST-positive mature astrocytes showed differences between groups. (Figure 3.4.2.2. c).

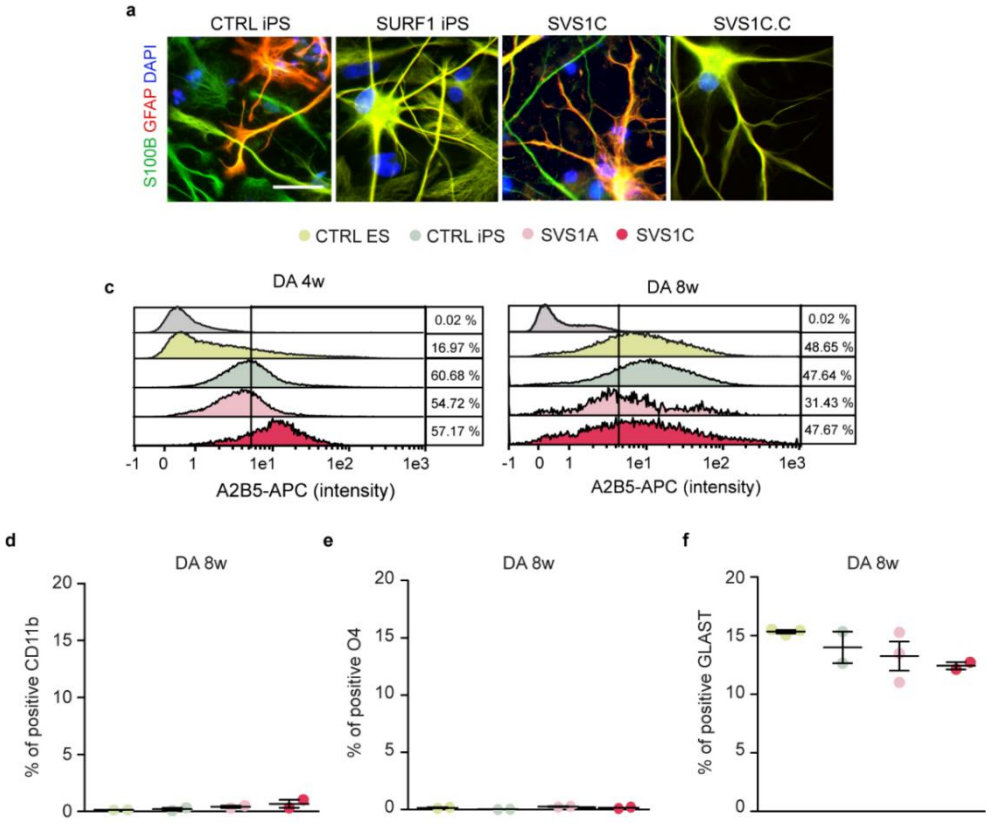

Figure 3.4.2.2.: Glial cell profile in DA-enriched composite cultures of all lines

a, *Astrocyte markers S100ß and GFAP markers are present in iPSC-derived 8w dopaminergic (DA)-enriched neuronal cultures from CTRL ES (H1) from CTRL iPSC (TFBJ and XM001), SURF1 iPSC (SVS1A and SVS1C), and isogenic pair line (*SVS1C and SVS1C.C) *(Scale bar: 50 µm).* ***b,*** *Representative Magnetic-Activated Cell sorting (MACS)-based histogram plots of A2B5-positive cell population in 4w and 8w DA composite cultures in comparison to negative sorted cells (in grey). Fluorescence intensity (x-axis) was plotted against*

the relative Cell number (y-axis). Percentage values refer to the number of positive cells over the total number of cells (n=3 independent experiments). ***d****, MACS-based quantification of glial surface markers: CD11b for microglia and O4 for oligodendrocytes, and GLAST for mature glial cells in CTRL ES (H1) from CTRL iPSC (TFBJ and XM001), SURF1 iPSC (SVS1A and SVS1C) derived 8w DA cultures (n=3 independent experiments).*

Additionally, MACS analysis was performed to understand if there are any other glial cell types present in the differentiated cultures derived from NPCs. CD11B was chosen to identify the microglial cells and O4 for oligodendrocyte population. There was no CD11B and O4 positive cells detected in DA cultures derived from NPCs in any of the lines. (Figure 3.4.2.2. d).

3.4.2.2.1. Transcriptomic profile of glial identity

First initial experiments did not show any significant differences in glial cell number between composite cultures derived from healthy controls and patient iPSCs. RNA-seq analysis showed upregulation of most of the glial genes such as *GFAP, S100B,* and *AQP4* in *SURF1*-iPSC-derived cultures in both weeks (Figure 3.4.2.2.1 a), whereas the differences were not significant. On the contrary, all of the glial genes were significantly downregulated in the patient line when it was compared to SVS1C.C (Figure 3.4.2.2.1 b).

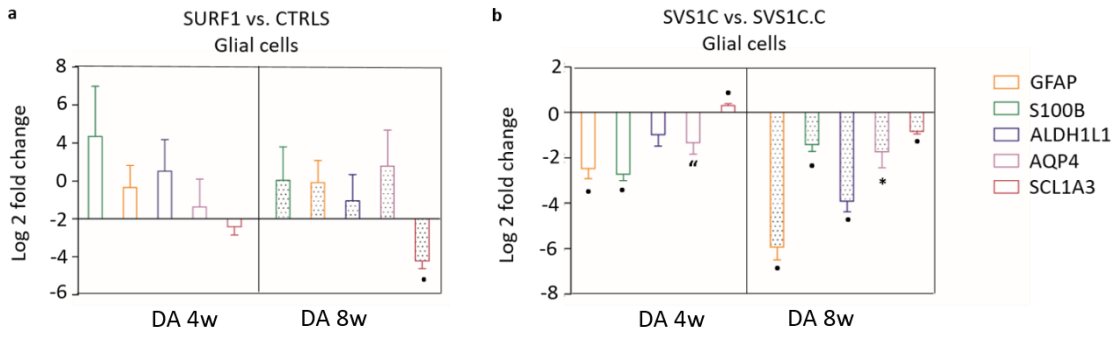

Figure 3.4.2.2.1.: Differentially regulated glial genes in DA-enriched composite cultures of all lines
a, *Log fold changes (LFC) of genes regulating astrocyte identity in iPSC-derived 4w (empty bars) and 8w (dotted bars) DA cultures from SURF1 iPSC (SVS1A and SVS1C) vs. CTRL (H1 and XM001).* ***b,*** *Log fold changes (LFC) of genes regulating astrocyte identity in iPSC-derived 4w (empty bars) and 8w (dotted bars) DA cultures from isogenic pair (SVS1C vs SVS1C.C) (mean +/- s.d.; * p<0.05, ´´ p<0.01, o p<0.001, • p<0.0001).*

3.4.2.2.2. Assessing the functionality of glial cells

The presence of glial cells in DA-enriched composite cultures can mimic the physiological condition seen in the CNS. There were variabilities in the transcriptomic analysis of glial cell profile among the groups. It is known that astrocytes tend to respond to damage or

insults by proliferating and undergoing hypertrophy. In order to understand if the glial cells present in differentiated DA-enriched composite cultures are resting or reactive, V-PLEX mesoscale inflammatory (panel I) was performed on the collected supernatants to look at their cytokine profile. It measured ten cytokines, which play a role in inflammation response. Supernatants from DA cultures at 4w and 8w were analyzed for each line separately and then were compared to understand if they show any differences. The cytokines were present in non-stimulated composite cultures, and the highly present ones were highlighted in red (Suppl. Table 3.4.2.2.2.). Only DA cultures derived from hESC line H1 also show the presence of TNF-α. The cytokines IL-13, IL-6, and IL-8 were present in all the samples but were not significantly altered in LS^{SURF1} cultures. There was no clear outcome from the glial profile analysis of the lines as they behaved differently. Cytokine panel analysis indicated that the glial cells are active in culture, whereas there were no differences in the reactivity profile between patient lines and healthy controls. (Figure 3.4.2.2.2).

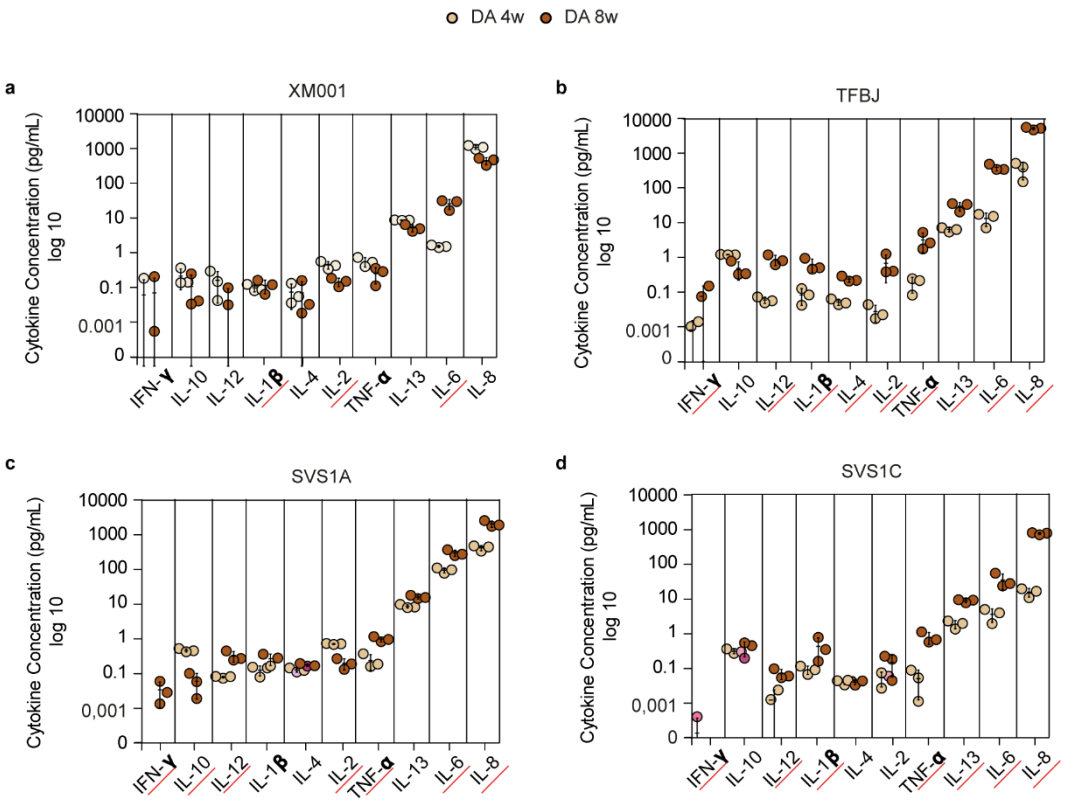

Figure 3.4.2.2.2.: Cytokine profiling in composite cultures of all lines

Cytokines measured using Mesoscale Inflammatory Panel I. Astrocyte-derived cytokines expression over time in mature in iPSC-derived 4w and 8w dopaminergic (DA)-enriched neuronal cultures from a, CTRL iPSC (XM001); ***b****, CTRL iPSC (TFBJ);* ***c-d,*** *SURF1 iPS (SVS1A and SVS1C). The significant differences between 4w (light color) and 8w (dark color) DA cultures are underlined with red.*

3.4.2.3. The bioenergetic profile

In order to understand if *SURF1* mutations have an exclusive effect on the bioenergetic profile of the DA-enriched composite cultures, the Seahorse XF Cell Mito Stress assay was conducted. DA-enriched composite cultures derived from patient lines exhibited significantly reduced mitochondrial respiration (basal OCR, maximal respiration, and ATP production) (Figure 3.4.2.3.A c-f) and the mitochondrial bioenergetics was restored upon mutation correction in SVS1C.C-derived cultures for both 4 and 8 weeks (Figure 3.4.2.3.B c-f). Bioenergetic defects became biochemically apparent already at the level of NPCs, shown previously (Figure 3.4.1.2. c, 3.4.1.3.A. b-d). *(Detailed explanation of this assay is provided in section 7.1.8.).*

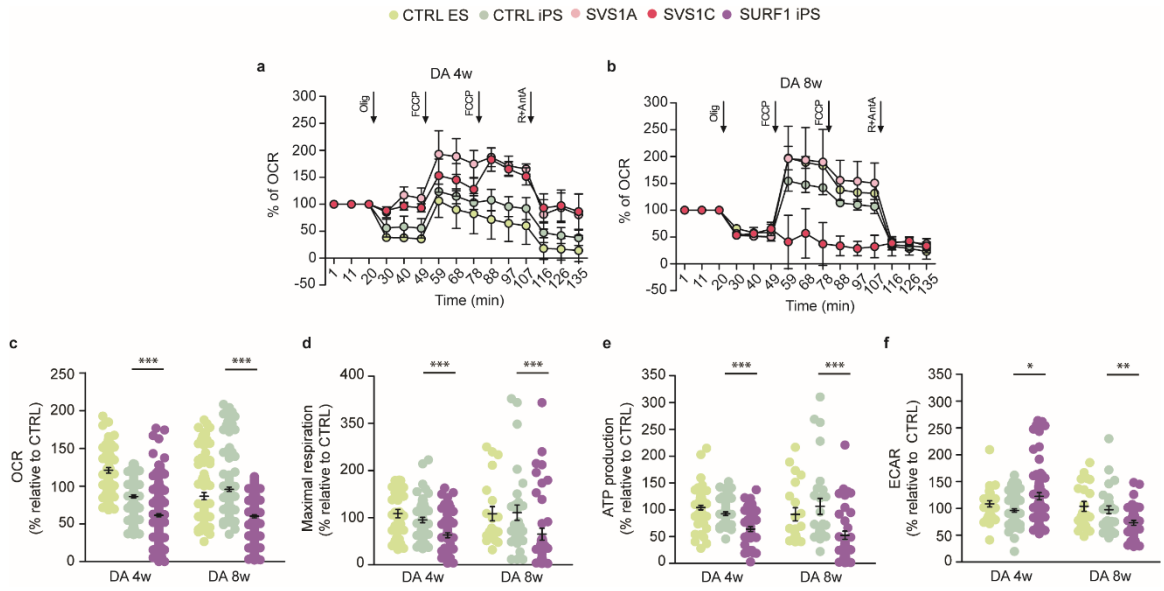

Figure 3.4.2.3.A.: Impaired bioenergetics in DA-enriched composite cultures of LS^{SURF1}
a-b, *Oxygen consumption rate (OCR) profile in iPSC-derived 4w and 8w dopaminergic (DA)-enriched neuronal cultures from CTRL ES (H1), CTRL iPSC (XM001) and SURF1 patients (SVS1A and SVS1C).* ***c-f,*** *OCR, maximal respiration, ATP production, and extracellular acidification rate (ECAR) in 4w and 8w DA cultures (mean +/- s.e.m.; n=5 independent experiments; * p<0.05; ** p<0.001; *** p<0.001; Mann-Whitney U test; one-way ANOVA followed by Bonferroni multiple comparison test, *** p<0,001).*

Moreover, patient-derived composite cultures exhibited higher ECAR levels at 4 weeks compared to composite cultures of healthy controls. On the contrary, patient-derived composite cultures displayed reduced ECAR levels at 8th weeks compared to composite cultures derived from healthy control lines. At this very mature stage, DA-enriched composite cultures of the patient lines seem to stop compensating energy demand via glycolysis. All parameters related to mitochondrial respiration and glycolysis were significantly lower in composite cultures of

patient lines compared to healthy controls and corrected lines at 8w. (Figure 3.4.2.3.A. f, Figure 3.4.2.3.B. f).

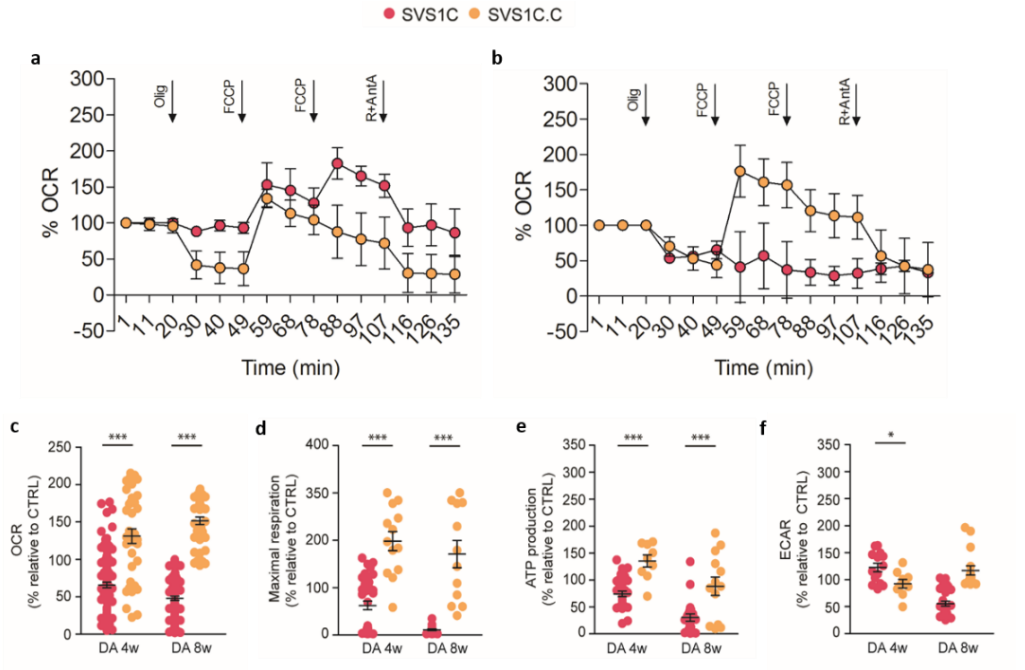

Figure 3.4.2.3.B.: Restored bioenergetics upon mutation correction in DA-enriched composite cultures of SVS1C.C

a-b, *Oxygen consumption rate (OCR) profile in iPSC-derived 4w and 8w dopaminergic (DA)-enriched neuronal cultures from SVS1C and genetically corrected SVS1C.C.* ***c-f****, OCR, maximal respiration, ATP production, extracellular acidification rate (ECAR) in 4w and 8w DA cultures (mean +/- s.e.m.; n=3 independent experiments; * p<0.05; *** p<0.001).*

Altogether *SURF1* mutations impair mitochondrial respiration in DA-enriched composite cultures at both 4 and 8th weeks, which was initially observed biochemically and bioenergetically at the NPC level. Additionally, the compensation mechanism of the differentiated culture of the patient lines via glycolytic respiration seems not to be sufficient anymore at 8th weeks, and this is where the severity of the phenotype becomes apparent.

3.4.2.3.1. Enzymatic assessment of lactate production

The supernatants collected from the DA-enriched composite cultures were used for enzymatic lactate assay, and cultures derived from patient lines tend to have higher lactate levels compared to cultures from healthy controls (Figure 3.4.2.3.1.). DA-enriched composite cultures of SVS1C produced an increased amount of glycolysis-derived lactate compared to the corrected line. The tendency in high lactate levels could be a result of the presence of immature cell types or astrocytes which are primarily glycolytic.

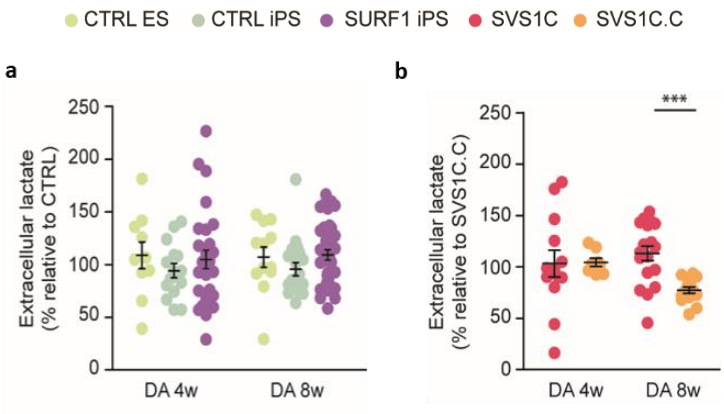

Figure 3.4.2.3.1.: Quantification of extracellular lactate in composite cultures of all lines
a, *Quantification of extracellular lactate in the supernatant of iPSC-derived 4w and 8w dopaminergic (DA)-enriched neuronal cultures from CTRL ES (H1), CTRL iPSC (TFBJ and XM001) and SURF1 patients (SVS1A and SVS1C)* ***b,*** *Quantification of extracellular lactate in the supernatant of iPSC-derived 4w and 8w dopaminergic (DA)-enriched neuronal cultures from isogenic lines SVS1C and SVS1C.C (mean +/- s.e.m.; n=4 independent experiments; *** p<0.001; Mann-Whitney U test).*

3.4.2.3.2. Transcriptomic profile of bioenergetics

In order to understand the disease-associated disrupted bioenergetic profile better and characterize DA-enriched composite cultures in a more evident way, transcriptome analysis was performed on 4w and 8w DA cultures from CTRL ES (H1), CTRL iPSC (XM001), and *SURF1* iPSC (SVS1A and SVS1C) (Figure 3.4.2.3.2. a) using polyA mRNA-sequencing and of 4w and 8w DA cultures from SVS1C and SVS1C.C using ribo-zero total RNA-seq (Figure 3.4.2.3.2. b).

8w neuronal cultures from *SURF1* iPSC downregulated *PPRGC1A (PGC1A)*, a master activator of mitochondrial biogenesis and OXPHOS metabolism that is important for neuronal maturation. *SURF1* iPSC 8w DA cultures also downregulated *PDK3* and *PDK4*, negative regulators of glucose oxidation and crucial for maintaining energy homeostasis. At the same time, 4w and 8w cultures from *SURF1* iPSC showed increased expression of glycolysis-promoting lactate dehydrogenase enzymes *LDHA* and *LDHD*. Interestingly, the genes that were shown for the bioenergetic profile indicated an upregulation of mtDNA-encoded genes (such as *MT-CO1*). At the beginning of differentiation, neuronal cells have increased energy demands and may thus attempt to compensate their COX deficiency through an augmented expression of components of the catalytic core of COX enzyme. However, upon prolonged differentiation, this compensatory mechanism may be shut down as it becomes insufficient. Taken together, maturing neuronal cultures carrying *SURF1* mutations might fail to activate mitochondrial metabolism over time and therefore retain features of glycolytic metabolism. Additionally, patient-derived composite cultures showed downregulation of *SNPH* and *KIF5C* which were

shown to mediate the activity-dependent immobilization of axonal mitochondria in time-lapsing imaging analysis of live neurons from *Snph* mouse models (Chen et al., 2009).

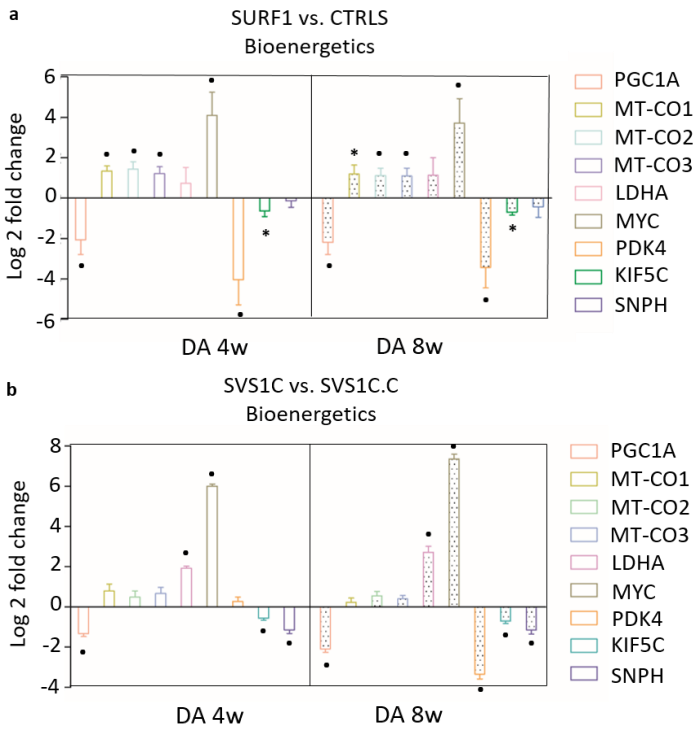

Figure 3.4.2.3.2.: Differentially regulated bioenergetics genes composite cultures of all lines
a-b, *Log fold changes (LFC) of genes regulating mitochondrial bioenergetics and dynamics in iPSC- in 4w (empty bars) and 8w (dotted bars) DA-enriched composite cultures from SURF1 iPSC (SVS1A and SVS1C) vs. CTRL (H1 and XM001) and in 4w (empty bars) and 8w (dotted bars) DA cultures from SVS1C and SVS1C.C (mean +/- s.d.; * p<0.05, ´´ p<0.01, o p<0.001, • p<0.0001).*

3.4.2.3.3.The functional consequences of bioenergetic defects

The mitochondrial dynamics and bioenergetics reciprocally influence each other, so the next aim was to assess the consequences of the bioenergetic defects in differentiated neurons through quantification of mitochondrial movement. iPSC-derived 4w and 8w DA cultures from healthy controls (H1 and XM001), patient lines (SVS1A and SVS1C), and corrected line (SVS1C.C) were live-stained with MitoTrackerRed and imaged with a spinning disk microscope for almost five minutes. All experiments were done in triplicates and stored. Only isogenic lines were analyzed due to time restrictions. The analysis showed that SVS1C-derived DA composite cultures showed a significant increase in mitochondrial motility in comparison to

SVS1C.C cultures, causing a significantly reduced number of stationary mitochondria (Figure 3.4.2.3.3.).

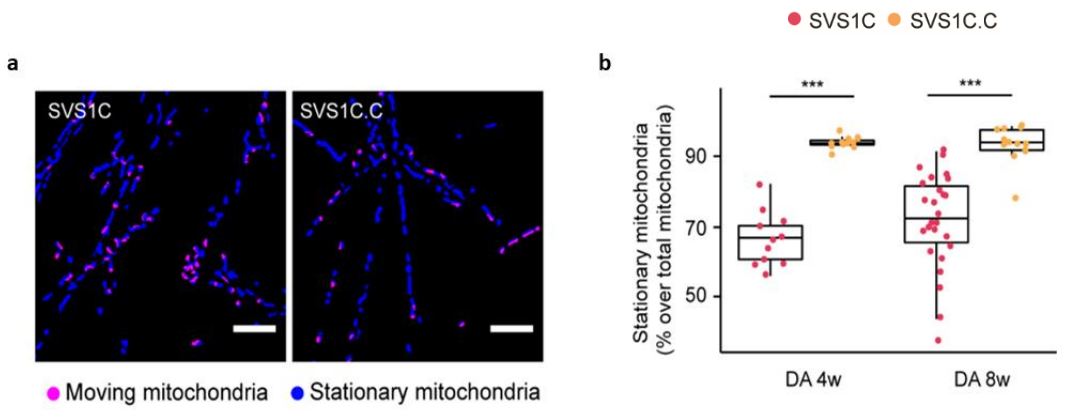

Figure 3.4.2.3.3.: Restored number of stationary mitochondria upon mutation correction in composite cultures of SVS1C isogenic line pair

a, *Representative images of iPSC-derived 8w DA cultures live-stained with MitoTrackerRed and imaged with a spinning disk microscope. Culture of SVS1C has 76 total mitochondria, 26 moving mitochondria (in pink) and the culture of SVS1C.C has 87 total mitochondria and 45 moving mitochondria. Scale bar: 10 µm.* ***b****, Quantification of stationary mitochondria in 4w and 8w DA cultures from SVS1C and genetically corrected SVS1C.C (median +/- 95% confidence interval; *** p<0.001, one way ANOVA followed by Tukey Honestly Significant Differences). (Contributions are indicated in section 8.3.).*

The uncoupler FCCP was given to culture to test the newly established system and analysis method, FCCP is known to reduce the motility of mitochondria by causing rapid dissipation of the membrane potential, which further reduces the mitochondrial calcium uptake, and therefore ATP levels fall below the levels needed for movement (Miller et al., 2004). Indeed after treating 4w and 8w DA cultures with FCCP, the percentage of moving mitochondria reduced significantly (Suppl. Figure 3.4.2.3.3.). Since neurons have sophisticated structural features and ATP has a limited diffusion capacity in the long axonal process (Hubley et al., 1996); neurons anchor ATP mitochondria in the regions where metabolism capacity is in high demand at distal ends. By anchoring mitochondria at the places, mitochondria serve as stationary power plants for stable ATP supply necessary to maintain the synaptic homeostasis (Courchet et al., 2013; Sheng, 2017). Hence, the disruption of mitochondrial bioenergetics and motility in *SURF1*-mutant cultures might negatively affect the branching and firing capacity of differentiating neurons.

3.4.2.4. Neuronal profiling

Neurons undergo a variety of complex morphological arrangements to assemble into neuronal circuits and propagate signals. As NPCs start to mature, they undergo axonal differentiation such as forming new branching and new dendritic formation. They become more elongated so that they can form synapses to communicate with each other. This whole mechanism indeed is not free for costs. Axonal growth required a considerable amount of energy for building material as well as for intracellular transport. Considering the defects seen in mitochondrial respiration defects, then next aim was to address the capacity of neurons to generate branches using high-content analysis (HCA)-based quantification of neurite length per neuron and branching points per neuron in 4w and 8w DA neuronal cultures in multi-well format.

The main regions within a neuron are the nucleus, cell body, neurites, and branch points. Processed images show nuclei was circled in red, cell bodies in cyan, neurites in green, and branch points in yellow color. This is illustrated in the following figure with their color annotations (Figure 3.4.2.4. a). When the neurons reach the maturity of 4 and 8 weeks, they were seeded on the assay plates and analyzed four days later. Therefore this is an assessment of outgrowth capacity of the neurons. Results showed that the neurite outgrowth capacity was significantly disrupted in neurons from *SURF1* iPSC compared to neurons from healthy controls (Figure 3.4.2.4. b-c). They had shorter neurite length and also fewer branch points. The branch points are where the elongated neurites split to output information. The difference in outgrowth capacity became particularly more evident at 8 weeks. Correction of *SURF1* mutation in SVS1C.C neurons restored the neuronal complexity in neurites and as it restored the energy capacity of the patient cells (Figure 3.4.2.4. d-e). This data also shows that energy capacity is critical for axonal outgrowth. Of course, there are also other essential factors for the formation of a healthy growth cone of an axon. Besides the intrinsic factors, extrinsic factors such as wisely known morphogens also play a critical role.

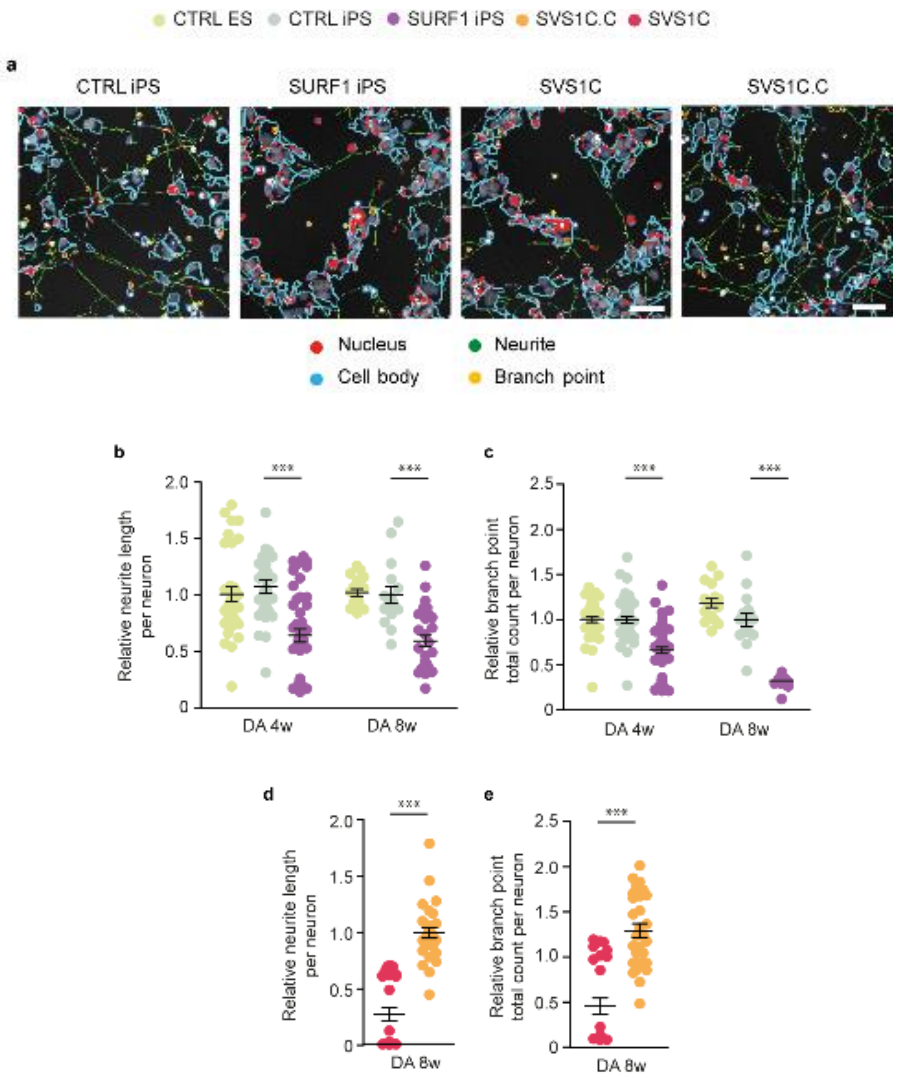

Figure 3.4.2.4.: Aberrant neuronal branching in neurons of DA-enriched composite cultures of LS^{SURF1}

a, *Representative images of the HCA mask for neuronal profiling showing shorter neurites (in green), fewer branch points (in yellow) in iPSC-derived 8w DA-enriched composite cultures from SVS1A and SVS1C. Scale bar: 50 µm.* ***b-c,*** *High content analysis (HCA)-based quantification of neuronal profiling based on TUJ1-expressing neurons in iPSC-derived DA cultures from CTRL ES (H1), CTRL iPSC (XM001) and SURF1 patients (SVS1A and SVS1C).* ***d-e,*** *High content analysis (HCA)-based quantification of neuronal profiling based on TUJ1-expressing neurons in iPSC-derived DA cultures from SVS1C and genetically corrected SVS1C.C (mean +/- s.e.m.; n=3 independent experiments; *** p<0.001; one way ANOVA followed by Bonferroni multiple comparison tests).*

3.4.2.4.1.Transcriptome analysis of axonal guidance

Addition to the energy capacity of the cells, axonal guidance cues help healthy growth cone to find the right target cells to form synapses. Axons express guidance receptors on their elongating tip and navigate to their targets by using the guidance cues which could be attractive or repulsive that can act over long distances or locally. Extrinsic cues implicated in axonal

branching vary a lot, and some of the important ones such as *NTN1,* semaphoring receptor *NRP1*, and *SLIT3* were downregulated in patient-derived DA neuronal cultures. Some studies showed that the absence of these proteins caused defects in axon guidance and target recognition, thus defects in synapse formation (Figure 3.4.2.4.1.) (Dominici et al., 2017). There was also a significant downregulation in intrinsic guidance molecules. For instance, a member of the ARP2/3 complex, *ARX*, which is known to help the formation of axon branches (Spillane et al., 2011; Wegner et al., 2008) was downregulated. The transcription factor *GATA3* also showed differential expression, which is known to be a downstream effector of Hoxb1 that controls the migratory properties of motor neurons (Pata et al., 1993; Bonito & Studer, 2017).

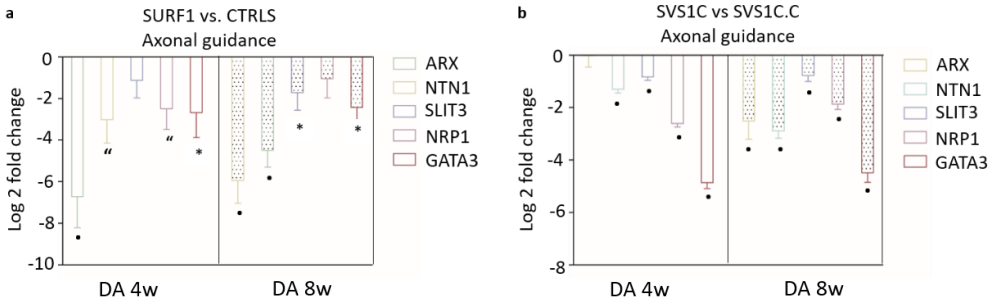

Figure 3.4.2.4.1. Differentially regulated axonal guidance genes in composite cultures of all lines
a-b, *Log fold changes (LFC) of genes essential for axonal guidance in iPSC- in 4w (empty bars) and 8w (dotted bars) DA cultures from SURF1 iPS (SVS1A and SVS1C) vs. CTRL (H1 and XM001) and in 4w (empty bars) and 8w (dotted bars) DA cultures from SVS1C and SVS1C.C (mean +/- s.d.; * p<0.05, ´´ p<0.01, o p<0.001, • p<0.0001).*

3.4.2.5. Passive and active membrane properties of the neurons

Altogether, *SURF1* mutations led to defects in bioenergetics, mitochondrial trafficking, and branching capacity, which are giving hints for possible defects in neurotransmission. Functional synapses require mitochondria to supply ATP and especially in high demand areas such as synapses. For instance, in the brain, synapses are the primary sites of ATP consumption and mitochondria supply most of the ATP (almost 90 %), while glycolysis contributes to the little part of the ATP (around 10 %) (Harris et al., 2012). In order to understand if there are any defects in the functionality of maturing neurons, patch-clamp electrophysiology recordings were done to assess passive membrane properties, to measure of neuronal function over time, potential firing properties, and synaptic activity at different maturation stages which are 4w, 6w and 8w.

Patch-clamp analysis demonstrated that differentiating neurons from healthy controls, patients, and corrected lines matured over time, as indicated by their passive membrane

properties showing time-dependent increase in cell capacitance (as neurons increase in size) (Suppl. Figure 3.4.2.5. a-b) and decrease in input resistance (as neurons acquire more ion channels in their plasma membrane) (Suppl. Figure 3.4.2.5. c-d). Although passive membrane properties were indicating the neurons were healthy, the active membrane properties of neurons (i.e., electrical potentials across the plasma membrane activated by voltage) differed between patients and controls. There was a significant increase in sodium and potassium currents at 8w compared to 4w neurons derived from healthy controls (Figure 3.4.2.5.A. a-b). On the contrary, this increase from 4w to 8w in neurons from patients was less pronounced for K currents and none for Na currents (Figure 3.4.2.5.A. c). The mutation correction significantly restored the Na and K currents for both 4w and 8w, and the functionality is recovered (Figure 3.4.2.5.A. c-d).

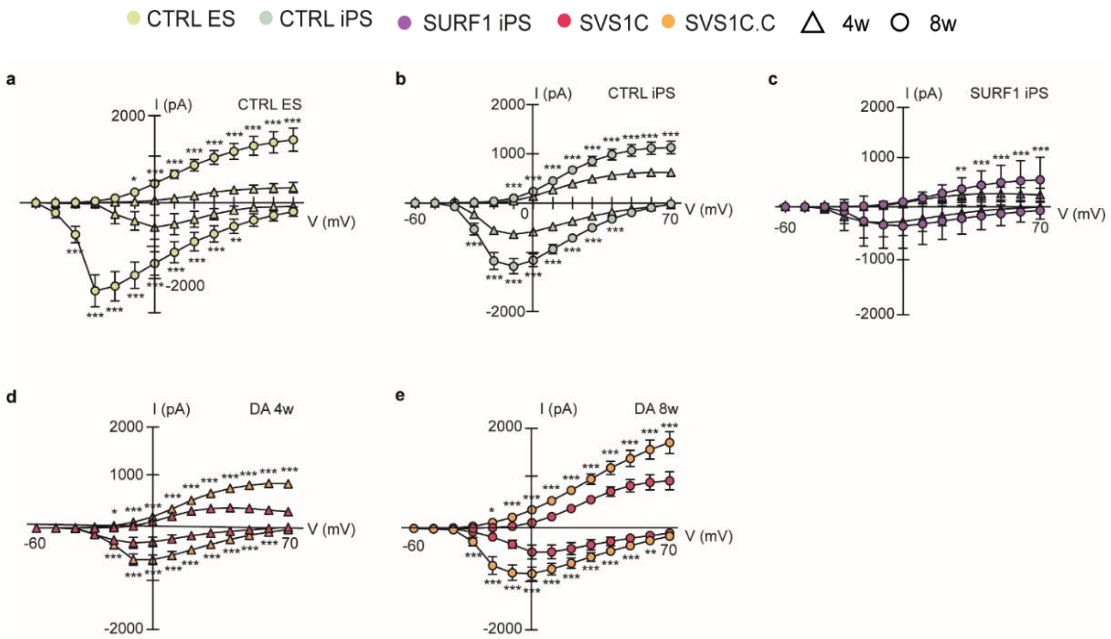

Figure 3.4.2.5.A.: Defects in sodium and potassium currents in neurons of DA-enriched composite cultures LS^{SURF1}

a-c, *Sodium and potassium currents in iPSC-derived 4w and 8w DA cultures from CTRL ES (H1)* ***(left),*** *CTRL iPS (TFBJ and XM001)* ***(middle),*** *and SURF1 iPS (SVS1A and SVS1C)* ***(right)****. (mean +/- s.d.; n= at least 2 independent experiments; * p<0.05, ** p<0.01, *** p<0.0001; two-way ANOVA).* ***d,e*** *Comparison of sodium and potassium currents in iPSC-derived 4w, 8w DA cultures from SVS1C and SVS1C.C. (mean +/- s.d.; n= at least 2 independent experiments; * p<0.05, ** p<0.01, *** p<0.0001; two-way ANOVA). (Contributions are indicated in section 8.3.).*

The number of spikes was counted for each recording to understand the spiking patterns of neurons, and they were classified as none (no spike), single spike (one spike), and multiple spikes (at least two spikes). Neurons communicate by sequences of short pulses, so-called action potentials, or spikes. Neurons in composite cultures from patient lines had a higher number of non-spikers, and fewer single-spikers compared to cultures from healthy controls and corrected lines (Figure 3.4.2.5.B. a, c). There were not any differences at multiple spiking profile between the lines at 4th weeks old. On the other hand, at 8th weeks, cultures from healthy control and corrected lines had much higher multiple-spikers compared to patient-derived neuronal cultures (Figure 3.4.2.5.B. b, d).

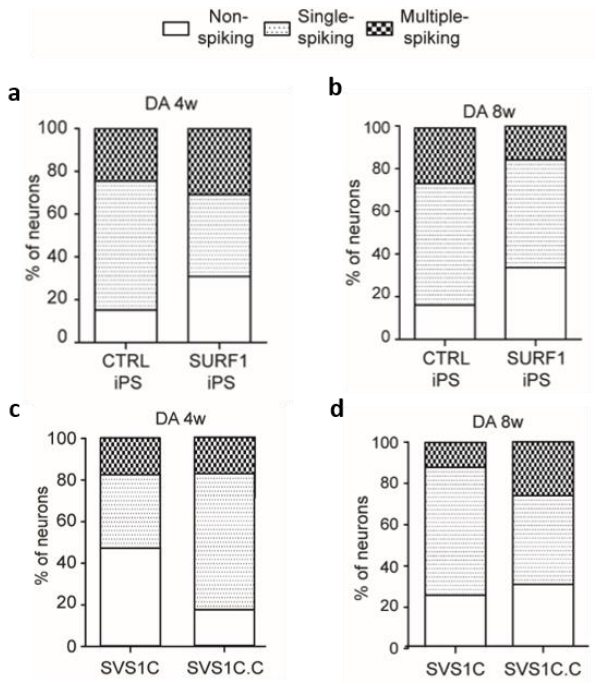

Figure 3.4.2.5.B.: Spiking profile of neurons in DA-enriched composite cultures of all lines
a-b, *Percentage of neurons (mean) that are not spiking, single spiking, or multiple spiking in iPSC-derived 4w* ***(left)*** *and 8w* ***(right)*** *DA cultures from CTRL ES (H1), CTRL iPS (TFBJ and XM001), and SURF1 iPS (SVS1A and SVS1C).* ***c-d,*** *Percentage of neurons (mean) that are not spiking, single spiking, or multiple spiking in iPSC-derived 4w* ***(left)*** *and 8w* ***(right)*** *DA cultures from SVS1C and SVS1C.C. DA neuronal cultures from control and corrected lines show an increased number of multiple spikes while neurons from patient lines show a decreased percentage in multiple spikes and an increase in the number of single spikes.*

In the next experiment, multiple spiking profile is analyzed in a more detailed way. There were a much higher number of spikes derived from the CTRL ES (H1) than any other lines (Figure 3.4.5.2.C. a). Neurons from CTRL iPSC tend to have a higher number of spikes compared to patient lines, whereas it was not significant. Neuronal cultures from CTRL ES and SVS1C.C exhibited post-synaptic currents indicative of synaptic activity, which was not observed in SVS1C

neuronal culture (Figure 3.4.5.2.C. b-c). There were no synaptic currents in the neuronal cultures from healthy controls, which highlights the importance of having an isogenic line in this study (Figure 3.4.5.2.C. b-c).

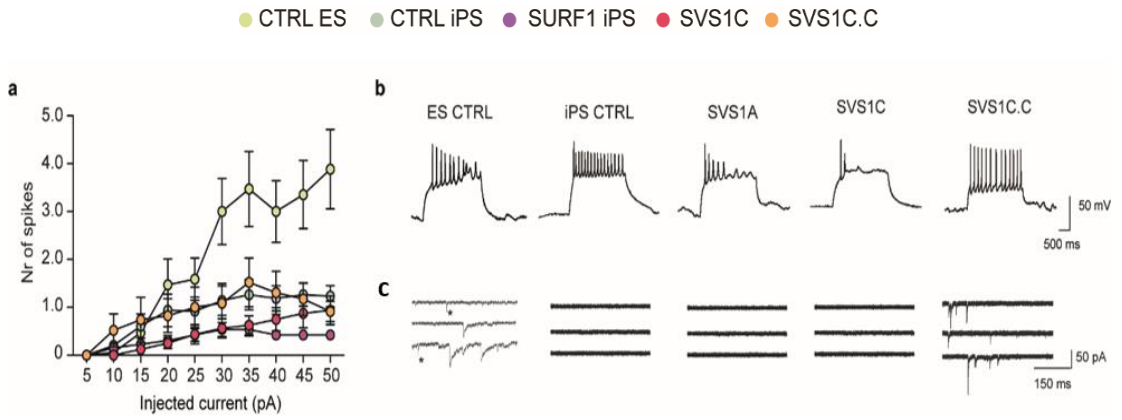

Figure 3.4.5.2.C.: Synaptic activity of neurons in DA-enriched composite cultures of all lines
a, *Number of spikes increases as injected current (pA) increases. iPSC-derived 8w DA cultures from CTRL ES (H1), CTRL iPS (TFBJ and XM001) and genetically corrected (SVS1C.C) tend to have a higher number of spikes (mean +/- s.d.; n= at least 2 independent experiments).* ***b,*** *Representative electrophysiology traces showing iPSC-derived 8w DA cultures from SVS1A and SVS1C showing less multiple spiking activity compared to CTRL ES (H1) and CTRL iPS (TFBJ and XM001) and genetically corrected (SVS1C.C).* ***c,*** *iPSC-derived 8w DA cultures from CTRL ES (H1) and genetically corrected line (SVS1C.C) showing postsynaptic currents. (Contributions are indicated in section 8.3.).*

3.4.2.5.1. Transcriptome analysis of neuronal activity profile

HCA-based neuronal profiling and patch-clamp recordings showed that *SURF1* mutations cause less branching complexity as well as impair the functionality of maturing neurons which disrupts their firing properties and their ability to establish synaptic connections.

In the transcriptomic analysis of DA-enriched composite cultures, *SURF1*-mutant 4w and 8w DA cultures showed downregulation of synaptic genes (*SYP, SYT13,* and *SNAP25*), potassium and sodium channel genes (*SCN2A, SCN9A, KCNC2, KCN3A*), as well as NMDA and AMPA receptors genes (*GRIN2B, GRIA4*) (Figure 3.4.5.2.1.).

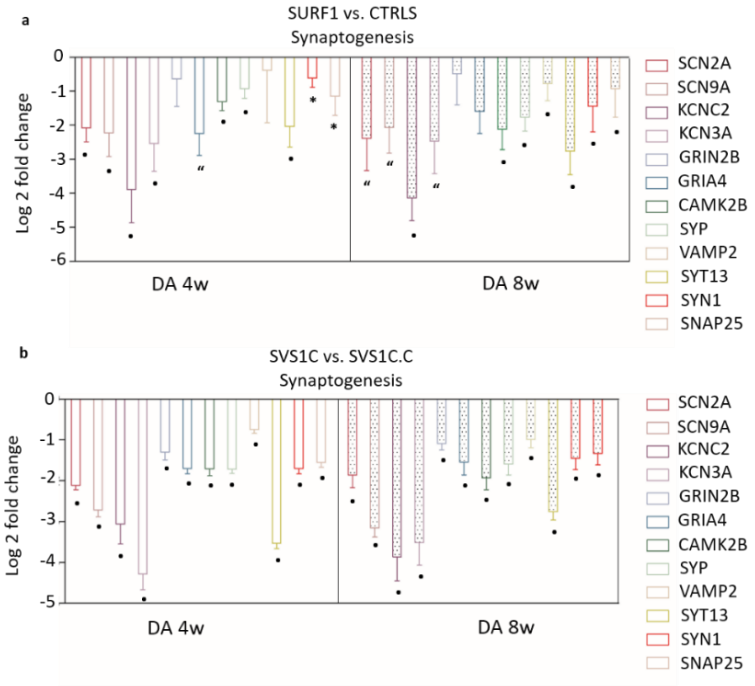

Figure 3.4.2.5.1.: Differentially regulated synaptogenesis genes in composite cultures of all lines
a-e, *Log fold changes (LFC) of genes regulating synaptogenesis in iPSC-derived 4w (empty bars) and 8w (dotted bars) DA cultures from CTRL ES (H1), CTRL iPS (TFBJ and XM001) and SURF1 patients (SVS1A and SVS1C) and isogenic lines (SVS1C and SVS1C.C) (mean +/- s.d.; * p<0.05, ´´ p<0.01, o p<0.001, • p<0.0001).*

3.5. Derivation of three-dimensional (3D) cerebral organoids from iPSC cultures

Since monolayer cultures do not allow studying the manifestation of spatial developmental defects, and currently there is not adequate *in vivo* model of LS, a three-dimensional (3D) model of neuronal development was employed to explore the consequences of *SURF1* mutations on organogenesis which would help to understand the disease etiology (Suppl. Figure 3.5.A.).

The first goal was to understand if there are any differences in the size of the organoids between the groups. Patient-derived organoids appeared smaller in many independent experiments during derivation of cerebral organoids in culture. The initial cell number seeded were the same, whereas it was already observable that at day ten, the size of organoids was differing from each other and remained different at day 40 (Figure 3.5.A. a). Cross-sectional analyses by ImageJ confirmed that cerebral organoids derived from SVS1C were significantly smaller in size than organoids derived from the isogenic controls SVS1C.C (clones 3p and 3bb) (Figure 3.5.A. b-c). The reduced size of the organoids mimics the neurodevelopmental disorder, microcephaly, which has been reported in some cases of LS patients as well.

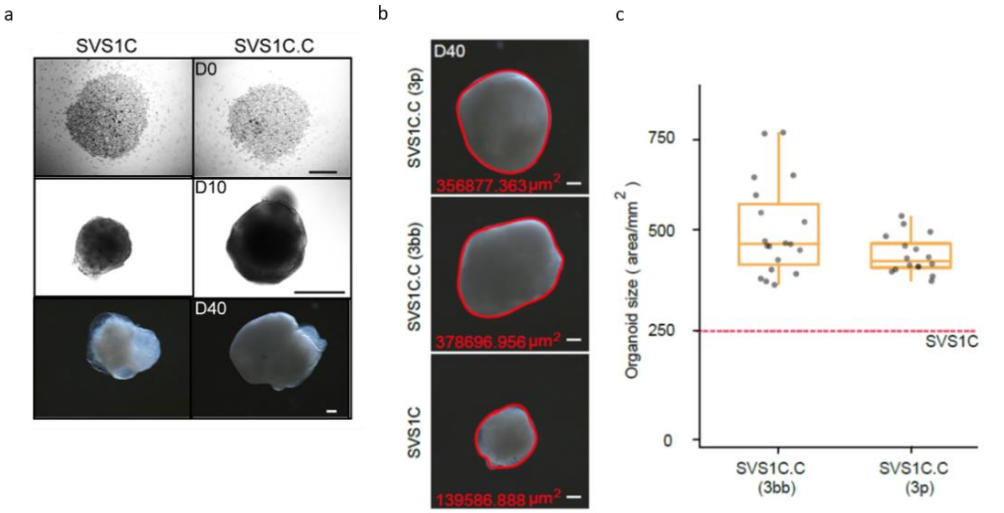

Figure 3.5.A.: Smaller cerebral organoids derived from iPSC cultures of LS^{SURF1}

a, *Representative images of cerebral organoids derived from SVS1C and SVS1C.C at several days of differentiation starting from the day embedded into Matrigel (day 0). Scale bars: d0: 500 µm, d10: 200 µm, d40: 200 µm.* ***b,*** *Representative images of brain organoids from isogenic lines at day 40 were done doing cross-sectional area analysis by Image J. Scale bar: 100 µm, (circled in red line).* ***c,*** *Quantification of the size cerebral organoids demonstrated that the two clones of SVS1C.C had a comparable size compared to organoids from SVS1C (pink dotted line) (median +/- 95% confidence interval; n=2 independent experiments). (Contributions are indicated in section 8.3.).*

Brain development *in vivo* exhibits a high degree of heterogeneity and regionalization. Immunohistochemical analysis of SVS1C organoids exhibited a dramatic disruption of the neuroepithelial layer surrounding fluid-filled cavities that are reminiscent of embryonic ventricles. Hoechst stainings taken at different magnifications showed very severe defects in the compartmentalization of cerebral organoids derived from patients (Figure 3.5.B. a). Next, quantitative real-time PCR analysis of cerebral organoids from isogenic lines was done to look at the gene expression profile with the appropriate primers, which were significantly different in 2D neuronal cultures. Staining the sections of cerebral organoids derived from patient lines with NPC markers *SOX2* and neuronal marker *TUJ1* showed the aberrant distribution of *SOX2* and *TUJ*1, suggesting defects in neuronal compartmentalization (Figure 3.5.B. c-d).

In agreement with previous findings in 2D DA cultures, SVS1C organoids showed downregulated expression of genes involved in neurogenesis like *DCX, NKX2.2, LHX2*, and of genes associated with neuronal firing and synaptic activity like *SYP, SYT3, KCNQ2*, and *SCN7A*, and of genes regulating axon guidance like *ARX, SPON1, NTN1,* and *GATA3*. (Figure 3.5.B. b). SVS1C organoids also showed reduced expression of genes regulating mitochondrial metabolisms like *PGC1A* and *PDK4*, while the expression of genes associated with glycolysis such

as *MYC* and *LDHA* increased in comparison to isogenic control SVS1C.C organoids (Figure 3.5.B. b).

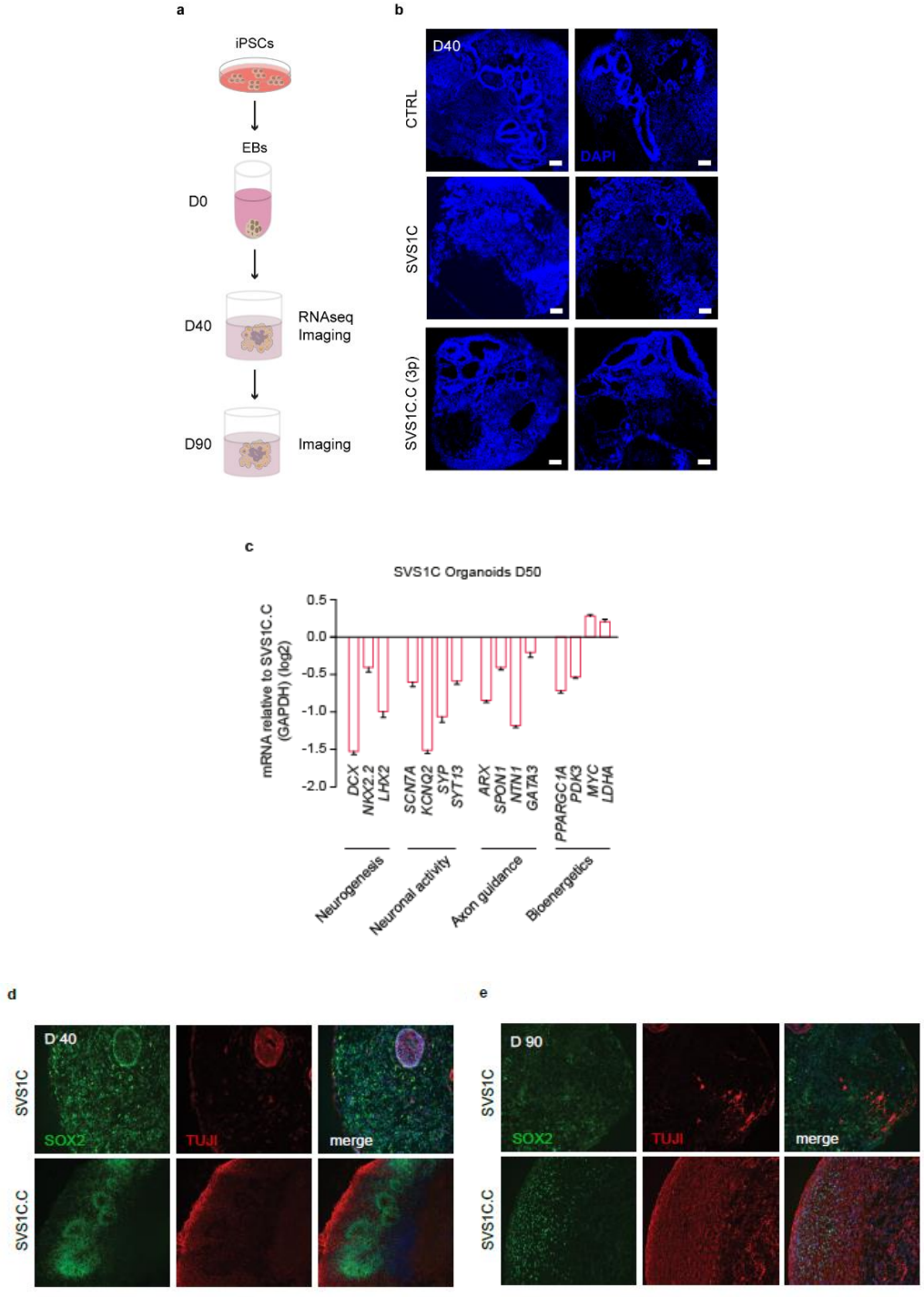

Figure 3.5.B.: Spatial defects in iPSC-derived cerebral organoids of LS^{SURF1}

a, *Summary of the workflow with day information and done experiments.* ***b,*** *Representative images of cerebral organoids derived from iPS CTRL (XM001), isogenic line pair (SVS1C and SVS1C.C) showing the disruption of the epithelial layers in SVS1C. Nuclei were counterstained with Hoechst. Scale bars: 500 µm (**above**), 1000 µm (**below**).* ***c.*** *Quantitative real-time PCR in cerebral organoids derived from SVS1C and SVS1C.C. Data were normalized to GAPDH (mean +/- s.d.).* ***d-e,*** *Representative images of cerebral organoids derived from SVS1C and SVS1C.C showing the reduced presence of SOX2-positive progenitors*

*(**in green**) and TUJ1-positive neurons **(in red**) at day 40 and 90 respectively. Nuclei were counterstained with Hoechst. Scale bar: 100 µm**.** (Contributions are indicated in section 8.3.).*

3.5.1. Transcriptome analysis of neurodevelopmental genes

Since DAPI staining suggested defects in compartmentalization in patient-derived organoids; human cerebral organoids might similarly display heterogeneous brain regions. The pluripotent and neural identity gene expression profiles were analyzed (Figure 3.5.1.A.). Important transcription factor *FOXG1*, a key player in neurodevelopment process whose downregulation is a sign for structural brain abnormalities, was significantly downregulated. Another developmental marker *SIX3* was also significantly down; it is known to be essential for early eye development, which might form the basis of the visual problems seen in LS patients. Usually, pluripotency markers *OCT4* (also known as *POU5F1*) and *NANOG* would diminish during organoid differentiation, whereas patient-derived organoids maintained the upregulation of pluripotent markers compared to the organoids derived from the corrected line. Meanwhile, it is expected to see neural identity markers *SOX1* and *PAX6* to be upregulated, indicating successful neural induction. *SOX1*, known as maintenance of neural progenitors, was upregulated. *PAX6*, a regulator in the coordination and pattern formation required for differentiation and proliferation, was downregulated. Dorsal cortical marker *EMX1* was also significantly downregulated, and it is known to be necessary for specification of positional identity as well as differentiation of specific neuronal phenotypes. *TBR1,* which is a critical neuron-specific factor for forebrain and have been implicated in neurodevelopmental disorders such as autism spectrum disorder, is downregulated in SVS1C-derived cerebral organoids. TBR1 is usually used as a marker of the pre-plate of the brain where reelin (*RELN*)-containing zone helps pyramidal neurons to migrate, which helps the formation of brain structures. *RELN* is also significantly downregulated, which could explain the defects seen in the cytoskeleton of the organoids. Another critical neurodevelopmental transcription factor *CTIP2* (*BCL11B*) and *SATB2* known to help projection identities, were also significantly differentially regulated. Overall, all these differentially regulated genes suggest that LS can be considered as a neurodevelopmental disorder. Additional detailed transcriptomic data were provided to show deregulation of cell fate specification, as well as midbrain dopaminergic neuron specification in detail. (Supp. Figure 3.5.1.A., Supp. Figure 3.5.1.B.).

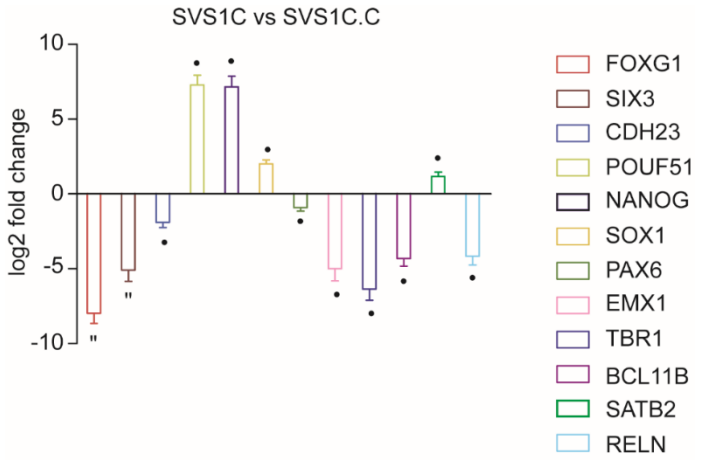

Figure 3.5.1.A.: Differentially regulated neurodevelopmental genes in cerebral organoids of LS^{SURF1}
Log fold changes (LFC) of genes regulating neurodevelopment in iPSC-derived cerebral organoid cultures from SVS1C compared to genetically edited line SVS1C.C (´´ p<0.01, • p<0.0001).

3.6. Overlap of differentially regulated genes in iPSC-derived 2D and 3D cultures

There is an overlap in genes differentially expressed in both 8w DA cultures (2D) and cerebral organoids (3D) of isogenic lines. The transcriptomic analysis highlighted defects in bioenergetics, neurogenesis and neuron projection, and morphogens for LS disease mechanism. Genes related to proliferation-pluripotency were highlighted in orange; morphogens in blue; bioenergetics in purple; and neurogenesis and neuronal wiring in green (Figure 3.6.).

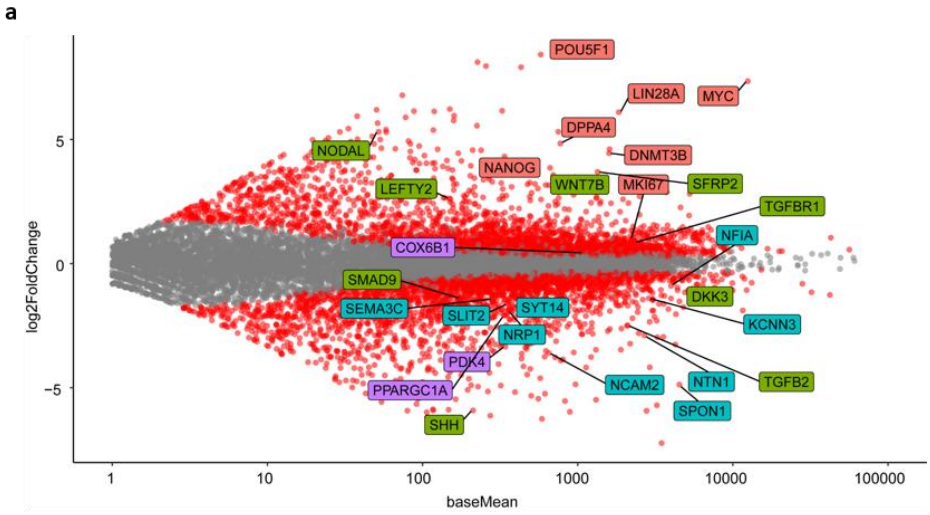

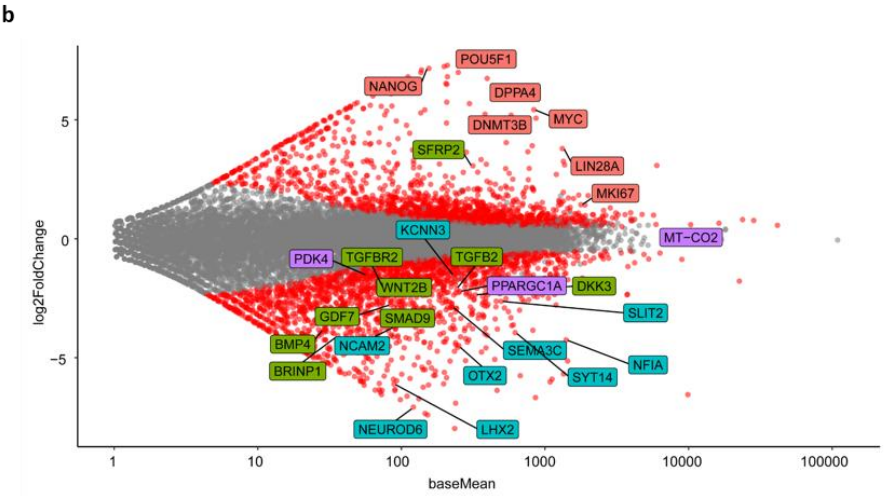

Figure 3.6.: Commonly differentially regulated genes in iPSC-derived 2D and 3D models
a, *MA plot showing log fold changes (LFC) of commonly differentially expressed genes in 8w DA cultures from SVS1C vs. SVS1C.C.* ***b,*** *MA plot showing fold (LFC) of commonly differentially expressed genes in cerebral organoids from SVS1C vs. SVS1C.C. (Highlighted genes in orange: proliferation-pluripotency, blue: morphogenes, purple: bioenergetics, and green: neurogenesis and neuronal wiring).*

Conclusively, the 3D model recapitulated the defects observed in the 2D monolayer neuronal cultures and confirmed that *SURF1* mutations impair the neural progenitor state, thereby disrupting the process of neurogenesis in terms of failing to generate functional neurons, which are the consequences of the defects in mitochondrial respiration of mitochondria. Additionally, the genes involved in general developmental pathways such as anatomical structural morphogenesis, regionalization, and system development stood out, indicating the defects in early neurodevelopmental processes.

3.7. Targeting NPC function to screen for potential therapeutic strategies

The generation of neuronal and cerebral organoid cultures from patient iPSCs gave a unique opportunity to identify LS-specific neuronal phenotypes. In addition to that, transcriptome analysis done on the cultures provided enormous data to support the findings as well as gave novel hints for possible therapeutic targets. While the neuronal and cerebral organoid models of *SURF1*-associated LS exhibit apparent disease phenotypes in neuronal profiling and bioenergetics, the dataset also showed that the defects start in early neurodevelopmental processes. Therefore, targeting NPC function and trying to prevent disease pathology as early as possible would be a good strategy for LS.

iPSC-derived NPC cultures encompass pre-mature neurons, and those derived from patient lines exhibited significantly smaller neurites and significantly reduced oxygen consumption

(Figure 3.4.1.4., 3.4.1.5.). These two phenotypes seen in pre-mature neurons were also in agreement with the phenotypes seen in mature DA neuronal cultures at both 4w and 8w (Figure 3.4.1.3.A, Figure 3.4.1.5). Therefore, the chosen therapeutic interventions were tested on those well-defined readouts, which would possibly give the first truthful hints for the maturing neurons.

3.7.1. *SURF1* gene augmentation

In this study, gene correction on the *SURF1* gene restored the COX activity, bioenergetics defects, promoted the neuronal generation, and maturation, which showed those phenotypes to be *SURF1* specific. Next, our goal was to understand if SURF1 overexpression would also be sufficient to rescue the defects in cellular bioenergetics and neuronal branching complexity seen in patient-derived NPCs.

NPCs from SVS1C were transduced with a lentiviral vector encoding wild-type SURF1 to assess the potential rescuing effect of SURF1 overexpression (SURF1-OE) and also with lentiviruses encoding only the GFP derivative mCitrine (GFP) as a control. SURF1-OE showed significantly improved mitochondrial respiration (OCR, maximal respiration, and ATP production) (Figure 3.7.1.A. a-c). Glycolytic capcaity was also analyzed, and SURF1 OE significantly decreased the ECAR levels almost to the levels of corrected line, whereas it was not reduced compared to GFP OE NPCs which is the real control for this experiment (Figure 3.7.1.A. d). Therefore, ECAR measurement was not a very clear readout, as shown previously. Additionally, the collected supernatants from the NPC cultures were used for enzymatic lactate assay, which led to a significant reduction of lactate production (Figure 3.7.1.A. e). Moreover, SURF1-OE improved the mitochondrial respiration and lowered the high lactate levels, indicating SURF1´s critical role in energy metabolism. Additionally, disrupted bioenergetics in DA 8w cultures were also counteracted by SURF1 overexpression (Supp. Figure 3.7.1.).

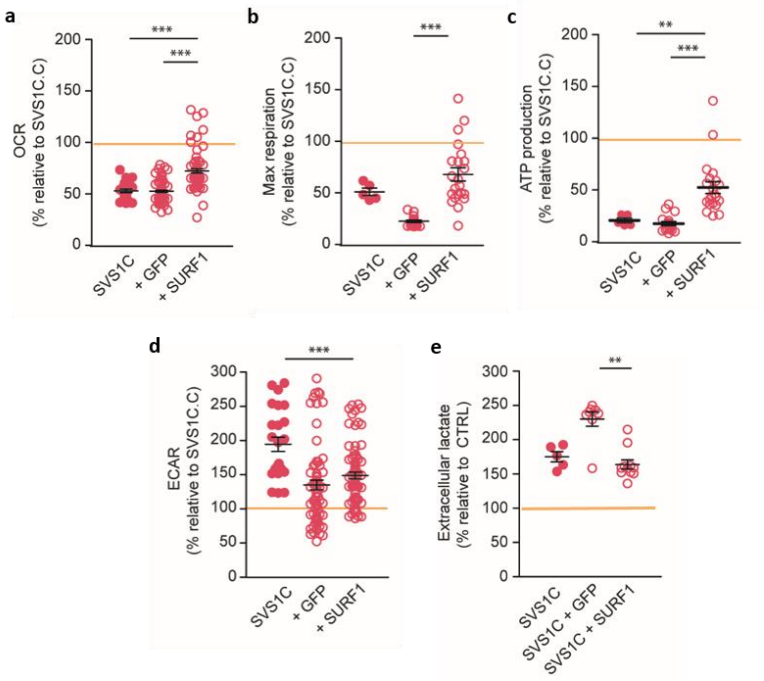

Figure 3.7.1.A.: Bioenergetic profiling in NPC cultures of SVS1C line upon stably expressing wild-type SURF1

a-e, *Oxygen consumption rate (OCR), maximal respiration, ATP production, extracellular acidification rate (ECAR) and extracellular lactate in NPC cultures from SVS1C lines stably expressing GFP derivative mCitrine (GFP) or wild-type SURF1 (SURF1-OE). Yellow line is the value for genetically corrected SVS1C.C line (mean +/- s.e.m.; n=2 independent experiments; * p<0.05, ** p<0.01, *** p<0.001; Mann-Whitney U test).*

The effect of SURF1 OE on branch complexity was assessed with HCA-based quantification. Unexpectedly, SURF1 OE did not promote axonal growth compared to GFP OE NPCs nor SVS1C NPCs itself; in fact, overexpression caused a further decrease in neurite length per neuron and branch point counts (Figure 3.7.1.B.). Overall, SURF1 overexpression does not ameliorate neurite outgrowth in NPCs, whereas SURF1 OE restored defects in neuronal branching in 8w DA cultures (Suppl. Figure 3.7.1.).

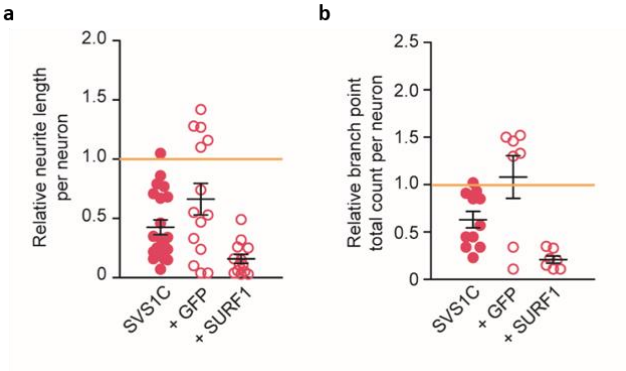

Figure 3.7.1.B.: Neuronal profiling in NPC cultures of SVS1C upon stably expressing wild-type SURF1
High content analysis (HCA)-based quantification of neuronal profiling such as neurite length per neuron ***(a)*** *and branch point total count* ***(b)*** *based on TUJ1-expressing neurons in NPC cultures of SVS1C lines stably expressing GFP derivative mCitrine (GFP) or wild-type SURF1 (SURF1-OE). Yellow line is the value for genetically corrected SVS1C.C line (mean +/- s.e.m.; n=2 independent experiments; * p<0.05, ** p<0.01, *** p<0.001; Mann-Whitney U test).*

3.7.2. Metabolic conditioning

In the next step, previously suggested metabolic conditioning strategies such as hypoxia, glucose, and pyruvate supplementation were tested to see if they improve the cellular bioenergetics and neural branching in patient-derived NPC cultures.

Hypoxic conditions were previously shown to be beneficial in animal models of LS harboring a mutation in complex I (Jain et al., 2016; Ferrari et al., 2017). The rationale behind is that hypoxia activates adaptive program allowing cells to cope with limited oxygen levels. Low oxygen levels shift the reliance from mitochondrial oxidative mechanism towards glycolysis. Secondly, glucose supplementation is suggested for LS patients during acute metabolic decompensation (Parikh, et al., 2001). Thirdly, pyruvate supplementation was suggested to restore the glycolysis pathway through decreasing the NADH/NAD(+) ratio which was initially increased due to OXPHOS defects also has been proposed as a treatment for LS caused by COX defects through decreasing the lactate-pyruvate ratio (Komaki et al., 2010).

Overnight culture under hypoxia (5% oxygen) significantly improved mitochondrial respiration in *SURF1*-NPCs. At the same time, however, hypoxia caused an undesired further significant increase in ECAR as well as lactate in SVS1C-NPCs (Figure 3.7.2.A. a, Suppl. Figure 3.7.2.). Moreover, glucose and pyruvate supplementation did not improve mitochondrial respiration in patient-derived NPCs, whereas they showed a possible beneficial effect in decreasing the ECAR levels.

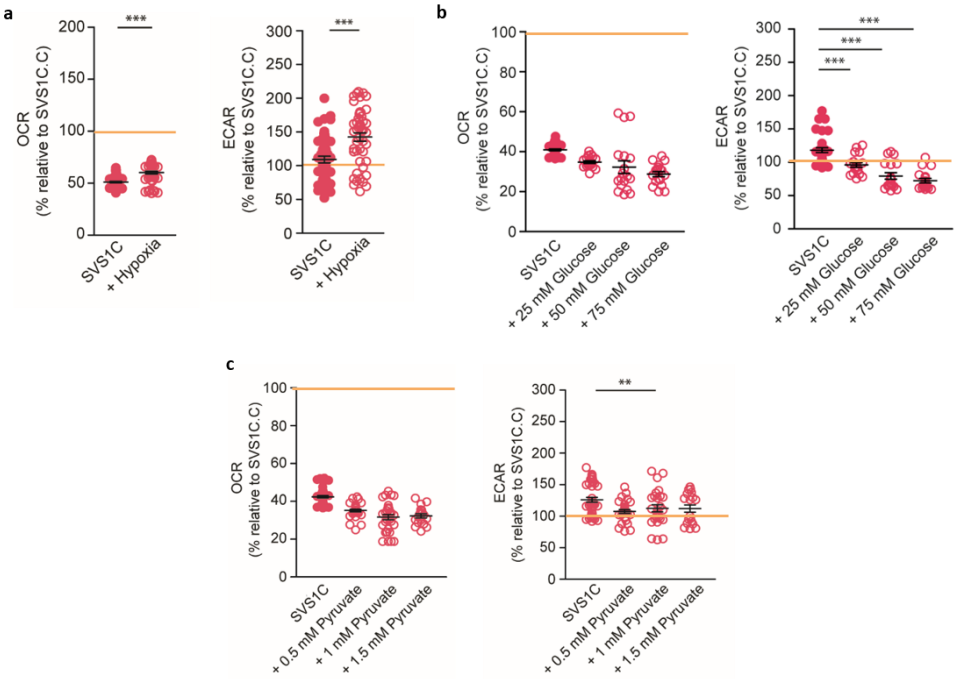

Figure 3.7.2.A.: Bioenergetic profiling in NPC cultures of SVS1C upon metabolic conditioning
a-c*, Oxygen consumption rate (OCR)* ***(left)*** *and extracellular acidification rate (ECAR)* ***(right)*** *in NPC cultures from SVS1C that were cultured overnight under hypoxia, different concentrations of glucose and pyruvate concentrations. Yellow line is the value for genetically corrected SVS1C.C line (mean +/- s.e.m.; n=2 independent experiments; * p<0.05, ** p<0.01, *** p<0.001; Mann-Whitney U test).*

Furthermore, the branching complexity was assessed with HCA-based quantification. Overnight culture under hypoxia (5% oxygen) had an adverse effect on neuronal profiling in NPCs derived from patient lines. It significantly reduced the neurite length per neuron and also the number of branch total count per neuron (Figure 3.7.2.B. a). On the other hand, overnight glucose and pyruvate supplementation did not show any beneficial effect on neurite length per neuron and branching total count in a dose-dependent manner in a consistent way (Figure 3.7.2.B. b-c).

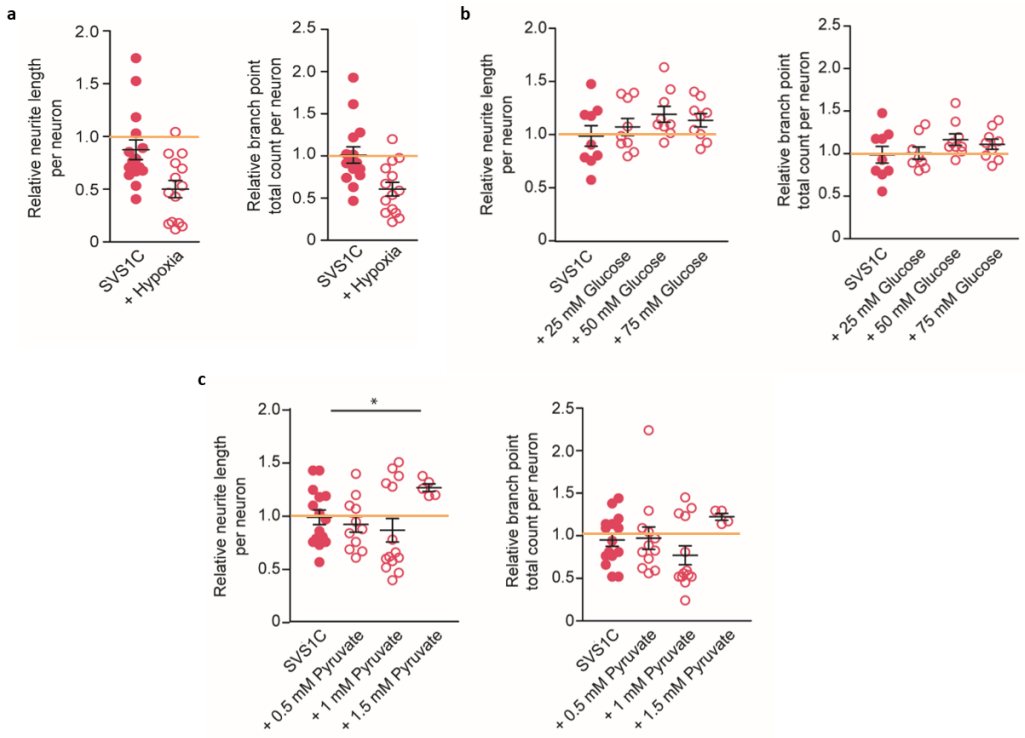

Figure 3.7.2.B.: Neuronal profiling in NPC cultures of SVS1C upon metabolic conditioning

a-c, *High content analysis (HCA)-based quantification of neuronal profiling such as neurite length per neuron (left) and branch point total count (right) based on TUJ1-expressing neurons in NPC cultures of SVS1C that SVS1C that were cultured overnight under hypoxia, different concentrations of glucose and pyruvate concentrations. Yellow line is the value for genetically corrected SVS1C.C line (mean +/- s.e.m.; n=2 independent experiments; * p<0.05, ** p<0.01, *** p<0.001; Mann-Whitney U test). (Contributions are indicated in section 8.3.).*

Overall, hypoxia partially rescues bioenergetics defects but harms neurite outgrowth. Pyruvate and glucose did not rescue mitochondrial respiration defects, whereas it was beneficial in decreasing ECAR levels; whereas did not ameliorate neurite outgrowth.

3.7.3. Dietary supplements: antioxidants

Another approach to manage the symptoms of patients with mitochondrial diseases has been by providing them vitamins or dietary supplements. Here the focus was given to the most commonly used supplementary ingredients acting as an antioxidant (N-acetyl cysteine, vitamin C, vitamin E, and alpha-lipoic acid), and as a compound that can be used as an alternative energy source such as Carnitine (Karaa et al., 2016).

Reduced levels of glutathione (GSH) is one of the signs for the dysfunction of mitochondrial respiration. NAC is one of the antioxidants used to prevent glutathione depletion

in the brain by systemically increasing cysteine levels, and it is beneficial for models of complex I disease (Wright et al., 2015; Polyak et al., 2018). Ascorbic acid (AA) is also known to increase intracellular GSH levels, which are also known to increase the rate of ATP synthesis. Also, vitamin E has a reducing effect of GSH, and its analog name is α-Tocotrienol (AT3). An *in vivo*-derived metabolite EPI-743 (2-electron redox cycling agent) is currently in clinical phase 2 trials (Matinelli et al., 2012; Pastore et al., 2013). Another critical antioxidant commonly used is lipoic acid which is an essential cofactor for mitochondrial metabolism which participates in catalysis of multiple enzyme complexes such as pyruvate dehydrogenase and is currently being used in studies and clinical trials to see their effect in RC-deficient patients (Patel et al., 2012). Lastly, L-Carnitine is used as an agent to increase substrate supply to the respiratory chain and is involved in B-oxidation of fatty acids and results in the generation of ATP via OXPHOS.

NPC cultures of SVS1C were cultured overnight with different concentrations of antioxidants NAC, AA, DHLA, L-Carnitine, and AT3 and seahorse analysis was performed to assess their bioenergetics profile for any improvement. None of the supplements improved the OCR levels, whereas all of them besides NAC decreased the ECAR levels significantly to the levels of the isogenic line (Figure 3.7.3.A.).

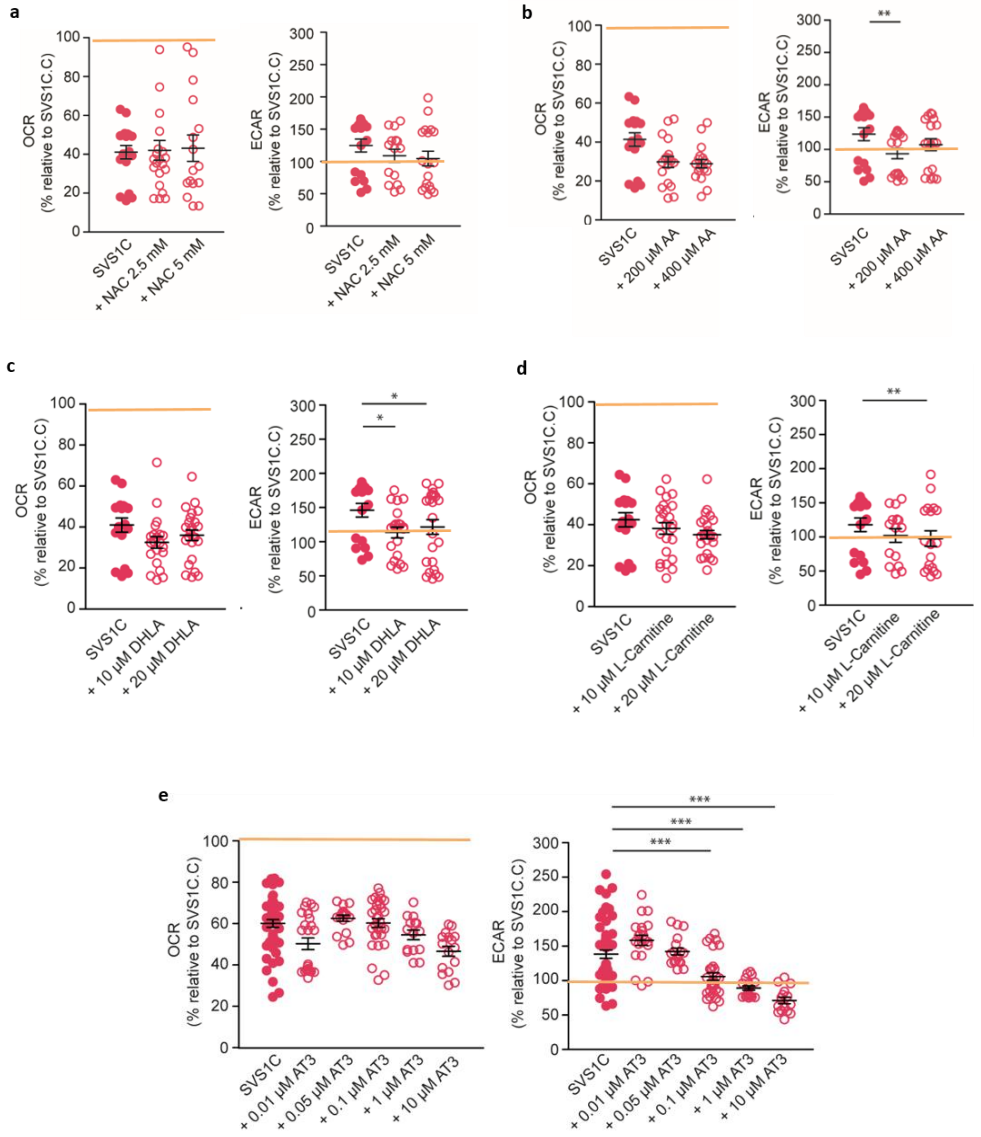

Figure 3.7.3.A.: Bioenergetic profiling in NPC cultures of SVS1C upon antioxidant treatments

a-e, *Oxygen consumption rate (OCR) (left), and extracellular acidification rate (ECAR) (right) in NPC cultures from SVS1C that were cultured overnight with different concentrations of antioxidants N-Acetyl L-Cysteine (NAC), ascorbic acid (AA), Dihydrolipoic acid (DHLA), L-Carnitine, and α-Tocotrienol (AT3). Yellow line is the value for genetically corrected SVS1C.C line (mean +/- s.e.m.; n=2 independent experiments; * p<0.05, ** p<0.01, *** p<0.001; Mann-Whitney U test). (Contributions are indicated in section 8.3.).*

Branch complexity was assessed with HCA-based quantification**.** Overnight treatment with antioxidants did not improve the defects in neurite length per neuron and branch total count in a dose-dependent manner. NAC and L-Carnitine had a slight effect of suggesting that they might be beneficial. More experiments might be needed to clarify the effect (Figure 3.7.3.B.).

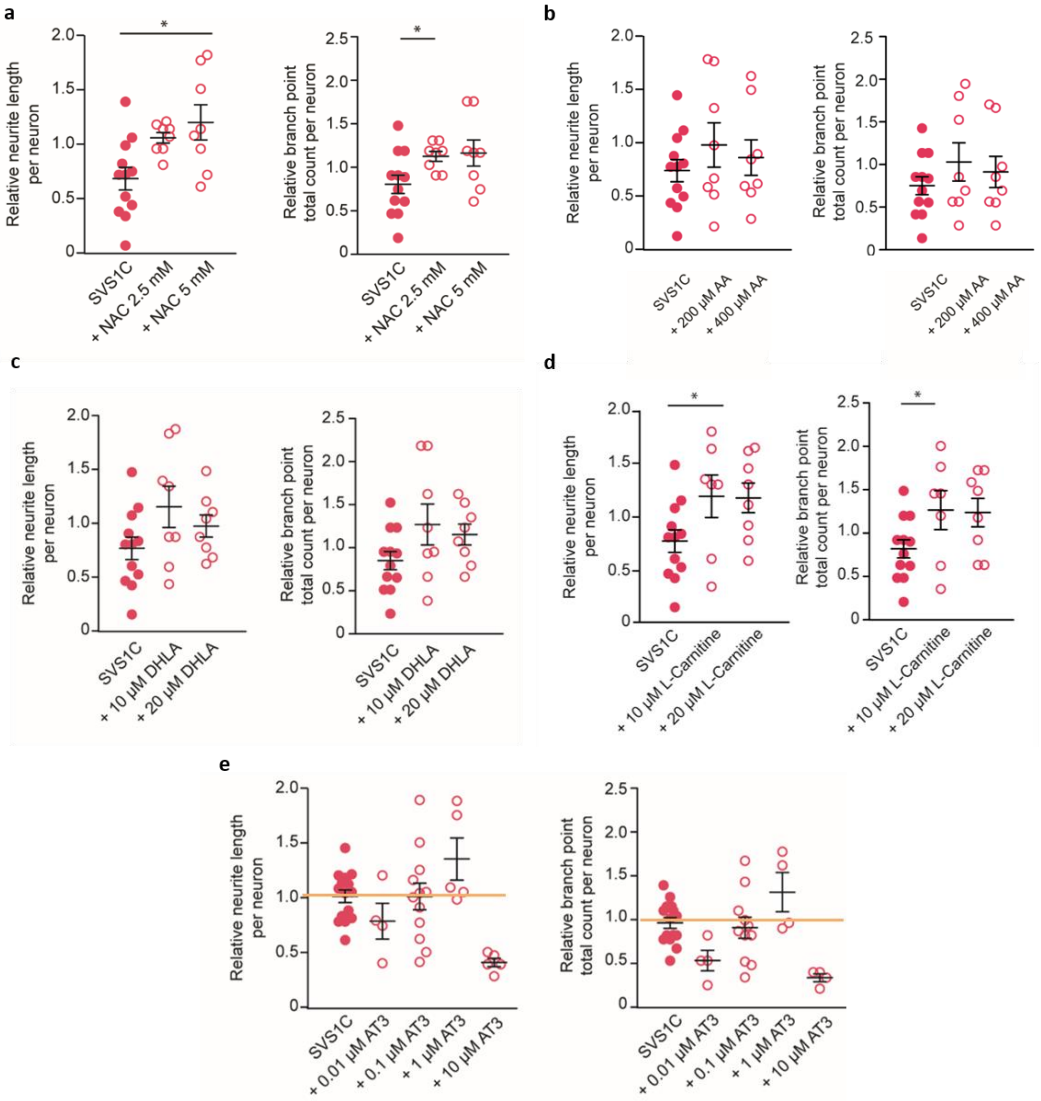

Figure 3.7.3.B.: Neuronal profiling in NPC cultures of SVS1C upon antioxidant treatments:
a-e, *High content analysis (HCA)-based quantification of neuronal profiling such as neurite length per neuron* ***(a)*** *and branch point total count* ***(b)*** *based on TUJ1-expressing neurons in NPC cultures of SVS1C that were cultured overnight with different concentrations of antioxidants N-Acetyl L-Cysteine (NAC), ascorbic acid (AA), Dihydrolipoic acid (DHLA), L-Carnitine, and a-Tocotrienol (AT3). Yellow line is the value for genetically corrected SVS1C.C line (mean +/- s.e.m.; n=2 independent experiments; * p<0.05, ** p<0.01, *** p<0.001; Mann-Whitney U test). (Contributions are indicated in section 8.3.).*

3.7.4. Small-molecules targeted pathways

A set of small molecule screenings were tested to identify potential treatment strategies for LS^{SURF1} patients. These small molecules were chosen for this study either have been previously identified to be advantageous for LS patients with other mutations or transcriptome dataset have shown differential regulation. The small molecules or drug treatments on NPCs

were done overnight and followed by either assessment of the cells bioenergetic and neuronal profiling.

RT-PCR, as well as transcriptome dataset of the patient-derived DA composite, and cerebral organoid cultures showed a very significant reduction in the expression of *PGC1-α* (Figure 3.4.2.3.2.b., Figure 3.5.c., Figure 3.6.) which is known to have neuroprotective effects by increasing mitochondrial biogenesis and its functioning (Lehmann et al., 2018; Kovářová, et al., 2012). Therefore, a pan-PPAR agonist, bezafibrate was chosen to be tested on *SURF1*-mutated NPC cultures. Bezafibrate was also shown previously to improve COX activity and mimic the effect of PGC1-α overexpression (Yatsuga et al., 2012). Another strategy was to deliver FGF21, which regulates glucose metabolism and promotes PGC1-α expression in human DA neurons (Kharitonenkov et al., 2014). Transcriptome analysis also showed a very significant upregulation of transforming growth factor beta (TGF-β) receptor (TGFßR1), which is known to regulate neuronal morphogenesis (Nakashima et al., 2018). Therefore, SB431542 (TGFβR1 inhibitor) was decided to be given as a treatment which is included in the neural induction media to induce differentiation of NPCs into DA-enriched composite cultures. Another tested small molecule was SAG (smoothened agonist), which is known to promote motor neuronal differentiation and health via sonic hedgehog (SHH) pathway which was significantly downregulated in the dataset of patient-derived neuronal cultures. Another exciting outcome of the transcriptomic dataset was the downregulation of brain-derived growth factor (BDNF), which is already in the differentiation media. Higher concentrations of BDNF were also tested. Also, retinoic acid (RA) was given to stimulate RA pathway, which is also known to be essential for motor neuronal health (Wada et al., 2009) and was also dysregulated in the dataset of patient cultures. Additionally, positive results have been reported on several mouse models using compounds increasing NAD^+ concentration, such as the NAD^+ precursor NR (Cerutti et al., 2014; Schönford et al., 2018). Additionally, PDE5 inhibitor Avanafil has been suggested effective in partially rescuing the diseased phenotype induced by the MT-ATP6 mutation (Lorenz et al., 2017). Thus different concentrations were also tested.

NPC cultures of SVS1C were cultured overnight with different concentrations of small molecules, and seahorse analysis was performed to assess their bioenergetics profile (Figure 3.7.4.A.). Bezafibrate improved bioenergetics profile by increasing OCR levels significantly in a dose-dependent manner. Also, Bezafibrate increased the maximum respiration and ATP production significantly, and in a dose-dependent manner (Suppl. Figure 3.7.4.). On the other hand, SB, as well as NR, led to a consistent decrease in ECAR levels in a dose-dependent manner. FGF21, SAG, RA, and Avanafil did not have any consistent effect on bioenergetics profile.

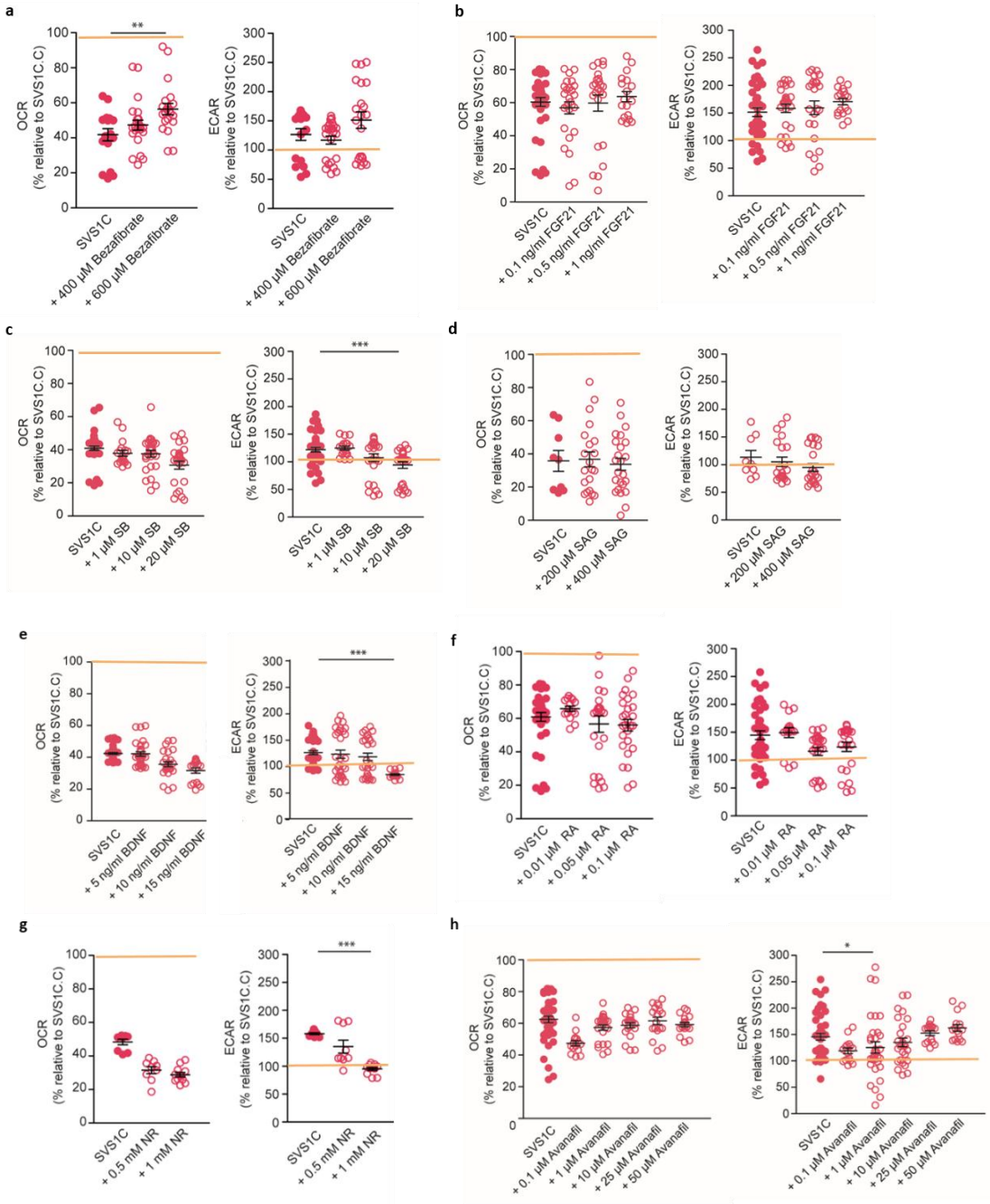

Figure 3.7.4.A.: Bioenergetic profiling in NPC cultures of SVS1C upon drug treatments

a-h, *Oxygen consumption rate (OCR)* ***(left),*** *and extracellular acidification rate (ECAR)* ***(right)*** *in NPC cultures from SVS1C that were cultured overnight with different concentrations of drugs of Bezafibrate, Fibroblast growth factor 21 (FGF21), SB-431542 (SB), smoothened agonist (SAG), brain-derived neurotrophic factor (BDNF), retinoic acid (RA), nicotinamide riboside (NR), and Avanafil. Yellow line is the value for genetically corrected SVS1C.C line (mean +/- s.e.m.; n=2 independent experiments; * p<0.05, ** p<0.01, *** p<0.001; Mann-Whitney U test). (Contributions are indicated in section 8.3.).*

Branch complexity was assessed with HCA-based quantification following an overnight treatment with small molecules.

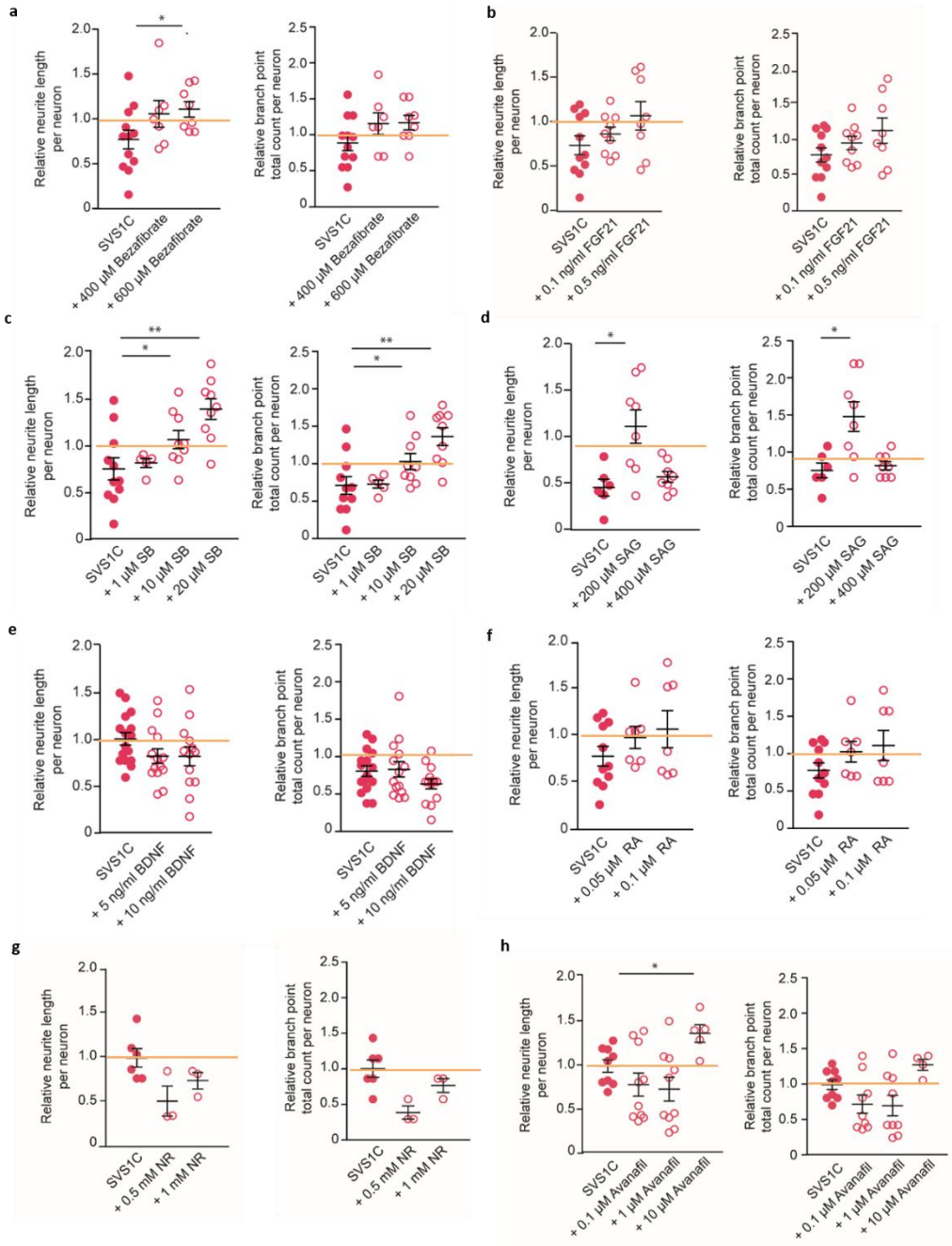

Figure 3.7.4.B.: Neuronal profiling in NPC cultures of SVS1C upon small molecule treatments

a-h, *High content analysis (HCA)-based quantification of neuronal profiling such as neurite length per neuron* ***(left)*** *and branch point total count* ***(right)*** *based on TUJ1-expressing neurons in NPC cultures of SVS1C that were cultured overnight with different of drugs of Bezafibrate, Fibroblast growth factor 21 (FGF21), SB-431542 (SB), smoothened agonist (SAG), brain-derived neurotrophic factor (BDNF), retinoic acid (RA), nicotinamide riboside (NR), and Avanafil. Yellow line is the value for genetically corrected SVS1C.C line (mean +/- s.e.m.; n=2 independent experiments; * p<0.05, ** p<0.01, *** p<0.001; Mann-Whitney U test).*

Results indicated that Bezafibrate and SB, which had a beneficial effect on bioenergetics, also increased the neurite length per neuron and branch total count in a dose-dependent manner significantly. FGF21 showed a dose-dependent increase, whereas it was not significant. SAG and Avanafil seem to have a slight beneficial effect, whereas more experiments need to be performed to understand if the effect is real. BDNF, RA, and NR did not have any effect on neuronal profiling (Figure 3.7.4.B.)

Overall, Bezafibrate as PGC1-α agonist rescues bioenergetics profile and SB-431542 as TGFßR1-inhibitor rescues neurite outgrowth in a dose-dependent manner in patient-derived NPC cultures.

4. Discussion

Leigh syndrome has been considered as an early-onset neurodegenerative disease. However, the mechanistic and pathophysiological understanding of LS^{SURF1} is hindered by the lack of effective model systems (Dell'agnello et al., 2007; Lin et al., 2013; Da-Re et al., 2014; Baden et al., 2007). *SURF1* knock-out has been carried out in several animals (flies, mice, zebrafish, and piglets), but all these efforts failed to recapitulate the neurological phenotypes of human LS^{SURF1} fully.

In this study, a human mechanistic model of LS^{SURF1} based on patient-derived 2D neural cultures and 3D brain organoids was generated. Using these models, I found that *SURF1* mutations impair the function and neurogenic potency of NPCs, ultimately leading to neurons with reduced complexity and activity. Data are in agreement with the clinical features of LS, which generally include developmental delay and cognitive impairment. Microcephaly has often been reported in LS patients (Sofou et al., 2014). *SURF1* knock-out piglets, while not fully recapitulating the clinical phenotype of LS^{SURF1}, also exhibited developmental alterations and reduced cortical thickness (Quadalti et al., 2018). Hence, it is possible that neurogenesis defects might contribute to the pathology seen in LS patients, which commonly involves severe neurodevelopmental manifestations and would explain why the onset of the disease displays itself in infancy and childhood.

Neurogenesis encompasses a series of complex cell fate transitions culminating in the terminal differentiation of NPCs into neurons. This process is accompanied by a metabolic shift from glycolysis to mitochondrial-based oxidative metabolism (Khacho et al., 2019; Lorenz et al., 2017). NPCs may represent the first cell type during this course to depend on the mitochondrial oxidative function. Moreover, in our lab, we previously demonstrated that human iPSC-derived NPCs activate the OXPHOS machinery and that they are equipped with functionally mature mitochondria. Should mitochondrial bioenergetics be impaired during brain development, NPCs might thus be the first cell population to be negatively affected. The dysfunction of bioenergetics occurred already at the level of NPCs and led to defects in neuronal generation and maturation, disrupting the branching capacity and firing activity of neurons. NPCs might be still compensating the defects through glycolysis until they are pushed towards neurons do not solely depend on OXPHOS mechanism. This shift is probably the time point where the phenotype becomes apparent and eventually severe. Classically, once the bulk of neurogenesis has occurred, NPCs can become glial cells at the end of the differentiation phase. The patient-derived glial cell profile varied among the lines without an apparent phenotype suggesting they might not be the

primarily affected. The reason why glial cells did not show an extreme phenotype might be because glial cells mainly rely on glycolytic metabolism.

LS^{SURF1} causes bioenergetics defects and failure in the development of mature neurons, and these phenotypes were reverted upon biallelic correction of *SURF1* mutation via CRISPR/Cas9 genome editing. However, SURF1 OE was not sufficient to rescue both phenotypes and failed to improve neurogenesis upon delivery of a lentiviral vector encoding wild-type SURF1. Currently, other suggested treatment strategies aim at providing energy support through hypoxia, glucose, and pyruvate conditioning which were also tested and also failed to rescue neurogenesis phenotype seen in LS^{SURF1} NPCs despite partially rescued bioenergetic profile. Other current experimental treatment schemes of LS have been centered around antioxidants to prevent the build-up of damaging free radicals (Baertling et al., 2014; Garone et al., 2018). However, blocking oxidative damage was not sufficient in restoring neurogenesis nor bioenergetics. Antioxidant regiments may also dampen the physiological effect of radicals signaling, thereby blunting compensatory responses (Dogan et al., 2018). Findings of this study may open the way to new therapeutic avenues for LS, focusing on improving neurogenesis rather than solely providing energy support or preventing the degeneration of fully functionally neurons.

Moreover, transcriptomics data of patient-derived 2D neural cultures and 3D brain organoids revealed enormous data of differentially expressed genes and pathways regulating neurogenesis, nervous system development, axonal guidance, synaptic function as well as mitochondrial biogenesis and OXPHOS metabolism. Among the several tested small molecules targeting one of those pathways stated above, two candidates reverted the phenotypes in LS^{SURF1} NPCs. Firstly, induction of PGC1α, the master regulator of mitochondrial biogenesis, restored the bioenergetics defects significantly and had a beneficial effect in neuronal profile in a dose-dependent manner. Secondly, inhibition of TGFß1 receptor restored neurogenesis defects significantly. In this study, a novel combination therapy approach may hold promise to enhance responses further.

4.1. iPSC technology: A versatile tool for modeling LS

The choice of a model organism to study human disease mechanisms has always been an important step. So far, many powerful experimental models such as mouse and fruits flies have been generated and used to understand neurological and mitochondrial disorders. However, use the animal models for diseases have recently come under scrutiny because of repeated failure of data and were not be able to translate to humans. Given that drug discovery

is a lengthy and costly process, pursuing the most efficient strategy is, therefore of utmost importance. iPSC modeling has been a powerful tool for studying LS for several reasons.

Specifically, a substantial obstacle in understanding the mechanisms of LS is the lack of effective modeling systems. In the case for LS due to mutations in the gene *SURF1*, where *Surf1*-knock-out animals show extended lifespan and no neurological defects. It is because COX assembly is species- and tissue-specific, and all data generated so far suggest COX assembly is much more dependent on SURF1 in humans than rodents. iPSCs sidestep the limitations and thus provide a powerful and versatile tool for disease modeling, especially for LS due to *SURF1* mutations. Skin fibroblasts from LS patients were reprogrammed to iPSCs, therefore avoiding the concerns of interspecies differences as associated with using animal models.

Furthermore, iPSC modeling does not involve the usage of human embryos as in the human ESC research; thus, it prevents all of the ethical and religious concerns that were raised in the past. However, with the induction of pluripotency, the cells need to undergo reprogramming phase where they need to overcome developmentally imposed epigenetic barriers. Thus the critical question raised in iPSC research was whether the iPSCs are as robust as the ESC and whether their genomes have similar pluripotent states. In this study, I have also used ESC line, and ESC-derived differentiated cell types in all experiments as a positive control and iPSC controls have behaved similarly to ESC control lines in most of the experiments. However, there were differences in spiking and cytokine profile of ESC compared to iPSCs, as ES-derived neurons showed synaptic activity, and they secreted much more cytokines (Figure 3.4.2.2.2., Figure 3.5.1.B.).

In order to investigate the link between genotype and phenotype, gene editing technology was applied to iPSCs in this study. The precise correction of the mutation in the same genetic background allowed a more accurate way of disease modeling. In this study, control lines were compared to the patient lines as well as one patient lines, were compared to its corrected isogenic pair. Most of the results have been in line. However isogenic line pair has given a more distinctive and clear signature of the phenotype, and this eventually allowed to identify the molecular mechanisms better. Also, I have observed that the S1A patient line was doing slightly better than S1C lines in every experiment; thus lacking an isogenic corrected line of S1A was disadvantageous. The initial aim was to correct the mutation on both patient iPSCs, whereas TALENs gene editing on S1A lines failed as there were no drive single cell-derived clones from the transfected lines found. Also, the clones screened so far always gave mixed sequencing results on the mutation site. The other problem was that the transfected and picked clones were differentiating as they were seeded on the plate and did not manage to maintain the pluripotent

state. However, it was still very advantageous to have S1C patient isogenic line to conclude the experiments.

Furthermore, there have been challenges in understanding and treating diseases by the absence of *in vitro* models because culturing primary cells affected by the disease was not possible. As LS has been considered as an early-onset neurodegenerative disease implying progressive loss of neurons by time, and, given that, the neuropathology represents itself mainly in basal ganglia region, the focus was given on differentiation protocol enriched with dopaminergic neuronal cells to understand the pathology a bit better. The DA cultures were maintained for 4 and 8 weeks to monitor the disease pathology and progression at specific time points. There was a reduction in the number of neurons in patient-derived DA-enriched composite cultures specifically at 8^{th} weeks, whereas there was no morphological features of cell death and no progressive neuronal loss observed in the cultures. The neurons were checked regularly under the microscope every third day, and patient-derived DA cultures also preserved the right amount of neurons at both weeks. Patient-derived neuronal cultures appeared not healthy, but they also required media every third day and sometimes even more than control DA-enriched composite cultures. The first clue on the state of patient-derived neurons came with the help of patch-clamp recordings. Neurons of patient lines showed a time-dependent increase in cell capacitance and a decrease in input resistance, which indeed supports the neurons were preserved. However, the active membrane properties of neurons differed between patients and controls, suggesting defects in the maturation of neurons and synaptic activity. The premature profile of the patient neurons was also confirmed by the defective branching complexity of patient-derived neurons by using high-content analysis based quantification.

On the other hand, another diseases-associated cell type, I was able to analyze in culture was glial cells. Leigh syndrome patients have gliosis and glial dysfunction in disease pathology. Thanks to the iPSC-derived composite cultures entailing astrocytes, I was able to have an insight into the glial mechanism, and I have called differentiated cultures as DA-enriched composite cultures. They mimic or model the disease pathology better than expected thanks to entailing both primary brain cells types of CNS in vitro. Typically, in the CNS, in case of neurotrauma, damaged central axons do not generally regenerate or become remyelinated. Astrocytes aim to promote and protect nerve growth by undergoing morphological and functional changes, and reactive glial cells become proliferative. It has always been a debate whether the role of reactive astrocytes at the injury site is beneficial or detrimental or maybe both. *In vitro* glial cells tend to appear as reactive, thus assessing glial cells in disease pathology

is not easy. Media collected from both composite cultures were used for cytokine detection assay, and there were no differences present. However, all of the cytokines were detected in the culture, which shows that glial cells were active and functional. The other possibility to analyze glial function is through assessing the bioenergetic profile of the composite culture.

iPSC-derived composite cultures were grown on the seahorse assay plates allowed assessment of mitochondrial and non-mitochondrial respirations lively. It is known that brain energy metabolism is highly dependent on the oxidation of glucose, glycolysis, and mostly followed by OXPHOS. The ratio of used oxygen to glucose consumption is ~6:1, and OXPHOS converts the molecules into ATP, which provides ~87 % of the ATP generated (Kety, 1957; Sokoloff 1960). However, when brain activity is increased, brain cells tend to back themselves up through glycolysis even though the net production of ATP is little. This requirement was shown with a regional stimulation electron tomography studies showed local blood flow increases by ~50%, and there is an increase in glucose consumption; whereas the increase in oxygen utilization was much less suggesting glucose to be metabolized through non-oxidative, probably through glycolysis (Madsen, 1999). This was also supported by the findings of elevated lactate levels upon stimulation of brain cells (Yellen et al., 2018; Mazuel et al., 2017). This outcome could also be thanks to the help from astrocytes as neurons regulate the energy supply by turning on glycolysis in astrocytes as well. When active neurons release glutamate, it is taken up by astrocytes and converted to glutamine, thus producing lactate to be exported back to neurons as a substrate for OXPHOS. However, astrocyte-neuron lactate shuttle theory has also been challenged. Lately, it has been suggested that this alternative mechanism is not very much needed, although its role in supporting neurons is desirable (Diaz-Garcia et al., 2018). It has also been argued that neurons might also be doing glycolysis on their own in response to stimulation and they might be exporting lactate rather than importing. Patient DA-enriched composite cultures showed higher ECAR and lactate levels compared to healthy composite cultures. The first explanation could be that patient-derived composite cultures compensate their defects in mitochondrial respiration by increasing the non-mitochondrial respiration. Another reason could be the presence of premature neuronal cells in the culture as transcriptome analysis indicated that patient-derived composite cultures upregulated pluripotent genes and downregulated the neuronal-specific genes. These cell types rely on the glycolytic mechanism rather than OXPHOS. The other explanation for high ECAR levels could be the activity of the glial cells as they also rely on glycolytic metabolism. Considering there were no differences in glial cell profile in number and cytokine profile that might not be the leading cause. ECAR and lactate levels were not consistent among the lines. Given that, transcriptomics data showed an

upregulation of pluripotent genes in patient-derived composite cultures; lactate may be a result of progenitor cells or immature neurons since they rely on glycolysis.

On the contrary, bioenergetics profiling experiments showed that patient-derived composite cultures exhibited significantly reduced mitochondrial respiration due to *SURF1* mutations. SURF1´s exact mechanism in COX assembly is still not known. As western blot results showed, patient neuronal cells do not express MT-CO2 protein; this overall might be another evidence for SURF1´s crucial role in the COX assembly through catalytic core subunits of COXII.

After bioenergetic profiling, the focus was given to mitochondria itself, which are highly specialized and dynamic organelles that modulate their function through biogenesis, fusion, and fission events. Mitochondria trafficking along the axons or docking of mitochondria at the synapse areas are very crucial for synaptic hemostasis. Additionally, mitochondrial biogenesis assists in maintaining healthy mitochondria in axons and dendrites and would have the potential to respond rapidly to local changes in case of stimulation or an insult. Each cell type has a different structure of mitochondria. During reprogramming of somatic cells into iPSCs, cellular metabolic demands change, and mitochondria need to undergo extensive alterations, and they increase their mitochondria number (St John, 2015; Zhang et al., 2011). For instance, mitochondria in PSCs are small and have globular morphology while neurons have elongated, cristae-rich mitochondria since they are highly dependent on OXPHOS and cannot compensate through glycolysis which is the primary energy source for PSCs (Cho et al., 2006; Prigione & Adjeye, 2010). Therefore, defects in mitochondria have different levels of severity in different cell types. It could be that the nastiest and cruel mutations are in the nuclear genes encoding respiratory chain subunits tend to present early in infancy and childhood and are usually fatal ones as it presents themselves as Leigh syndrome. By applying old mitochondria tracking methods from the primary neurons of the animal models (Zhang et al., 2011), I was able to stain mitochondria in iPSC-derived composite cultures. Patient-derived composite cultures showed an abnormal increase in mitochondrial motility, which means less stationary mitochondria. Stationary mitochondria are crucial for axonal branching and synaptic hemostasis. Given that iPSC-derived composite cultures entail astrocytes, it would be necessary to use a neuronal marker to differentiate the cell types and mask them with image processor aiming to analyze mitochondria movement only in neurons. In this study, the defective mitochondrial movement in a broad view was the outcome. However, the transcriptome analysis showed downregulation of *SNPH* in patient-derived composite cultures, and SNPH is neuronal specific and known to be the ´static-anchor´ specific for axonal mitochondria (Chen & Sheng, 2013).

Recently, there have also been technological advances allowing iPSCs to be cultured in three dimensions, to produce organoids representing various human tissues such as the brain. iPSC-derived cerebral organoids allow us to look at the developmental features in detail. Patient-derived cerebral organoids led to disrupted neuronal layering and reduced cortical thickness. Since DAPI staining suggested defects in compartmentalization in patient-derived organoids; human cerebral organoids might similarly display different brain regions. The pluripotent and neural identity gene expression was analyzed from the transcriptomics data (Figure 3.6). Important transcription factor *FOXG1*, an essential key player in neurodevelopment process whose downregulation is a sign for structural brain abnormalities, was significantly downregulated. Classically, neurogenesis starts with precursor cell proliferation in neurodevelopmental biology and continues as their capacity to generate new cell types, and if they survive, they will get functionally integrated. Radial glial cell types have different fate choices as they can differentiate into neurons, or they could also give rise to glial cells. This balance is tightly maintained, regulating the neurogenic capacity of the stem cell pool. Patient-derived organoids show upregulation in genes for proliferating responsible for precursor cell types (Figure 3.6). Then there is a downregulation of genes responsible for neurogenesis and postmitotic maturation cell types. Patient-derived cerebral organoids showed repression of astrogenesis genes compared to the edited line as all of the genes were downregulated (Figure 3.5.1.A.) (Sloan et al., 2018) Overall, patient-derived cerebral organoids suggested dysfunctional neurogenesis in the pathogenesis of LS^{SURF1} and added another meaningful angle to defects seen in 2D cultures at NPC levels.

Additionally, patient-derived iPSCs were differentiated into disease-relevant cell types, and comprehensive transcriptome analysis of the composite cultures provide hints for targets, in this study. Some of them were tested in the high content platform. Screenings conducted on such differentiated cells were based on highly significant cellular phenotypes that become apparent within patient-specific disease-relevant cellular contexts. For instance, I have used high-content screening for neuronal profiling to look at the branching complexity as well as seahorse platform for bioenergetics assessments with several determined small molecules in a multi-well format. Two candidates were proven to improve the phenotypes, and the combinatory delivery of these two molecules may hold a potential to improve both phenotypes simultaneously for better results.

4.2. COX activity as a biomarker of neuronal activity

COX is the only complex among the respiratory chain that has alternative isoforms, which suggest additional levels of regulation of COX activity due to its importance. Several theories were explaining why additional regulation exists for COX, such as high free energy released in enzymatic reactions and irreversibility of the COX reactions. The identity of the cell is associated with mitochondrial function as well. For instance, PSCs are glycolytic, and they have low mitochondria in number and fewer cristae structures. When they are pushed to differentiate into neurons, they increase their mitochondrial content and activity (Cho et al., 2009). Overall, it has been stated more clearly very recently that the COX genes are involved in the transcriptional networks of the neurons that COX activity can be considered as a biomarker of neurons and likely crucial for differentiation as well (Chicherin et al., 2019).

In previous studies, it has been shown that by altering the activity of neurons as with tetrodotoxin (TTX)-induced impulse blockade or with KCl-mediated depolarizing stimulation, the levels of cytochrome c oxidase in affected neurons were also altered. Such alterations were not only observed in the activity of the enzyme, but also its protein and mRNA amount, and at a transcriptional level (Wong-Riley, 1989; Wong-Riley, 2012). Additionally, every assembly factor of COX has tissue specificity. For instance, in LS^{SURF1,} muscle cells do not usually show the same level of impairment as neuronal cells. Conversely, mutations in the gene encoding SCO2, which is a different assembly factor of COX, more strongly impair cardiac bioenergetics leading to cardiomyopathy rather than LS. In this study, patient-derived DA-enriched composite cultures with COX defects due to *SURF1* mutations exhibited impairment in neuronal differentiation, maturation, and activity thus it supports the crucial role of COX activity in neuronal development and *SURF1´*s neuronal specificity.

Moreover, specificity factor 4 (Sp4) has been suggested to regulate all of COX subunits in primary neurons by regulating the transcription factors (TFAM, TFAMb, and TFB2M) and SURF1. Correctly, SURF1 has been shown to regulate the expression of NMDA receptor subunits GRIN1, GRIN2A, and GRIN2B (Johar et al., 2013; Priya et al., 2013). Indeed, transcriptomics data of patient-derived composite cultures showed significant downregulation of all of the NMDA receptors (Figure 3.4.2.5.1.) which are the critical mediators of excitatory neurotransmission, and glutamate is the primary excitatory neurotransmitter which binds to NMDA, AMPA, and kainate receptors. In this study, patient-derived neurons were lacking synaptic activity, and genetic correction of *SURF1* reconstituted the full neuronal activity as they exhibited post-synaptic currents. Given the importance of NMDA receptors in energy metabolism and neurons, mutations related to NMDA receptors lead to severe diseases. *GRIN2B* gene was shown to play

a crucial role in neuronal development and mutations on this gene were shown to impair neuronal differentiation in human neurons (Bell et al., 2018), as well as mutations of this gene, were implicated in several neurodevelopmental disorders such as autism spectrum disorder (ASD) or attention deficit hyperactivity disorder (ADHD) (Hu et al., 2016).

4.3. Using NPC function for therapeutic screening

The generation of neuronal and cerebral organoid cultures from patient iPSCs gave a unique opportunity to identify LS-specific neuronal phenotypes and 2D and 3D models of *SURF1*-associated LS exhibit apparent disease-associated defects starting in early neurodevelopmental processes. Therefore, targeting NPC function and trying to fix the problem as early as possible would be a good strategy for LS.

2D and 3D cultures hold few disadvantages and are an unsuitable model to screen for therapeutic strategies in this study. Differentiation protocol and derivation of cerebral organoids are long lasting; there was a necessity to use another compatible cell type like NPCs that can fasten the screening process for potential therapeutics. iPSC-derived NPCs have two essential properties that make them useful model in this study. The first one is that they are capable of robust, immortal expansion, which makes it easier to handle in culture. The second one is that they already undergo a neuronal-like metabolic switch towards OXPHOS which is useful for us to foresee the possible phenotypes of mature neuronal cells derived from patient iPSCs in our assays (explained in section 1.3.). Additionally, the severity of the mitochondrial defect leads to the fragile neuronal population in patient-derived cultures, making them difficult to handle, especially for large-scale screenings. Also, both the neurons and organoid model system are non-expandable and takes a substantial amount of time to be generated. iPSC-derived NPCs have been previously employed for identifying treatment interventions in the context of mitochondrial diseases in our lab (Lorenz et al., 2017). Moreover, a mutation in the mtDNA gene *MT-ATP6* that is associated with LS also caused abnormal NPC functionality. Hence, it is possible that neurogenesis defects might contribute to other forms of LS and other mitochondrial disorders, which commonly involve severe neurodevelopmental manifestations (Falk et al., 2010).

4.3.1. Gene augmentation therapy (GAT) as a potential strategy

In this study, a lentivector wild-type SURF1 was delivered to patient NPC cultures to assess the potential rescuing effect of SURF1 overexpression. Results showed that *SURF1* rescued the bioenergetics defects significantly, but did not promote neurogenesis ar NPC level. Moreover, SURF1 overexpression by lentivirus delivery promoted neurogenesis as it increased

the percentage of neuronal cells, neurite length per neurons, and branch total count in patient-derived neuronal cultures at 8w (Figure 3.7.1.). There are ongoing clinical trials on GAT for CNS disorders (Anguela et al., 2019). GAT also ameliorated the LS-like phenotypes in the complex I gene *Ndusf4* knock-out mice (Di Meo et al., 2017). Given the proposed impairment of neurogenesis, GAT in LS^{SURF1} should be carried out as early as possible to enable the formation of functional neurons and neuronal networks in the patients. Further studies are needed to investigate in details the potential adverse reactions of SURF1- GAT in live animals and to identify the most effective strategy concerning viral vector types, timing, and sites of delivery.

4.3.2. Bezafibrate: Coactivator of PGC1-α receptor

Upregulation of mitochondrial biogenesis pathways has emerged as one of the most commonly suggested mitochondrial therapies. While the strategy does not solve the underlying cause of the disorders, it may help to increase OXPHOS through the added number and mass of mitochondria. PGC-1α is known as the master regulator of mitochondrial biogenesis and cellular energy metabolism. It is expressed at high levels in mitochondria-rich cells with high energy demands such as neurons. PGC-1α is another crucial regulator of COX in neurons as stimulates induction of transcription factors NRF1 and NRF2. They have been shown to regulate all subunits of COX complexes as well as the expression of several genes crucial for neurons such as NMDA receptors (Priya et al., 2012). Thus, there is a tight coupling of neuronal activity, energy generation, and energy consumption at a molecular level. It is known that during neuronal differentiation and maturation, the number of mitochondria per cell increases because of the energy demand of neurons increases as they become excitable and form synapses. Addition to its role increasing cellular energy, it has also been shown to be involved in the formation, maintenance, and reorganization of synapses via increasing dendritic spines (Sheng, 2014). The idea that increasing the amount/or function of mitochondria could be beneficial in mitochondrial disease, Bezafibrate, a PPAR pan-agonist, was first tested in fibroblasts of patients with mitochondrial diseases and it increased enzyme activities of complexes I, III, and IV (Bastin et al., 2008). However, bezafibrate was not effective in Cox deficiency *Surf1* knockout (Viscomi et al., 2011) or deleted mice (Yastuga et al., 2012).

During this study, bezafibrate was administered to patient S1A by Prof Dr. Schülke, and he reported that the patient did not go through a metabolic crisis during the administration period, and it was beneficial. Also, transcriptomic gathered from iPSC-derived patient 2D, and 3D models showed significant downregulation of PGC-1α. Therefore, bezafibrate was tested in the patient-derived NPC models, and the results showed that bezafibrate rescued the

bioenergetics defects and also it improved neuronal complexity in a dose-dependent manner. Considering that *in vivo* models were not recapitulating the disease mechanism seen in patients, it was worth to try this FDA approved the drug on human neuronal cells. These are the first findings showing bezafibrate´s therapeutical potential in human-derived neuronal cells of COX deficiency. Detailed analysis is needed to understand the mechanism.

4.3.3. SB-43152: Inhibition of TGF-β1 receptor

Proper functioning of the nervous system depends on how accurate the neurons wired and specifically in the neuronal circuits. Extracellular signals are essential to make a permissive environment that supports neurons to develop and extend. Morphogens are secreted proteins expressed in a restricted region of a tissue that instructs cells about their fate and cells differentiate in response to morphogen signaling depending on their position within the gradient and thus their distance from the morphogen source (Teleman et al., 2001). Classical and relevant morphogens have been reported to be Shh, Wnt, and TGFβ/Bmp signaling (Sánchez-Camacho & Bovolenta, 2009). Transcriptomic data of the patient-derived 2D and 3D models showed deregulation of these three crucial signaling pathways and also some of the morphogens such as NTN1, SLIT, Semaphorins (Figure 3.6.) which are known to play an essential role in guiding axons.

In this study, neuronal induction from NPCs to DA-enriched composite cultures was initiated by inhibition of both BMP and TGFβ signaling by delivering small molecules dorsomorphin (DM) and SB43152 (SB). Specifically, transcriptomics data revealed the upregulation of TGFβ1R; and the different concentrations of SB was tested on NPC cultures. The results showed that SB partially rescued bioenergetics in terms of decreasing ECAR levels, whereas the most striking effect was that it improved neuronal complexity in a dose-dependent manner significantly. Canonical TGFβ signaling has a variety of cellular processes, including cell differentiation, proliferation, and specification of developmental fate (Shi and Massague, 2003). TGFβ family contains two subfamilies, the TGFβ/Activin/Nodal subfamily and the BMP/GDF/MIS subfamily. In the dataset, most of those pathways seem to be also dysregulated, whereas further analysis is needed to understand the exact mechanism.

5. Conclusions and future perspectives

Overall, the first human mechanistic neuronal 2D and 3D models of *SURF1* mutations have been generated, and novel insights into the understanding of the disease mechanisms have been investigated. Most of the neuropathology seen in patients has been recapitulated in these models as *SURF1* mutations caused aberrant bioenergetics profile, as well as they, prevented neuronal generation and maturation. Plus, the phenotypic experiments and transcriptomics results showed that defects start at NPC level and leading to prematurely cell types, which major the primary neuropathology saw in patients. Ultimately, data suggested LS be considered and approached as a neurodevelopmental disorder rather than neurodegenerative disease, and most of the deregulated genes also indicate defects to be happening during the migration phase where immature neurons go from their birthplaces to their final positions, outgrowth of axons and dendrites from neurons, guidance of the motile growth cone, and generation of synapses. The transcriptomic data gathered from neuronal models were analyzed, and some of the targets were tested on NPC function to check if they improve the well-defined phenotypes. Two candidate therapeutic targets have been suggested.

In this study, the activation of the master metabolic regulator PGC1α with Bezafibrate restored bioenergetics defects, and inhibition of the TGF-β1 receptor with SB-431542 ameliorated neural progenitor function and early neuronal branching. Impaired neuronal morphogenesis in 2D and 3D models of the pediatric mitochondrial disease might be ameliorated via both PGC1α and TGFβ combo modulation. Similar interventions may represent potential therapeutic strategies for LS, which is currently incurable. Our data also underlies the importance of mitochondrial homeostasis for neural progenitor function in healthy and diseased states. Moreover, it would be fascinating to test these suggested therapeutical approaches in the iPSC-derived 3D model of LS^{SURF1}.

Several open questions remain, more detailed explanation of the disease mechanism is still needed. Mass spectrometry-based metabolomics and proteomics would allow quantifying significantly altered metabolites and relative proteins abundance, which would deepen the insight into the underlying mechanism of this neurometabolic disorder. Therefore, the collected pellets and supernatants from DA composite cultures derived from isogenic line SVS1C and SVS1C.C were sent for proteomics and metabolomics. Currently, our lab has established a collaboration which is working on the integration of multi-omics data implying the integration of transcriptomics, proteomics, and metabolomics data. Each type of omics data provides a list of differences associated with the disease and integration of different omics data types would then elucidate potential causative changes leading to disease. A fundamental

expectation from these analyses is predicting the phenotypic traits, elucidating essential biomarkers, and ultimately generating insights into the genetic underpinnings of the heritability of complex traits. However, there have been challenges to find compelling and advanced analysis strategies to harness the utility of these enormous high-throughput data fully.

Furthermore, elaborating on the first findings of cerebral organoids would be necessary, so more detail immunohistochemical analyses have to be performed with more protein markers specific to different neuronal or progenitor types. Thus, it can be better understood if these structural defects are exclusive to migration, differentiation, or maturation processes. High-density micro-electrode arrays (MEAs) recordings could be performed to understand the functionality of neuronal connectivity in cerebral organoids. Also, single-cell genomic methods could be applied to characterize these organoid models with more resolution and less bias than previous immunohistological or bulk RNA-seq descriptions of organoid development.

6. Material

6.1. Biological material and experimental models

6.1.1. Cells

Different cell lines were used in this study. The skin fibroblasts were obtained from three LS^{SURF1} patients from two distinct consanguineous families: SURF1 A (S1A) line carries the homozygous mutation c.530T>G (p.V177G), and SURF1 B (S1B) and SURF1 C (S1C) lines which were taken from siblings carry the same homozygous mutation c.769>A (p.G257R). All of the mutations are missense mutations which lead to a change in one amino acid in a protein. Prof. Schülke has the written consent of the parents of the patients´, and they are according to the Declaration of Helsinki to all aspects of the study. The study was approved by the ethics committee of the Charité (EA2/131/13 and EA2/107/14). The healthy control fibroblasts BJ and CON1 were previously characterized in our lab, and also established in our study (Lorenz et al., 2017). The fibroblast cell lines used in this study are summarized in Table 6.1.1.A. with the background information.

Fibroblasts						
Name	**Disease**	**Age**	**Gender**	**Gene**	**Mutation**	**Source**
BJ	Control	0	M	-	-	ATCC
CON1	Control	32	M	-	-	Dr. Doss
S1A	LS	9	M	SURF1	p.Val177Gly	Prof. Schülke
S1B	LS	8	F	SURF1	p.Gly257Arg	Prof. Schülke
S1C	LS	1,7	M	SURF1	p.Gly257Arg	Prof. Schülke

Table 6.1.1.A.: Background information of the fibroblasts

ESCs and iPSC lines used and generated in this study were explained in section 3.2. and specified in Table 6.1.1.A. hESC line H1 was purchased from WiCell and was used by the German license of Alessandro Prigione issued by the Robert Koch Institute (AZ: 3.04.02/0077-E01). Ethical approval was obtained by local authorities to use patient fibroblasts for iPSC derivation. The healthy control lines used in this study were previously characterized. TFBJ (BJ derived episomal plasmid transfected iPSCs) (Yu et al., 2011) was already characterized in our lab and used in a study (Lorenz et al., 2017). The other healthy control iPSC line XM001 (episomal plasmid transfected) was characterized in another lab and was published in a study as well (Wang et al., 2018). Additionally, human embryonic stem cell lines (hESC) H1 and H9 were purchased from WiCell and used according to the German law (personal license to A.P., #AZ: 3.04.02/0077-E01). The background information of the ESCs and iPSCs used in this study are summarized in Table 6.1.1.B.

ESCs and iPSCs						
Name	**Disease**	**Age**	**Gender**	**Gene**	**Mutation**	**Source**
H1	Control	-	M	-	-	WiCell Research Institute
H9	Control	-	F	-	-	WiCell Research Institute
TFBJ	Control	0	M	-	-	ATCC
XM001	Control	47	F	SURF1	-	Heiko Lickert
SVS1A	LS	9	M	SURF1	p.Val177Gly	Gizem Inak
SVS1C	LS	1,8	M	SURF1	p.Gly257Arg	Gizem Inak

Table 6.1.1.B.: Background information of the ESCs and iPSCs

After generation of clinically feasible SVS1C iPSCs; the aim was to employ Clustered regularly interspaced short palindromic repeats (CRISPR)/Cas9 system for precise correction of 769G>A on *SURF1* gene in SVS1C iPSCs. The information about biallelic correction and resulted in SVS1C.C iPSC lines were given in section 3.3.2. and specified in Table 6.1.1.C.

Gene edited iPSCs					
Name	**Disease**	**Gender**	**Gene**	**Mutation**	**Source**
SVS1C.C 3p	Isogenic control	M	SURF1	Corrected p.Gly257Arg	Gizem Inak
SVS1C.C 3bb	Isogenic control	M	SURF1	Corrected p.Gly257Arg	Gizem Inak
SVS1C.C 3c	Isogenic control	M	SURF1	Corrected p.Gly257Arg	Gizem Inak

Table 6.1.1.C.: Background information of gene-edited iPSCs

6.1.2. iPSC-derived models

2D and 3D iPSC-derived models were used in this study to model LS. iPSC-derived NPC and DA enriched composite cultures are 2D modeling system. They were explained in detail in section 3.4. and summarized in Table 6.1.1.D. and 6.1.1.E., respectively.

smNPCs					
Name	**Disease**	**Gender**	**Gene**	**Mutation**	**Source**
H1	Control	M	-	-	Gizem Inak
TFBJ	Control	M	-	-	Gizem Inak
XM001	Control	F	SURF1	-	Gizem Inak
SVS1A	LS	M	SURF1	p.Val177Gly	Gizem Inak
SVS1C	LS	M	SURF1	p.Gly257Arg	Gizem Inak
SVS1C.C 3p	Isogenic control	M	SURF1	Corrected p.Gly257Arg	Gizem Inak
SVS1C.C 3bb	Isogenic control	M	SURF1	Corrected p.Gly257Arg	Gizem Inak
SVS1C.C 3c	Isogenic control	M	SURF1	Corrected p.Gly257Arg	Gizem Inak

Table 6.1.1.D.: Background information on iPSC-derived NPC cultures (2D)

DA enriched composite cultures					
Name	**Disease**	**Gender**	**Gene**	**Mutation**	**Source**
H1	Control	M	-	-	Gizem Inak
TFBJ	Control	M	-	-	Gizem Inak
XM001	Control	F	SURF1	-	Gizem Inak
SVS1A	LS	M	SURF1	p.Val177Gly	Gizem Inak
SVS1C	LS	M	SURF1	p.Gly257Arg	Gizem Inak
SVS1C.C 3p	Isogenic control	M	SURF1	Corrected p.Gly257Arg	Gizem Inak
SVS1C.C 3bb	Isogenic control	M	SURF1	Corrected p.Gly257Arg	Gizem Inak

Table 6.1.1.E.: Background information on iPSC-derived DA enriched composite cultures (2D)

The information about iPSC-derived 3D cerebral organoids can be found in section 3.7. and specified in Table 6.1.1.F. Additionally, iPSC-derived cerebral organoids experiments were done in close collaboration with Dr. Agnieszka Rybak-Wolf, and the protocol was adopted from (Lancaster et al., 2013) to make cerebral organoids (section 5.3.).

Cerebral organoids					
Name	**Disease**	**Gender**	**Gene**	**Mutation**	**Source**
XM001	Control	F	SURF1	-	Dr. Agnieszka Rybak-Wolf
SVS1C	LS	M	SURF1	p.Gly257Arg	Dr. Agnieszka Rybak-Wolf
SVS1C.C 3p	Isogenic control	M	SURF1	Corrected p.Gly257Arg	Dr. Agnieszka Rybak-Wolf
SVS1C.C 3bb	Isogenic control	M	SURF1	Corrected p.Gly257Arg	Dr. Agnieszka Rybak-Wolf

Table 6.1.1.F: Background information on iPSC-derived cerebral organoids (3D)

6.2. Laboratory equipment

Relevant technical appliances used to prepare this study are listed.

Devices		
Item	**Product name**	**Supplier**
Centrifuge	Universal 32 R	Hettich
	5810R	Eppendorf
	Heraeus Pico Microcentrifuge	Thermo Fischer Scientific
Cell culture Bench	UVF	BDK Luft und Reinraum
	BDK-S	Technik GmbH
	Maxisafe 2020 TF	Thermo Fischer Scientific
Cell sorter	BD FACSAria TM III	BD Biosciences
	Gentle MACS Dissociater	Miltenyi Bioscie3nce
	OctoMACS Seperator	Miltenyi Bioscie3nce
HCA Cellomics microscope	CX7	Thermo Fisher Scientific
Columns	LS Columns	Miltenyi Biotec
	MS Columns	

Concentrator	10K centrifugal filter	Amicon® Ultra-15
Electrochemiluminescence (ECL)	MESO QuickPlex SQ 120	MSD
Electrophereseses	EPS 301	Amersham Biosciences
	Transilluminator TM-36	UVP Inc.
	GeneGenius Gel Imaging System	Syngene
	Microwave	Privileg
	Electrophoresis chamber	
Fluorescent microscope	Imager Z1 Carl	Zeiss GmbH
Filter	Pre-seperation filters	Miltenyi Bioscie3nce
Freezing container	Mr. Frosty	Nalgene
Freezer, -20	Comfort	Liebherr
Freezer, -80	Innova4725	New Brunswick
Fridge	UP3021	Scientific Liebherr
Hemocytometer	Neubauer Plus	ThermoFisher Scientific
High Content Analysis Platform Incubator	CellInsight CX7	ThermoFisher Scientific
Incubator	Heraeus BBD 6220	ThermoFisher Scientific
	Binder BD 6220	
	Binder BCB 160	Binder GmbH
	Binder CB 160	
Liquid Nitrogen device		Thermo Fisher Scientific
Luminescent Image analyser	LAS-3000	Fujifilm
Microcentrifuge	Biofuge pico	Heraeus
Microscope	Leica m80	Leica Microsystems
	Eclipse Ni-E Ts2	Nikon
	x710 microscope	Keyence
	P902 electron microscope	Zeiss
	Upright microscope	(Axioskop, Zeiss)
	Spinning disk microscope CSU-W	Andor/Nikon
Patch-clamp amplifier	EPC-9	HEKA Elektronik
Pipettes (2-1000ul)	Pipetman Classic	Gilson
Pipetaid	PIPETBOY acu 2	Integra Biosciences
Plate reader	Tecan Infinite M200	Tecan
Process BeadChip	iScan system	Illumina
qPCR machine	ViiA TM 7	Thermo Fischer Scientific TM
Seahorse XF Analyser	Seahorse Xfe96 Analyser	Agilent Technologies
Serological pipettor	Pipetboy acu	INTEGRA Biosciences
Shaker	Rocky	LTF Labortechnik
Single Channel Electronic Pipette 0.5- 10µl, 5-100µl, 20-300µl, 50-1000µl	Research Pro	Eppendorf

Spectrophotometer	NanoDrop8000	Thermo Fischer Scientific TM
	MJ Research PTC 200	MJ Research
Thermal Cyclers	Simpli Amp Thermal cycler	Life Technologies
	Mastercycler X50s	Eppendorf
Thermomixer	Thermomixer comfort	Eppendorf
Vortexer	Vortex Genie 2	Scientific industries
Water Bath	Isotemp 220	Thermo Fisher Scientific
	TW8 Water Bath	Julabo

6.2.1. Chemicals and consumables

6.2.1.1. General consumables

General consumables and respective producers are listed in this section.

Items	**Supplier**
Cell spatula	TPP
Coverslips	Greiner Bio
Cell culture plates, 6-well, 24-well	Greiner Bio
Conical tubes (15 ml, 50 ml)	Greiner Bio One
Cryovials	Corning
DNA Gel Loading Dye (6X)	Thermo Fisher Scientific
dNTP Set	Thermo Fisher Scientific
Falcon tubes, 15 mL and 50 mL	Falcon
Falcon polystyrene test tubes	Corning
Glas pipettes	Sarstedt
KnockOut DMEM	Thermo Fisher Scientific
Matrigel Matrix	Corning
Multi-well plates (6-well, 12-well, 24-well)	Greiner Bio-One
NuPAGE™ Novex® Bis-Tris gel system	Invitrogen
Opti-MEM	Thermo Fisher Scientific
orbital shaker (80 rpm)	IKA
Pipette tips, 2 µL, 10 µL, 200 µL, 1000 µL	Greiner Bio
Pasteur pipettes, glass, 150mm	Applied Biosystems
Plastic flasks (T-25, T-50, T-150)	Greiner Bio-One

Pipette tips, 2 mL, 5 mL, 10 mL, 25 mL	Sarstedt AG & Co. KG
PCR SingleCap 8er-SoftStrips 0.1ml	Biozym
QUICKPLEX assay plate	MSD
Reaction tubes, 500 µL, 1.5 mL, 2 mL	Sarstedt AG & Co. KG
RNase H Hybridase Thermostable RNase H	Epicentre
Seahorse 96 well plate	Seahorse Bioscience
Seahorse cartridge	Seahorse Bioscience
Shandon Immuno-Mount	Thermo Fisher Scientific
slides	Thermo Fisher Scientific
Tissue-Tek®	O.C.T.™
Ultra-low attachment culture dish	Corning
Vacuum filtration 250 mL, 500 mL, 0.22 µm	Applied Biosystems
96 well black, clear bottom cell culture microplates	Falcon
96-well Seahorse XFe96 cell culture microplate	Agilent
100 bp DNA Ladder	Thermo Fisher Scientific
384-well black, clear bottom microplate	Falcon
13 mm Ø Coverslips	Thermo Fischer Scientific
384-well plates for qPCR	Thermo Fisher Scientific

6.2.1.2. Cellular consumables

Item	**Supplier**
a-Tocotrienol	Cayman Chemicals
Accutase	ThermoFisher
Antimycin A	Sigma Aldrich
Amino acids	Gibco
Ascorbic acid	Sigma Aldrich
Avanafil	Selleckchem
BDNF	MACS Miltenyi
Bezafibrate	Selleckchem
B-27 supplement (10x)	Gibco
CHIR-99021, GSK-3 inhibitor	Cayman Chemical

Compound E	Merck Millipore
db-cAMP	sigma Aldrich
Disinfection solution	Gigasept Schuelke
Dihydrolipoicacid	Santacruz Biotech
Dimethyl sulfoxide (DMSO), sterile-filtered	Sigma Aldrich
DMEM, 4.5g/l glucose, 500ml	Gibco
DMEM/F12, 500ml	Gibco
Donkey normal serum	Gibco
DNase/RNase-free distilled water	Gibco
FBS, fetal bovine serum	Gibco
FCCP, 25mM	Sigma Aldrich
FGF2	PeproTech
FGF8	MACS Miltenyi
Glucose	Sigma Aldrich
GDNF	MACS Miltenyi
hLIF	Merck Millipore
Hoechst 33342	Life Technologies
KO-DMEM	ThermoFisher Scientific
KO-SR	Gibco
L-Glutamine	Lonza
Mitomycin C	Sigma-Aldrich
MitoTrackerRed CMXRos	Thermo Fischer Scientific
Matrigel matrix, growth factor reduced	BD Biosciences
Immu-Mount Media	Thermo Fisher Scientific
MycoZap Plus-CL	Lonza
N-2 supplement (10x)	Gibco
N-acetly cysteine	Sigma Aldrich
Neurobasal medium	Gibco
Pen/Strep	Lonza
PBS	Sigma Aldrich
Phenol Red	Sigma Aldrich
Purmorphamine	Millipore
Pyruvate	Gibco

Retinoic acid	Sigma Aldrich
ROCK inhibitor (Y-27632)	Enzo Life Sciences
Rotenone	Sigma Aldrich
SAG, SHH agonist	Enzo Life Science
SB-431542, TGFB1R inhibitor	Selleckchem
StemMACS iPS-Brew XF, human	Miltenyi Biotech
TGF-B3	MACS Miltenyi
Triton X-100	Sigma Aldrich
Tween-20	Sigma Aldrich

6.2.1.3. Molecular and chemical consumables

Item	**Supplier**
Acrylamide, 30%	Sigma Aldrich
APS	Sigma Aldrich
AscI	NEBR0558S
Ava II	NEB #R01535
Bbs1	NEB #R3189
BsaJI	NEB #R0536S
BsiWI	NEB #R3553S
DNA Extension Ladder 1kb	Life Technologies
DNA Extension Ladder 100bp	Life Technologies
DNA Gel Loading Dye (6X)	Life Technologies
DNA Kit FlexiGene	Qiagen
DNase I	Invitrogen
dNTP	25 mM USB
EDTA	Carl Roth
Ethanol 70 %	Carl Roth
Ethidium bromide	Carl Roth
Glycerol, 85%	Carl Roth
GoTaq Flexi buffer	Promega
GoTaq DNA Polymerase	Promega
Isopropanol, 100%	Carl Roth

$MgCl_2$, 25mM	Carl Roth
Not I	NEB #R3189S
Nsil	NEB #R0127S
oligo-dT, 1ug/ul	Invitrogen
Phusion Hot StartII DNA Polymerase	Thermo Fisher Scientific.
5X Phusion GC Buffer	Thermo Fisher Scientific
Protease	Qiagen
Reverse transcriptase	Affymetrix
Reverse transcriptase Buffer	Affymetrix
RNeasy Mini Kit	Qiagen
RNase-free distilled water	Gibco
SYBR green PCR mix	Applied Biosystems
TEMED	Sigma Aldrich
Tween-20	Sigma Aldrich
TrisBase	Sigma Aldrich
Sma I	NEB #R01415

6.2.2. Media

All media were sterile-filtered and pre-warmed to 37 °C before usage. Maintenance and freezing media are listed below with their components and suppliers.

Embryoid Body				
		Volume	**Stock conc.**	**Final conc.**
EB	KO-DMEM	40 ml	1x	1x
	KO-SR	10 ml	1x	5x
	Pen/Strep	500 µl	0.1 mg/ml	10 mg/ml
	Glutamine	500 µl	2 mM	200 mM
	NEAA	500 µl	1x	100x
	Pyruvate	500 µl	1 mM	100 mM

ESC/iPSC				
		Volume	**Stock conc.**	**Final conc.**
ES	KO-DMEM	450 ml	1x	1x
	KO-SR	100 ml	1x	50x
	Amino acids	5 ml	1x	100x
	Pyruvate	5 ml	1 mM	100 mM
	bFGF (FGF2)	650 µl	9 ng/ml	8 µg/ml
	Pen/Strep	5 ml	0.1 mg/ml	10 mg/ml
	MycoZap	1 ml	1x	500x
	Glutamine	5 ml	2 mM	200 mM
		Volume	**Stock conc.**	**Final conc.**
iPS Brew	iPS Brew Supplement	10 ml	50x	1x
	MycoZap	1 ml	500x	1x
	Pen/Strep	5 ml	10 mg/ml	0.1 mg/ml
		Volume	**Stock conc.**	**Final conc.**
mTeSR	mTeSR1 Basal medium	400 ml	1x	1x
	mTeSR1 5x Supplement	100 ml	5x	1x
	MycoZap	1 ml	500x	1x
	Pen/Strep	5 ml	10 mg/ml	0.1 mg/ml

NPC culture

		Volume	Stock conc.	Final conc.
SM-	Ham's F-12	240 ml	1x	0.5 x
	Neurobasal	240 ml	1x	0.5 x
	N2	2.5 ml	100x	0.5x
	B27	5 ml	50x	0.5x
	Pen/Strep	5 ml	10 mg/ml	0.1 mg/ml
	Glutamine	5 ml	200 mM	2 mM
	MycoZap	1ml	500 x	1x

		Volume	Stock conc.	Final conc.
SM+	SM-	10 ml	1x	1x
	Pu	7.69 µl	0.65 mM	0.5 µM
	CHIR	5 µl	6 mM	3 µM
	Vit. C	10 µl	0.2 M	200 µM

DA enriched composite culture

		Volume	Stock conc.	Final conc.
DSM+	SM-	10 ml	1x	1x
	FGF8	2 µl	500 µg/ml	100 ng/ml
	Pu	15.38	0.65 mM	1 µM
	Vit.C	10 µl	0.2 M	200 µM

		Volume	Stock conc.	Final conc.
DSM2+	SM -	10 ml	1x	1x
	BDNF	10 µl	10 µg/ml	10 ng/ml
	GDNF	10 µl	10 µg/ml	10 ng/ml
	TGF-B3	10 µl	1µg/ml	1 ng/ml
	Vit.C	10 µl	0.2 M	200 µM
	db c-AMP	50 µl	100 mM	500 µM
	Pu	7.69µl	0.65mM	0.5µM

		Volume	Stock conc.	Final conc.
DMSM+	SM-	10 ml	1x	1x
	BDNF	10 µl	10 µg/ml	10 ng/ml
	GDNF	10 µl	10 µg/ml	10 ng/ml
	TGF-b3	10 µl	1µg/ml	1 ng/ml
	Vit.C	10 µl	0.2 M	200 µM
	db c-AMP	50 µl	100 mM	500 µM

CRISPR/Cas9 FACS media				
		Volume	**Stock conc.**	**Final conc.**
	PBS	9,2 ml	1x	1x
	FBS	500 µl	1x	1 to 20
Pre-FACS media	Pen/Strep	100 µl	10 mg/ml	1 to 100
	Gentamycin	100 µl	10 mg/ml	1 to 100
	EDTA	100 µl	2 mM	1 to 100
		Volume	**Stock conc.**	**Final conc.**
Post-FACS media	mTESR1	1 ml	1x	1x
	ROCK inhibitor	1 µl	3,2 mg/ml	3,2 µl/ml

Seahorse media		
		Amount
	ddH2O	1 L
u-DMEM	DMEM base	8.3 g
	NaCl	1.85 g
	Phenol red	15 mg
	Glutamine	10 mL

6.2.3. Buffers and solutions

4 % PFA	4 g PFA dissolved in 100 ml, pH 7.4
4x SDS loading buffer	200 mM Tris pH 6.8 400 mM DTT 8% SDS 40% glycerol bromophenol blue
Blocking buffer (IHC)	5 % DNS in PBS-T
Blocking buffer (WB)	3 % milk powder in PBS-T
	50 mM HEPES pH 7.4 150 mM NaCl

Cell lysis buffer	1.5 mM MgCl2 0.1% NP 40 1 mM EDTA 1x Complete™ protease inhibitors 2u/ml benzonase
Coomassie staining solution	30 % ethanol 10 % acetic acid 0.05 % Coomassie brilliant blue R250

6.2.4. Oligonucleotides and sequences

qRT-PCR		
Gene	**Forward**	**Reverse**
NANOG	CCTGTGATTTGTGGGCCTG	GACAGTCTCCGTGTGAGGCAT
SOX2	GTATCAGGAGTTGTCAAGGCAGAG	TCCTAGTCTTAAAGAGGCAGCAAAC
GDF3	TTGGCACAAGTGGATCATTGC	TTGGCACAAGTGGATCATTGC
DPPA4	TGGTGTCAGGTGGTGTGTGG	CCAGGCTTGACCAGCATGAA
DNMT3B	GCTCACAGGGCCCGATACT	GCAGTCCTGCAGCTCGAGTTTA
OCT4	GTGGAGGAAGCTGACAACAA	ATTCTCCAGGTTGCCTCTCA
DCX	GAAGCCATCAAACTGGAGAC	GAAATCATGGAGACAAGTTACCTG
NKX2.2	CCTTCAGTACTCCCTGCAC	TGTCATTGTCCGGTGACTC
LHX2	GAAGGGGCGGCCGAGGAAAC	GCTGGTCACGGTCCAGGTGC
SCN7A	CTTTGTGGCAACAGGACAGA	AATAAGGCCCAGCCAAAACT
KCNQ2	GGCTTCAGCATCTCCCAGT	GACTCTCCCTCCGCAATGTA
SYP	ATTGTGCCAACAAGACCGAGAGT	AGGAAGATGTAGGTGGCCAGAG
SYT13	TGGGTTCCTCCCTCTTTCTT	GAAAATGTGTGCTGGTGGT
ARX	CTGCTGAAACGCAAACAGAGGC	CTCGGTCAAGTCCAGCCTCATG
SPON1	CTCTTCCTGCAGAGGAGTAGTGTCA	CTGGGACTCAGGC ATAGTCACTTC
NTN1	TGCAAGAAGGACTATGCCGTC	GCTC GTGCCCTGCTTATACAC
GATA3	TGTCTGCAGCCAGGAGAGC	ATG CATCAAACAACTGTGGCCA
PPARGC1A	GCTTTCTGGGTGGACTCAAGT	TCTAGTGTCTCTGTGAGGACTG
PDK3	CGCTCTCCATCAAACAATTCCT	CCACTGAAGGGCGGTTAAGTA

MYC	CCAGCAGCGACTCTGAGGA	GAGCCTGCCTCTTTTCCACAG
LDHA	TATGGAGTGGAATGAATGTTGC	CCCTTAATCATGGTGGAAACTC
ACTB	TCAAGATCATTGCTCCTCCTGAG	ACATCTGCTGGAAGGTGGACA
GAPDH	CTGGTAAAGTGGATATTGTTGCCAT	TGGAATCATATTGGAACATGTAAACC

Mutation analysis		
S1A	TGATGGCAAGCTATGAGGGG	CCGCCATATACACATGTGAGAAC
S1C	ACTTCCGTACGTTGTGGACC	GCAGCTGATCTGTCACACAC
Primer induced restriction analysis (PIRA)		
S1A	CATTACCCTAGAGTCACCATCCCG G	GGAGCCTGGTGGACTCCC
S1C	GGGATGGTCACCCAACGTAA	ACCAGTAGCACATGATCCAGCATA

TALEN		
	Forward	**Reverse**
M13 primer	TGTAAAACGACGGCCAGT	CGGATAACAATTTCACACAGG
sgRNA	GTCCCTGGAAGACCCATTGG	

TALEN Library design	
TAL 1 - (5´-3´)	TAL 2 – (5´-3´)
I-GAGC : 2 / D / 6	IV-AGC : 9 / A / 10
II-CAGC : 4 / D / 6	III-CTAG : 7 / E / 3
III-CCTG : 7 / C / 7	II-ACAA : 3 / G / 9
IV- TTT : 9 / F / 4	I-AGGA : 1 / D / 5

TALEN strings

TALE 1

TGGGTCgcggccgcCCCAGCCCTACCTTGAGGGAGTGGAGGCAGGGGTGGCTCCCTAGAGGGCTATT
TGGGAGTTAAGAGATGGGAAGAACATTCCAGGCAAAGCAAATGACAGGTACAGGAGCACCTGTGT
GATTAACTAGGGAACTGGAGGATTCACGTAAAAATGAAAATACCTGGGGCTCTTGTTAACCCATGG
GTTCCTGTTTTAGGGCTGGGATGGGGCCCAAGTACTCATCTCCAGCAGGCTGGGGTGCCAGGGCTG
CTCCTCACGGCTGCCTTGGTTAGGAGGAGGGATTGGAGACAGCTCTTGCCATAGTTCAGGGGAGAG
GTGTGGGGTCTAAACTCTGGCGTGGCAGCGTTGCTCACCAGTTGCACGTTGTAGTAGGTAGACCAC
AAGAAGCAGAGATAGAAGGGGAAAGCCACACTGGTAAAAAGGTAGTGATGGTGGCAGGGAGCCT
TTTACCAACCACGAAGGTGCCTCAAGAGAGGAAGACTTTGCCTGTGTGGCACTGCCAGGGCTCCAC
TGAGCCAGCCCTGTTTTAA**CCCTAGAAAGATAATCATATTGTGA**cgtacgTT

TALE 2: To correct the mutation

TCAAGAatgcat**GCGTCAATTTTACGCAGACTATCTTTCTAGGG**TTAAAAGCCTTCCTTGGT**GCTCTAG**
TTGTTCCTATGGGTGCCTGAGTGACCATGAGTGACTGTCTTTAGTCAAAAACCCTCCCCACCTGAAG
TAGCACTTTCATTACCCTAGAGTCACCATCCTGGTAAATAGAGGGTTCGTTCCCAGGAAGAAAGTGA
ATCCTGAAACCCGGCAGAAAGGCCAGGTAAGGGACATGGACTCTTCCTACTTTAGAGAAGGCTCTG
GGAGTCCACCAGGCTCCATGCAATCTCACACACCTTCCTTTATAGATTGAGGGAGAAGTGGACCTCA
TTGGGATGGTGAGGCTGACAGAAACCAGGCAGCCTTTTGTCCCTGAGAACAATCCAGAAAGGAACC
ACTGGCATTATCGAGACCTGGAAGCTATGGCCAGAATCACAGGCGCAGAGCCCATCTTCATTGATG
CCAACTTCCGTACGTTGTGGACCAGCCCATCTCGGAACAAGTAGCTTTTGTGAATACTGTCCTTCCTC
CTAACCCTCATTGCCCAGTCACTACTGTGGCggcgcgccTGCAT

TALE 3: To introduce the mutation

TCAAGAatgcat**GCGTCAATTTTACGCAGACTATCTTTCTAGGG**TTAAAAGCCTTCCTTGGT**GCTCTAG**
TTGTTCCTATGGGTGCCTGAGTGACCATGAGTGACTGTCTTTAGTCAAAAACCCTCCCCACCTGAAG
TAGCACTTTCATTACCCTAGAGTCACCATCCTGGGAAATAGAGGGTTCGTTCCCAGGAAGAAAGTGA
ATCCTGAAACCCGGCAGAAAGGCCAGGTAAGGGACATGGACTCTTCCTACTTTAGAGAAGGCTCTG
GGAGTCCACCAGGCTCCATGCAATCTCACACACCTTCCTTTATAGATTGAGGGAGAAGTGGACCTCA
TTGGGATGGTGAGGCTGACAGAAACCAGGCAGCCTTTTGTCCCTGAGAACAATCCAGAAAGGAACC
ACTGGCATTATCGAGACCTGGAAGCTATGGCCAGAATCACAGGCGCAGAGCCCATCTTCATTGATG
CCAACTTCCGTACGTTGTGGACCAGCCCATCTCGGAACAAGTAGCTTTTGTGAATACTGTCCTTCCTC
CTAACCCTCATTGCCCAGTCACTACTGTGGCggcgcgccTGCAT

(Red letters indicate where the mutation reside and correction is aimed. Red highlighted area indicates TTAA box, TAL1 is highlighted in pink. TAL2 is highlighted in light blue.)

CRISPR/Cas9	**Forward**	**Reverse**
For SVS1C sequencing	ACTTCCGTACGTTGTGGACC	GCAGCTGATCTGTCACACAC
Oligomer pairs	CACCGTCCCTGGAAGACCCA TTGG	AAACCCAATGGGTCTTCCAGGGAC
Primer U6 (for sequencing)	GAGGGCCTATTTCCCATG	
sgRNA	GTCCCTGGAAGACCCATTGG	
ssODN HDR template with 2 silent mutations	GTGGTGCAGAGGCTGGCAGGCCAGTAGGGGGTGGACTTGAGTCTGCTGTCT CCACAGAGAGCACAGTCCCTGG**A**GG**A**CC**a**AT**c**GGAGGGCAAACCAGAGTTA CTCTGAGGAACGAGCATCTGCAGTACATCGTGACCTGGTGAGTCCCC	

(Underlined letters indicate mismatch and small case letters indicate silent mutations.)

SURF1 lentiviral construct; amino acid sequence (NP_003163.1):

MAAVAALQLGLRAAGLGRAPASAAWRSVLRVSPRPGVAWRPSRCGSSAAEASATKAEDDSFLQWVLLLIP VTAFGLGTWQVQRRKWKLNLIAELESRVLAEPVPLPADPMELKNLEYRPVKVRGCFDHSKELYMMPRTMV DPVREAREGGLISSSTQSGAYVVTPFHCTDLGVTILVNRGFVPRKKVNPETRQKGQIEGEVDLIGMVRLTETR QPFVPENNPERNHWHYRDLEAMARITGAEPIFIDANFQSTVPGGPIGGQTRVTLRNEHLQYIVTWYGLSAA TSYLWFKKFLRGTPGV

Mycoplasm analysis		
Myco 1	CGCCTGAGTAGTACGTTCGC	
Myco 2	CGCCTGAGTAGTACGTACGC	
Myco3	TGCCTGAGTAGTCACTTCGC	
Myco 4	CGCCTGGGTAGTACATTCGC	
Myco 5	CGCCTGAGTAGTAGTCTCGC	
Myco 6	TGCCTGGGTAGTACATTCGC	
Myco r1		GCGGTGTGTACAAGACCCGA
Myco r2		GCGGTGTGTACAAAACCCGA
Myco r3		GCGGTGTGTACAAACCCCGA

6.2.5. Antibodies

Primary Antibody			
IHC analysis			
Target protein	**Used dilution**	**Provider**	**species**
TUJ1	1 to 3000	Sigma-Aldrich	mouse
FOXA2	1 to 100	Seven hills	rabbit
SYP	1 to 500	Sigma-Aldrich	mouse
GFAP	1 to 500	Synaptic systems	guinea pig
OCT4	1 to 300	Biotechnology	mouse
NANOG	1 to 300	R & D Systems	goat
SOX2	1 to 100	Sigma-Aldrich	mouse
TRA-1-60	1 to 200	Sigma-Aldrich	mouse
S100ß	1 to 600	abcam	mouse
HES5	1 to 50	Biotechnology	Rabbit
TH	1 to 500	Biotechnology	rabbit
NURR1	1 to 500	Sigma-Aldrich	rabbit

VAMP2	1 to 500	Synaptic systems	rabbit
SMA	1 to 200	Dako Cytomation	mouse
PAX6	1 to 200	Covance	rabbit
SOX2	1 to 100	Santa Cruz	goat
SOX17	1 to 50	R & D Systems	goat
LIN28		Protein Tech Europe	Rabbit
MAP2	1 to 100	Synaptic systems	guinea pig
Hoechst	1 to 10,000	Thermo Fischer	
WB analysis			
MT-CO2	1 to 1,500	abcam	Mouse
Tubulin	1 to 4,000	Sigma-Aldrich	mouse

Secondary Antibody			
	Used dilution	**Provider**	**Against species**
Alexa Fluor 488	1 to 300	Invitrogen	donkey anti-mouse
Cy2	1 to 300	Sigma-Aldrich	goat anti-mouse
	1 to 300	Sigma-Aldrich	donkey anti-rabbit
Cy3	1 to 300	Merck Millipore	donkey anti-mouse
	1 to 300	Merck Millipore	donkey anti-goat
	1 to 300	Sigma-Aldrich	donkey anti-guinea pig
Cy5	1 to 300	Sigma-Aldrich	donkey anti-mouse
	1 to 300	Sigma-Aldrich	donkey anti-goat

MACS Quant Analysis		
Target protein	**Used dilution**	**Provider**
A2B5-APC	1 to 11	Miltenyi Biotec
GLAST (ACSA-1)-APC	1 to 11	Miltenyi Biotec
PSA-NCAM-PE	1 to 11	Miltenyi Biotec
CD11B-Vioblue	1 to 50	Miltenyi Biotec
O4-APC	1 to 11	Miltenyi Biotec
Viobility 405/520	1 µL	Miltenyi Biotec

6.2.6. Kits

Kit	**Suplier**
AmpliTaq Gold™ 360 Master Mix	Thermo Fisher Scientific
BCA Protein assay	Pierce
Clone Jet PCR Cloning	Thermo Fisher Scientific
CytoTune-iPS 2.0	Thermo Fisher Scientific
CyQUANT	Molecular Probes
DNeasy blood and tissue kitx	QIAGEN
FlexiGene DNA Kit 250	QIAGEN
High Output	TG NextSeq® 500/550
Infinium OmniExpressExome-8	Illumina
Lactate Fluorometric Assay Kit	BioVision
Lipofectamine 3000	Thermo Fisher Scientific
Lipofectamine 2000	Thermo Fisher Scientific
MSB Spin PCRapace	Stratec Biomedical
NativePAGE™ Novex® Bis-Tris gel system	Invitrogen
NucleoBond Xtra Maxi Plus	MACHEREY-NAGEL GmbH & Co. KG
PCR Clean-Up System	Promega
Pure Yield Plasmid Miniprep System	Promega Corporation
Phire Animal Tissue Direct PCR	Thermo Fisher Scientific
Pro-inflammatory Panel I	MSD
QIAprep Spin Miniprep	QIAGEN
Qiagen RNeasy Mini	QIAGEN
TruSeq Stranded Total LT Sample Prep	Illumina
Wizard SV Gel and PCR Clean-Up System	Promega Corporation
WesternBright™ Chemiluminescent HRP substrate	Quantum™

6.2.7. Plasmids

Purpose	Identifier	Provider
TALEN	PB-MV-Puro-TK	Addgene
CRISPR/Cas9	pU6(BbsI)-CAG-Cas9-venus-bpA (#1)	Dr. Pawel Lisowski
	614.CAG-hRad52-EF1BFP (#2)	Dr. Bruna Paulsen
	602.pCAG-i53-EF1BFP (#3)	Dr. Bruna Paulsen
SURF1 gene augmentation	pLenti PGK Neo DEST	Addgene
	pLenti_PGK_SURF1	Dr. Chris Secker
	pLenti_PGK_Neo_mCitrine-stop	Dr. Chris Secker

6.2.8. Software

Programme	Supplier
Adobe illustrator	Adobe Inc.
AxioVision v46-3-0	Zeiss
BD FACSDiva Software v8.0.2	BD Biosciences
Cellomics Neuronal Profiling v3.5	Thermo Fisher Scientific
CLC Genomics Workbench v11	QIAGEN Bioinformatics
DESeq2 v1.20.00 R package	Biocondoctor
FiJi verison v1.52h	ImageJ
FlowLogic v7.2.1.	Inivai
GraphPad Prism v5	GraphPad Software
HCS Studio Cell Analysis Software v6.6.1.	Thermo Fisher Scientific
Image J	NIH
KaryoStudio v1.4	Illumina
Serial Cloner v2.1	Serial Basics
STAR Aligner v2.6.0c	GitHub
WinTida v5.0	HEKA Electronics

7. Methods [2]

7.1. Cell biology

7.1.1. Cell culture

For different kinds of experiments, different cell types and models were used: skin fibroblasts, induced pluripotent stem cells (iPSCs), and iPSC-derived NPCs, NPC-derived composite cultures (neurons and glial cells). Lastly, iPSC-derived cerebral organoids used in this study. I have cultivated and maintained the first four cell types for this study. Cerebral organoids were managed by Dr. Agnieszka Rybak-Wolf. Each cell type needs a specific condition for optimal growth and maintenance of cell specific properties. T75 cell culturing flasks, different format of well plates (6, 12, 24 and 96), mini or 150mm, low attachment Petri dishes were used depending on the designed experiment. Cells were maintained in standard cell culture media supplemented with appropriate compositions of small molecules and additional supplements supporting the survival of the specific cell tape. All media were sterile-filtered and pre-warmed to 37°C before usage. Media composition and can be found in section 6.2.2.

7.1.1.1. Cultivating conditions

Different cell types require different culturing conditions. Skin fibroblasts do not need coating on the plates, whereas iPSCs, NPCs, and composite cultures needed matrigel coating to attach and survive. Matrigel (the membrane-like matrix) was used in a concentration of 5 mg/ml. Knock Out DMEM (Dulbecco's Modified Eagle Medium) was used to dilute the gel stock solution. Plates are coated one day before use and stored overnight in +4°C.

Skin fibroblasts were cultured in DMEM media, and the media was changed once in three days. They were split with Trypsin at 1:8 ratio. iPSCs were cultured in three different media types: ES ´lab made´, mTeSR1 provided by "Stem Cell Technologies" or iPSBrew provide by "Miltenyi Biotec". Under normal conditions, cells were cultured feeder-free and in mTeSR1 or iPS Brew. Media was changed daily. Cells were split regularly once a week in a split ratio of 1:4, mechanically. For transfection purposes, iPSCs were split with Accutase in a ratio of 1:1. Under stressful conditions such as post-FACS transfection phase, iPSCs were plated on feeders (MEFs) to provide support and promote survival and were given either ES, iPS Brew or mTesR1. Neuronal progenitor cells were cultured in SM+ media. Media was changed once in three days. Cells were split regularly once a

[2] *Methods have partially been reused with modifications from the published version:* ***Inak, G.,*** *Rybak-Wolf, A., Lisowski, P., Juettner, R., Zink, A., Mlody, B., … Prigione, A. (2019). SURF1 mutations causative of Leigh syndrome impair human neurogenesis. BioRxiv. https://doi.org/10.1101/551390*

week in a split ratio of 1:8 by Accutase. If NPCs were directed to differentiate further to DA-enriched composite cultures, they were split by Accutase and DSM+ media was given when the good confluency was around 70%. After they were kept in culture for 8 days, they were given DSM2+ media. On the 10th day, the cells were split with Accutase, and they were plated on matrigel plates and were given DMSM+ ROCK inhibitor. DMSM+ media was changed every 4 days, and the cells were maintained for 4, 6, or 8 weeks, depending on the maturation stage aimed for the specific experiment. Because neurons do not proliferate anymore, regular splitting is not necessary.

7.1.1.2. Splitting cells

Fibroblasts were split when they were at 80-90 % confluency. Cells were incubated with 0,05 % Trypsin-EDTA for 5 minutes at 37 °C until the cells were detached. Afterward, they were collected into DMEM media and centrifuged at 120 rcf for 5 minutes. The cell pellet was resuspended in DMEM medium, and cells were plated according to splitting ratio.

iPSCs were split mechanically, and they were picked as single clones. The aim of picking single colonies is to get rid of the differentiated cell types. A special laminar hood "BDK-S" is used for working with uncovered cells directly under the "Leica M80" microscope. Picked cells were transferred into new wells containing fresh media and ROCK Y-27632 inhibitor.

NPCs were split with the enzyme Accutase for single cell splitting. Cultivation media was sucked up, and Accutase was given. After 3 mins of incubation at 37 °C, cells were collected by pipetting up and down and transferred into a new Falcone tube. To stop the Accutase activity, the cells were washed one time in Dulbecco's Phosphate Buffered Saline (DPBS) or the required media and centrifuged with 120 rcf for 4 mins. To seed the cells, the pellet was resolved in the acquired amount of the cell type-specific media and transferred in wanted split ration into a new well, containing fresh media and, in the case of composite cultures, ROCK Y-27632 inhibitor to prevent apoptosis on the fragile cell types as neurons. Neurons were split with gently as they were centrifuged at a low speed and for fewer minutes (40 RCF, 2 minutes). Cells of composite cultures tend to sink to the bottom by gravity. They survive better when they were plated as single cells, so Accutase splitting is important.

7.1.1.3. Cryopreservation and Thawing

In order to ensure different reproducibility passages of all cell lines were frequently frozen. Therefore, harvested cells in 0.5-1 ml culture medium together with an equal volume of 2 x freezing medium were transferred into 2 ml low temperature freezing vials. Within a freezing container allowing slow freezing at a rate of −1 °C/min ('Mr. Frosty,' Thermo Fisher Scientific) the

vials were placed at −80 °C overnight before liquid nitrogen storage. Frozen cells have been thawed rapidly in 37 °C water bath and centrifuged at 120 rcf for 4 min. Subsequently, the cell pellet was resuspended in the required growth medium (Table 6.2.2.) with ROCK Y-27632 inhibitor and seeded on appropriately prepared culture plates.

7.1.2. iPSC generation

Patient fibroblasts were reprogrammed using Sendai viruses (CytoTune-iPS 2.0 from Thermo Fisher Scientific). All pluripotent stem cells (PSCs) were cultivated on Matrigel (BD Bioscience)-coated plates using StemMACS iPS-Brew XF medium (Miltenyi Biotec GmbH, #130-104-368), supplemented with Pen/Strep (Thermo Fisher Scientific) and 1ml Mycozap. We routinely monitored against mycoplasma contamination using PCR. 10 µM Rock inhibitor (Enzo, ALX-270-333-M005) was added after splitting to promote survival. PSC cultures were kept in a humidified atmosphere of 5% CO_2 at 37 °C and 5% oxygen. All other cultures were kept under atmospheric oxygen condition. Karyotype analysis was performed by MDC Stem Cell Core Facility. Briefly, DNA was isolated using the DNeasy blood and tissue kit (Qiagen, Valencia, CA). SNP karyotyping was assessed using the Infinium OmniExpressExome-8 Kit and the iScan system from Illumina. CNV and SNP visualization was performed using KaryoStudio v1.4 (Illumina).

7.1.3. FACS Sorting

CRISPR/Cas9 transfected cells were sorted by flow cytometer BD FACS Aria. By using the unedited CH4 line, cells were sorted in the first step in order of granularity/surface by the side scatter (SSC-A), and size by forward scatter (FSC-A). To eliminate doublets during sorting, the resulting population from analyses were gated and first adjusted in FSC-W against FSC-H and second in SSC-W against SSC-H. This led to the exclusion of cell droplets with incorrect cell size and cell signal ratio. After adjusting the morphology properties, the cell population was screened for cells containing pU6(Bbsl)-CAG-eCas9-venus-bpA(#1) by using the GFP channel for Venus-positive cells and cells containing pCAG-i53-EF1BFP and CAG-hBRCA1-EF1BFP by using BFP channel for BFP positive cell. Only double positive cells were used for further cultivation and analyses of edited events. Cells were kept in Pre-FACS media before and during sorting, then they were transferred into a prepared tube with post-FACS medium and then plated onto MEFs 6 well plates. Around 500 cells were plated into each well aiming single-cell-derived clones.

7.1.3.1. Generation of feeder cells

Mouse embryonic fibroblasts (MEFs, feeders) served as feeder cells during PSC-culturing. Those cells were obtained from 2-week-old mouse embryos (strain CF1) and plated on Petri dishes maintained in DMEM. The medium was changed every 2-5 days, and at 80-90 % confluence cells were passaged. After sufficient expansion, the MEFs were mitotically inactivated by incubating them with Mitomycin C (Sigma-Aldrich) for two h at 37 °C. Finally, cells were counted with a Neubauer hemocytometer and frozen as aliquots of 1.3 x106 cells/vial for one 6-well-plate. MEFs were used as a support for the survival of FACS-sorted cells. MEFs plates were prepared one day before as they need almost one day to attach. Therefore DMEM-medium had to be warmed, and Matrigel plates had to be incubated in the binder incubator at 37°C for 20 min. The frozen MEFs had to be thawed and filled into a 15 ml falcon. Some ml of DMEM were added. The mixture was centrifuged for 4 min at 120 rcf. The supernatant was discarded, and the pellet was solved in 9 ml of DMEM and resuspended 15 times. For a six well-plate 1.5 ml DMEM was added to each well before adding 500 µl cell suspension to each well. Afterward, the cells were checked under a microscope.

7.1.4. Differentiation of NPCs and DA neuronal cultures

NPCs and dopaminergic (DA) neurons were obtained using a previously published protocol (Reinhardt et al., 2013). Briefly, PSCs were detached from Matrigel-coated plates using Accutase (1 mg/mL), and the collected cells were transferred into low-attachment Petri dishes and kept for two days in SM- media. From day 2 to day 6, SM+ media was added to have 1:1 ratio. On day 6, the suspended cells were transferred onto Matrigel-coated well plates using SM+ media. NPCs were maintained on this media without rock inhibitor and used for experiments between passage 7 and 20. For DA differentiation, I used NPCs between passage 7 and 13. To initiate the differentiation, the media was changed to DSM+ media. After seven days, the media condition was replaced with DSM2+ media. On day 9, cells were split with Accutase gently and seeded on Matrigel-coated plates in DMSM+ media. Media composition can be found in section 6.2.2. The scheme of the differentiation protocol used in this study is summarized in Figure 7.1.4. (Reinhardt et al., 2013). After neurospheres were plated on Matrigel-coated plates on day 4, the small molecules (DM, SB) were added to basal media to inhibit both bone morphogenetic proteins (BMP) and transforming growth factor (TGFß) signaling pathways. Purmorphamine was added to stimulate sonic hedgehog (SHH) pathway, and in order to stimulate the canonical WNT pathway, glycogen synthase kinase-3 (GSK3) is inhibited by CHIR. At day 10, NPCs were formed, and they were maintained until they reach passage 6 to have a

homogenous population. If the passage number of NPCs were between 6 and 13, they were further differentiated into dopaminergic neuron-enriched cultures (DA). The cells were then treated with the developmental patterning factors such as SHH and fibroblast growth factor 8 (FGF8), which specify the formation of ventral midbrain dopaminergic neural cells. The neural-like cells were kept in culture for further maturation stages for 4 weeks (28 days) or 8 weeks (56 days). They were treated with ascorbic acid (vitamin C), brain-derived neurotrophic factor (BDNF), glial cell line-derived neurotrophic factor (GDNF), transforming growth factor beta 1 (TGFß), and cyclic adenosine monophosphate (cAMP) which are known to promote neuronal survival and growth.

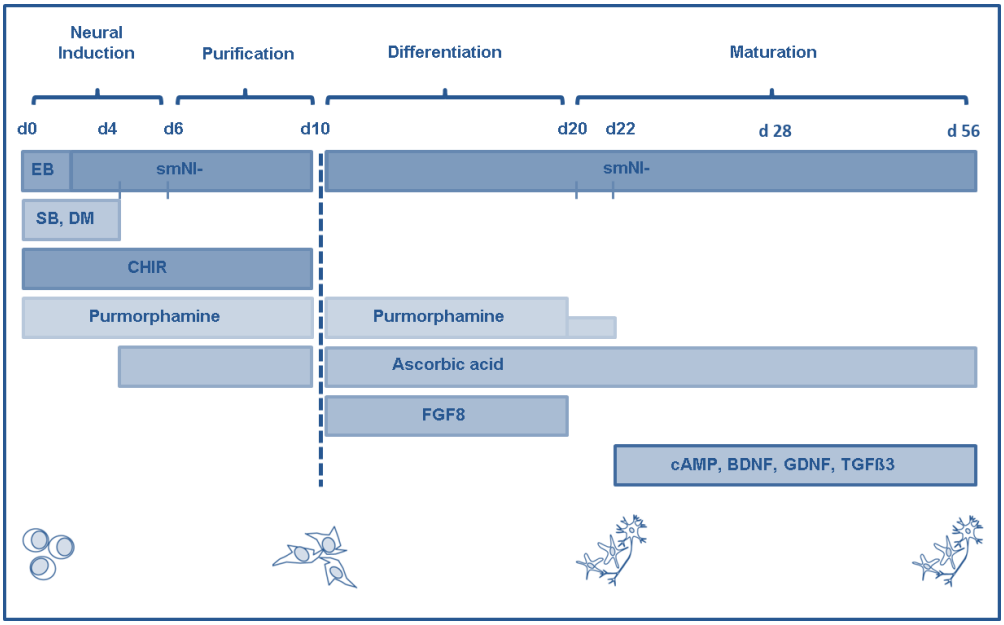

Figure 7.1.4.: Scheme of the differentiation protocol from iPSCs to fully differentiated NPC-derived neurons

***d 0-10**, Embryoid bodies (EBs) derived from iPSCs were directed towards to neural lineage through the small molecules dorsomorphin (DM) and SB43152 (SB), and CHIR99021 (CHIR). The SHH pathway was stimulated using the small molecule purmorphamine (PMA). Epithelium cells were formed and expanded. d **10-22**, PMA and FGF8 were given to NPCs for eight days, which helps the specification of ventral midbrain cells, including midbrain dopaminergic neurons. Then only PMA and ascorbic acid were given for two days. **d 22-56**, Neurons were given cAMP, BDNF, GDNF, and TGF-b3 for maturation for 28 days or 56 days.*

7.1.5. Electrophysiology

To analyze passive and active membrane properties, spiking and synaptic activity in DA neuronal cultures, whole-cell patch clamp recordings were carried out on week 4, 6, and 8 weeks of differentiation. DA neurons were visualized under phase contrast optics on an upright microscope (Axioskop, Zeiss) by using a 63x/0.95 water immersion objective. Recordings were performed using a patch-clamp amplifier (EPC-9, HEKA Elektronik). Recording pipettes were

filled with an intracellular solution containing (in mM): 4 NaCl, 120 KCl, 5 EGTA, 10 HEPES, 5 glucose, 4 MgCl2, 0.5 CaCl2 (pH 7.3, 270 mOsmol/kg). The pipette to bath resistance ranged from 5 to 7 MOhm. Series resistance compensation was applied as much as possible (50– 70%). The effective series resistance was in the range of 20–40 MOhm and was checked throughout the whole experiment by using a short depolarizing pulse (10 mV, 20 ms). Recordings were accepted only if the series resistance was less than 40 MOhm. Bath solution contained (in mM): 136 NaCl, 2.5 KCl, 20 glucose, 20 HEPES, 2 CaCl2, 1 MgCl2 (pH 7.3, 305 mOsmol/kg). Whole cell input resistance (RIN) was estimated based on passive current responses to moderate depolarizing voltage pulses of short duration (±10 mV for 20 ms). Whole-cell membrane capacitance (CN) was estimated by integration of the capacitive current transient and division by the respective stimulation voltage. Voltage-gated Na+- and K+-currents were elicited by a series of 200 ms depolarizing pulses applied from the holding potential of -70 mV, in 10 mV increments between -70 and +70 mV. Passive responses were subtracted by using a hyperpolarizing pulse of -20 mV. Spontaneous synaptic currents were recorded in voltage-clamp mode at a holding potential of -70 mV without specific blockers. To evaluate action potential generation and discharge properties, cells were adjusted to -90 mV by steady current injection and depolarized by injection of positive current pulses (5 – 50 pA) of 1-sec duration under current clamp conditions. Signals were acquired at a rate of 10 kHz and analyzed off-line using WinTida 5.0 (HEKA Electronics). All patch clamp experiments were performed at room temperature (20–25 °C).

7.1.6. Generation of iPSC-derived cerebral organoids

Cerebral organoids were generated according to the protocol described by Lancaster et al., 2014 with some modifications. Shortly, after dissociation into single-cell suspension with accutase, 10,000 cells were seeded per one well of 96 well-plate in 100 µl of EB (medium supplemented with bFGF and 50 µM ROCK inhibitor). After 4 days, the medium was replaced with EB medium without bFGF and ROCK inhibitor and at day 6 with neural induction medium (NIM). At day 11, organoids were embedded in Matrigel (Corning, 356234) and kept in NIM for two days, and in organoid differentiation medium without retinoic acid (RA) for another four days. Next, organoids were transferred to ultra-low attachment 6-well plates and culture on an orbital shaker (80 rpm) in organoid maturation medium. The composition of the original organoids maturation medium was changed by adding: chemically defined lipid concentrate (1x), ascorbic acid (0.4mM), BDNF (20ng/ml), HEPES. The organoid size was analyzed by measuring the area using ImageJ software. Each human cerebral organoid was fixed in 4% paraformaldehyde overnight at 4°C,

dehydrated by 40% sucrose in PBS and embedded in Tissue-Tek® O.C.T.™ Compound. 12 µm sections were cut and mounted onto slides (Thermo Fisher Scientific). Mounted sections were incubated for 1 h at room temperature with blocking solution (5% normal goat serum+0.3% Triton X-100 in PBS) and incubated with primary antibodies diluted in blocking solution overnight at 4°C. After three washes with PBST (0.1% TritonX100), corresponding fluorophore-conjugated secondary antibodies diluted in the blocking solution were added and incubated for 2 h at room temperature and followed by DAPI staining. Finally, stained slides were washed with PBST three times, mounted, and analyzed using a Keyence bz-x710 microscope.

7.1.7. Immunostaining

Cells grown on Matrigel-coated coverslips were fixed with 4% paraformaldehyde (PFA, Science Services) for 20 min at RT and washed two times with PBS. For permeabilization, cells were incubated with blocking solution containing 10% normal donkey serum (DNS) and 1% Triton X-100 (Sigma-Aldrich) in PBS with 0.05% Tween 20 (Sigma-Aldrich) (PBS-T) for 1 h at RT. Primary antibodies were diluted in blocking solution and incubated overnight at 4^{o}C on a shaker. Primary antibodies used were as follows: PAX6 (Covance, 1:200), SOX2 (Santa Cruz, 1:100), TUJ-1 (Sigma-Aldrich, 1:3000), OCT4 (Santa Cruz, 1:300), LIN28 (ProteinTech Europe, 1:300), TRA-1-60 (Millipore, 1:200), MAP2 (Synaptic System, 1:100), GFAP (Synaptic Systems, 1:500), NANOG (R&D Systems, 1:200), (SMA) (DakoCytomation, 1:200), SOX17 (R&D Systems, 1:50), TH (Millipore, 1:300), FOXA2 (Sevenhills, 1:100), S100ß (Abcam, 1:500), SYP (Sigma-Alrich, 1:500); VAMP2 (Synaptic Systems, 1:500), NURR1 (Sigma-Aldrich, 1:500). Corresponding secondary antibody (Alexa Fluor, 1:2000, Life Technologies) were diluted in blocking solution for with h at RT on a shaker. Counterstaining of nuclei was carried out using 1:10,000 Hoechst (ThermoFisher). All images were acquired using the confocal microscope LSM510 Meta (Zeiss) in combination with the Axiovision V46-3-0- software (Zeiss) and further processed with AxioVision software and ImageJ.

7.1.8. Bioenergetic profiling

Live-cell assessment of cellular bioenergetics was performed using Seahorse XF96 extracellular flux analyzer (Seahorse Bioscience), as described previously 51. Briefly, 20,000 cells were plated into each Matrigel-coated well of the XF96 well plates. NPCs were maintained in the plates for two days, while DA cultures were maintained in the plates for 4 weeks or 8 weeks. On the assay day, the cells were incubated at 37 °C 5% CO2 for 60 min to allow media temperature and pH to reach equilibrium before starting the simultaneous measurement of

mitochondrial respiration (oxygen consumption rate, OCR) and anaerobic glycolysis (extracellular acidification rate, ECAR) using the sequential introduction of oligomycin, FCCP, and then rotenone plus antimycin A (all products at 1 µM and from Sigma). Normalization to DNA content in each well of the plate was performed using the CyQUANT Kit (Molecular Probes). The supernatants were stored before and after the seahorse assay and used for lactate measurement using a Lactate Fluorometric Assay Kit (BioVision).

With this device, it was possible to measure simultaneously oxygen consumption rates (OCR), indicating the mitochondrial respiration (OXPHOS), and extracellular acidification rates (ECAR) indicating glycolytic activity. The ratio between those parameters allowed assessing a cellular preference for OXPHOS or glycolysis. Furthermore, cells were metabolically perturbed by the addition of four different compounds which shifted the bioenergetic profile. The first injection after basal measurements of OCR and ECAR was Oligomycin, which blocks Complex V of the electron transport chain (ETC). This prevention of ATP synthesis led to an increase of the proton gradient across the mitochondrial inner membrane while the consumption of oxygen decreased. The mobile ion carrier FCCP served as an uncoupler of the mitochondrial membrane. Upon this second injection, the proton flux re-established nonspecifically, and mitochondrial membrane potential collapses, leading to a fast consumption of energy and oxygen. In this case, also ECAR increased because the disruption of OXPHOS leads the cells to attempt to generate their ATP by using glycolysis. An additional injection of FCCP was performed to determine the continuous mitochondrial uncoupling. Finally, the last injection was a combination of the ETC inhibitors Rotenone (Complex I blocker) and Antimycin A (Complex III blocker) (Figure 7.1.8.) This simultaneous addition completely inhibited mitochondrial respiration and shut down OCR but pushed ECAR as the cells shifted to a more glycolytic state to produce ATP. The monitoring of OCR and ECAR values upon these treatments enables calculations of several bioenergetic parameters (Table 7.1.8.).

Parameter	**Calculation**
OCR Basal Respiration	Ø Basal – Ø (Antimycin A + Rotenone)
Maximal Respiration	Ø FCCP1 – Ø (Antimycin A + Rotenone)
Spare Respiratory Capacity	Ø FCCP1 – Ø Basal
ECAR	Basal Glycolysis Ø Basal
Glycolytic Reserve	Ø Oligomycin – Ø Basal
OCR/ECAR	rate 3 OCR / rate 3 ECAR

Table 7.1.8 Calculation of bioenergetics parameters from Seahorse data

7.1.9. CyQUANT Cell Proliferation Assay

The fluorescence-based method CyQUANT was used for quantifying cells and for setting a normalization count on the XF96 Seahorse data. As the Seahorse assay finished, the cell plate was washed twice with PBS and dried by blotting the plate on a clean paper tissue. For a freezing step, which was important for efficient cell lysis, the plate was stored at -20 °C overnight or -60 °C for 5 minutes. For the CyQUANT assay component B (20 x cell lysis buffer) was diluted 1:20 in ddH_2O and component A (GR dye stock) was diluted 1:200 in 1 x component B for a detection range up to 100000 cells. Then 50 µl of the component A/B mixture was added per well of the thawed XF96 plate. After 5 min dark adaption, the fluorescence was measured at 480 nm excitation and 520 nm emission in a Tecan reader. Data analysis was performed using Microsoft Excel.

7.1.10. Cell proliferation assay

For cell proliferation assay, NPCs were seeded with a concentration of 5,000 cells per well on Matrigel-coated black-wall clear-bottom 96 well-plates containing 100 µl SM+ medium. Each plate was marked as either Day 0, Day 2, Day 4, or Day 7 plate. After 4 hours, the cells in Day 0 plate were washed 2x with PBS - 0.05% Tween, and then fixed with 4% Paraformaldehyde (PFA, Thermo Fischer) for 15 min, followed by 2x washings with PBS. The other plates were fixed on day 2, 4, and 7 post-seeding with the same procedure. The fixed plates were kept at 4^{o}C until all plates were ready for quantification. Quantification of cells was done through Hoechst (8.1 µM) staining. TECAN plate-reader (Infinite M200, Thermo Fischer Scientific) was used to quantify Hoechst fluorescence in the wells, and the data were analyzed in relation to the value of Day 0 plate.

7.1.11. Mycoplasma test

For the PCR based test of mycoplasma, 9 primers (6 forward, 3 reverse) are used to amplify the 6 most common mycoplasma strains. Supernatant directly taken from the well is used as PCR template, without further isolation of mycoplasma DNA. Supernatant from a contaminated cell line is used as a positive control (provided by AG Kühn). Table 7.1.10 shows the protocol for one reaction.

Mycoplasma-PCR				
Reagent	**Volume [µl]**	**Temperature [°C]**	**Time [sec]**	
Supernatant, media	2	95	180	
10x dream tag buffer	2,5	95	20	x29 times
5mM dNTPs	0,5	65	30	
Primer mix	0,5	72	60	
Dream Taq DNA polymerase	0,25	72	240	
Nuclease-free water	19,25	16	pause	

Table 7.1.10. The PCR protocol for mycoplasma test

7.2. Molecular biology

7.2.1. TALEN vector construction

First desired constructs are HR+TALE1+TALE2 to correct the mutation, and the second vector is HR+TALE1+TALE3 to introduce the mutation. The sequence of the strings and the vector are listed in supplementary data. Strings and the vectors were digested at specific restrictions sites and were ligated into amplified and purified HR vectors like seen in the scheme (Figure 7.2.1.).

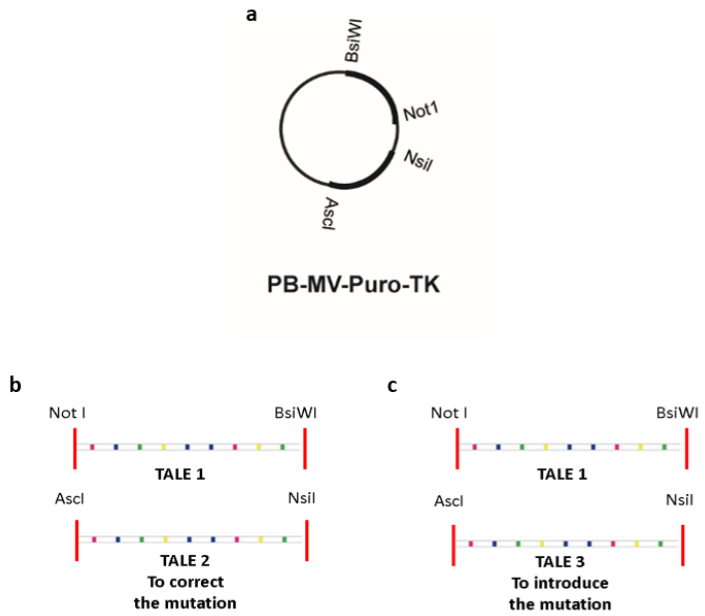

Figure 7.2.1.: The scheme of TALEN constructs for SVS1A

a*, The HR vector diagram showing where the restriction sites are.* ***d-e,*** *Diagrammatic summary how to clone homologous arms into the HR-vector for introducing TALEN mediated genome corrections/mutations with the restriction sites Not I, BsiWI, AscI, and NsiI.*

The first step was the ligation of string TALE1 into the HR vector and to do minipreps. Picked clones were subjected to test digestion with NotI and BsiWI to understand if the ligation was correct. The expected band size for TALE1 string is around 500 bp, and the HR vector is around 5800 bp. Clone 4 has the right expected band sizes after the digestion with respective enzymes, whereas other clones seem to have mismatched bands (Suppl. Figure 7.2.1. a). Non-digested HR vector was loaded as a control.

Once HR vector+TALE1, TALE2, and TALE3 were digested with AscI and NsiI enzymes and followed by ligation steps. *E.coli* were transfected with ligated vectors, and the mini-preps were prepared. The clones were picked the next day. The test digestion was done to check if HR vector + TALE 1 + TALE2 and HR vector + TALE 1 + TALE 3 have the expected band sizes (Suppl. Figure 7.2.1. b). TALE2 and TALE3 have lower band sizes because they do not have TALE 1 string integrated. After the test digestion, the bands were extracted from the gels and sent for Sanger sequencing with M13 reverse primer, which is listed in supplementary data. The HR Vector + TALE 1 + TALE 2 and HR Vector + TALE 1 + TALE 3 were confirmed to have the right sequences.

7.2.2. CRISPR/Cas9 genome editing

We prepared CRISPR/eSpCas9 sgRNA plasmid for SVS1C following a published protocol. We first designed a sgRNA sequence (within 10 nucleotides from the target site corresponding to A>G mutation using CRISPR (http://crispor.tefor.net/). We annealed the oligomer pairs and cloned them into pU6(BbsI)-CAG-Cas9-venus-bpA(#1) plasmid (Addgene ID 86986) carrying eSpCas9 variant from eSpCas9(1.1) plasmid (Addgene ID 71814) with reduced off-target effects and improved on-target cleavage (Sabir, et al., 2016). The PCR product of the eSpCas9 variant was sub-cloned into a CAG expression plasmid (Addgene ID 86986). DNA was submitted for Sanger sequencing to confirm correct sgRNA sequence. We designed 149 nt single-strand oligo-deoxynucleotide (ssODN) HDR template to convert G>A (mutation correction) with two silent mutations within sgRNA sequence in the proximity to the protospacer adjacent motif (PAM) site (3 and 6 nt downstream) to prevent recurrent Cas9 cutting in edited cells. To improve the recombination of ssODN with eCas9-induced double-strand break via single-stranded template repair (SSTR) and ssODN, we applied ectopic expression of RAD52 and of a dominant-negative subfragment of 53BP1 (dn53BP1), which may counteract the endogenous 53BP1 (Paulsen et al., 2017). Plasmids encoding components of the DNA repair pathways (human RAD52, and mouse dn53BP1) were kindly obtained from Bruna Paulsen. For the generation of dn53BP1, a fragment containing the Tudor domain (residues 1,221 to 1,718 of mouse 53BP1) was sub-cloned, and the PCR products of the genes were then sub-cloned into a

CAG expression plasmid and sequenced. Transient transfection of plasmids was carried out in SVS1C grown in feeder-free conditions in StemMACS™ iPS-Brew XF culture media (MACS Miltenyi Biotec) in a 6-cell culture plate. One day before transfection, we dissociated the cells using Accutase and seeded ~ 1 x 105 cells per well of a pre-coated 6-well plate as single cells or small clumps. Cell was cultivated in fresh medium containing 10 mM Y-27632 overnight. Lipofection was performed using Lipofectamine 3000 Kit (Thermo Fisher Scientific) according to the manufacturer's protocol. The plasmids were diluted up to 2 mg DNA in 125 ml of Opti-MEM reduced serum medium and added as the DNA-lipid complex to one well of a 6-well plate in a dropwise manner with the addition of 5 mM Y-27632 to the culture medium for 24 h. The medium was changed on the following da, and the cells were kept 48h in culture until fluorescence-activated cell sorting (FACS). Dissociated cells using Accutase for 5 min were washed and resuspended with DPBS. Then, cells were filtered using Falcon polystyrene test tubes (#352235, Corning) and transferred to Falcon polypropylene test tubes (#352063, Corning). Sorting was performed using BD FACSAria III at the MDC FACS Facility. Sorted cells were suspended in recovery mTeSR™ medium (STEMCELL Technologies) with 1X Penicillin-Streptomycin (P/S) (Gemini Bio-products) and ROCK inhibitor and plated onto 6-well plates (5K cells/well). Growing single-cell-derived colonies were transferred from 6-well plates to one well each of 24-well plate and maintained until the colony grew big enough to be partially harvested for DNA isolation using Phire Animal Tissue Direct PCR Kit (Thermo Fisher Scientific) according to manufacturer's protocol. PCR reaction was carried out using 100 ng gDNA in 50 ml with Phusion High-Fidelity DNA Taq polymerase (Thermo Fisher Scientific) according to manufacturer's instructions and annealing temperature 61˚C. For Sanger sequencing or fragment analysis, the PCR products were gel purified using, e.g. the Wizard SV Gel and PCR Clean-Up System (Promega). *SURF1* gene product was amplified with SVS1C primers (product length 550 nt). For primer induced restriction analysis (PIRA) the PCR product of 550 nt was cut by *Bbs1* (NEB #R3539) into 221+324 nt fragments only in the presence of the mutation c.769G>A. PCR products were submitted to LGC https://www.lgcgroup.com) for Sanger sequencing. Primer sequences, gRNA sequences, and HDR sequence are reported in section 6.2.4. Samples sent for sequencing contain 11 µl of DNA sample (100 ng / µl) and S1C forward or reverse primer (10 µM / µl).

Samples		1	2	3	4	5
	Stock Concentration	sgRNA +HDR	sgRNA +HDR	sgRNA +HDR	sgRNA +HDR	sgRNA +HDR
Confluency per well (6wp)	-	90%	90%	90%	90%	90%
OptiMEM A [µl]	-	125	125	125	125	125
HDR ssODN [µl]	1.5 µg/µl	3	3	3	3	3
Plasmid #1 [µl]	1.3 µg/µl	2	2	2	2	2
Plasmid #2 [µl]	0.9 µg/µl	1.5	1.5	1.5	1.5	1.5
Plasmid #3 [µl]	1.5 µg/µl	1	1	1	1	1
p 3000 [µl]	-	3.75	3.75	3.75	3.75	3.75
OptiMEM B [µl]	-	125	125	125	125	125
Lipofect3000 [µl]	-	5	5	5	5	5

Table 7.2.1.: The transfection amounts for CRISPR/Cas9

7.2.3. RNA-sequencing

PolyA mRNA-seq was carried out for the samples: DA 4w of H1, XM001, SVS1A, SVS1C and DA 8w of H1, XM001, SVS1A, SVS1C (each done in biological triplicate). Total RNA was isolated using the Qiagen RNeasy Mini Kit (#74106, Qiagen) and quality-checked by Nanodrop analysis (Nanodrop Technologies). mRNA-seq was performed by BGI using an oligo dT selection (mRNA enrichment) strategy with oligo dT beads to select mRNA with poly A tail using BGISEQ-500 with DNB seq technology. Ribo-zero total RNA-seq was carried out for the samples: DA 4w of SVS1C and SVS1C.C and DA 8w of SVS1C and SVS1C.C (each done in biological triplicate). 500 ng of total RNA were rRNA depleted using RNase H-based protocol. Briefly, total RNA was mixed with 1 µg of a DNA oligonucleotide pool comprising 50-nt long oligonucleotide mix covering the reverse complement of the entire length of each mouse rRNA (28S rRNA, 18S rRNA, 16S rRNA, 5.8S rRNA, 5S rRNA, 12S rRNA), incubated with 1U of RNase H (Hybridase Thermostable RNase H, Epicentre), purified using RNA Cleanup XP beads (Agencourt), DNase treated using TURBO DNase rigorous treatment protocol (Thermo Fisher Scientific) and purified again with RNA Cleanup XP beads. rRNA-depleted RNA samples were further fragmented and processed into strand-specific cDNA libraries using TruSeq Stranded Total LT Sample Prep Kit (Illumina) and sequenced on NextSeq 500, High Output Kit, 1x 150 cycles. Raw sequencing reads were mapped to the human genome (GRCh38 assembly) using STAR (version 2.6.0c) aligner (Dobin et al., 2013). We used the default settings, except --outFilterMismatchNoverLmax, which was set to 0.05. Reads were counted using the htseq-count tool, version 0.9.1 (Anders et al., 2015), with

gene annotation from GENCODE release 27 (Frankish et al., 2019). Differential gene expression analysis was performed using the DESeq2 (version 1.20.00) R package (Love et al., 2014). For mRNA-seq, read counts for genes expressed in H1, XM001, SVS1A, and SVS1C were summed up across the triplicates. SVS1A and SVS1C were treated as disease replicates, and compared to H1 and XM001. For ribozero sequencing, SVS1C was compared to the SVS1C.C. All genes with the adjusted P-value lower than 0.05 were considered differentially expressed. Functional enrichment analysis was done using the gProfileR R package (Reimand et al., 2016), version 0.6.6, with default settings. All expressed genes were used as background. All R scripts are available on request. All RNA-seq data have been deposited in the GEO database (Accession number GSEEI26360).

7.2.4. qRT-PCR analyses

Cells were harvested, washed with PBS and pelletized by centrifugation. Total RNA was extracted using the RNeasy Mini Kit (Qiagen) according to the protocol “RNA-isolation from Animal Cells.” The RNA concentration was measured by NanoDrop (Thermo Scientific). Isolated RNA was used for qRT-PCR. For quantitative gene expression analysis cDNA was generated from isolated RNA using the reverse transcriptase M-MLV (Affymetrix/USB). For each sample, 1 µg RNA was diluted in 9 µl with RNase/DNase-free distilled water (Gibco) and 1 µl oligo-dT (0.5 µg/µl, 15mer) was added (final volume 10 µl). The mixture was incubated at 72 °C for 5 min and cooled down on the ice. Meanwhile, a master mix for the reverse transcription according to the manufacturer´s guideline. Subsequently, 15 µl of this master mix was added to 10 µl RNA/oligo-dT sample and incubated at 42 °C for 1 h, followed by inactivation of the enzyme at 65 °C for 10 min. The resulting cDNA was diluted 1:10 in nuclease-free water and stored at −20 °C. Gene expression analysis was performed by quantitative real-time RT-PCR (qPCR) using SYBR Green PCR Master Mix and the ViiA™ 7 Real-Time PCR System (Applied Biosystems). For each target gene, cDNA samples and negative controls were measured in triplicates using 384-Well Optical Reaction Plates (Applied Biosystems). Relative transcript levels of each gene were calculated based on the 2− ΔΔCT methods. Data were normalized to the housekeeping gene ACTB and are presented as mean LOG2 ratios in relation to control cell lines.

Master mix for RT	
Reagent	**Volume [µl]**
dNTP, 25mM	0,5
M-MLV RT	0,1
M-MLV Rxn Buffer	5
distilled water	9,4

Master mix for Rxn	
Reagent	**Volume [µl]**
1,8 ul Fwd primer (0,3uM)	1,8
1,8 ul Rev primer (0,3uM)	1,8
6,0 ul SYBR Green PCR mix	6
0,4 ul distilled water	0,4

Table 7.2.4.: Master mixes for the reverse transcription

7.2.5. Primer induced restriction analysis

For primer induced restriction analysis (PIRA) of S1A, the PCR product of 141 bp was cut by SmaI (NEB #R0141S) into 23+118 bp in the presence of c.530T>G mutation. For PIRA of S1C, the PCR product of 437 bp was cut by *Ava II* (NEB #R0153S) into 292+145 bp fragments only in the presence of the mutation c.769G>A. For PIRA of SVS1C, the PCR product of 550 bp was cut by *Bbs1* (NEB #R3539) into 221+324 bp fragments only in the presence of the mutation c.769G>A. Primer sequences are reported in Table 6.2.4.

Protocol calculation for one reaction	
Components	**Volume**
GC Buffer	10 µl
dNTPs (10 µM)	1 µl
Primer Fwd (10 µM)	2,5 µl
Primer Rev (10 µM)	2,5 µl
DNA Template	400 ng
DMSO	1,5 µl
Phusion Taq	0,25 µl
$MgCl_2$	0,5 µl

Protocol for 35 cycles		
Temperature	**Time in [sec]**	**Nr of cycles**
98°C	30	1x
98°C	10	35x
61°C	30	
72°C	30	
72°C	600	1x
4°C	hold	1x

Autoclaved water	30,75 µl

Table 7.2.5.: The protocols for the PCR & PIRA PCR

7.2.6. SURF1 overexpression

SURF1 (amino acid sequence NP_003163.1) (the amino acid sequences is *provided in section 6.2.4.)* and mCitrine expressing lentiviral plasmids were generated using the Gateway™ cloning system (Katzen, 2007). Open reading frames from entry vectors encoding the GFP derivative mCitrine or the SURF1 protein (entry clone id: RZPDo839E0486) were shuttled into a lentiviral destination vector harboring a phosphoglycerate kinase (PGK) promoter (pLenti PGK Neo DEST (w531-1) was a gift from Eric Campeau & Paul Kaufman (Addgene plasmid # 19067; http://n2t.net/addgene: 19067; RRID: Addgene_19067) (Campeau et al., 2009). Lentivirus preparation was performed by the Viral Core Facility of the Charité Berlin as previously described (Lois et al., 2002). In brief, HEK293T cells were co-transfected with 10 µg of shuttle vector, 5 µg of helper plasmids pCMV-dR8.9, and 5 µg of pCMV-VCV-G using X-tremeGENE 9 DNA transfection reagent (Roche Diagnostics). Cell culture supernatant containing the virus was collected after 72 h and filtered for purification. Virus aliquots were flash-frozen in liquid nitrogen and stored at -80°C. NPCs were seeded on 6 well plates at a concentration of approximately 500,000 cells per well. The next day, cells were transduced with mCitrine viruses (GFP) or wild-type SURF1 (SURF1-OE) with a titer of 1,85E+08 and 1,32E+08 particles per ml, respectively. One day later, the medium was changed, and NPCs were kept in the incubator for two days to recover. Antibiotic selection was carried out using 500 µg per ml of gentamycin (G418) for 5 days according to killing curves previously performed on NPCs.

Transduction	**Titration**	**Virus concentration**		
	(particle per cell)	**(particle/cell)**	**Volume [µl]**	**Cell number**
smS1C	no			500*10^3
smS1C + mCitrine	1,85E+08	5	13,51	500*10^3
smS1C + SURF1	1,32E+08	5	18,94	500*10^3

Table Figure 7.2.6.: The transduction amounts for lentivirus

7.3. Protein biochemistry

7.3.1. Western blotting

NPCs were lysed in Lysis Buffer (200mM NaCl, 50mM Tris-HCl pH 8.0, 0.05% SDS, 2mM EDTA, 1% NP40, 0.5% sodium deoxycholate supplemented with (100mM NaF, 10µM PMSF, 1:25 EDTA-free protease inhibitor cocktail (Merck), 1:1000 Benzonase (Roche)) for 1 h at 4°C. Protein

concentration was determined using the Pierce™ BCA assay (Thermo Fisher Scientific). 120 µg proteins for each sample were loaded on NuPAGE Novex 4-12% Bis-Tris precast SDS-PAGE gels (ThermoFisher Scientific) and transferred onto Immobilin-FL PVDF membranes (Merck Millipore) by semi-dry transfer. The primary antibodies used were as follows: MT-CO2 (ab110258 Abcam, 1:1,500) and anti-tubulin (Sigma, 1:4,000). Chemiluminescence was measured in a Fujifilm LAS-3000 after the addition of Pierce ECL Western Blotting Substrate (Thermo Fisher Scientific).

7.3.2. COX enzyme activity and histochemistry

The activities of cytochrome c oxidase (COX) for complex IV and of succinate dehydrogenase (SDH) for complex II were assessed using a colorimetric assay on iPSC-derived NPCs. Enzyme histochemical stains of cytochrome C oxidase and succinate dehydrogenase were performed using standard procedures (Dubowitz et al., 2013). After gentle centrifugation, NPCs from SVS1C and genetically corrected SVS1C.C (clones 3p and 3bb) were carefully transferred on tissue tek on a cork plate and shock frozen in isopentane pre-cooled in liquid nitrogen. 10 µm thick cryosections of these cells were stained by SDH, COX, and combined COX-SDH.

7.3.3. Magnetic-Activated Cell sorting

We performed magnetic-activated cell sorting (MACs) in order to quantify A2B5-positive cells, NCAM-positive cells, GLAST-positive cells, CD11b-positive cells, and O4-positive cells from 4w and 8w DA neuronal cultures. We used A2B5-APC antibody (130-093-582; Miltenyi Biotec), GLAST (ACSA-1)-APC antibody (130-095-814; Miltenyi Biotec), PSA-NCAM-PE antibody (130–093-274; Miltenyi Biotec), CD11b-VioBlue antibody (130–095-822; Miltenyi Biotec), and O4-APC antibody (130–109-153; Miltenyi Biotec), according to the manufacturer's instructions.

7.3.4. Cytokine secretion analysis

The supernatant of the samples used for RNA-Seq (DA 4w of H1, XM001, SVS1A, SVS1C, and DA 8w of H1, XM001, SVS1A, SVS1C) was collected and concentrated with Amicon 10K. The samples were assayed in triplicates using the Pro-inflammatory Panel I (MesoScale Discovery, Gaithersburg, MD, USA) for quantitative measurement of 10 cytokines from a single sample volume of 25 µL using an electrochemiluminescent detection method. The cytokines measured were: interferon (IFN)-γ, interleukin (IL)-1β, IL-2, IL-4, IL-6, IL-8, IL-10, IL-12p70, IL-13, and tumor necrosis factor α (TNFα).

7.4. Microscopic investigation

7.4.1. Transmission electron microscopy

Skeletal muscle and mitochondria biopsy was carried out for patient S1C. Ultrastructural analysis was performed after fixation of the cells in 2.5% glutaraldehyde for 48 hours at 4°C, postfixation in 1% osmium tetroxide, and sample embedding in. Semi-thin sections were used to identify viable and characteristic cells, and respective ultrathin sections were stained with uranyl acetate and lead citrate. A P902 electron microscope (Zeiss, Oberkochem, Germany) was used to analyze the specimens.

7.4.2. High-content analysis

HCA-based quantification of neuronal cells and branch complexity was assessed using the CX7 microscope (Thermo Fisher Scientific). Briefly, NPCs or neurons (at 4 weeks or 8 weeks of differentiation) were split using Accutase and seeded at a density of 10,000 cells/ on Matrigel-coated 96 well plates with black-wall and clear-bottom (Corning). The cells were stained with TUJ1 antibody and counter-stained with Hoechst (see below for details on staining method). The morphological changes of TUJ1-positive cells were quantified using the "Cellomics Neuronal Profiling v3.5 BioApplication" (XTI Infinity High Content Platform, Thermo Fisher Scientific). Hypoxia and drug treatments were conducted O.N. one day before the assay day.

7.4.3. Mitochondrial movement

DA cultures were grown on 35 mm dishes with coated bottom and 1.5 coverslips. 25 nM MitoTrackerRed CMXRos (Thermo Fischer Scientific) was added for 10 min and then replaced with DA culture media. Live-cell imaging recordings were conducted using a spinning disk microscope (CSU-W, Andor/Nikon) which incubating conditions of 37°C with 5% CO2. We used a 40x oil objective, and we imaged the cells every 2 sec. The raw image files were stored as 16-bit in ".nd2" format at 337x337 µm (1024x1024 pixel) at an interval of 2 sec and a total of 200 images per series (total time per series: 6:40 min). The image pre-processing was carried out with Fiji (ImageJ 1.52h) adapted from a previous report (Iaenetti et al., 2016). To compensate for photo-bleaching during the time series, we applied the "Bleach Correction" tool, followed by a top-hat spatial filter to increase gray values of mitochondrial objects. The total mitochondria count was calculated by creating a binary image where the minimum gray value (min) was set to min=Mean+StdDev, and the maximum gray value (max) was set to max= Mean+StdDev+1, where "Mean," and "StdDev" were obtained by using the "Measure" tool. Next, the "watershed" tool was applied to break up large mitochondria networks. A total number of mitochondria was

quantified using the “Analyze Particles” tool with standard setting and a size preference for 8-200 pixel. The moving mitochondria were defined by a particle size of at least 6 pixels that changed location over the time course of 4 frames (=8 seconds). This was accomplished by subtracting the following 4th frame for each frame in the time series (on the top-hat filtered image). Afterward, the subtracted image series was converted into a binary image series. The number of moving mitochondria was similarly counted using the “Analyze Particles” tool with standard setting and a size preference for 6-200 pixel. Finally, the percentage of moving mitochondria per sample was calculated by dividing the average number of moving mitochondria by the average number of total mitochondria, multiplied with 100. The percentage of stationary mitochondria was obtained by the subtraction of moving mitochondria from 100.

7.5. Statistical analysis

Data were analyzed using GraphPad-Prism software (Prism 4.0, GraphPad Software, Inc.) ad R package. Data presentation and respective statistical analysis of each graph are described in the respective figure legends.

8. Supplementary Information

8.1. Supplementary Data

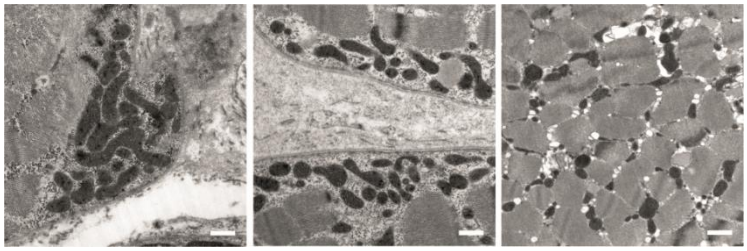

Suppl. Figure 3.1.3: EM images of muscles from S1C patients
Transmission electron microscopy (TEM) image are showing normal mitochondria in muscle biopsy from patient S1C. Scale bar: 500 nm. (Contributions are indicated in section 8.3.).

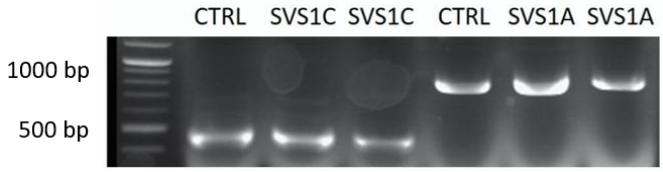

Suppl. Figure 3.2.2.1.: Molecular characterization of iPSCs from LS^{SURF1} patients
PCR products were separated on a 1.5% agarose gel. The expected band sizes for the SVS1C and SVS1A were 550 bps and 800 bps, respectively.

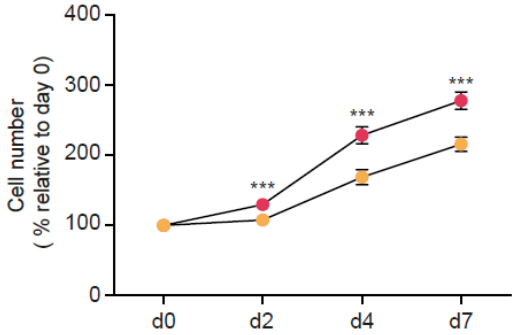

Suppl. Figure 3.4.1.4..: Cellular proliferation assay in NPC cultures of SVS1C isogenic line
*Cellular proliferation assay in NPC cultures from isogenic lines SVS1C and SVS1C.C (mean +/- s.e.m.; n=4 independent experiments; *** p<0.001; Mann-Whitney U test). (Contributions are indicated in section 8.3.).*

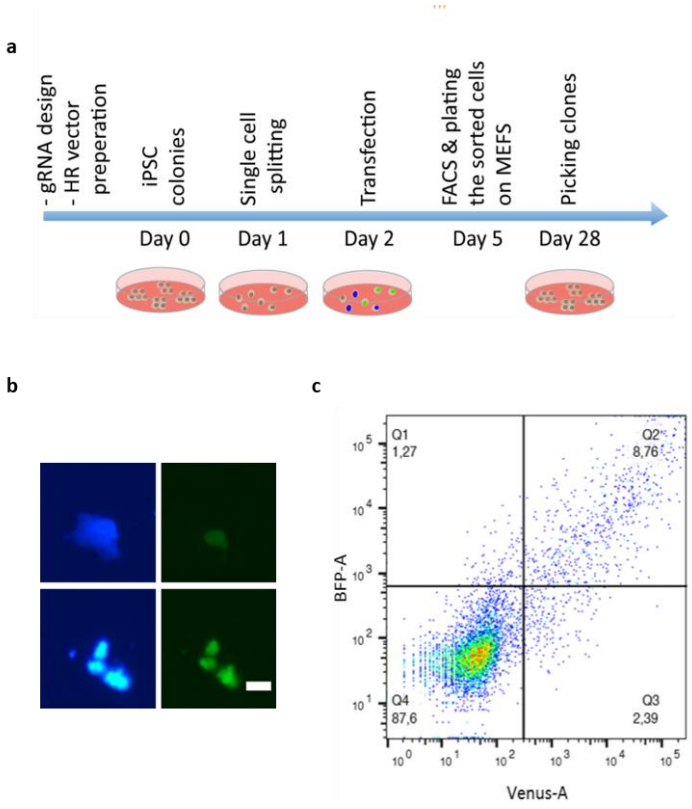

Suppl. Figure 3.3.2.2.: The workflow and screening strategy for CRISPR/ Cas9 corrected clones

a, *The scheme shows the workflow of the CRISPR/Cas9 correction strategy on iPSCs and the microscopic images of single cell-derived iPSC clones. Scale bar: 10 µm.* ***b-c****, The dot plots show the FACS sorted cells in two different channels: Venus and BFP. Q1 shows BFP- positive cells, Q2 shows BFP/Venus-positive cells, Q3 shows Venus-positive cells, and Q4 shows BFP/Venus-negative cells. Each dot represents a cell. Representative transfected double positive single cell images. Scale bar: 10 µm. (Contributions are indicated in section 8.3.).*

			IFN-γ		IL-10		IL-12p70		IL-13		IL-1β		IL-2		IL-4		IL-6		IL-8		TNF-α	
Type	Name	DA	AVG	SD	AVG	SD	AVG	SD	AVG	SD	AVG	SD	AVG	SD	AVG	SD	AVG	SD	AVG	SD	AVG	SD
ES CTRL	H1	4w	0.83	0.22	4.21	3.92	2.44	0.30	65.17	4.80	2.27	0.17	3.59	0.25	0.73	0.08	863.51	150.03	6202.0	30.12	12.46	2.16
ES CTRL	H1	8w	2.55	0.96	1.79	0.34	6.44	0.84	58.56	3.54	3.03	0.46	6.63	3.19	2.79	0.36	2628.1	111.71	6518.5	222.46	10.00	0.49
iPS CTRL	TFBJ	4w	0.01	0.01	1.19	0.02	0.06	0.01	6.28	0.89	0.08	0.04	0.03	0.01	0.05	0.01	13.19	5.44	352.30	183.55	0.18	0.09
iPS CTRL	TFBJ	8w	0.07	0.07	0.48	0.26	0.86	0.29	29.55	8.11	0.63	0.27	0.67	0.49	0.24	0.04	389.15	83.37	5155.0	456.99	3.20	1.84
iPS CTRL	XM001	4w	0.11	0.20	0.40	0.24	0.30	0.24	16.22	0.24	0.18	0.04	0.83	0.21	0.14	0.09	2.86	0.24	2040.6	258.82	1.03	0.31
iPS CTRL	XM001	8w	0.13	0.22	0.20	0.22	0.08	0.09	9.67	2.23	0.21	0.09	0.27	0.08	0.13	0.14	48.30	15.23	829.87	190.68	0.46	0.23
iPS SURF1	SVS1A	4w	0.01	0.00	0.44	0.05	0.07	0.00	8.20	0.93	0.12	0.04	0.68	0.03	0.12	0.02	90.38	15.53	397.69	69.93	0.23	0.11
iPS SURF1	SVS1A	8w	0.03	0.02	0.06	0.04	0.30	0.10	15.21	1.78	0.26	0.09	0.19	0.07	0.17	0.02	282.59	58.47	1961.1	400.20	0.93	0.15
iPS SURF1	SVS1C	4w	0.01	0.00	0.31	0.05	0.01	0.01	1.89	0.49	0.09	0.02	0.05	0.02	0.04	0.01	3.66	1.55	15.86	4.44	0.05	0.04
iPS SURF1	SVS1C	8w	0.01	0.00	0.04	0.18	0.07	0.02	8.89	0.97	0.43	0.32	0.15	0.09	0.04	0.01	35.75	17.09	776.53	57.50	0.79	0.29

Suppl. Table 3.4.2.2.2.: Summary of the values for cytokine profiling in composite cultures of all lines

Table showing how much non-stimulated human astrocytes in culture expressed IFN-y, IL-10, IL-12p70, IL-13, IL-1ß, IL-2, IL-4, IL-6, IL-8, (n=2 independent experiments). Highlighted in red are the cytokines that are significantly detected in non-stimulated DA cultures. Only DA cultures derived from hESC line H1 also show the presence of TNF-alpha. The cytokines IL-13, IL-6, and IL-8 were present in all the samples but were not significantly altered in LS^{SURF1} cultures.

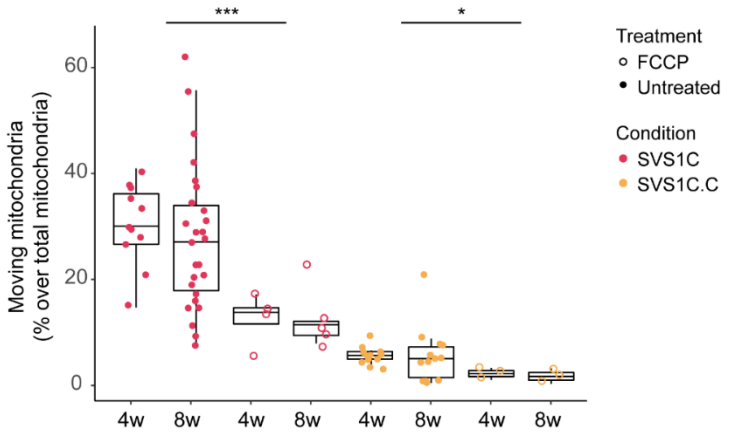

Suppl. Figure 3.4.2.3.3: FCCP treatment decreases the number of motile mitochondria in DA-enriched composite cultures

*Quantification of moving mitochondria in 4w and 8w DA cultures from SVS1C and genetically corrected SVS1C.C. The cells were treated with an uncoupler FCCP (10 um) to induce a decrease in motility of mitochondria (median +/- 95% confidence interval; * p<0.05, *** p<0.001, one way ANOVA followed by Tukey Honestly Significant Differences). (Contributions are indicated in section 8.3.).*

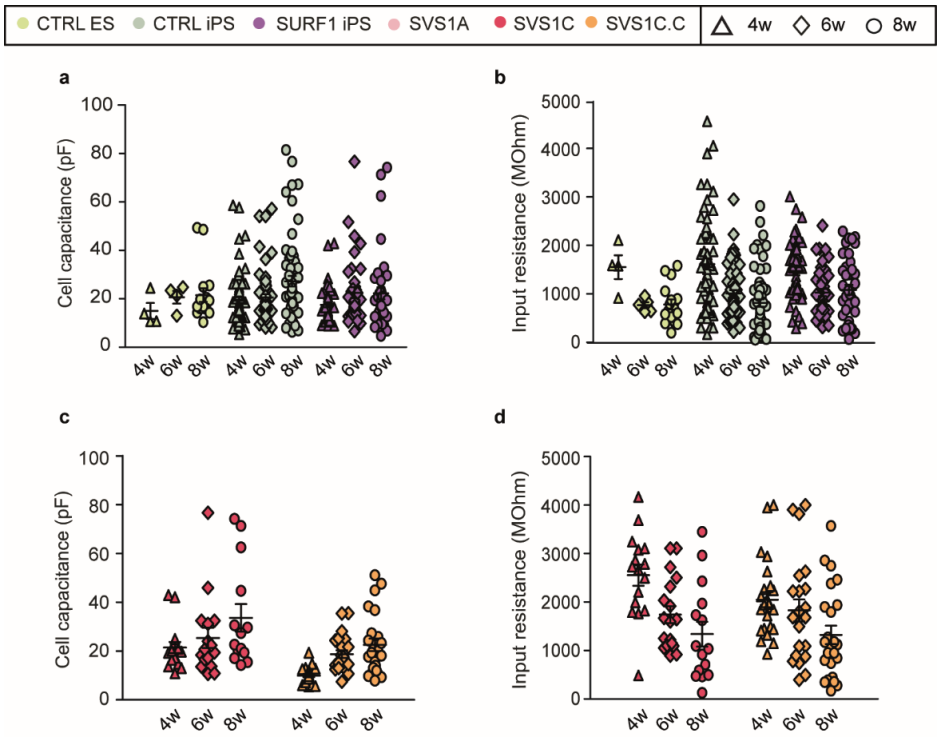

Suppl. Figure 3.4.2.5.: Passive membrane properties of neurons in DA-enriched composite cultures of all lines

Comparison of passive membrane properties. ***a,*** *Cell capacitance (in picofarad, pF) in iPS-derived 4w, 6w and 8w DA neuronal cultures from CTRL ES (H1), CTRL iPS (XM001) and SURF1 patients (SVS1A and SVS1C) and c, in DA neuronal cultures from SVS1C and SVS1C.C (mean +/- s.e.m.; at least n=2 independent experiments).* ***b,*** *Input resistance (in MilliOhm, Mohm) in iPSC-derived 4w, 6w, and 8w DA cultures from CTRL ES (H1), CTRL iPS (XM001) and SURF1 patients (SVS1A and SVS1C) and* ***d,*** *in DA neuronal cultures*

from SVS1C and SVS1C.C (mean +/- s.e.m.; at least n=2 independent experiments). (Contributions are indicated in section 8.3.).

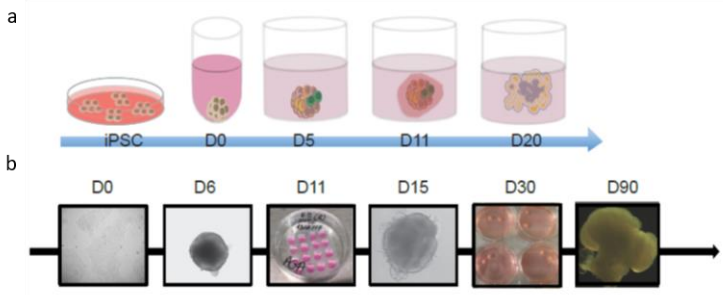

Suppl. Figure 3.5.A.: Derivation of cerebral organoids from iPSCs
a, *Schematic of the generation of cerebral organoids from iPSCs with days information.* ***b,*** *Representative bright field images are showing the transition of the cells undergoing differentiation to three-dimensional structures. (Contributions are indicated in section 8.3.).*

Additional Suppl. Figure 3.5.1.A.

Classically, neurogenesis starts with precursor cell proliferation in neurodevelopmental biology and continues as their capacity to generate new cell types, and if they survive, they will get functionally integrated. Radial glia cell types have different fate choices as they can differentiate into neurons, or they could also give rise to glial cells (Suppl. Figure 3.5.1.A a). This balance is tightly maintained, regulating the neurogenic capacity of the stem cell pool.

In the mammalian system, the first divisions of neural stem cells (NSCs) (NESTIN, SOX2, KI67) are exclusively neurogenic, either giving rise to neural-restricted intermediate progenitors (TBR2, and NCAM) or immature neuron (CALRETININ/CALB) or to mature neurons (NEUN/FOX3). Once the bulk of neurogenesis has occurred, NSCs then become primarily gliogenic at the end of the differentiation phase. Patient-derived organoids show upregulation in genes for proliferating responsible for precursor cell types (Suppl. Figure 3.5.1.A b). Then there is a downregulation of genes responsible for neurogenesis and postmitotic maturation cell types. Interestingly, Calretinin (CALb2) is significantly upregulated, which is a marker of maturing new neuron types. As the neurons get mature enough, they switch the expression of calcium-binding protein calretinin to calbindin (Brandt et al. 2003). This could suggest the presence of pre-mature neuronal types as it has been discussed in the outcome of 2D neuronal experiments. Previous studies done on cell fate specification comes from miR-124, which is a crucial regulator of cell fate determination, stimulating neuronal lineages by suppressing glial lineage-specific genes such as SOX9 and STAT3. STAT3 activity especially is crucial for astrogenesis as it is a direct

transcriptional activator of the astrocytic genes GFAP and S100B. Patient-derived cerebral organoids showed repression of astrogenesis genes compared to the edited line as all of the genes are downregulated (Supp. Figure 3.5.1.A.). (Sloan et al., 201). Overall, patient-derived cerebral organoids show defects in cell fate specification and maturation.

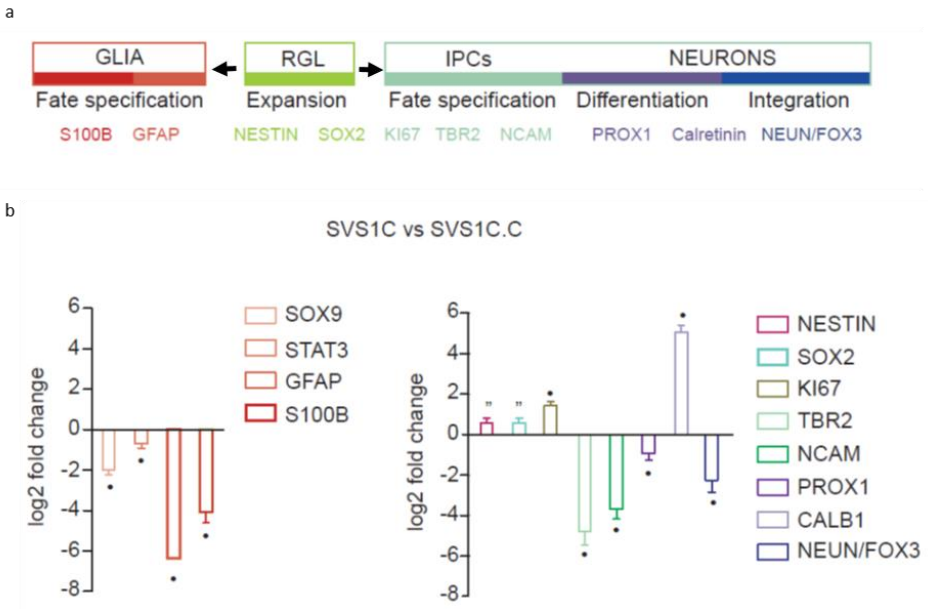

Suppl. Figure 3.5.1.A.: Differentially regulated cell specification genes in cerebral organoids of LS^{SURF1}
a, *Summary of the developmental process of neurogenesis and its relevant markers. Radial ganglion cells (RGL) are either giving rise to intermediate progenitors (IPCs) to neuronal types* ***(right)*** *or giving rise to glial cells* ***(left).*** ***b,*** *Log fold changes (LFC) of genes regulating neurogenesis in iPSC-derived cerebral organoid cultures from SVS1C compared to genetically edited line SVS1C.C (´´ p<0.01, • p<0.0001).*

Additional Suppl. Figure 3.5.1.B.

Two main signaling pathways Wnt/ß-Catenin and SHH-Smoothened regulate the dopaminergic neurogenic niche in the ventral midbrain. Several members of the Wnt family have been shown to regulate distinct aspects of the development of ventral midbrain DA neurons. For instance, Wnt5a regulates the differentiation of DA neurons while WNT1, WNT2, and WNT3 are in favor of generating initial DA progenitors in the ventral midbrain (Andersson et al., 2013). Patient-derived cerebral organoids showed downregulation in WNT5 and no difference in other WNTs, which suggests a defect in the differentiation stage of DA neurons (Figure 3.5.1.B.). Moreover, patient-derived cerebral organoids displayed significant downregulation of mDA progenitors OTX1 and OTX2. FOXA2 and OTX2 regulate the expression of two LIM homeobox transcription factors. LMX1A is required for the specification of mDA neurons. Normally, LMX1A

orchestrates the induction of MSX1, which induces the proneuronal protein expression NGN2 as well as the suppression of NKX6-1 ($LMX1A^{+}/MSX1^{+}/NKX6\text{-}1^{-}$) (Andersson et al., 2006). This network is essential not only for the specification of the DA progenitors but also for the suppression of alternative neural fates in which patient-derived cerebral organoids fail to implement this by looking at the expression profile of the genes. LMX1B, on the other hand, is necessary for the differentiation of mDA progenitors and involved in the maturation of postmitotic DA neurons along with *NURR1 (NR4A2),* and patient-derived organoids showed significantly different expression profile of *LMX1B* and *NURR1* suggesting differentiation defects as well. Additionally, the expression of the *GIRK2* protein is used broadly to identify the A9 midbrain dopamine populations, which was also significantly downregulated. Overall, transcriptomics data suggest *SURF1* mutations cause defects in the specification, differentiation of mDA progenitors, and also maturation stages of midbrain dopaminergic neurons.

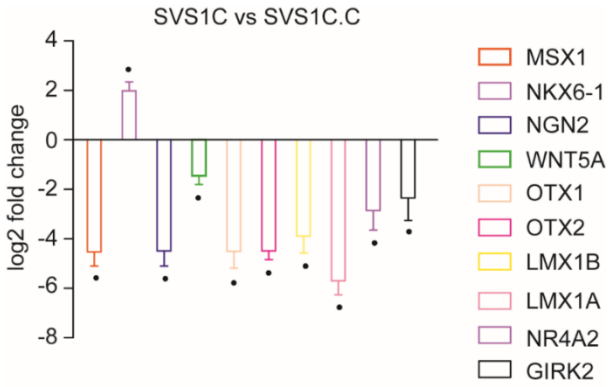

Suppl. Figure 3.5.1.B..: Differentially regulated midbrain dopaminergic genes in cerebral organoids of LS^{SURF1}

Log fold changes (LFC) of genes regulating midbrain dopaminergic (mDA) neuronal development-related genes in iPSC-derived cerebral organoid cultures from SVS1C compared to genetically edited line SVS1C.C (´´ p<0.01, • p<0.0001).

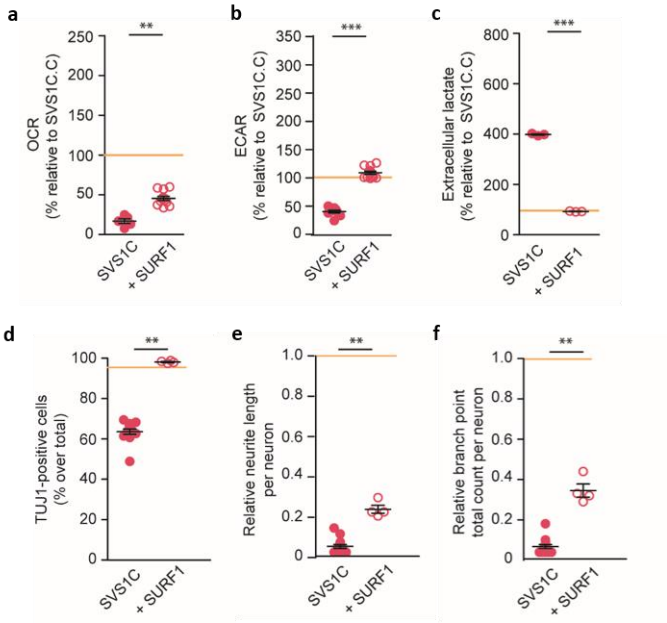

Suppl. Figure 3.7.1: Bioenergetic and neuronal profiling of 8w DA composite cultures of SVS1C upon stably expressing wild-type SURF1

a-e*, Oxygen consumption rate (OCR), extracellular acidification rate (ECAR) and extracellular lactate in 8w DA composite cultures of SVS1C lines stably expressing GFP derivative mCitrine (GFP) or wild-type SURF1 (SURF1-OE).* ***d-f****, High content analysis (HCA)-based quantification of neuronal profiling such as neurite length per neuron* ***(left)*** *and branch point total count* ***(right)*** *based on TUJ1-expressing neurons in NPC cultures of SVS1C upon stably expressing wild-type SURF1. Yellow line is the value for genetically corrected SVS1C.C line (mean +/- s.e.m.; n=2 independent experiments; * p<0.05, ** p<0.01, *** p<0.001; Mann-Whitney U test). (Contributions are indicated in section 8.3.).*

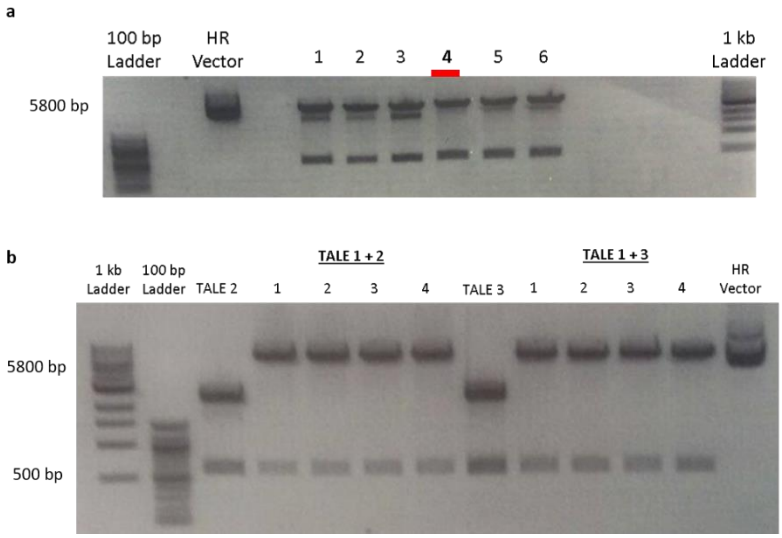

Supp. Figure 7.2.1.: Screening for the right TALEN constructs

a, *TALE 1 and the HR vector were digested at specific restrictions sites and were ligated into amplified and purified HR vectors. Red underlined clone number 4 has the right size band after subjected to test digestion with NotI and BsiWI.* ***b****, Clone 4 is then used to ligate TALE 2 and TALE 3, respectively. The expected band size for TALE2 or TALE 3 strings are around 500 bp, and the HR vector is 5800 bp and TALE1 is 550 bp.*

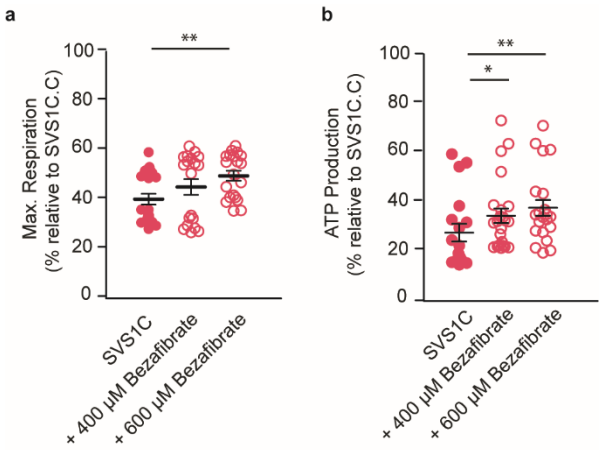

Supp. Figure 3.7.4.: Restored bioenergetic profile in NPC cultures of SVS1C upon Bezafibrate treatment a-b, *Maximal respiration, and ATP production in NPC cultures upon different concentrations of Bezafibrate. Yellow line is the value for genetically corrected SVS1C.C line (mean +/- s.e.m.; n=2 independent experiments; * p<0.05, ** p<0.01, *** p<0.001; Mann-Whitney U test). (Contributions are indicated in section 8.3.).*

8.3. Contributions

*** Figure 3.1.2.** The pedigree of patients´ families and the PCR images were provided by Prof. Markus Schülke (Charité Universitätsmedizin).

*** Figure 3.1.3.** The MRI images of the patients were taken by Prof. Markus Schülke (Charité Universitätsmedizin).

*** Figure 3.2.2.3. / Figure 3.3.3.3.2.** The virtual karyotyping of the generated iPSCs was performed by Stem Cell Core facility, (MDC and BIH, 2017-2018). Dr. Barbara Mlody did the bioinformatics analyses (MDC, 2017-2018).

*** Figure 3.3.** DNA cleavage binding domain was engineered to design TALs by BIH stem cell core facility, (MDC, 2016).

*** Figure 3.3.2.1.** Dr. Pawel Lisowski planned the strategy of the CRISPR/Cas9 (MDC, 2017-2018).

*** Figure 3.3.2.2. / Suppl. Figure 3.3.2.2.** Elisa Massow helped to screen the transfected clones via PIRA PCR, and FACS for the CRISPR/Cas9 experiments during her bachelor thesis (TU Berlin, 2018) under my and Dr. Pawel Lisowski´s supervision. Master student Tobias Hahn helped to find the corrected clones during his master thesis (Hochschule Albstadt-Sigmaringen, 2018).

*** Figure 3.4.1.2.** Celina Kassner gave technical support for Western Blot experiments.

*** Figure 3.4.1.2. / Suppl. Figure 3.1.3.** The TEM images of mitochondria and the assessment of mitochondria enzyme activity were taken/performed by Prof. Werner Stenzel (Charité Universitätsmedizin, 2018-2019).

*** Figure 3.4.1.2.c** The mitochondrial enzyme activity experiments were performed by Prof. Werner Stenzel (Charité – Universitätsmedizin, 2018-2019).

*** Figure 3.4.1.1. / Figure 3.6.** The transcriptome analyses of iPSC-derived 2D and 3D cultures were done by Peter Glazar (BIMSB and MDC, 2018-2019).

*** Figure 3.4.2.3.3.** The analyses of stationary and moving mitochondria in iPSC-derived 2D cultures were done by Dr. Barbara Mlody (MDC, 2018). I did the recordings at Advanced Light Microscopy, MDC and Dr. Anje Sporbert helped me to set it up.

*** Figure of 3.4.2.5.C.** The patch clamp recordings of the iPSC-derived neurons were performed by Dr. Rene Jüttner (MDC, 2015-2018).

*** Figures of 3.5.B.** The derivation of the iPSC-derived 3D cultures was conducted by the collaboration partner Dr. Agnieszka Rybak-Wolf (BIMSB and MDC, 2018-2019). Dr. Agnieszka Rybak-Wolf did the RNA-Seq and the RT-PCR experiments of the iPSC-derived cerebral organoids.

*** Figures in section 3.7. / Suppl. Figure 3.4.1.4.** The experiments of the investigation of treatment strategies and cell proliferation assay were completed by Ummi Ciptasari during her master thesis (Charité Universitätsmedizin, 2019) under my supervision.

*** Figure 7.2.6.** Thanks to Dr. Christopher Secker and to the Viral Core Facility (Charité, 2018) for generating lentiviral particles.

8.4. List of publications

I Lorenz, C., Lesimple, P., Bukowiecki, R., Zink, A., **Inak, G.,** Mlody, B., … Prigione, A. (2017). Human iPSC-Derived Neural Progenitors Are an Effective Drug Discovery Model for Neurological mtDNA Disorders. *Cell Stem Cell*. https://doi.org/10.1016/j.stem.2016.12.013

II **Inak, G.,** Lorenz, C., Lisowski, P., Zink, A., Mlody, B., & Prigione, A. (2017). Concise Review: Induced Pluripotent Stem Cell-Based Drug Discovery for Mitochondrial Disease. *Stem Cells*. https://doi.org/10.1002/stem.2637

III **Inak, G.,** Rybak-Wolf, A., Lisowski, P., Juettner, R., Zink, A., Mlody, B., … Prigione, A. (2019). SURF1 mutations causative of Leigh syndrome impair human neurogenesis. *BioRxiv*. https://doi.org/10.1101/551390

8.4 List of figures

8.5. List of tables

Units

°C	degrees Celcius
µg	microgram
µl	microliter
µM	micromolar
g	gram/gravity
l	litre
M	molarity
mg	milligram
min	minute
ml	millilitre
mM	millimolar
ng	nanogram
nm	nanometer
pmol	picomolar
s	seconds
U	unit
V	volt
kDa	KiloDalton
mmol/l	millimol / liter
Mohm	electrical resistance and conductance
NCP	non collagen protein
ms	millisecond
mm^2	square millimeter
µg	microgram
µl	microliter
µM	micromolar
g gram	gravity
hr/hrs	hour/hours
M	mole
mg	milligram
min	minute
ml	millilitre
mm	millimetre
mM	millimolar
ng	nanogram
nm	nanometer
pmol	picomole
s	second
U	unit
V	volt
kDa	KiloDalton
mmol/l	millimol / liter
NCP	non collagen protein
nt	nucleotide
kb	kilobase
w	weight

V	volt
pA	ampere
mV	millivolt
ms	millisecond
mm2	square millimeter
bp	basepair
U	μmol/min
nt	nucleotide
kb	kilobase
w	weight
V	volt
pA	ampere
mV	millivolt
bp	basepair
U	μmol/min

Abbrevations

2D	Two-dimensional
3D	Three-dimensional
AA	Ascorbic acid
ACTB	Actin Beta
ADHD	Attention deficit hyperactivity disorder
ALDH1L1	Aldehyde Dehydrogenase 1 Family Member L1
AMPA	α-amino-3-hydroxy-5-methyl-4-isoxazolepropionic acid
AQP4	Aquaporin-4
ARX	Aristaless related homeobox
ASD	Autism spectrum disorder
AT3	α-Tocotrienol
ATP	Adenosine triphosphate
Acetly-CoA	Acetly coenzyme A
BDNF	Brain-derived neurotrophic factor
BMP4	Bone morphogenetic protein 4
BSA	Bovine serum albumin
BW	Body weight
CAMKB	Calcium/Calmodulin Dependent Protein Kinase II Beta
CD11b	Integrin a-M
CHIR	GSK-3ß inhibitor
CNS	Central nervous system
CNVs	Copy number variations
COX	Cytochrome C oxidase
CRISPR/Cas9	Clustered regularly interspaced short palindromic repeats
CTIP2	B-cell lymphoma/leukemia 11B
Ca2+	Calcium ions
Cu	Copper
DA	Dopaminergic
DAB	3,3'-Diaminobenzidine
DHLA	Dihydrolipoic acid
DMEM	Dulbecco's Modified Eagle Medium
DMSO	Dimethyl sulfoxide
DNA	Deoxyribonucleic acid
DNMT3B	DNA Methyltransferase 3 Beta
DPPA3	Developmental Pluripotency Associated 3
EBs	Embryoid bodies
ECAR	Extracellular acidification rate
EDTA	Ethylenediaminetetraacetic acid
EMX1	Empty Spiracles Homeobox 1
EN1	Engrailed homebox 1
ESCs	Embryonic stem cells
ETC	Electron transport chain
FACS	Fluorescent activate cell sorter
FAD	Flavin adenine dinucleotide
FBS	fetal bovine serum

FBSN	familial bilateral striatal necrosis
FCCP	Carbonyl cyanide 4-(trifluoromethoxy) phenylhydrazone
FCS	fetal calf serum
FDA	Food and Drug Administration
FGF 8/21	Fibroblast growth factor 8/21
FOXG1	Forkhead box protein G1
FOXA2	Forkhead box a2
GAPDH	Glyceraldehyde 3-phosphate dehydrogenase
GATA3	Gata binding protein3
GDF3	Growth Differentiation Factor 3
GDNF	Glial cell-derived neurotrophic factor
GFAP	Glial fibriallary acidic protein
GFP	Green fluorescent protein
GLAST	GLutamate ASpartate Transporter 1
GRIA4	Glutamate Ionotropic Receptor AMPA Type Subunit 4
GRIN2B	Glutamate [NMDA] receptor subunit epsilon-2,
GSH	gluthatione
GSK	Glycogen synthase kinase
HCA	High-content analysis
HDR	Homologous direct repair
HES5	Hes Family BHLH Transcription Factor 5
I	Current
IFN-y	Interferon gamma
IL	interleukin
K	Potassium
KCN3A / KCNC2	Potassium-channel gene
KCl	Potassium chloride
KD	Knock-down
KLF4	Kruppel Like Factor 4
KO	Knock out
LDHA	Lactate Dehydrogenase A
LDHD	Lactate Dehydrogenase D
LEFTY2	Left-Right Determination Factor 2
LHX2	LIM/homeobox protein
LIN28	Lin-28 Homolog A
LMX1A	LIM Homeobox Transcription Factor 1 Alpha
LMX1B	LIM Homeobox Transcription Factor 1 Beta
LRPPRC	Leucine Rich Pentatricopeptide Repeat Containing
MACS	Magnetic actovated cell sorter
MAOB	Monoamine oxidase b
MAP2	Microtubule associated protein 2
MEAs	Microelectrode array
MEFs	Mouse embryonic fibroblasts
MELAS	Mitochondrial encephalomyopathy, lactic acidosis and stroke-like episodes
MKI76	Proliferation Marker Protein Ki-67
MILS	Maternally inherited Leigh syndrome

MRI	Magnetic resonance imaging
MSX	Msh homeobox 1
MYC	MYC proto-oncogene
Mg2+	Magnesium ions
NAC	N-acetyl-cystein
NADH	Nicotinamide adenine dinucleotide
NADPH	Nicotinamide adenine dinucleotide phosphate
NANOG	Nanog homeobox
NARP	Neurogenic muscle weakness, ataxia and retinosis pigmentosa
NBT	Nitro Blue Tetrazolium
NCAM 1/2	neural cell adhesion molecule 1/2
NDUFA4	COX subunit
NDUSF4	NADH:Ubiquinone Oxidoreductase Subunit S4
NEAA	Non essential amino acids
NEUROD6	Neuronal Differentiation 6
NFIA	Nuclear factor I A
NHEJ	non-homologous end joining
NKX6-1	NK6 Homeobox 1
NMDA	N-Methyl-D-Aspartat
NPCs	neural progenitor cells
NRP1	Neuropilin 1
NTN1	netrin1
NURR1	The Nuclear receptor related 1 protein
Na	Sodium
Nr	Number
O4	Oligodendrocyte
OCR	Oxygen consumption rate
ON	Overnight
OSKM	OCT4, SOX2, KLF4 and c-MYC
OTX2	Orthodenticle Homeobox 2
OXPHOS	Oxidative phosphorylation system
Olig	Oligomycin
PAM	Protospacer adjacent motif
PAX6	Paired box protein
PCA	Principle component analysis
PCR	Polymerase chain reaction
PDHA1	Pyruvate dehydrogenase E1 alpha 1 subunit
PDK	Pyruvate dehydrogenase kinase
PET100	COX chaperone
PFA	Paraformaldehyde
PGC1α	Peroxisome proliferator-activated receptor gamma coactivator 1 alpha
PHOX2B	Paired like homeobox 2B
PIRA PCR	Primer-introduced restriction analysis
POUF51	OCT4 / octamer-binding transcription factor 4
PPAR	Peroxisome proliferator-activated receptors
PSCs	Pluripotent stem cells
Pu	Purmorphamine

Q	Ubiquinone
RC	Respiatory chain
REELN	Reelin
RNA-seq	RNA sequencing
ROS	Reactive oxygen species
RT	Room temperature
Rot	Rotenone
S100ß	S100 calcium-binding protein B
S2R cells	Schnedier S2 cells
SAG	Smoothened agonist
SATB	Special AT-rich sequence
SCL1A3	Glutamate transporter 3
SCN2A / SCN9A	Sodium Voltage-Gated Channel subunits
SCO2	Cytochrome C Oxidase Assembly Protein 2
SDH	Succinate dehydrogenase 2
SEMA	Semaphorin
SFRP2	Specificty protein 2
SHH	Sonic hedhehog
SLIT	Slit guidance ligand
SMA	Spinal muscle atrophy
SMAD9	SMAD Family Member 9
SNAP	Synaptosome Associated Protein
SNP	single-nucleotide-polymorphism
SOX 2/17	SRY-related HMG-box 2/17
SSEA	Stage-specific embryonic antigen
SURF1	Surfeit 1 locus protein
SYN1	Synapsin1
SYP	Synaptophysin
SYT13	Synaptotagmin 13
Shy1	Yeast homolg of human SURF1
T2WI	T2 weighted image
TACO1	Translational Activator of COX I
TAL	Transcription-activator-like
TALE	Transcription activator-like effectors
TALEN	Transcription activator-like effector nucleases
TBR1	T-Box, Brain 1
TEM	Tramsmission electron microscopy
TFAM	Transcription factor A
TFB2M	Transcription Factor B2
TGFβ	Transforming growth factor beta
TGFβR1	Transforming growth factor beta receptor 1
TH	Tyrosine hydroxylase
TNF-a	Tumor necrosis factor alpha
TRA-1-60	Podocalyxin
TTX	Tetrodotoxin
TUJ1	Neuron-specific Class III β-tubulin
USP44	Ubiquitin specific peptidase 44

Vit. C	Vitamin C
WGS	Whole genome sequencing
WNT	Wingless-INT
WT	Wild type
cDNA	Complementary DNA
complex V	ATP Synthase
conc.	Concentration
cyt c	Cytochrome c
dNTPs	Deoxyribonucleotide triphosphates
db-cAMP	N(6),2'-O-dibutyryladenosine 3':5' cyclic monophosphate
dn53BP1	Tumour protein p53-binding protein 1
e.g.	Exempli gratia
gRNA	Guide RNA
hLIF	Human leukemia inhibitory factor
iPSCs	Induced pluripotent stem cells
kif5c	Kinesin family member 5C
mRNA	Messenger RNA
max.	Maximum
mtDNA	Mitochondrial DNA
nDNA	Nuclear DNA
qRT-PCR	Real-time quantitative reverse transcription PCR
sm	Small molecule
smNPCs	Small molecule neural progenitor cells
snph	Syntaphilin
srp4	Specificity protein 4
ssODN	Single-stranded donor oligonucleotides
w	Weeks

References

Agostino, A., Invernizzi, F., Tiveron, C., Fagiolari, G., Prelle, A., Lamantea, E., … Zeviani, M. (2003). Constitutive knockout of Surf1 is associated with high embryonic lethality, mitochondrial disease and cytochrome c oxidase deficiency in mice. *Human Molecular Genetics*.

Anders, S., Pyl, P. T., & Huber, W. (2015). HTSeq-A Python framework to work with high-throughput sequencing data. *Bioinformatics*. https://doi.org/10.1093/bioinformatics/btu638

Andersson, E. R., Salto, C., Villaescusa, J. C., Cajanek, L., Yang, S., Bryjova, L., … Arenas, E. (2013). Wnt5a cooperates with canonical Wnts to generate midbrain dopaminergic neurons in vivo and in stem cells. *Proceedings of the National Academy of Sciences*. https://doi.org/10.1073/pnas.1208524110

Andersson, E., Tryggvason, U., Deng, Q., Friling, S., Alekseenko, Z., Robert, B., … Ericson, J. (2006). Identification of intrinsic determinants of midbrain dopamine neurons. *Cell*. https://doi.org/10.1016/j.cell.2005.10.037

Anguela, X. M., & High, K. A. (2018). Entering the Modern Era of Gene Therapy. *Annual Review of Medicine*. https://doi.org/10.1146/annurev-med-012017-043332

Antonicka, H., Leary, S. C., Guercin, G. H., Agar, J. N., Horvath, R., Kennaway, N. G., … Shoubridge, E. A. (2003). Mutations in COX10 result in a defect in mitochondrial heme A biosynthesis and account for multiple, early-onset clinical phenotypes associated with isolated COX deficiency. *Human Molecular Genetics*, *12*(20), 2693–2702. https://doi.org/10.1093/hmg/ddg284

Arenas, E., Denham, M., & Villaescusa, J. C. (2015). How to make a midbrain dopaminergic neuron. *Development*, *142*(11), 1918–1936. https://doi.org/10.1242/dev.097394

Baden, K. N., Murray, J., Capaldi, R. A., & Guillemin, K. (2007). Early developmental pathology due to cytochrome c oxidase deficiency is revealed by a new zebrafish model. *Journal of Biological Chemistry*. https://doi.org/10.1074/jbc.M703528200

Baertling, F., Rodenburg, R. J., Schaper, J., Smeitink, J. A., Koopman, W. J. H., Mayatepek, E., … Distelmaier, F. (2014). A guide to diagnosis and treatment of Leigh syndrome. *Journal of Neurology, Neurosurgery and Psychiatry*. https://doi.org/10.1136/jnnp-2012-304426

Balsa, E., Marco, R., Perales-Clemente, E., Szklarczyk, R., Calvo, E., Landázuri, M. O., & Enríquez, J. A. (2012). NDUFA4 is a subunit of complex IV of the mammalian electron transport chain. *Cell Metabolism*, *16*(3), 378–386. https://doi.org/10.1016/j.cmet.2012.07.015

Ban, H., Nishishita, N., Fusaki, N., Tabata, T., Saeki, K., Shikamura, M., … Nishikawa, S.-I. (2011). Efficient generation of transgene-free human induced pluripotent stem cells (iPSCs) by temperature-sensitive Sendai virus vectors. *Proceedings of the National Academy of Sciences of the United States of America*. https://doi.org/10.1073/pnas.1103509108

Barrientos, A., Gouget, K., Horn, D., Soto, I. C., & Fontanesi, F. (2009). Suppression mechanisms of COX assembly defects in yeast and human: Insights into the COX assembly process. *Biochimica et Biophysica Acta - Molecular Cell Research*. https://doi.org/10.1016/j.bbamcr.2008.05.003

Bastin, J., Aubey, F., Rötig, A., Munnich, A., & Djouadi, F. (2008). Activation of peroxisome proliferator-activated receptor pathway stimulates the mitochondrial respiratory chain and can correct deficiencies in patients' cells lacking its components. *Journal of Clinical Endocrinology and Metabolism*. https://doi.org/10.1210/jc.2007-1701

Beckervordersandforth, R., Ebert, B., Schäffner, I., Moss, J., Fiebig, C., Shin, J., … Lie, D. C. (2017). Role of Mitochondrial Metabolism in the Control of Early Lineage Progression and Aging Phenotypes in Adult Hippocampal Neurogenesis. *Neuron*. https://doi.org/10.1016/j.neuron.2016.12.017

Bell, S., Maussion, G., Jefri, M., Peng, H., Theroux, J. F., Silveira, H., … Ernst, C. (2018). Disruption of GRIN2B Impairs Differentiation in Human Neurons. *Stem Cell Reports*. https://doi.org/10.1016/j.stemcr.2018.05.018

Ben Haim, L., & Rowitch, D. H. (2016). Functional diversity of astrocytes in neural circuit regulation. *Nature Reviews Neuroscience*, *18*(1), 31–41. https://doi.org/10.1038/nrn.2016.159

Bénit, P., El-Khoury, R., Schiff, M., Sainsard-Chanet, A., & Rustin, P. (2010). Genetic background influences mitochondrial function: modeling mitochondrial disease for therapeutic development. *Trends in Molecular Medicine*. https://doi.org/10.1016/j.molmed.2010.03.001

Böhm, M., Pronicka, E., Karczmarewicz, E., Pronicki, M., Piekutowska-Abramczuk, D., Sykut-Cegielska, J., … Zeman, J. (2006). Retrospective, multicentric study of 180 children with cytochrome c oxidase deficiency. *Pediatric Research*, *59*(1), 21–26. https://doi.org/10.1203/01.pdr.0000190572.68191.13

Brandt, M. D., Jessberger, S., Steiner, B., Kronenberg, G., Reuter, K., Bick-Sander, A., … Kempermann, G. (2003). Transient calretinin expression defines early postmitotic step of neuronal differentiation in adult hippocampal neurogenesis of mice. *Molecular and Cellular Neuroscience*, *24*(3), 603–613. https://doi.org/10.1016/S1044-7431(03)00207-0

Brandt, M. D., Jessberger, S., Steiner, B., Kronenberg, G., Reuter, K., Bick-Sander, A., … Kempermann, G. (2003). Transient calretinin expression defines early postmitotic step of neuronal differentiation in adult hippocampal neurogenesis of mice. *Molecular and Cellular Neuroscience*. https://doi.org/10.1016/S1044-7431(03)00207-0

Bugiani, M., Tiranti, V., Farina, L., Uziel, G., & Zeviani, M. (2005). Novel mutations in COX15 in a long surviving Leigh syndrome patient with cytochrome c oxidase deficiency. *Journal of Medical Genetics*, *42*(5), 10–13. https://doi.org/10.1136/jmg.2004.029926

Candelario, K. M., Shuttleworth, C. W., & Cunningham, L. A. (2013). Neural stem/progenitor cells display a low requirement for oxidative metabolism independent of hypoxia inducible factor-1alpha expression. *Journal of Neurochemistry*. https://doi.org/10.1111/jnc.12204

Capa, R. A., An, L. D. I., & Buist, D. N. R. M. (1990). *Isoforms of Mammalian Cytochrome c Oxidase : 28*(5).

Cerar, L. . (2017). Outcome of ELBW infants-one country experience. *Journal of Perinatal Medicine*, *45*(Supplement 2), 145. https://doi.org/10.1146/annurev.genet.39.110304.095751.A

Cerutti, R., Pirinen, E., Lamperti, C., Marchet, S., Sauve, A. A., Li, W., … Zeviani, M. (2014). NAD + -dependent activation of Sirt1 corrects the phenotype in a mouse model of mitochondrial disease. *Cell Metabolism*. https://doi.org/10.1016/j.cmet.2014.04.001

Chang, D. T. W., Honick, A. S., & Reynolds, I. J. (2006). Mitochondrial Trafficking to Synapses in Cultured Primary Cortical Neurons. *Journal of Neuroscience*, *26*(26), 7035–7045. https://doi.org/10.1523/JNEUROSCI.1012-06.2006

Chen, Y., & Sheng, Z. H. (2013). Kinesin-1-syntaphilin coupling mediates activity-dependent regulation of axonal mitochondrial transport. *Journal of Cell Biology*, *202*(2), 351–364. https://doi.org/10.1083/jcb.201302040

Chen, Y., & Sheng, Z. H. (2013). Kinesin-1-syntaphilin coupling mediates activity-dependent regulation of axonal mitochondrial transport. *Journal of Cell Biology*. https://doi.org/10.1083/jcb.201302040

Cho, D.-H., Nakamura, T., Fang, J., Cieplak, P., Godzik, A., Gu, Z., & Lipton, S. A. (2009). S-nitrosylation of Drp1 mediates beta-amyloid-related mitochondrial fission and neuronal injury. *Science (New York, N.Y.)*. https://doi.org/10.1126/science.1171091

Cho, Y. M., Kwon, S., Pak, Y. K., Seol, H. W., Choi, Y. M., Park, D. J., … Lee, H. K. (2006). Dynamic changes in mitochondrial biogenesis and antioxidant enzymes during the spontaneous differentiation of human embryonic stem cells. *Biochemical and Biophysical Research Communications*. https://doi.org/10.1016/j.bbrc.2006.08.020

Choi, H. W., Kim, J. H., Chung, M. K., Hong, Y. J., Jang, H. S., Seo, B. J., … Do, J. T. (2015). Mitochondrial and metabolic remodeling during reprogramming and differentiation of the reprogrammed cells. *Stem Cells and Development*. https://doi.org/10.1089/scd.2014.0561

Cogliati, S., Enriquez, J. A., & Scorrano, L. (2016). Mitochondrial Cristae: Where Beauty Meets Functionality. *Trends in Biochemical Sciences*, *41*(3), 261–273. https://doi.org/10.1016/j.tibs.2016.01.001

Conditions, G. (2013). *Leigh syndrome - Genetics Home Reference*. Retrieved from http://ghr.nlm.nih.gov/condition/leigh-syndrome

Dalmonte, M. E., Forte, E., Genova, M. L., Giuffrè, A., Sarti, P., & Lenaz, G. (2009). Control of Respiration by Cytochrome c Oxidase in Intact Cells . *Journal of Biological Chemistry*, *284*(47), 32331–32335. https://doi.org/10.1074/jbc.m109.050146

Da-Rè, C., Von Stockum, S., Biscontin, A., Millino, C., Cisotto, P., Zordan, M. A., … Costa, R. (2014). Leigh Syndrome in Drosophila melanogaster morphological and biochemical characterization of Surf1 post-transcriptional silencing. *Journal of Biological Chemistry*. https://doi.org/10.1074/jbc.M114.602938

Darin, N., Oldfors, A., Moslemi, A. R., Holme, E., & Tulinius, M. (2001). The incidence of mitochondrial encephalomyopathies in childhood: Clinical features and morphological, biochemical, and DNA abnormalities. *Annals of Neurology*, *49*(3), 377–383. https://doi.org/10.1002/ana.75

Debray, F. G., Morin, C., Janvier, A., Villeneuve, J., Maranda, B., Laframboise, R., … Mitchell, G. A. (2011). LRPPRC mutations cause a phenotypically distinct form of Leigh syndrome with cytochrome c oxidase deficiency. *Journal of Medical Genetics*. https://doi.org/10.1136/jmg.2010.081976

Dell'Agnello, C., Leo, S., Agostino, A., Szabadkai, G., Tiveron, C. C., Zulian, A. A., … Zeviani, M. (2007). Increased longevity and refractoriness to Ca2+-dependent neurodegeneration in Surf1 knockout mice. *Human Molecular Genetics*. https://doi.org/10.1093/hmg/ddl477

Di Bonito, M., Studer, M., & Puelles, L. (2017). Nuclear derivatives and axonal projections originating from rhombomere 4 in the mouse hindbrain. *Brain Structure and Function*. https://doi.org/10.1007/s00429-017-1416-0

Di Meo, I., Marchet, S., Lamperti, C., Zeviani, M., & Viscomi, C. (2017). AAV9-based gene therapy partially ameliorates the clinical phenotype of a mouse model of Leigh syndrome. *Gene Therapy*. https://doi.org/10.1038/gt.2017.53

Diaz, F. (2010). Cytochrome c oxidase deficiency: Patients and animal models. *Biochimica et Biophysica Acta - Molecular Basis of Disease*. https://doi.org/10.1016/j.bbadis.2009.07.013

Differentiation, N., Meyers, E. A., & Kessler, J. A. (2018). *TGF- b Family Signaling in Neural and and Function*. 1–26.

Dimauro, S., & Schon, E. A. (2003). *Mitochondrial Respiratory-Chain Diseases*. 2656–2668.

Dobin, A., Davis, C. A., Schlesinger, F., Drenkow, J., Zaleski, C., Jha, S., … Gingeras, T. R. (2013). STAR: Ultrafast universal RNA-seq aligner. *Bioinformatics*. https://doi.org/10.1093/bioinformatics/bts635

Dogan, S. A., Cerutti, R., Benincá, C., Brea-Calvo, G., Jacobs, H. T., Zeviani, M., … Viscomi, C. (2018). Perturbed Redox Signaling Exacerbates a Mitochondrial Myopathy. *Cell Metabolism*. https://doi.org/10.1016/j.cmet.2018.07.012

Dominici, C., Moreno-Bravo, J. A., Puiggros, S. R., Rappeneau, Q., Rama, N., Vieugue, P., … Chédotal, A. (2017). Floor-plate-derived netrin-1 is dispensable for commissural axon guidance. *Nature*. https://doi.org/10.1038/nature22331

Dostert, Nicolas; Roque, Jose; Cano, Asunción; La Torre, M; Weigend, M. (2012). *Hoja botánica : Algarrobo Prosopis pallida (Humb. & Bonpl. ex Willd.) Kunth*. *46*(6), 50–59. https://doi.org/10.1016/j.freeradbiomed.2008.12.018.Vitamin

Fang, D., Qing, Y., Yan, S., Chen, D., & Yan, S. S. Du. (2016). Development and Dynamic Regulation of Mitochondrial Network in Human Midbrain Dopaminergic Neurons Differentiated from iPSCs. *Stem Cell Reports*, *7*(4), 678–692. https://doi.org/10.1016/j.stemcr.2016.08.014

Feigin, I., & Kim, H. S. (1977). Subacute necrotizing encephalomyelopathy in a neonatal infant. *Journal of Neuropathology and Experimental Neurology*, *36*(2), 364–372. https://doi.org/10.1097/00005072-197703000-00010

Ferrari, M., Jain, I. H., Goldberger, O., Rezoagli, E., Thoonen, R., Cheng, K.-H., … Zapol, W. M. (2017). Hypoxia treatment reverses neurodegenerative disease in a mouse model of Leigh syndrome. *Proceedings of the National Academy of Sciences*. https://doi.org/10.1073/pnas.1621511114

Frankish, A., Diekhans, M., Ferreira, A. M., Johnson, R., Jungreis, I., Loveland, J., … Flicek, P. (2019). GENCODE reference annotation for the human and mouse genomes. *Nucleic Acids Research*. https://doi.org/10.1093/nar/gky955

Fusaki, N., Ban, H., Nishiyama, A., Saeki, K., & Hasegawa, M. (2009). Efficient induction of transgene-free human pluripotent stem cells using a vector based on Sendai virus, an RNA virus that does not integrate into the host genome. *Proceedings of the Japan Academy. Series B, Physical and Biological Sciences*.

Garone, C., & Viscomi, C. (2018). Towards a therapy for mitochondrial disease: an update. *Biochemical Society Transactions*. https://doi.org/10.1042/bst20180134

Gerards, M., Sallevelt, S. C. E. H., & Smeets, H. J. M. (2016). Leigh syndrome: Resolving the clinical and genetic heterogeneity paves the way for treatment options. *Molecular Genetics and Metabolism*. https://doi.org/10.1016/j.ymgme.2015.12.004

Guenther, M. G., Frampton, G. M., Soldner, F., Hockemeyer, D., Mitalipova, M., Jaenisch, R., & Young, R. A. (2010). Chromatin structure and gene expression programs of human embryonic and induced pluripotent stem cells. *Cell Stem Cell*. https://doi.org/10.1016/j.stem.2010.06.015

Guillaud, L., Setou, M., & Hirokawa, N. (2003). KIF17 dynamics and regulation of NR2B trafficking in hippocampal neurons. *The Journal of Neuroscience : The Official Journal of the Society for Neuroscience*, *23*(1), 131–140. Retrieved from http://www.ncbi.nlm.nih.gov/pubmed/12514209

Hannappel, A., Bundschuh, F. A., & Ludwig, B. (2012). Role of Surf1 in heme recruitment for bacterial COX biogenesis. *Biochimica et Biophysica Acta - Bioenergetics*. https://doi.org/10.1016/j.bbabio.2011.09.007

Harris, J. J., Jolivet, R., & Attwell, D. (2012). Synaptic Energy Use and Supply. *Neuron*. https://doi.org/10.1016/j.neuron.2012.08.019

Hasin, Y., Seldin, M., & Lusis, A. (2017). Multi-omics approaches to disease. *Genome Biology*, *18*(1), 1–15. https://doi.org/10.1186/s13059-017-1215-1

He, Y., Zhang, H., Yung, A., Villeda, S. A., Jaeger, P. A., Olayiwola, O., … Wyss-Coray, T. (2014). ALK5-dependent TGF-β 2 signaling is a major determinant of late-stage adult neurogenesis. *Nature Neuroscience*, *17*(7), 943–952. https://doi.org/10.1038/nn.3732

Herst, P. M., Rowe, M. R., Carson, G. M., & Berridge, M. V. (2017). Functional mitochondria in health and disease. *Frontiers in Endocrinology*, *8*(NOV). https://doi.org/10.3389/fendo.2017.00296

Hu, C., Chen, W., Myers, S. J., Yuan, H., & Traynelis, S. F. (2016). Human GRIN2B variants in neurodevelopmental disorders. *Journal of Pharmacological Sciences*. https://doi.org/10.1016/j.jphs.2016.10.002

Hüttemann, M., Kadenbach, B., & Grossman, L. I. (2001). Mammalian subunit IV isoforms of cytochrome c oxidase. *Gene*. https://doi.org/10.1016/S0378-1119(01)00385-7

Hyman, C., Hofer, M., Barde, Y. A., Juhasz, M., Yancopoulos, G. D., Squinto, S. P., & Lindsay, R. M. (1991). BDNF is a neurotrophic factor for dopaminergic neurons of the substantia nigra. *Nature*, *350*(6315), 230–232. https://doi.org/10.1038/350230a0

Iannetti, E. F., Smeitink, J. A. M., Beyrath, J., Willems, P. H. G. M., & Koopman, W. J. H. (2016). Multiplexed high-content analysis of mitochondrial morphofunction using live-cell microscopy. *Nature Protocols*. https://doi.org/10.1038/nprot.2016.094

Inak, G., Lorenz, C., Lisowski, P., Zink, A., Mlody, B., & Prigione, A. (2017). Concise Review: Induced Pluripotent Stem Cell-Based Drug Discovery for Mitochondrial Disease. *Stem Cells*. https://doi.org/10.1002/stem.2637

Inak, G., Rybak-Wolf, A., Lisowski, P., Juettner, R., Zink, A., Mlody, B., … Prigione, A. (2019). SURF1 mutations causative of Leigh syndrome impair human neurogenesis. *BioRxiv*. https://doi.org/10.1101/551390

Jain, I. H., Zazzeron, L., Goli, R., Alexa, K., Schatzman-Bone, S., Dhillon, H., … Mootha, V. K. (2016). Hypoxia as a therapy for mitochondrial disease. *Science*. https://doi.org/10.1126/science.aad9642

Johar, K., Priya, A., Dhar, S., Liu, Q., & Wong-Riley, M. T. T. (2013). Neuron-specific specificity protein 4 bigenomically regulates the transcription of all mitochondria- and nucleus-encoded cytochrome c oxidase subunit genes in neurons. *Journal of Neurochemistry*, *127*(4), 496–508. https://doi.org/10.1111/jnc.12433

Johar, K., Priya, A., Dhar, S., Liu, Q., & Wong-Riley, M. T. T. (2013). Neuron-specific specificity protein 4 bigenomically regulates the transcription of all mitochondria- and nucleus-encoded cytochrome c oxidase subunit genes in neurons. *Journal of Neurochemistry*. https://doi.org/10.1111/jnc.12433

Joost, K., Rodenburg, R., Piirsoo, A., van den Heuvel, B., Zordania, R., & Õunap, K. (2010). A Novel Mutation in the SCO2 Gene in a Neonate With Early-Onset Cardioencephalomyopathy. *Pediatric Neurology*. https://doi.org/10.1016/j.pediatrneurol.2009.10.004

Kadenbach, B., & Hüttemann, M. (2015). The subunit composition and function of mammalian cytochrome c oxidase. *Mitochondrion*. https://doi.org/10.1016/j.mito.2015.07.002

Kang, X., Yu, Q., Huang, Y., Song, B., Chen, Y., Gao, X., … Fan, Y. (2015). Effects of integrating and non-integrating reprogramming methods on copy number variation and genomic stability of human induced pluripotent stem cells. *PLoS ONE*. https://doi.org/10.1371/journal.pone.0131128

Karaa, A., Kriger, J., Grier, J., Holbert, A., Thompson, J. L. P., Parikh, S., & Hirano, M. (2016). Mitochondrial disease patients' perception of dietary supplements' use. *Molecular Genetics and Metabolism*. https://doi.org/10.1016/j.ymgme.2016.07.005

Keenaway, N. G., Carrero-Valenzuela, R. D., Ewart, G., Balan, V. K., Lightowlers, R., Zhang, Y.-Z., … Buist, N. R. M. (2007). Isoforms of Mammalian Cytochrome c Oxidase:Correlation with Human Cytochrome c Oxidase Deficiency. *Pediatric Research*. https://doi.org/10.1203/00006450-199011000-00024

Kelava, I., & Lancaster, M. A. (2016). Stem Cell Models of Human Brain Development. *Cell Stem Cell*. https://doi.org/10.1016/j.stem.2016.05.022

KETY, S. S. (2013). THE GENERAL METABOLISM OF THE BRAIN IN VIVO. In *Metabolism of the Nervous System*. https://doi.org/10.1016/b978-0-08-009062-7.50026-6

Khacho, M., Harris, R., & Slack, R. S. (2019). Mitochondria as central regulators of neural stem cell fate and cognitive function. *Nature Reviews Neuroscience*. https://doi.org/10.1038/s41583-018-0091-3

Khalimonchuk, O., Bestwick, M., Meunier, B., Watts, T. C., & Winge, D. R. (2010). Formation of the Redox Cofactor Centers during Cox1 Maturation in Yeast Cytochrome Oxidase. *Molecular and Cellular Biology*. https://doi.org/10.1128/mcb.00640-09

Kharitonenkov, A., & Adams, A. C. (2014). Inventing new medicines: The FGF21 story. *Molecular Metabolism*. https://doi.org/10.1016/j.molmet.2013.12.003

Khurana, V., Tardiff, D. F., Chung, C. Y., & Lindquist, S. (2015). Toward stem cell-based phenotypic screens for neurodegenerative diseases. *Nature Reviews Neurology*. https://doi.org/10.1038/nrneurol.2015.79

Komaki, H., Nishigaki, Y., Fuku, N., Hosoya, H., Murayama, K., Ohtake, A., … Tanaka, M. (2010). Pyruvate therapy for Leigh syndrome due to cytochrome c oxidase deficiency. *Biochimica et Biophysica Acta - General Subjects*. https://doi.org/10.1016/j.bbagen.2009.07.008

Kovářová, N., Čížková Vrbacká, A., Pecina, P., Stránecký, V., Pronicka, E., Kmoch, S., & Houštěk, J. (2012). Adaptation of respiratory chain biogenesis to cytochrome c oxidase deficiency caused by SURF1 gene mutations. *Biochimica et Biophysica Acta - Molecular Basis of Disease*. https://doi.org/10.1016/j.bbadis.2012.03.007

Kovářová, N., Pecina, P., Nůsková, H., Vrbacký, M., Zeviani, M., Mráček, T., … Houštěk, J. (2016). Tissue- and species-specific differences in cytochrome c oxidase assembly induced by SURF1 defects. *Biochimica et Biophysica Acta - Molecular Basis of Disease*. https://doi.org/10.1016/j.bbadis.2016.01.007

Krauss, S., Brand, M. D., & Buttgereit, F. (2001). Signaling takes a breath - New quantitative perspectives on bioenergetics and signal transduction. *Immunity*. https://doi.org/10.1016/S1074-7613(01)00205-9

Krieglstein, K., Suter-Crazzolara, C., Fischer, W. H., & Unsicker, K. (1995). TGF-beta superfamily members promote survival of midbrain dopaminergic neurons and protect them against MPP+ toxicity. *The EMBO Journal*, *14*(4), 736–742. https://doi.org/10.1002/j.1460-2075.1995.tb07052.x

Lake, N. J., Bird, M. J., Isohanni, P., & Paetau, A. (2015). Leigh Syndrome: Neuropathology and Pathogenesis. *Journal of Neuropathology and Experimental Neurology*, *74*(6), 482–492. https://doi.org/10.1097/NEN.0000000000000195

Lake, N. J., Compton, A. G., Rahman, S., & Thorburn, D. R. (2016). Leigh syndrome: One disorder, more than 75 monogenic causes. *Annals of Neurology*, *79*(2), 190–203. https://doi.org/10.1002/ana.24551

Lancaster, M. A., Renner, M., Martin, C.-A., Wenzel, D., Bicknell, L. S., Hurles, M. E., … Knoblich, J. A. (2013). Cerebral organoids model human brain development and microcephaly. *Nature*. https://doi.org/10.1038/nature12517

Le Scouarnec, S., & Gribble, S. M. (2012). Characterising chromosome rearrangements: Recent technical advances in molecular cytogenetics. *Heredity*. https://doi.org/10.1038/hdy.2011.100

Le Scouarnec, S., & Gribble, S. M. (2012). Characterising chromosome rearrangements: Recent technical advances in molecular cytogenetics. *Heredity*, *108*(1), 75–85. https://doi.org/10.1038/hdy.2011.100

Leary, S. C., Antonicka, H., Sasarman, F., Weraarpachai, W., Cobine, P. A., Pan, M., … Shoubridge, E. A. (2013). Novel mutations in SCO1 as a cause of fatal infantile encephalopathy and lactic acidosis. *Human Mutation*, *34*(10), 1366–1370. https://doi.org/10.1002/humu.22385

Lee, C. F., Caudal, A., Abell, L., Nagana Gowda, G. A., & Tian, R. (2019). Targeting NAD + Metabolism as Interventions for Mitochondrial Disease. *Scientific Reports*, *9*(1), 1–10. https://doi.org/10.1038/s41598-019-39419-4

Lehmann, D., & McFarland, R. (2018). Overview of Approaches to Mitochondrial Disease Therapy. *Journal of Inborn Errors of Metabolism and Screening*. https://doi.org/10.1177/2326409817752960

LEIGH, D. (1951). Subacute necrotizing encephalomyelopathy in an infant. *Journal of Neurology, Neurosurgery, and Psychiatry*.

Li, M., Wang, X., Meintzer, M. K., Laessig, T., Birnbaum, M. J., & Heidenreich, K. A. (2002). Cyclic AMP Promotes Neuronal Survival by Phosphorylation of Glycogen Synthase Kinase 3beta. *Molecular and Cellular Biology*, *20*(24), 9356–9363. https://doi.org/10.1128/mcb.20.24.9356-9363.2000

Lim, S. C., Smith, K. R., Stroud, D. A., Compton, A. G., Tucker, E. J., Dasvarma, A., … Thorburn, D. R. (2014). A founder mutation in PET100 causes isolated complex IV deficiency in Lebanese individuals with Leigh syndrome. *American Journal of Human Genetics*, *94*(2), 209–222. https://doi.org/10.1016/j.ajhg.2013.12.015

Liu, C., Oikonomopoulos, A., Sayed, N., & Wu, J. C. (2018). Modeling human diseases with induced pluripotent stem cells: from 2D to 3D and beyond. *Development*. https://doi.org/10.1242/dev.156166

Liu, C., Oikonomopoulos, A., Sayed, N., & Wu, J. C. (2018). Modeling human diseases with induced pluripotent stem cells: from 2D to 3D and beyond. *Development*, *145*(5), dev156166. https://doi.org/10.1242/dev.156166

Lorenz, C., Lesimple, P., Bukowiecki, R., Zink, A., Inak, G., Mlody, B., … Prigione, A. (2017). Human iPSC-Derived Neural Progenitors Are an Effective Drug Discovery Model for Neurological mtDNA Disorders. *Cell Stem Cell*. https://doi.org/10.1016/j.stem.2016.12.013

Love, M. I., Huber, W., & Anders, S. (2014). Moderated estimation of fold change and dispersion for RNA-seq data with DESeq2. *Genome Biology*. https://doi.org/10.1186/s13059-014-0550-8

Madsen, P. L., Cruz, N. F., Sokoloff, L., & Dienel, G. A. (1999). Cerebral oxygen/glucose ratio is low during sensory stimulation and rises above normal during recovery: Excess glucose consumption during stimulation is not accounted for by lactate efflux from or accumulation in brain tissue. *Journal of Cerebral Blood Flow and Metabolism*. https://doi.org/10.1097/00004647-199904000-00005

Manley, G. (2013). *Public Access NIH Public Access*. *71*(2), 233–236. https://doi.org/10.1038/mp.2011.182.doi

Martinelli, D., Catteruccia, M., Piemonte, F., Pastore, A., Tozzi, G., Dionisi-Vici, C., … Miller, G. (2012). EPI-743 reverses the progression of the pediatric mitochondrial disease-Genetically defined Leigh Syndrome. *Molecular Genetics and Metabolism*. https://doi.org/10.1016/j.ymgme.2012.09.007

Mashkevich, G., Repetto, B., Glerum, D. M., Jin, C., & Tzagoloff, A. (1997). SHY1, the yeast homolog of the mammalian SURF-1 gene, encodes a mitochondrial protein required for respiration. *Journal of Biological Chemistry*. https://doi.org/10.1074/jbc.272.22.14356

Matthews, P. M., Marchington, D. R., Land, J., Brown, M., & Brown, G. K. (1993). *Molecular Genetic X-linked Form of Leigh ' s Syndrome*. 0–3.

Mazuel, L., Blanc, J., Repond, C., Bouchaud, V., Raffard, G., Déglon, N., … Bouzier-Sore, A. K. (2017). A neuronal MCT2 knockdown in the rat somatosensory cortex reduces both the NMR lactate signal and the BOLD response during whisker stimulation. *PLoS ONE*. https://doi.org/10.1371/journal.pone.0174990

McCauley, H. A., & Wells, J. M. (2017). Pluripotent stem cell-derived organoids: using principles of developmental biology to grow human tissues in a dish. *Development*. https://doi.org/10.1242/dev.140731

McFarland, R., Taylor, R. W., & Turnbull, D. M. (2010). A neurological perspective on mitochondrial disease. *The Lancet Neurology*, *9*(8), 829–840. https://doi.org/10.1016/S1474-4422(10)70116-2

McQuate, A., Latorre-Esteves, E., & Barria, A. (2017). A Wnt/Calcium Signaling Cascade Regulates Neuronal Excitability and Trafficking of NMDARs. *Cell Reports*, *21*(1), 60–69. https://doi.org/10.1016/j.celrep.2017.09.023

Mlody, B., & Prigione, A. (2016). A Glycolytic Solution for Pluripotent Stem Cells. *Cell Stem Cell*. https://doi.org/10.1016/j.stem.2016.09.005

Morin, C., Mitchell, G., Larochelle, J., Lambert, M., Ogier, H., Robinson, B. H., & De Braekeleer, M. (1993). Clinical, metabolic, and genetic aspects of cytochrome C oxidase deficiency in Saguenay-Lac-Saint-Jean. *American Journal of Human Genetics*, *53*(2), 488–496. Retrieved from http://www.ncbi.nlm.nih.gov/pubmed/8392291%0Ahttp://www.pubmedcentral.nih.gov/articlerender.fcgi?artid=PMC1682365

Nakashima, H., Tsujimura, K., Irie, K., Ishizu, M., Pan, M., Kameda, T., & Nakashima, K. (2018). Canonical TGF-β Signaling Negatively Regulates Neuronal Morphogenesis through TGIF/Smad Complex-Mediated CRMP2 Suppression. *The Journal of Neuroscience*. https://doi.org/10.1523/JNEUROSCI.2423-17.2018

Nijtmans, L. G. J., Taanman, J. W., Muijsers, A. O., Speijer, D., & Van Den Bogert, C. (1998). Assembly of cytochrome-c oxidase in cultured human cells. *European Journal of Biochemistry*. https://doi.org/10.1046/j.1432-1327.1998.2540389.x

Ostergaard, E., Bindoff, L. A., Tzoulis, C., Tulinius, M., Lönnqvist, T., Naess, K., … De Meirleir, L. (2014). A multicenter study on Leigh syndrome: disease course and predictors of survival. *Orphanet Journal of Rare Diseases*, *9*(1), 52. https://doi.org/10.1186/1750-1172-9-52

Ostergaard, E., Hansen, F. J., Sorensen, N., Duno, M., Vissing, J., Larsen, P. L., … Schwartz, M. (2007). Mitochondrial encephalomyopathy with elevated methylmalonic acid is caused by SUCLA2 mutations. *Brain*, *130*(3), 853–861. https://doi.org/10.1093/brain/awl383

Panov, A., Orynbayeva, Z., Vavilin, V., & Lyakhovich, V. (2014). Fatty Acids in Energy Metabolism of the Central Nervous System. *BioMed Research International*, *2014*, 1–22. https://doi.org/10.1155/2014/472459

Parikh, P., Mani, U., & Iyer, U. (2003). Role of Spirulina in the Control of Glycemia and Lipidemia in Type 2 Diabetes Mellitus . *Journal of Medicinal Food*. https://doi.org/10.1089/10966200152744463

Pastore, A., Petrillo, S., Tozzi, G., Carrozzo, R., Martinelli, D., Dionisi-Vici, C., … Piemonte, F. (2013). Glutathione: A redox signature in monitoring EPI-743 therapy in children with mitochondrial encephalomyopathies. *Molecular Genetics and Metabolism*. https://doi.org/10.1016/j.ymgme.2013.03.011

Pata, I., Studer, M., van Doorninck, J. H., Briscoe, J., Kuuse, S., Engel, J. D., … Karis, A. (1999). The transcription factor GATA3 is a downstream effector of Hoxb1 specification in rhombomere 4. *Development (Cambridge, England)*.

Patel, K. P., O'Brien, T. W., Subramony, S. H., Shuster, J., & Stacpoole, P. W. (2012). The spectrum of pyruvate dehydrogenase complex deficiency: clinical, biochemical and genetic features in 371 patients. *Molecular Genetics and Metabolism*.

Paulsen, B. S., Mandal, P. K., Frock, R. L., Boyraz, B., Yadav, R., Upadhyayula, S., … Rossi, D. J. (2017). Ectopic expression of RAD52 and dn53BP1 improves homology-directed repair during CRISPR-Cas9 genome editing. *Nature Biomedical Engineering*. https://doi.org/10.1038/s41551-017-0145-2

Paulsen, B. S., Mandal, P. K., Frock, R. L., Boyraz, B., Yadav, R., Upadhyayula, S., … Rossi, D. J. (2017). Ectopic expression of RAD52 and dn53BP1 improves homology-directed repair during CRISPR-Cas9 genome editing. *Nature Biomedical Engineering*. https://doi.org/10.1038/s41551-017-0145-2

Pecina, P., Čapková, M., Chowdhury, S. K. R., Drahota, Z., Dubot, A., Vojtíšková, A., … Houštěk, J. (2003). Functional alteration of cytochrome c oxidase by SURF1 mutations in Leigh syndrome. *Biochimica et Biophysica Acta - Molecular Basis of Disease*, *1639*(1), 53–63. https://doi.org/10.1016/S0925-4439(03)00127-3

Pecinai, P., Houšťková, H., Hansíková, H., Zeman, J., & Houštěk, J. (2004). Genetic Defects of Cytochrome c Oxidase Assembly. *Physiological Research*.

Pitceathly, R. D. S., Rahman, S., Wedatilake, Y., Polke, J. M., Cirak, S., Foley, A. R., … Hanna, M. G. (2013). NDUFA4 Mutations Underlie Dysfunction of a Cytochrome c Oxidase Subunit Linked to Human Neurological Disease. *Cell Reports*, *3*(6), 1795–1805. https://doi.org/10.1016/j.celrep.2013.05.005

Pquignot, M. O., Dey, R., Zeviani, M., Tiranti, V., Godinot, C., Poyau, A., … Marsac, C. (2001). Mutations in the SURF1 gene associated with Leigh Syndrome and cytochrome c oxidase deficiency. *Human Mutation*. https://doi.org/10.1002/humu.1112

Prigione, A., & Adjaye, J. (2011). Modulation of mitochondrial biogenesis and bioenergetic metabolism upon in vitro and in vivo differentiation of human ES and iPS cells. *International Journal of Developmental Biology*. https://doi.org/10.1387/ijdb.103198ap

Priya, A., Johar, K., & Wong-Riley, M. T. T. (2013). Nuclear respiratory factor 2 regulates the expression of the same NMDA receptor subunit genes as NRF-1: Both factors act by a concurrent and parallel

mechanism to couple energy metabolism and synaptic transmission. *Biochimica et Biophysica Acta - Molecular Cell Research*. https://doi.org/10.1016/j.bbamcr.2012.10.014

Qian, X., Nguyen, H. N., Jacob, F., Song, H., & Ming, G. (2017). Using brain organoids to understand Zika virus-induced microcephaly. *Development*. https://doi.org/10.1242/dev.140707

Quadalti, C., Brunetti, D., Lagutina, I., Duchi, R., Perota, A., Lazzari, G., … Galli, C. (2018). SURF1 knockout cloned pigs: Early onset of a severe lethal phenotype. *Biochimica et Biophysica Acta - Molecular Basis of Disease*. https://doi.org/10.1016/j.bbadis.2018.03.021

Rahman, J., Noronha, A., Thiele, I., & Rahman, S. (2017). Leigh Map: a novel diagnostic resource for mitochondrial disease. *Neuromuscular Disorders*, *27*, S19. https://doi.org/10.1016/s0960-8966(17)30274-2

Rahman, S., Block, R. ., Dahl, H. ., Danks, D. ., Kirby, D. ., Chow, C. ., … Thorburn, D. R. (1996). Leigh Syndrome : Clinical Features and Bi & he & al and DNA Abnormahties. *The Amcrican Neurological Association*, 343–351.

Reimand, J., Arak, T., Adler, P., Kolberg, L., Reisberg, S., Peterson, H., & Vilo, J. (2016). g:Profiler-a web server for functional interpretation of gene lists (2016 update). *Nucleic Acids Research*. https://doi.org/10.1093/nar/gkw199

Reinhardt, P., Glatza, M., Hemmer, K., Tsytsyura, Y., Thiel, C. S., Höing, S., … Sterneckert, J. (2013). Derivation and Expansion Using Only Small Molecules of Human Neural Progenitors for Neurodegenerative Disease Modeling. *PLoS ONE*. https://doi.org/10.1371/journal.pone.0059252

Ross, J. M. (2011). Visualization of Mitochondrial Respiratory Function using Cytochrome C Oxidase / Succinate Dehydrogenase (COX/SDH) Double-labeling Histochemistry. *Journal of Visualized Experiments*, (57), 1–6. https://doi.org/10.3791/3266

Rossi, A., Biancheri, R., Bruno, C., Di Rocco, M., Calvi, A., Pessagno, A., & Tortori-Donati, P. (2003). Leigh syndrome with COX deficiency and SURF1 gene mutations: MR imaging findings. *American Journal of Neuroradiology*, *24*(6), 1188–1191.

Rossi, A., Biancheri, R., Bruno, C., Di Rocco, M., Calvi, A., Pessagno, A., & Tortori-Donati, P. (2003). Leigh syndrome with COX deficiency and SURF1 gene mutations: MR imaging findings. *American Journal of Neuroradiology*.

Ruhoy, I. S., & Saneto, R. P. (2014). The genetics of leigh syndrome and its implications for clinical practice and risk management. *Application of Clinical Genetics*, *7*, 221–234. https://doi.org/10.2147/TACG.S46176

Sabir, J. S. M., Lam, T. T. Y., Ahmed, M. M. M., Li, L., Shen, Y., Abo-Aba, S. E. M., … Guan, Y. (2016). Rationally engineered Cas9 nucleases with improved specificity. *Science*. https://doi.org/10.1126/science.aac8608

Sánchez-Camacho, C., & Bovolenta, P. (2009). Emerging mechanisms in morphogen-mediated axon guidance. *BioEssays*. https://doi.org/10.1002/bies.200900063

Sayed, N., Liu, C., & Wu, J. C. (2016). Translation of Human-Induced Pluripotent Stem Cells from Clinical Trial in a Dish to Precision Medicine. *Journal of the American College of Cardiology*. https://doi.org/10.1016/j.jacc.2016.01.083

Schatz, G. (1967). Mitochondrial Oxidative Phosphorylation. *Angewandte Chemie International Edition in English*, *6*(12), 1035–1046. https://doi.org/10.1002/anie.196710351

Schöndorf, D. C., Ivanyuk, D., Baden, P., Sanchez-Martinez, A., De Cicco, S., Yu, C., … Deleidi, M. (2018). The NAD+ Precursor Nicotinamide Riboside Rescues Mitochondrial Defects and Neuronal Loss in iPSC and Fly Models of Parkinson's Disease. *Cell Reports*. https://doi.org/10.1016/j.celrep.2018.05.009

Schöndorf, D. C., Ivanyuk, D., Baden, P., Sanchez-Martinez, A., De Cicco, S., Yu, C., … Deleidi, M. (2018). The NAD+ Precursor Nicotinamide Riboside Rescues Mitochondrial Defects and Neuronal Loss in iPSC and Fly Models of Parkinson's Disease. *Cell Reports*, *23*(10), 2976–2988. https://doi.org/10.1016/j.celrep.2018.05.009

Scorrano, L., Ashiya, M., Buttle, K., Weiler, S., Oakes, S. A., Mannella, C. A., & Korsmeyer, S. J. (2002). *<Dev Cell 2002 Scorrano-1.pdf>*. *2*, 55–67. https://doi.org/10.1016/S1534-5807(01)00116-2

Seki, T., Yuasa, S., & Fukuda, K. (2012). Generation of induced pluripotent stem cells from a small amount of human peripheral blood using a combination of activated T cells and Sendai virus. *Nature Protocols*. https://doi.org/10.1038/nprot.2012.015

Seth, B., Yadav, A., Agarwal, S., Tiwari, S. K., & Chaturvedi, R. K. (2017). Inhibition of the transforming growth factor-/SMAD cascade mitigates the anti-neurogenic effects of the carbamate pesticide carbofuran. *Journal of Biological Chemistry*, *292*(47), 19423–19440. https://doi.org/10.1074/jbc.M117.798074

Setou, M., Nakagawa, T., & Seog, D. (2012). Receptor-Containing Vesicle Transport Kinesin Superfamily Motor Protein KIF17 and mLin-10 in NMDA Receptor – Containing Vesicle Transport. *Science*, *1796*(2000), 1796–1803. https://doi.org/10.1126/science.288.5472.1796

Sheng, Z. H. (2014). Mitochondrial trafficking and anchoring in neurons: New insight and implications. *Journal of Cell Biology*, *204*(7), 1087–1098. https://doi.org/10.1083/jcb.201312123

Sheng, Z. H. (2017). The Interplay of Axonal Energy Homeostasis and Mitochondrial Trafficking and Anchoring. *Trends in Cell Biology*, *27*(6), 403–416. https://doi.org/10.1016/j.tcb.2017.01.005

Sheng, Z. H. (2014). Mitochondrial trafficking and anchoring in neurons: New insight and implications. *Journal of Cell Biology*. https://doi.org/10.1083/jcb.201312123

Shi, Y., Inoue, H., Wu, J. C., & Yamanaka, S. (2017). Induced pluripotent stem cell technology: A decade of progress. *Nature Reviews Drug Discovery*. https://doi.org/10.1038/nrd.2016.245

Shi, Y., & Massagué, J. (2003). Mechanisms of TGF-β signaling from cell membrane to the nucleus. *Cell*. https://doi.org/10.1016/S0092-8674(03)00432-X

Signes, A., & Fernandez-Vizarra, E. (2018). Assembly of mammalian oxidative phosphorylation complexes I–V and supercomplexes. *Essays In Biochemistry*, *62*(3), 255–270. https://doi.org/10.1042/ebc20170098

Sinkler, C. A., Kalpage, H., Shay, J., Lee, I., Malek, M. H., Grossman, L. I., & Hüttemann, M. (2017). Tissue- and Condition-Specific Isoforms of Mammalian Cytochrome c Oxidase Subunits: From Function to Human Disease. *Oxidative Medicine and Cellular Longevity*, *2017*. https://doi.org/10.1155/2017/1534056

Sloan, S. A., Andersen, J., Paşca, A. M., Birey, F., & Paşca, S. P. (2018). Generation and assembly of human brain region-specific three-dimensional cultures. *Nature Protocols*. https://doi.org/10.1038/s41596-018-0032-7

Smeitink, J. A., Zeviani, M., Turnbull, D. M., & Jacobs, H. T. (2006). Mitochondrial medicine: A metabolic perspective on the pathology of oxidative phosphorylation disorders. *Cell Metabolism*, *3*(1), 9–13. https://doi.org/10.1016/j.cmet.2005.12.001

Smith, D., Gray, J., Mitchell, L., Antholine, W. E., & Hosler, J. P. (2005). Assembly of cytochrome-c oxidase in the absence of assembly protein Surf1p leads to loss of the active site heme. *Journal of Biological Chemistry*. https://doi.org/10.1074/jbc.C500061200

Sokoloff, L., Reivich, M., Kennedy, C., Rosiers, M. H. D., Patlak, C. S., Pettigrew, K. D., … Shinohara, M. (1977). THE [14C]DEOXYGLUCOSE METHOD FOR THE MEASUREMENT OF LOCAL CEREBRAL GLUCOSE UTILIZATION: THEORY, PROCEDURE, AND NORMAL VALUES IN THE CONSCIOUS AND ANESTHETIZED ALBINO RAT. *Journal of Neurochemistry*. https://doi.org/10.1111/j.1471-4159.1977.tb10649.x

Soldner, F., & Jaenisch, R. (2012). iPSC disease modeling. *Science*, *338*(6111), 1155–1156. https://doi.org/10.1126/science.1227682

Spillane, M., Ketschek, A., Jones, S. L., Korobova, F., Marsick, B., Lanier, L., … Gallo, G. (2011). The actin-nucleating Arp2/3 complex contributes to the formation of axonal filopodia and branches through the regulation of actin patch precursors to filopodia. *Developmental Neurobiology*. https://doi.org/10.1002/dneu.20907

Springs, S. F. (2011). Embryonic stem cells / induced pluripotent stem cells. Concise Review : Deciphering the Mechanism Behind Induced Pluripotent Stem Cell Generation. *Cell*, 1645–1649. https://doi.org/10.1002/stem.744

St. John, J. C., Ramalho-Santos, J., Gray, H. L., Petrosko, P., Rawe, V. Y., Navara, C. S., … Schatten, G. P. (2005). The Expression of Mitochondrial DNA Transcription Factors during Early Cardiomyocyte In Vitro Differentiation from Human Embryonic Stem Cells. *Cloning and Stem Cells*. https://doi.org/10.1089/clo.2005.7.141

Takahashi, K., & Yamanaka, S. (2006). Induction of pluripotent stem cells from mouse embryonic and adult fibroblast cultures by defined factors. *Cell*. https://doi.org/10.1016/j.cell.2006.07.024

Teleman, A. A., Strigini, M., & Cohen, S. M. (2001). Shaping morphogen gradients. *Cell*. https://doi.org/10.1016/S0092-8674(01)00377-4

Timón-Gómez, A., Nývltová, E., Abriata, L. A., Vila, A. J., Hosler, J., & Barrientos, A. (2018). Mitochondrial cytochrome c oxidase biogenesis: Recent Developments. *Seminars in Cell and Developmental Biology*, *76*, 163–178. https://doi.org/10.1016/j.semcdb.2017.08.055

Tiranti, V., Hoertnagel, K., Carrozzo, R., Galimberti, C., Munaro, M., Granatiero, M., … Zeviani, M. (2002). Mutations of SURF-1 in Leigh Disease Associated with Cytochrome c Oxidase Deficiency. *The American Journal of Human Genetics*, *63*(6), 1609–1621. https://doi.org/10.1086/302150

Tokusumi, T., Iida, A., Hirata, T., Kato, A., Nagai, Y., & Hasegawa, M. (2002). Recombinant Sendai viruses expressing different levels of a foreign reporter gene. *Virus Research*. https://doi.org/10.1016/S0168-1702(02)00047-3

Vaarmann, A., Mandel, M., Zeb, A., Wareski, P., Liiv, J., Kuum, M., … Kaasik, A. (2016). Mitochondrial biogenesis is required for axonal growth. *Journal of Cell Science*, *129*(12), e1.2-e1.2. https://doi.org/10.1242/jcs.193037

Vafai, S. B., & Mootha, V. K. (2012). Mitochondrial disorders as windows into an ancient organelle. *Nature*, *491*(7424), 374–383. https://doi.org/10.1038/nature11707

Villani, G., Greco, M., Papa, S., & Attardi, G. (1999). Low reserve of cytochrome c oxidase capacity in vivo in the respiratory chain of a variety of human cell types. *Journal of Biological Chemistry*, *273*(48), 31829–31836. https://doi.org/10.1074/jbc.273.48.31829

Viscomi, C., Bottani, E., Civiletto, G., Cerutti, R., Moggio, M., Fagiolari, G., … Zeviani, M. (2011). In vivo correction of COX deficiency by activation of the AMPK/PGC-1α axis. *Cell Metabolism*. https://doi.org/10.1016/j.cmet.2011.04.011

Viscomi, C., Bottani, E., & Zeviani, M. (2015). Emerging concepts in the therapy of mitochondrial disease. *Biochimica et Biophysica Acta - Bioenergetics*. https://doi.org/10.1016/j.bbabio.2015.03.001

Vladimirovich, C. I., Erdem, D., Mariia, B., Igor, K., Sergey, L., & Piotr, K. (2019). Cytochrome c Oxidase on the Crossroads of Transcriptional Regulation and Bioenergetics. *Frontiers in Physiology*, *10*(May), 1–6. https://doi.org/10.3389/fphys.2019.00644

Wada, T., Honda, M., Minami, I., Tooi, N., Amagai, Y., Nakatsuji, N., & Aiba, K. (2009). Highly efficient differentiation and enrichment of spinal motor neurons derived from human and monkey embryonic stem cells. *PLoS ONE*. https://doi.org/10.1371/journal.pone.0006722

Wang, X., Sterr, M., Burtscher, I., Chen, S., Hieronimus, A., Machicao, F., … Lickert, H. (2018). Genome-wide analysis of PDX1 target genes in human pancreatic progenitors. *Molecular Metabolism*. https://doi.org/10.1016/j.molmet.2018.01.011

Wang, X., Sterr, M., Burtscher, I., Chen, S., Hieronimus, A., Machicao, F., … Lickert, H. (2018). Genome-wide analysis of PDX1 target genes in human pancreatic progenitors. *Molecular Metabolism*. https://doi.org/10.1016/j.molmet.2018.01.011

Wedatilake, Y., Brown, R. M., McFarland, R., Yaplito-Lee, J., Morris, A. A. M., Champion, M., … Rahman, S. (2013). SURF1 deficiency: A multi-center natural history study. *Orphanet Journal of Rare Diseases*. https://doi.org/10.1186/1750-1172-8-96

Wedatilake, Y., Brown, R. M., McFarland, R., Yaplito-Lee, J., Morris, A. A. M., Champion, M., … Rahman, S. (2013). SURF1 deficiency: A multi-center natural history study. *Orphanet Journal of Rare Diseases*, *8*(1), 1. https://doi.org/10.1186/1750-1172-8-96

Wegner, A. M., Nebhan, C. A., Hu, L., Majumdar, D., Meier, K. M., Weaver, A. M., & Webb, D. J. (2008). N-WASP and the Arp2/3 complex are critical regulators of actin in the development of dendritic spines and synapses. *Journal of Biological Chemistry*. https://doi.org/10.1074/jbc.M801555200

Weraarpachai, W., Antonicka, H., Sasarman, F., Seeger, J., Schrank, B., Kolesar, J. E., … Shoubridge, E. A. (2009). Mutation in TACO1, encoding a translational activator of COX I, results in cytochrome c oxidase deficiency and late-onset Leigh syndrome. *Nature Genetics*. https://doi.org/10.1038/ng.390

Wikström, M., & Sharma, V. (2018). Proton pumping by cytochrome c oxidase – A 40 year anniversary. *Biochimica et Biophysica Acta - Bioenergetics*. https://doi.org/10.1016/j.bbabio.2018.03.009

Williams, S. L., Valnot, I., Rustin, P., & Taanman, J. W. (2004). Cytochrome c Oxidase Subassemblies in Fibroblast Cultures from Patients Carrying Mutations in COX10, SCO1, or SURF1. *Journal of Biological Chemistry*, *279*(9), 7462–7469. https://doi.org/10.1074/jbc.M309232200

Wong-Riley, M. T. T. (2012). Bigenomic regulation of cytochrome c oxidase in neurons and the tight coupling between neuronal activity and energy metabolism. *Advances in Experimental Medicine and Biology*. https://doi.org/10.1007/978-1-4614-3573-0_12

Wong-Riley, M. T. T. (1989). Cytochrome oxidase: an endogenous metabolic marker for neuronal activity. *Trends in Neurosciences*. https://doi.org/10.1016/0166-2236(89)90165-3

Xia, X., & Wong, S. T. (2012). Concise review: A high-content screening approach to stem cell research and drug discovery. *Stem Cells*. https://doi.org/10.1002/stem.1168

Yao, J., & Shoubridge, E. A. (1999). Expression and functional analysis of SURF1 in Leigh syndrome patients with cytochrome c oxidase deficiency. *Human Molecular Genetics*. https://doi.org/10.1093/hmg/8.13.2541

Yatsuga, S., & Suomalainen, A. (2012). Effect of bezafibrate treatment on late-onset mitochondrial myopathy in mice. *Human Molecular Genetics*, *21*(3), 526–535. https://doi.org/10.1093/hmg/ddr482

Yatsuga, S., & Suomalainen, A. (2012). Effect of bezafibrate treatment on late-onset mitochondrial myopathy in mice. *Human Molecular Genetics*. https://doi.org/10.1093/hmg/ddr482

Yellen, G. (2018). Fueling thought: Management of glycolysis and oxidative phosphorylation in neuronal metabolism. *Journal of Cell Biology*. https://doi.org/10.1083/jcb.201803152

Yu, J., Chau, K. F., Vodyanik, M. A., Jiang, J., & Jiang, Y. (2011). Efficient feeder-free episomal reprogramming with small molecules. *PLoS ONE*. https://doi.org/10.1371/journal.pone.0017557

Zazzeron, L., Zhang, F., Goli, R., Zapol, W. M., Dhillon, H., Goldberger, O., … Peng, J. (2016). Hypoxia as a therapy for mitochondrial disease. *Science*, *352*(6281), 54–61. https://doi.org/10.1126/science.aad9642

Zhang, J., Khvorostov, I., Hong, J. S., Oktay, Y., Vergnes, L., Nuebel, E., … Teitell, M. A. (2011). UCP2 regulates energy metabolism and differentiation potential of human pluripotent stem cells. *EMBO Journal*. https://doi.org/10.1038/emboj.2011.401

Zhang, K., Osakada, Y., Xie, W., & Cui, B. (2011). Automated image analysis for tracking cargo transport in axons. *Microscopy Research and Technique*. https://doi.org/10.1002/jemt.20934

Zhao, M.-T., Chen, H., Liu, Q., Shao, N.-Y., Sayed, N., Wo, H.-T., … Wu, J. C. (2017). Molecular and functional resemblance of differentiated cells derived from isogenic human iPSCs and SCNT-derived ESCs. *Proceedings of the National Academy of Sciences*. https://doi.org/10.1073/pnas.1708991114

Zhu, Z., Yao, J., Johns, T., Fu, K., De Bie, I., Macmillan, C., … Shoubridge, E. A. (1998). SURF1, encoding a factor involved in the biogenesis of cytochrome c oxidase, is mutated in Leigh syndrome. *Nature Genetics*. https://doi.org/10.1038/3804

Zhu, Z., Yao, J., Johns, T., Fu, K., De Bie, I., Macmillan, C., … Shoubridge, E. A. (1998). SURF1, encoding a factor involved in the biogenesis of cytochrome c oxidase, is mutated in Leigh syndrome. *Nature Genetics*. https://doi.org/10.1038/3804

Zhu, Z., Yao, J., Johns, T., Fu, K., De Bie, I., Macmillan, C., … Shoubridge, E. A. (1998). SURF1, encoding a factor involved in the biogenesis of cytochrome c oxidase, is mutated in Leigh syndrome. *Nature Genetics*, *20*(4), 337–343. https://doi.org/10.1038/3804

Zordan, M. A., Cisotto, P., Benna, C., Agostino, A., Rizzo, G., Piccin, A., … Costa, R. (2006). Post-transcriptional silencing and functional characterization of the Drosophila melanogaster homolog of human Surf1. *Genetics*. https://doi.org/10.1534/genetics.105.049072

Declaration of Authorship

I hereby certify that this submitted thesis has been composed by me and is based on my own work, unless stated otherwise. No other person's work has been used without acknowledgement in this thesis. All references and verbatim extracts have been quoted, and all sources of information, including graphs and data sets, have been specifically acknowledged.

Berlin, 27 June 2019

Gizem Inak-Girrbach